Nuclear Structure of Positive Parity Levels in ^{15}N as Studied by Inelastic Electron Scattering

by

Salah Abdel-Kawy Salem

Presented as a Thesis for the Degree of Doctor of Philosophy
to the Department of Physics and Astronomy,
The University of Glasgow,
December 1987.

Abstract

High resolution measurements of inelastic electron scattering cross sections from the states in ^{15}N (gas target of 99% ^{15}N enrichment) up to 23.5 MeV excitation have been performed at NIKHEF-K Amsterdam. The measurements were carried out at 70, 130, 300, and 430 MeV incident electron energy with an angular range from 40° to 98.5° covering a momentum transfer region between 0.5 and 3.2 fm^{-1}. The data of the present experiment together with the existing data obtained at a scattering angle of 180° were used to obtain the longitudinal and transverse components of the form factors for most of the observed excitations. The positive parity states are presented in this thesis while the negative parity states have been discussed in a Ph.D thesis by J.W. deVries at Utrecht University, The Netherlands (November 1987).

A model independent analysis was used to extract the transition charge density and reduced transition probability for most of the states below 12 MeV of excitations. The B(E1) values are in an overall agreement with those measured by (γ, γ') and those calculated by the shell model.

The longitudinal and transverse form factors were compared with the predictions of a nuclear shell model calculation performed in a $3\hbar\omega$ space. The agreement with the shell model predictions was found to be generally satisfactory. A much improved description of the longitudinal data for the low-lying octupole transitions is obtained by mixing contributions from a collective state.

A number of M4 transitions identified by this experiment are in agreement with those measured by the pion scattering experiment. The (e,e') data were used to remove one of the two possible solutions of the spectroscopic amplitudes in the (π, π') analysis.

A large number of states beyond 13 MeV of excitation were observed in this experiment. In the region beyond 18 MeV several new states were identified and width parameters for these states have been obtained.

Finally, in the giant resonance region on ^{15}N the work of Ansaldo has been extended up to much higher momentum transfer.

Acknowledgements

I would like to thank, above all, Dr. Ravi Singhal, thesis supervisor, who has been the principal driving and inspiring force behind this work. His enthusiasm and physical intuition were the decisive factors for the completion of this project. His guidance, patience and expert advice during the period of this work can not be adequately acknowledged.

I gratefully acknowledge the receipt of a full grant from the Ministry of Higher Education, Egypt, during the period of this research.

I would like to thank Dr. Kees de Jager of the National Institute for Nuclear Physics and High-Energy Physics (NIKHEF-K) who afforded me the use of the NIKHEF facilities. Special thanks to Johannes de Vries for his help during data taking and analysis.

Many thanks to Dr. John Millener for providing us with shell model calculations presented here.

My thanks to Professors Owens and Reid, who as Directors of the Kelvin Laboratory, afforded me the use of the Kelvin Laboratory facilities.

May I thank everyone at the Kelvin Laboratory, staff and students, for their enthusiasm and frequent assistance with computing problems.

I would like to thank the system staff Andy Sibbald and Arrick Wilkinson who showed much patience in dealing with my computing problems. Many thanks also to Mrs. Eileen Taylor who helped in the preparation of the diagrams. My warm thanks to Steve Dancer, Gary Miller and Peter Wallace who lighted days of heavy physics with irrespressible humour.

I am extremely grateful to the Science and Engineering Research Council who have funded my attendance at NIKHEF. Many thanks also to Professors Laing and Hughes, who as successive heads of department, have provided funding for conferences.

A big thank must go to my wife, Mona, and my son, Ahmed, for their patience and encouragement.

Finally, I would like to dedicate this thesis to my much loved Parents for their encouragement and support.

Contents

List of Figures

List of Tables

Chapter 1

Introduction

Our knowledge concerning the structure of nuclei has improved through the development of nuclear models. Very often, due to continuing improvements of the models, it was possible not only to reach a qualitative description of the observed phenomena, but also to account for them quantitatively. In the analysis of experimental nuclear data, the models may be classified as: *macroscopic* and *microscopic* according to the assumptions introduced.

Macroscopic models describe the nuclear system in terms of collective variables like the radius and the skin thickness of the charge distribution and can easily be used to fit the data to provide meaningful parameters such as the transition strength and the transition radius. The rotational and vibrational models are examples of commonly used macroscopic models. On the other hand in microscopic models the nucleus is described in terms of motion of individual particles. These are more fundamental descriptions of the nucleus and the nuclear shell model is an example of a widely used microscopic model which has been quite successful in explaining a large body of experimental data.

In the nuclear shell model it is assumed that each nucleon moves in a potential that represents the average interaction with the other nucleons in the nucleus. The potential is generally assumed to be harmonic oscillator or Woods-Saxon type. The model predicts that nucleons occupy well defined angular momentum states in a nucleus. A study of the charge density difference $\Delta\rho(r)$ between ^{205}Tl and ^{206}Pb has provided clear evidence that the concept of a shell model wave function even in the centre of a heavy nucleus like lead is well founded[1].

Improvements in nuclear models depend on the availability of more sophisticated data from nuclear reactions. In general, one studies different aspects of nuclear structure by performing experiments with different nuclear probes e.g. hadron scattering experiments are mostly sensitive to the nuclear surface while photon and electron beams interact with the full volume of the nucleus and hence require a knowledge of the distribution of nucleons in the nuclear interior as well.

Electron scattering has some special features that make it one of the best tools for nuclear-structure studies. The electron interacts with the nuclear charge and current distributions through the electromagnetic interaction, which is well known. Acting as a source of virtual photons, it provides a momentum transfer map of a specified nuclear excitation. The spatial transition charge, current, and magnetization densities can then be obtained from the momentum transfer (q) dependence of a nuclear transition in a manner which is relatively free from ambiguities of unknown reaction mechanisms. This makes electron scattering an ideal probe which enables one to test nuclear models.

Most electron scattering results, for a long time, were interpreted in terms of macroscopic models. These models have had considerable success, partly because most of the early data did not extend to high enough q to allow an extraction of the details of the nuclear interior. Further, in many cases strongly excited levels were studied, e.g. collective quadrupole and octupole transitions. Therefore the macroscopic model was able to describe the gross features of the measured transition charge density in terms of a surface peaked shape. Modern electron scattering facilities provide higher precision data which also extend to high enough q values and allow study of structures in the nuclear interior that cannot be described by macroscopic models. A microscopic treatment is necessary in order to understand the details of the new data.

In electron scattering both longitudinal and transverse components of the transition are excited and their comprehensive experimental measurement is highly desirable for tests of nuclear models. Unfortunately very few experiments to date have measured the longitudinal as well as the transverse components of the electron scattering cross section. This is because the longitudinal transitions

in the spin zero ground state nuclei have in general extremely weak transverse components which are difficult to measure even with a 180° system where the sensitivity to transverse cross sections is a maximum. For non-zero ground state spins, transitions generally involve several multipoles which are difficult to separate and a comparison with theoretical predictions becomes cumbersome.

The purpose of the present experiment was to provide accurate longitudinal and transverse cross sections of ^{15}N states up to 25 MeV excitation energy and over a large range of momentum transfer. There are several reasons which make ^{15}N an interesting nucleus to study. ^{15}N has a ground state of $J^{\pi} = 1/2^{-}$ and longitudinal cross sections are determined by only one multipole. The transverse excitations include, in general, a magnetic and a transverse electric component. Thus both the longitudinal and transverse cross sections can be measured without too many multipoles crowding the measured data. Since there are only 15 nucleons in ^{15}N, it is possible to perform shell model calculations without severe truncation of the model space. Thus it is felt that ^{15}N provides a situation where a relatively rigorous comparisons between theory and experiment could be made.

This work is part of the bigger project for studying the p-shell nuclei by electron scattering. The cross sections for electron scattering from ^{15}N were measured at NIKHEF-K in Amsterdam. A gas target was used and spectra up to 25 MeV excitation energy were recorded at forward angles covering a momentum transfer range 0.5 - 3.2 fm^{-1}. The corresponding transverse cross sections were obtained previously at a scattering angle of 180° with the MIT-Bates electron scattering facility. The longitudinal and transverse parts of the cross sections could then be individually obtained from these experiments.

Previously, the ^{15}N nucleus has been studied extensively both theoretically and experimentally by many authors using different techniques.

Theoretically, the properties of ^{15}N levels were studied by several investigators [17], [8]. Detailed calculations were carried out by Lie and Engeland for levels below 12 MeV excitation energy in the framework of a weak coupling model. The positive parity states were taken to be admixtures of 1p-2h and 3p-4h configurations with respect to an ^{16}O core i.e. the particles were assumed

to occupy the (2s,1d) orbitals and the holes the p orbital. Recently another calculation was performed by Millener[18]. In this calculation the full $1\hbar\omega$ and a truncated $3\hbar\omega$ model space was included. The truncation of the $3\hbar\omega$ basis is described in reference [19]. The recent shell model calculations provide more detailed descriptions of the nucleus and the weak coupling model can be considered an approximation of these calculations. For this reason, we shall concentrate on the interpretation of our data in relation to the predictions of the shell model calculations.

Electron scattering cross sections for ^{15}N have been measured in the past at several laboratories[20], [21], and [22]. The Stanford experiment[20] suffered from poor resolution ($\geq$ 400 keV), but a more serious limitation of these data is that no longitudinal transverse separation was carried out. Since nuclear model calculations predict the longitudinal and transverse parts of the form factors separately, this seriously restricts the usefulness of these data for comparison with theory. The data on the inelastic scattering to the low-lying states extended to excitations up to 8 MeV and cross sections and angular distributions corresponding only to the doublet at 5.30 MeV, to the level at 6.3 MeV, and to the three unresolved levels at 7.16, 7.31, and 7.57 MeV were reported. Because of the use of a liquid NH_3 target, the data suffer from an uncertain normalization of the order of 20 % [2]. The Saskatoon experiment[21] was performed with a resolution of approximately 200 keV. The data were accumulated up to 9.5 MeV excitation energy and momentum transfer values between 0.6 and 1.1 fm^{-1} were studied. The cross sections and angular distributions corresponding to the doublet at 5.3 MeV, to the two unresolved levels at 7.16 and 7.31 MeV, and to level at 7.57 MeV were obtained. The data of this experiment were analysed without taking into account Coulomb distortion of the incident and scattered electrons, and it has been shown that such analysis can lead to errors in the resulting reduced transition probabilities. The previous Glasgow data[22] were accumulated up to 7 MeV excitation energies, and momentum transfers between 0.29 to 1.1 fm^{-1}. Cross section values corresponding only to the doublet at 5.3 MeV and to the level at 6.3 MeV were measured. Longitudinal transverse separations were performed and spectroscopic factors were extracted. None of

the existing measurements are adequate for a detailed test of nuclear model and it was felt that new better data are needed to improve and extend the scope of comparison with the shell model for this important nucleus.

The $^{15}N(\gamma,\gamma')$ reaction was used by Moreh et.al[3] to measure the ground-state radiative width of nine levels below 10.2 MeV. These levels are $3/2_1^-$(6.32 MeV), $3/2_1^+$(7.32 MeV), $1/2_2^+$(8.30 MeV), $3/2_2^+$(8.57 MeV), $1/2_3^+$(9.05 MeV), $3/2_2^-$(9.15 MeV), $5/2_1^-$(9.76 MeV), $3/2_3^-$(9.92 MeV), and $3/2_3^+$(10.07 MeV), see figure 1.1. The $1/2_2^+$(8.30 MeV) and the $3/2_2^+$(8.57 MeV) levels were very weakly excited and hence for these states only a rough determination of the width was possible. The $1/2_1^+$(5.29 MeV) and $5/2_1^+$(5.27 MeV) levels were not observed in this experiment because their widths are below the sensitivity of the measurements. The results were compared with the predictions of several nuclear models and relatively good agreement was noted with a large basis shell model calculations without effective charges.

The nucleus ^{15}N has also been studied extensively with strongly interacting probes. Generally, the information obtained from such reactions is not easily interpreted. However, inelastic scattering experiments with protons(p,p'), neutrons(n,n'), etc. have identified the energies and angular momenta of a large number of excited states. Particle and cluster transfer reactions are very successful in identifying levels of definite characteristic e.g. $^{14}C(d,n)^{15}N$ and $^{14}N(d,p)^{15}N$ reactions populate states in ^{15}N which have , respectively, $^{14}C\otimes p$ and $^{14}N\otimes n$ as the dominant structures. The single-particle transfer reactions provide nuclear spectroscopic factors which can be directly compared to the prediction of microscopic models and in general the results of such studies have supported the predictions of recent large basis shell model calculations[18]. The single nucleon transfer reactions with the deuteron as incident particle, the range of angular momenta which can be transfered is limited. These reactions have been very successful in identifying states dominated by 1p-2h configurations[4,5,6,7] with respect to an ^{16}O core, e.g. Kretschmer et al. have been able to identify low-lying positive parity states up to 8.57 MeV in ^{15}N via $^{14}N(d,p)^{15}N$ reaction.

In cluster transfer reactions instead of a single nucleon a multinucleon clus-

ter, e.g., d, t, ^{3}He and α, is transfered and are more sensitive to states with significant 2p-3h, 3p-4h configuration amplitudes. For example the ^{13}C(α,d)^{15}N reaction has been studied by Yasue et al.[11] and many states dominated by 2p-3h configurations have been identified. Because of the posibility of transfering a large angular momentum the cluster transfer reactions have been used to identify many high spin states[13,23,26,24,25]. For example Tserruya et. al[26] have identified high spin states in ^{15}N via ^{12}C(^{7}Li,α)^{15}N reaction.

Finally, a large number of levels were identified in the giant resonance region by Weller et al.[14] and Harakeh et al.[13] using the ^{14}C(p,γ)^{15}N reaction. Ansaldo et al.[15] used electron scattering and obtained longitudinal transverse separation of the cross section in the giant resonance region.

The present thesis is restricted to the study of electroexcitation cross sections of positive parity states in ^{15}N. The negative parity states are the subject of a Ph.D thesis by J.W. deVries[2]. The positive parity states below 12 MeV excitation energy include the $1/2^+$ states at 5.29, 8.31, 9.05 and 11.44 MeV; the $3/2^+$ states at 7.31, 8.57, 10.07, 10.8 and 11.77 MeV; the 5/2+ states at 5.27, 7.15, 9.15 and 10.53 MeV; the $7/2^+$ state at 7.57 MeV and the $9/2^+$ state at 10.69 MeV. The low energy excitation spectrum of ^{15}N states is shown in figure 1.1. A number of states were also observed in the higher excitation energy region. In chapter 2, electron scattering formalism and theoretical models used in the analysis of the present data are discussed. The experimental set up, data collection procedures and the extraction of cross sections are presented in chapter 3. In chapter 4, the analysis of the experimental data to obtain spectroscopic information about ^{15}N and a comparison with shell model results is discussed. Finally, chapter 5 contains the conclusions.

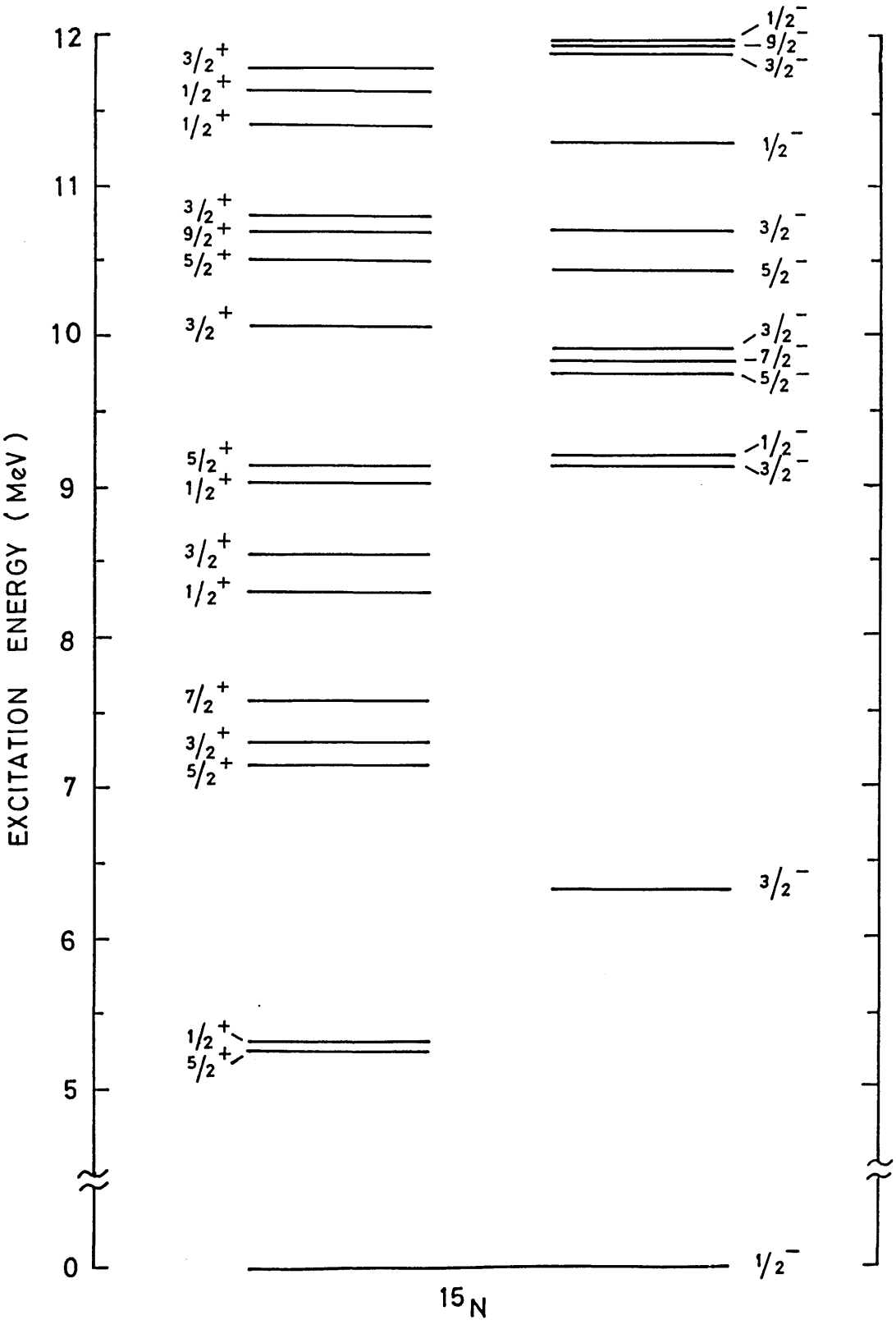

Figure 1.1: *Positive and Negative Parity Levels up to 12 MeV in* ^{15}N.

Chapter 2

Theoretical Background

This chapter consists of two parts. In the first part a resume of the formulas used in inelastic electron scattering will be given. In the second part the various models that have been used to analyse the data are discussed.

2.1 Electron Scattering Formalism

Electrons as a probe have a special place in the various methods of studying nuclear structure. This is because the interaction of electrons with nucleons, the electromagnetic interaction, is well understood. It can be easily and reliably related to nuclear charge, current, and magnetization distributions, as discussed later in this section. Unlike the processes involving real photons for which $\mathbf{q}^2 = \omega^2$, in electron scattering experiments $\mathbf{q}^2 - \omega^2 > 0$, so that for a given state of excitation energy(ω), a range of momentum transfer $\mathbf{q}$ can be selected by varying the incident electron energy and/or the scattered electron angle. This is the key to the determination of nuclear transition densities as the density at a certain r is basically a Fourier transform of the cross section over a complete range of q for the excitation of that state. The different contributions to the electron scattering process can be described conveniently in terms of Feynman diagrams. Figure 2.1(a) represents the one photon exchange Plane Wave Born Approximation (PWBA). The remaining diagrams appear as corrections to PWBA. The corrections to PWBA can be divided into two categories. First, the radiative corrections which result from the contributions of diagrams (b) - (g) in figure 2.1 and the target thickness effects. These effects are discussed in

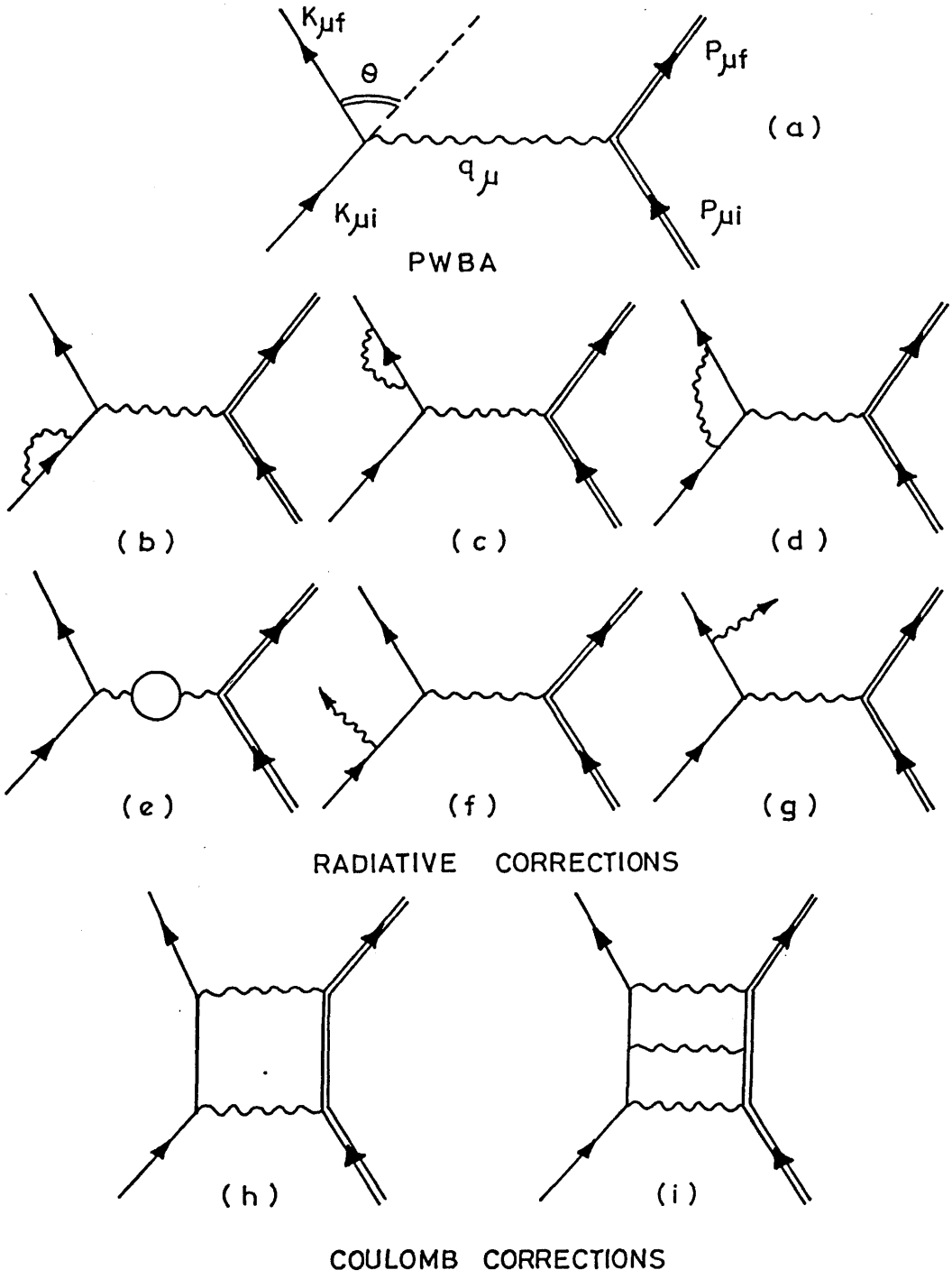

Figure 2.1: *Feynman Diagrams for Electron Scattering Contributions*

subsec. 2.1.3. The second category is the effect arising from the distortion of the electron waves by the Coulomb field of the target nucleus (figure 2.1 (h), (i)) and is discussed in subsec. 2.1.4.

2.1.1 Kinematics

The interaction between the incoming electron and the target nucleus can be described by figure 2.1(a), where

$K_{\mu i}$, $K_{\mu f}$ = the initial and final electron 4-momenta, where
$K_{\mu i} = (iE_i,\mathbf{k}_i)$, $K_{\mu f} = (iE_f,\mathbf{k}_f)$

$P_{\mu i}$, $P_{\mu f}$ = the initial and final nucleus 4-momenta,

θ = the scattering angle of the electron, and

q_μ = the transferred 4-momentum:

$q_\mu^2 = (K_{\mu i} - K_{\mu f})^2 = \mathbf{q}^2 - \omega^2$, where,

$\mathbf{q}$ = three-momentum transfer $\mathbf{q}=\mathbf{k}_i - \mathbf{k}_f$

ω = energy transfer

Note that in the above equation and in the following, the system of natural units is used, $\hbar = c = 1$. This means that energy, momentum, and mass all have the same dimension. Usually the unit used is fm^{-1}. The conversion factor from fm^{-1} to MeV is: $fm^{-1} = 197.33$ MeV.

Using the conservation laws for energy and momentum and neglecting the electron mass, one gets the following formulae:

$$\begin{aligned} q_\mu^2 &= 4E_iE_f \sin^2(\theta/2) \\ E_f &= (E_i - K)/\eta \end{aligned} \tag{2.1}$$

where K = $E_{exc}(1 + E_{exc}/M)$,

E_{exc} = the energy of the state to which the nucleus is excited,

M = the mass of the nucleus, and

η = the recoil factor
= $1 + 2\ E_i \sin^2(\theta/2)/M$.

2.1.2 Electron Scattering Cross Section

The derivation of the cross section for the scattering of high energy electrons from nuclei in PWBA can be found in several review articles [27,28]. It is usually written in the following form :

$$\frac{d\sigma}{d\Omega} = \frac{4\pi\sigma_M}{\eta}\left[\sum_{\lambda=0}^{\infty} \mid F_\lambda^C(q) \mid^2 + (\frac{1}{2} + \tan^2(\theta/2)) \sum_{\lambda=1}^{\infty} \left\{ \mid F_\lambda^E(q) \mid^2 + \mid F_\lambda^M(q) \mid^2 \right\}\right] \tag{2.2}$$

Here σ_M is the Mott cross section given by :

$$\sigma_M = \frac{Z^2\alpha^2\cos^2(\theta/2)}{4E_i^2\sin^4(\theta/2)} \tag{2.3}$$

α being the fine structure constant.

In the derivation of equation 2.2, one-photon exchange is assumed. Further, apart from using plane waves for the incoming and outgoing electron, the approximations m_e=0 and $\hbar\omega = E_i - E_f \ll \hbar cq$ have been made. The nuclear structure enters into the cross section only through the longitudinal form factor F^C and the transverse form factors F^E and F^M. These form factors are functions of the momentum transfer q only. They can be related to the electromagnetic transition operators (M_λ^c, T_λ^e, T_λ^m) as

$$\mid F_\lambda^C(q) \mid^2 = \frac{4\pi}{Z^2(2J_i+1)} \mid < J_f \parallel M_\lambda^c(q) \parallel J_i > \mid^2 \tag{2.4}$$

$$\mid F_\lambda^E(q) \mid^2 = \frac{4\pi}{Z^2(2J_i+1)} \mid < J_f \parallel T_\lambda^e(q) \parallel J_i > \mid^2 \tag{2.5}$$

$$\mid F_\lambda^M(q) \mid^2 = \frac{4\pi}{Z^2(2J_i+1)} \mid < J_f \parallel T_\lambda^m(q) \parallel J_i > \mid^2 \tag{2.6}$$

$$M_{\lambda\mu}^c(q) = \int d^3r j_\lambda(qr) Y_{\lambda\mu} \hat{\rho}(\mathbf{r}) \tag{2.7}$$

$$T_{\lambda\mu}^e(q) = \frac{1}{q}\int d^3r \{\nabla \times j_\lambda(qr)\mathbf{Y}_{\lambda\lambda 1}^\mu\} \cdot \hat{\mathbf{J}}(\mathbf{r}) + q^2 \int d^3r \{j_\lambda(qr)\mathbf{Y}_{\lambda\lambda 1}^\mu\} \cdot \hat{\mu}(\mathbf{r}) \tag{2.8}$$

and

$$T_{\lambda\mu}^m(q) = \int d^3r \{j_\lambda(qr)\mathbf{Y}_{\lambda\lambda 1}^\mu\} \cdot \hat{\mathbf{J}}(\mathbf{r}) + \int d^3r \{\nabla \times j_\lambda(qr)\mathbf{Y}_{\lambda\lambda 1}^\mu\} \cdot \hat{\mu}(\mathbf{r}) \tag{2.9}$$

where $\hat{\rho}(\mathbf{r})$, $\hat{J}(\mathbf{r})$, and $\hat{\mu}(\mathbf{r})$, are the nuclear charge, convection current, and magnetisation current density operators, respectively, $j_\lambda(qr)$ is the spherical

Bessel function of order λ, $Y_{\lambda\mu}$ is the spherical harmonic, and $\mathbf{Y}_{\lambda\lambda 1}$ is the vector spherical harmonic.

The matrix elements of these operators, which appear in equations 2.4 to 2.6 are the reduced matrix elements; these are related to the ordinary matrix elements of the operators through the Wigner Eckart Theorem [32] viz.

$$< J_f M_f \mid \hat{M}_{\lambda\mu} \mid J_i M_i >= (-1)^{J_f - M_f} \begin{pmatrix} J_f & \lambda & J_i \\ -M_f & \mu & M_i \end{pmatrix} < J_f \parallel \hat{M}_\lambda \parallel J_i >$$

The matrix element between two nuclear states with angular momenta J_i and J_f must satisfy the rule

$$\mid J_i - J_f \mid \leq \lambda \leq \mid J_i + J_f \mid .$$

The operators have restrictions on the multipolarity and parity given by

$$\begin{array}{llll} \hat{M}^c_\lambda & \lambda \geq 0 & (\pi) = (-1)^\lambda \\ \hat{T}^e_\lambda & \lambda \geq 1 & (\pi) = (-1)^\lambda \\ \hat{T}^m_\lambda & \lambda \geq 1 & (\pi) = (-1)^{\lambda+1} \end{array}$$

Experimentally, the measurement of the cross section is a measurement of the sum of form factors where the momentum transfer q can be varied either through changing the incident energy or the scattering angle or both. The relative contribution of the transverse form factor to the total cross section differes in forward and in backward direction through the term $(1/2 + \tan^2(\theta/2))$ in equation 2.2. Thus a measurement in forward and in backward directions at the same momentum transfer provides a means of separation of the longitudinal and transverse form factors. In this separation ideally, the backward measurement is done at 180 degree, where the contributions from the longitudinal form factor is zero. We have used this method to calculate the longitudinal form factor, see chapter 3.

2.1.3 Radiative Corrections to Electron Scattering

In the analysis of an electron scattering experiment, necessary corrections due to radiation and ionization effects must be made. These effects may be grouped into the following categories :

(a) Radiation effects during the scattering by the nucleus.

(b) Straggling due to ionization effects.

(c) Emission of hard photon during scattering process.

These will be discussed briefly. A more extensive discussion can be obtained from [28].

a- The Schwinger Correction

While the electron scatters off a given nucleus, it will interact with the nuclear radiation field, emitting real and virtual photons. The Schwinger correction arises from the emission and reabsorption of virtual photons by the electron, and from the emission of soft, unresolved real photons. Figures 2.1(b-g) represents the Feynman diagrams corresponding to the Schwinger correction. This correction involves the multiplication of the theoretical scattering cross section $(\mathrm{d}\sigma/\mathrm{d}\Omega)_{th}$ by a correction factor e^{δ_s} with $\delta_s > 0$, so that the observed cross section measured under the peak out to some cut off energy ΔE is

$$\frac{d\sigma(\Delta E)}{d\Omega} = (\frac{d\sigma}{d\Omega})_{th} e^{-\delta_s}$$

a compelete expression for δ_s may be found in [29]

b- Landau Straggling

This effect is caused by the ionization straggling, in which the multiple small- energy losses come from atomic ionization[30] and cause a broadening of the peaks, and contributes a correction factor (1 - δ_I) to the theoretical cross sections.

c- Hard-Photon Bremsstrahlung

This arises from the emission of a hard photon , $k > \Delta E$, during the scattering process (figures 2.1 (f),(g)) such that the energy of the electron is

reduced below the cut off at energy ΔE , so that it is not counted in the area under the peak. The area of a higher-energy excited level is determined by subtracting from the measured peak the radiation tail of the elastic peak and of all lower-lying excited levels.

The preceding effects give rise to two different type of corrections of experimental spectrum of scattered electrons which must be considered.

(1) Line shape correction

In order to correct the experimental spectrum for radiative corrections(figures 2.1 (b - e)) , the simple way is to convolute the theoretical line shape function with the detector resolution function and the intrinsic nuclear excitation function, and the resulting line shape is used to fit the measured data to obtain the experimental non-radiative cross section directly(see chapter 3)

(2) Radiative tail correction

The background that contributes to the inelastic spectrum (figures 2.1 (f),(g)) by the radiation tail of lower excited levels or of the elastic peak must be calculated and subtracted from the peaks. Figure 3.3 illustrates the inelastic peaks sitting on the top of the radiation tail of the elastic peak.

2.1.4 Coulomb Correction

The Coulomb field of the target nucleus causes the distortion of incoming and outgoing electron waves. For small Z nuclei where the distortion effects are not too large, the following simple method accounts for these effects satisfactorily[28]. The basis of this approach is that as the electron approaches the nucleus it is accelerated by the static nuclear Coulomb potential. This results an increase in the momentum transfered to the nucleus to an effective momentum transfer, q_{eff} ,

$$q_{eff} = q\left[1 + f(E)\frac{Z\alpha\hbar c}{E_i R_{eq}}\right]$$

where $R_{eq} = (5/3)^{1/2} < r^2 >^{1/2}$

By comparing the evaluated plane-wave Born approximation cross section with

those calculated in the distorted-wave Born approximation, it was found that, for $\lambda = 1$

$$f(E) = 0.139 + 5.02 \times 10^{-3}E - 4.9 \times 10^{-6}E^2$$

and for $\lambda = 2,3$

$$f(E) = 0.169 + 6.1 \times 10^{-3}E - 7.8 \times 10^{-6}E^2$$

This prescription was used for comparison of the data with theoretical calculations which were performed in PWBA.

2.2 Nuclear Structure Models

It was pointed out in section 2.1 that electron scattering form factors are Fourier Bessel transform of the corresponding nuclear transition density. In order to extract the densities from the experimental data it is generally necessary to assume a form of the density and see if it provides a good description of the data. In the following, the models used in interpretation of the present data are discussed.

2.2.1 Model Independent Analysis

The theoretical interpretation of electron scattering data, starting from first principles with a microscopic description of the nuclear charge and current distributions depends on the theoretical model for the approximation of the nuclear many body problem and the choice of the empirical two nucleon interaction potential. Up to now microscopic models are still too crude to match the experimentally quoted errors for cross sections, in particular for high momentum transfers which reveal the nuclear structure in more detail. Further, the commonly used scheme for scattering data evaluation is model dependent in a more direct manner, where phenomenological models are used which allow to define nuclear charge and current distributions by a small set of parameters.

In any of these cases, the experimental error information can only be transferred to the input-parameters of the model, but cannot be directly related

to the nuclear charge and current distributions; at least not in a model independent manner. Since any theoretical interpretation of the experimental data is, by definition model dependent, the meaning of a model independent analysis must be restricted to the mathematical procedure of data reduction of experimental cross section information to obtain nuclear charge and current densities.

The Fourier-Bessel analysis has been used frequently and is quite successful in fitting (e,e') data. This method is based upon the expansion of the nuclear charge density, $\rho(r)$, in terms of spherical Bessel functions. Thus the charge density for multipole λ is given by :

$$\rho(r) = \begin{cases} \sum_\mu A_\mu q_\mu^{\lambda-1} j_\lambda(q_\mu^{\lambda-1} r) & r \leq R_c \\ 0 & r > R_c \end{cases} \tag{2.10}$$

with $q_\mu^\lambda R_c$ being the μ^{th} zero of the spherical Bessel function of order λ[31] , and R_c is the cut off radius chosen far enough outside the nucleus that this approximation is valid (we used $R_c = 7fm$), see section 4.2.

The advantages of the Fourier-Bessel expansion are as follows: (a) the coefficients can be determined in a fairly uncorrelated way; (b) there is a direct correlation between the q range of the experimental data and the number of coefficients that are determined from these data. These two features can be seen in the PWBA approximation, where the form factor at $q = q_\mu$ is given by

$$F_\lambda(q_\mu) = [\pi(2\lambda+1)]^{1/2} R_c^3 j_{\lambda+1}^2(q_\mu R_c) A_\mu \tag{2.11}$$

Thus the coefficient A_μ is determined by the form factor at q_μ. If the data were taken only at exactly q_μ and if the PWBA were completely accurate the coefficients could be determined in an uncorrelated way. The DWBA introduces some correlation between the coefficients A_μ as does the fact that the data are usually not taken at only these restricted values of q. It has been found that an experiment measuring the cross section up to q_{max} determines mainly those coefficients A_μ for which $q_\mu < q_{max}$. Thus the number of terms determined by the experiment is given through the q range over which the cross section has been measured. This qualitative relation still holds if one uses DWBA.

However, in this case the number of coefficients obtainable from the data, N, is determined such that q_N is the closest q_μ to

$$q_{max}^{eff} = q_{max}\left[1 + 4/3\frac{Z\alpha\hbar c}{E_i R_{eq}}\right] \tag{2.12}$$

By using q^{eff} one includes approximately the distortion of the electron wave for which two effects are dominant: the attraction of the electron and the nucleus and the focusing of the electron wave.

The higher order A_μ coefficients for $\mu > N$ can be determined because it has been observed that the measured form factors drop off very rapidly for momenta above about twice the Fermi momentum of the nucleon in the nucleus[31]. This has been observed on the 2^+ level in ^{58}Ni[36] and the 3^-[37] and 5^- levels in ^{208}Pb[38]. We assume that in this region the form factor is zero with an error envelope given by the tangent to the maxima in the measured form factor at lower q.

One of the frequently occuring problems with the Fourier-Bessel analysis is that the resulting density has oscillations at radii which are more or less outside the nucleus. To avoid these oscillations a tail bias is usually applied: as a first step a desired shape given by $\rho(r) \propto e^{-\alpha r}$ was used. In addition a radius R_1 beyond which the transition density follows the above shape has to be chosen. R_1= 4 fm has been used in the present analysis. Finally, one has to find a variance. This was done through a pseudo χ^2 which is added to the χ^2 and the total χ^2 is then minimized with respect to all Fourier-Bessel amplitudes and with respect to α.

In chapter 4 the longitudinal form factors are analysed in a model independent framework providing the transition charge densities and also the reduced transition probabilities.

2.2.2 The Single-Particle Model

The single-particle model is a description of the nucleus where each nucleon is considered individually and is assumed to move nearly independently of all the other nucleons in an average potential $U(r)$ due to the other nucleons.

The most frequently used potentials are :

(1) The harmonic oscillator potential

$$U_{HO} = \frac{1}{2}\hbar\omega r^2/b^2 + constant$$

where ω is the angular frequency and $b = (\hbar/m\omega)^{1/2}$ is the characteristic length of the harmonic oscillator potential.

(2) The Woods-Saxon potential

$$U_{WS} = -V_o f(r) + V_{so}\frac{1}{m_p r}f(r) < \mathbf{l}\cdot\mathbf{s} > + V_c(r)\frac{1}{2}(1+\tau_z)$$

where $f(r) = [\ 1 + \exp(r - R_o)/a]^{-1}$, V_c is the Coulomb potential for a uniform spherical charge distribution, V_o is the central potential depth, V_{so} is the spin-orbit strength, and τ_z is the isospin of the nucleon($\tau_z = 1$ for proton and -1 for neutron). The harmonic oscillator potential is frequently favoured because of the advantage that many mathematical operations can be performed analytically. An unrealistic feature is the fact that the harmonic oscillator potential goes to infinity when the distance from the origin r increases (see fig 2.2). The Woods-Saxon well is more realistic but its use requires numerical methods of solution. Furthermore, the correction for the center-of-mass motion can be made exactly only for the harmonic oscillator potential. For these practical reasons, most analysis is performed using harmonic oscillator wave functions .

Single-Particle Matrix Element

The electron operator is a one body operator and hence in the scattering process state of only one nucleon is changed. For this reason, the matrix elements of the single-particle multipole operators M^c_λ, T^e_λ, T^m_λ required in equations 2.4 - 2.6 reduce to simple matrix elements between single-particle states.

The nuclear charge , current , and spin operators in the shell model are just sums of the operators for the individual nucleons[35]

$$\hat{\rho}(\mathbf{r}) = e\sum_{j=1}^{A}\epsilon_j\delta(\mathbf{r}-\mathbf{r}_j)$$

$$\hat{\mathbf{J}}(\mathbf{r}) = \frac{e}{2M}\sum_{j=1}^{A}\epsilon_j\delta(\mathbf{r}-\mathbf{r}_j)\hat{p}_j$$

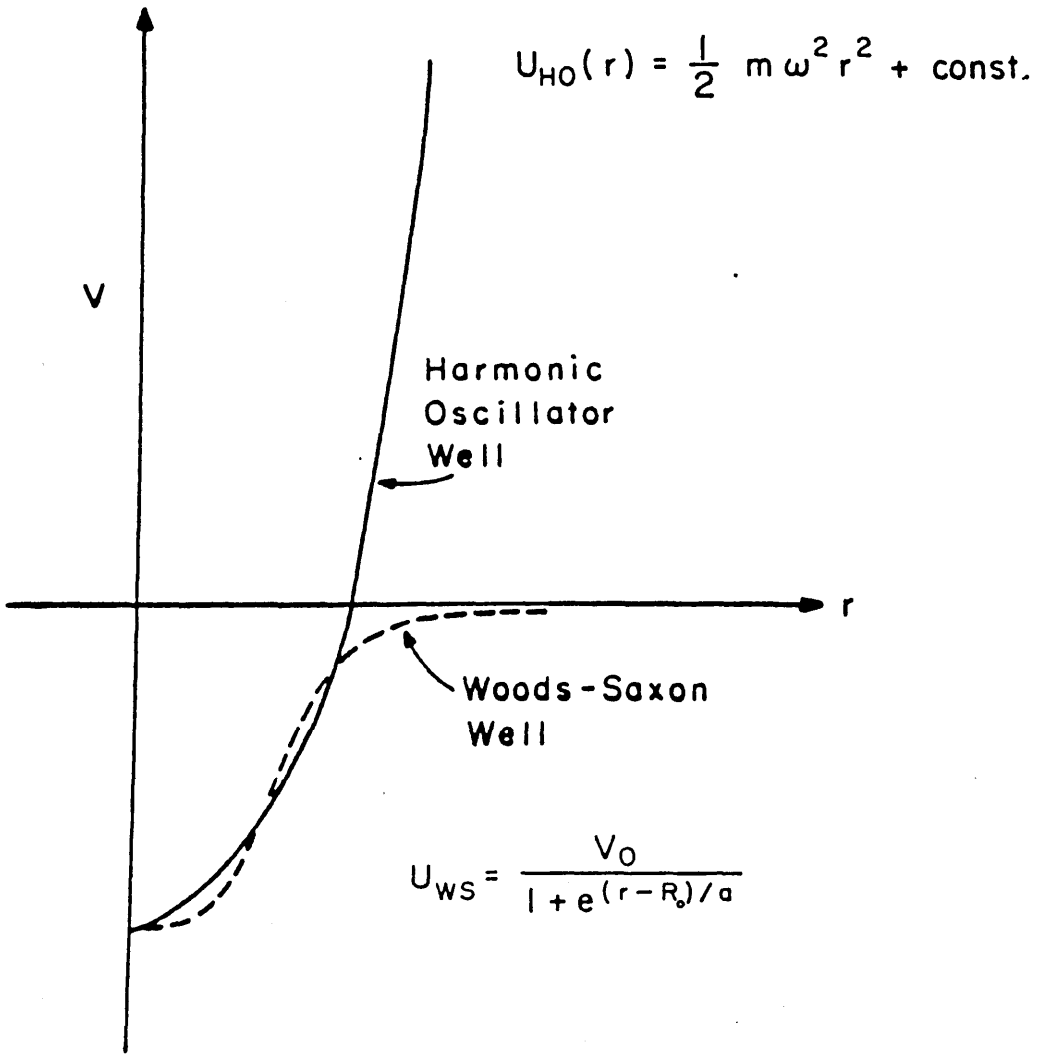

Figure 2.2: *Harmonic Oscillator and Woods-Saxon Potentials*

$$\hat{\mu}(\mathbf{r}) = \frac{e}{2M}\sum_{j=1}^{A}\mu_j\delta(\mathbf{r}-\mathbf{r}_j)\hat{\sigma}_j$$

where

$$\epsilon_j = 1/2(1+\tau_{jz})\epsilon_p + 1/2(1-\tau_{jz})\epsilon_n, \mu_j = 1/2(1+\tau_{jz})\mu_p + 1/2(1-\tau_{jz})\mu_n$$

$\epsilon_p = 1$, $\epsilon_n = 0$, $\mu_p = 2.79$ and $\mu_n = -1.91$

These operators are the single-particle operators whereas the initial and final states are many-particle states . However , the overall nuclear matrix elements can be expressed as a summation of single nucleon matrix elements :

$$< \psi_f \parallel \hat{O} \parallel \psi i >= \sum_{\alpha,\beta}\rho_{\alpha\beta} < \alpha \parallel \hat{O} \parallel \beta >$$

where α, β are single-particle states and the $\rho_{\alpha\beta}$ are coefficients , which give the contribution of each single-particle transition . For example, in the case of Coulomb multipole operators the reduced matrix element may be given by[27,73]

$$< n'(l'\tfrac{1}{2})j' \parallel M_J(r) \parallel n(l\tfrac{1}{2})j > = (-1)^{j+J+\frac{1}{2}}\left(\frac{(2l'+1)(2l+1)(2j'+1)(2j+1)(2J+1)}{4\pi}\right)^{1/2} \times \begin{Bmatrix} l' & j' & \frac{1}{2} \\ j & l & J \end{Bmatrix} \begin{pmatrix} l' & J & l \\ 0 & 0 & 0 \end{pmatrix} < n'l' \mid j_J(qr) \mid nl > \tag{2.13}$$

where

$$< n'l' \mid j_J(qr) \mid nl >= \int_0^\infty R_{n'l'}(r) j_L(qr) R_{nl}(r) r^2 dr. \tag{2.14}$$

R_{nl} is the radial part of the wave functions. In the case of harmonic oscillator potential, the radial wave functions R_{nl} are:

$$R_{nl}(r) = \left(\frac{2(n-1)!}{b^3[\Gamma(n+l+\frac{1}{2})]^3}\right)^{1/2}\left(\frac{r}{b}\right)^l exp\left[-\frac{1}{2}\left(\frac{r}{b}\right)^2\right] L_{n-1}^{l+\frac{1}{2}}\left(\frac{r^2}{b^2}\right) \tag{2.15}$$

where $L_{n-1}^{l+\frac{1}{2}}$ is the Laguerre polynomial defined by :

$$L_p^a(z) = \frac{\Gamma(a+p+1)}{\Gamma(p+1)}\frac{e^z}{z^a}\frac{d^p}{dz^p}[z^{a+p}exp(-z)]$$

The Coulomb form factor may then be calculated using equation 2.4 .

Center of Mass and Finite Size Corrections

Two corrections must be made before a form factor calculated from the shell model can be compared with experimental data. Firstly, since the operators and the wave functions upon which they operate assume that the nucleons are point particles, the finite size of the nucleons must be taking into account. This is accomplished by multiplying the calculated form factor by a single nucleon form factor $f_{SN}(q)$. In this work the Mainz-four-pole fit[34] is used.

$$f_{SN}(q^2) = \sum_{i=1}^{4} \frac{a_i}{1 + q^2/m_i}$$

$a_{1,..,4}$ = 0.312, 1.312, -0.709, and 0.085 , $m_{1,..,4}$ = 6.0, 15.02, 44.08, and 154.2 , and q is in fm$-$1

Secondly, the shell model wave functions are calculated relative to an origin which is not the same as the center of mass of the nucleus. Thus the shell model form factor must be multiplied by a factor $f_{CM}(q)$. For harmonic oscillator potential the factor has the form [27]

$$f_{CM}(q) = exp\left[(qb)^2/4A\right]$$

where b is the oscillator parameter and A is the nucleus mass number.

2.2.3 The Shell Model

The single-particle model discussed in the previous subsection has been quite successful in predicting the level sequences for many odd-mass nuclei, and especially for those with nucleon numbers near major closed shells, e.g. ^{209}Pb, but, it fails to predict many observed nuclear moments. Moreover, it cannot account for the fragmentation of the single-particle levels observed in the nuclei with several valence particle outside the shells. The shell model which is an extension of the single-particle model involves consideration of both its major assumptions, namely the independence of motion in a central potential, and the incomplete treatment of the residual interactions.

The Hamiltonian for the shell model is given by

$$H_{SM} = \sum_{i=1}^{A}[T_i + U(r_i)] + 1/2 \sum_{i,j\neq i}^{A} V(r_{ij}) \qquad (2.16)$$

where the first term represents the single-particle motion, and the second term describes the residual interaction. In the shell model calculations the attention is then concentrated on the potential energy shifts due to the residual interaction V_{ij}, and on the single-particle states that may be occupied by the particles between which the residual forces act; these states define the model space of the single-particle model. The procedure for the shell model calculations is to specify the nucleon configuration that may contribute to the wave function of a given level and then evaluate the matrix elements of the assumed residual interaction between the states of the model space. Finally, using these matrix elements increased by single-particle terms and spin-orbit energies the full Hamiltonian matrix is set up. From this the eigenvalues giving the energies of the states and the eigenvectors giving their wave functions are obtained by standard methods. The eigenfunctions can then be used in the evaluation of nuclear moments and transition probabilities, etc.

More realistic calculations must introduce the repulsive core of the internucleon force. When the residual interaction is set up in this way, so that the resulting Hamiltonian acting on a limited range of wave functions produces a result hoped to be equivalent to those of a full, unlimited calculations, it is said to be an effective interaction. Calculations using effective interactions and experimental single-particle energies can now be made on a very large scale, using several nucleons distributed between several single-particle levels.

It may be noted that in spite of the great successes of the shell model in the prediction of ground state spins and parities, magic numbers, etc, this model still has exhibited many limitations. For example, experimentally observed nuclear quadrupole moments are in most cases much larger than the shell model predictions; the transition probabilities of low-lying states exceed the single-particle estimates; and typical rotational and vibrational band structures occur which are not easily accounted for in the shell model.

In order to compare the results of these theoretical calculations with the electron scattering data, electron scattering form factors were obtained from the shell model wave functions by using the density matrix technique as follows: Any one particle operator, $\hat{O}$, such as the electromagnetic transition operators

$\hat{M}^e_\lambda$, $\hat{T}^e_\lambda$, and $\hat{T}^m_\lambda$, can be expanded

$$< \psi_f \mid \hat{O} \mid \psi_i >= \sum_{\alpha,\beta} \rho_{\alpha\beta} < \beta \mid \hat{O} \mid \alpha > \tag{2.17}$$

$< \beta \mid \hat{O} \mid \alpha >$ are the matrix elements of $\hat{O}$ between the spherical harmonic oscillator orbitals α and β, $\rho_{\alpha\beta}$ is known as the density matrix, and $\mid \psi_i >$ and $\mid \psi_f >$ are the initial and final state wave functions respectively.

Thus the matrix elements of the operators, $\hat{M}^e_\lambda$, $\hat{T}^e_\lambda$, and $\hat{T}^m_\lambda$, evaluated between the wave functions produced by the extended shell model, can be built up from the matrix elements of these operators, evaluated between single-particle states. For the Coulomb operator, these single-particle matrix elements can be calculated from equation 2.13; the corresponding expressions for the matrix elements of $\hat{T}^e_\lambda$ and $\hat{T}^m_\lambda$ can be found in [27].

Shell model calculations used in this analysis were performed in $3\hbar\omega$ space by Millener[12], and by the Utrecht group of Glaudemans[71]. These are discussed in more detail in chapter 4. The comparison between the present data and the shell model predictions are also presented in chapter 4.

Chapter 3

Experimental Method

The present experiment was carried out with the 500 MeV electron scattering facility at the National Institute for Nuclear Physics and High Energy Physics (NIKHEF) in Amsterdam. A brief description of the experimental conditions is given below. A more extensive description can be obtained from [40]. In this chapter the data reduction procedures leading to cross section values are also discussed.

3.1 Beam Parameters

The electron beam produced by the Medium Energy Accelerator (MEA) is transported with the desired properties to the target through the beam handling system (AFBU). The beam handling system can be tuned in two modes,viz. *Normal Mode* (NM) and *Dispersion Matching Mode* (DMM). In NM the beam is brought to a non-dispersive point focus at the target. The resolution that can be obtaind in the spectrometer strongly depends on the energy spread in the beam, which can only be reduced by narrowing the energy-defining slit. This means that in order to obtain high resolution, a large part of the available beam power is lost in the slit system. In DMM the beam is dispersed at the target. When the dispersion on the target matches the dispersion of the spectrometer, the position of an electron in the focal plane only depends on the energy lost in scattering in the target and not on the energy of the electron in the beam. This means that the momentum resolution is independent of the momentum spread on the target, and all electrons which have lost a given amount of energy in

the scattering process are focused at the same position in the focal plane of the spectrometer. As a result most of the available beam power can be used for the actual experiment. On that account NM was not used in these experiments.

Table 3.1: Beam Parameters

energy range	70-430	[MeV]
peak current	$\leq$10	[mA]
repetition rate	250-300	[Hz]
pulse length	30-40	[μs]
average current	$\leq$60	[μA]
energy spread on target	$\leq 3.10^{-3}$	[Δp/p]
intrinsic resolution	4.10^{-5}	[Δp/p]

The beam parameters obtained during the various runs for the present experiment are listed in table 3.1.

3.2 The Target

In the present experiment a room-temperature gas target cell was constructed in the form of a thin walled cylinder, 40 mm in diameter and 50 mm in height and oriented with its axis of symmetry perpendicular to the scattering plane. The walls which were of thickness 40 μm, consisted of a special aluminium alloy which maintains its high tensile strength at high temperatures. With a maximum pressure of 4.5 atmospheres, the cell could stand average beam currents of up to 50-60 μA. Besides the ^{15}N target of which the specifications are given in table 3.2, three other targets were used under the same experimental conditions. A gas target cells filled with ^{4}He or ^{1}H provided cross section normalization while an empty cell was used to enable background subtraction. Energy calibration was achieved with a natural BN solid target.

The targets were mounted in the target ladder equipment capable of containing eight standard frames. A chromium-doped aluminium oxide target was used for visual inspection of the beam spot with a TV camera. A thin platinum target enabled on-line tuning of the beam handling system and the optimization

Table 3.2: Composition of the ^{15}N gas

Abundance :	$^{15}N \approx$	96%
Impurities :	$^{14}N \approx$	3.2%
	$^{16}O \approx$	0.5%
	$CO_2 \approx$	0.3%

of the quadrupole of the QDD spectrometer for optimal resolution.

3.3 The Spectrometer

For the (e,e') experiments under consideration the high-resolution QDD spectrometer[40] was used. The spectrometer consists of an entrance quadrupole(Q) in front of a solid angle defining slit and two dipoles. In a number of cases the large solid angle QDQ spectrometer at a more forward angle was also employed to monitor the product of the beam intensity and target thickness.

Table 3.3: Main Parameters of QDD

Maximum particle momentum	600	[MeV/c]
Maximum field strength	1.43	[T]
Deflecting angle of dipoles	2×75°	
Momentum acceptance	± 5	[%]
Angular acceptance ($\Delta\varphi$,$\Delta\vartheta$)	± 40	[mrad]
Solid angle $\Delta\Omega$	5.6	[msr]
Focussing conditions $< x \mid \vartheta >$, $< y \mid y >$	0	[mrad/mm]
Angular magnification $< \vartheta \mid \vartheta >$,$< y \mid \varphi >$	-1.67,+0.87	[mrad/mm]
Resolution	$<1.10^{-4}$	
Dispersion	6.78	[cm/%]
Focal plane angle	41°	

The main parameters of the QDD spectrometer are listed in table 3.3. Both spectrometers are shown schematically in figure 3.1.

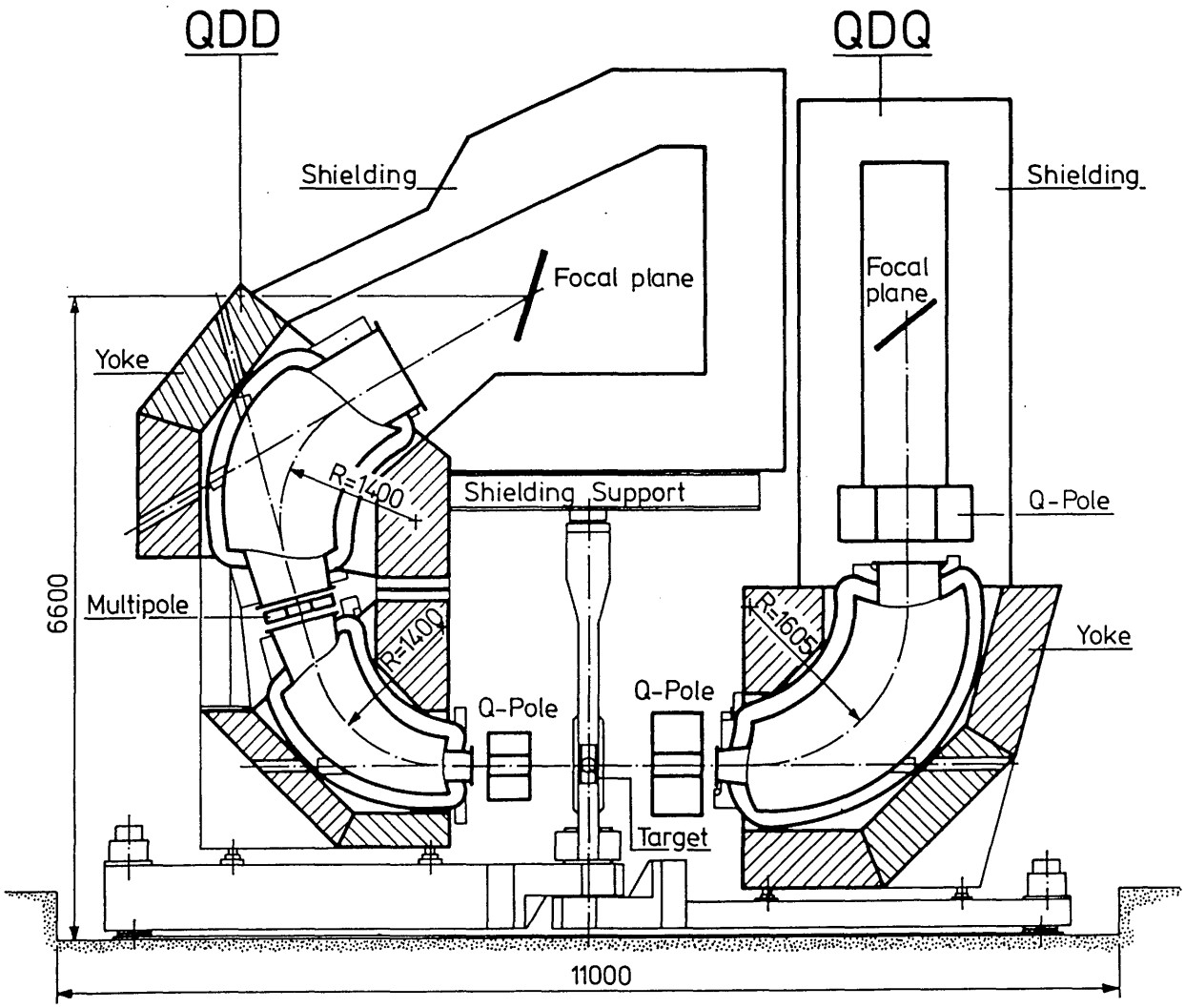

Figure 3.1: *Lay-out of the two spectrometers setup, showing the rotatable platforms,magnet configuration and shielding. Also indicated are the scattering chamber and slit systems. The beam enters perpendicular to the plane of drawing. Measures are in mm.*[40].

3.4 Detection System

The detection system of the QDD spectrometer consists of three multi-wire drift chambers(MWDC) and a set of five scintillators covering the focal plane backed by a Cerenkov counter as shown in figure 3.2. The drift chambers, the first of which (the X1-chamber) coincides with the straight focal plane, are placed parallel to each other. The X1-chamber determines the position of the electron trajectory in the dispersive direction, while in combination with the X2-chamber the angle in the dispersive direction can be determined. The wires of the Y-chamber are placed at an angle of 26.5° with respect to that of the X1-chamber. With the y-chamber the distance of the electron trajectory from the symmetry plane can be determined and hence the angle in the reaction plane can be calculated. The angle with respect to the particle trajectory ($\approx$ 41°) together with the wire pitch (4mm) and the cathode-sense wire distance(4mm) ensures firing of at least two (double hit) and up to four wires (quadruple hit). Distinction between double and triple events yields a spatial resolution of 2 mm. The mesurement of the drift times to the sense wires results in a fine-channel distribution of 16 channels per wire which corresponds to a spatial resolution of 0.25 mm. The processing time of an event is 300ns. During a beam burst a maximum of 128 events can be buffered.

In single-arm experiments, two data-taking modes exist :

a- *list mode* : The full information per event is directly stored on tape. This allows off-line analysis of the data to improve the resolution.

b- *spectrum mode* : The spectra of all chambers are directly accumulated and afterwards stored on disk.

3.5 Data collection

Spectra were taken in a number of data collection runs spread out over a period of two years. The measurements were made at incident energies 70, 90, 130, 170, 300, and 430 MeV and scattering angles between 40° and 98.5°. This covers a range of effective momentum transfer from 0.4 fm^{-1} up to 3.2 fm^{-1} (see table A1, appendix A, for energy-angle combinations). Some typical

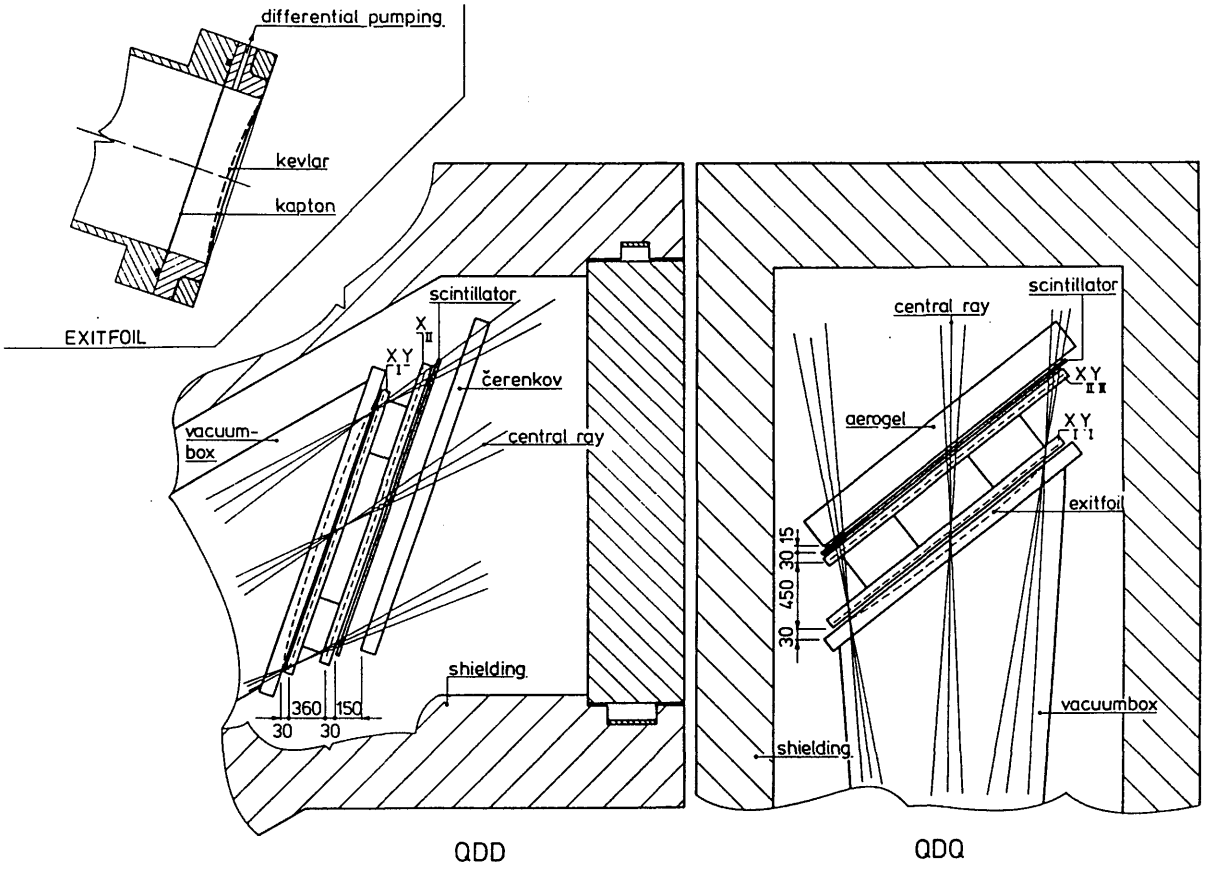

Figure 3.2: *Lay-out of the focal plane detection system, showing the wire chambers,scintillators and Cerenkov detectors. The X1-chamber coincides with the focal plane*[40].

spectra are shown in figures 3.3 - 3.8.

The measurements complemented data obtained previously[46] at a scattering angle of 180° with the MIT-Bates electron scattering facility. The results of the 180° experiment allow the transverse parts of the cross sections to be subtracted from the present forward angle data. At each energy-angle combination data were also obtained with the ^{4}He or ^{1}H target for cross section normalization and with the empty target to enable background subtraction.

Before cross sections can be extracted from the raw data, a number of corrections must be applied. These procedures are discussed below.

3.5.1 Spectrum reconstruction from list mode data

As discussed in the previous chapter, two modes of data taking have been used : spectrum mode and list mode. When a spectrum is recorded in list mode, it can be corrected later for two effects. The first correction is for kinematical broadening and is caused by the horizontal acceptance of the spectrometer. As a result of this acceptance there is a spread in recoil-shift in the spectrum given by :

$$\Delta E = (E_i/M)\sin(\theta)\Delta\theta$$

where,

E_i is the beam energy,

M is the mass of the target nucleus,

θ is the scattering angle, and

$\Delta\theta$ is the horizontal acceptance of the spectrometer.

By reconstructing the trajectory of each electron through the spectrometer, the individual scattering angles can be calculated and thus the kinematical broadening can be corrected[41]. The second correction is for abberations in the spectrometer optics. By analysing a number of spectra with the computer program TESTKRAK[41] the coefficients describing the abberations can be optimized.

3.5.2 Dead time correction

Since the MWDC's have a finite event-processing time, the chambers are

not ready to accept a new event for a time τ_d after registering an event. As a consequence of this dead time a certain amount of counts is lost. An overall correction is performed by multiplying all fine-channel contents with a correction factor C_d :

$$C_d = (1 - \tau_d M)^{-1}$$

where,

τ_d is the average MWDC dead time :$\tau_d = 500$ ns,

M is the instantaneous count rate :

$$M = \frac{N_{tr}}{N_b \tau_b}$$

where,

N_{tr} is the total number of triggers,

N_b is the total number of beam bursts, and τ_b is the effective beam burst length.

3.5.3 Efficiency correction

There are two kinds of efficiencies which must be considered: wire efficiency, representing the fluctuations in the relative detection efficiency of the wires in the X1-chamber ; fine-channel efficiency due to the unequal widths of the fine channels. Because of these efficiencies, not all counts are distributed correctly among the fine channels of a spectrum.

The correction depends on the kind of spectrum (list mode or spectrum mode) and on whether the detector stepping facility was used or not. This stepping implies a movement of the detector along the focal plane in 16 steps, covering the distance between two wires. During the recording of a spectrum, an equal charge is collected after every step of the detector, in that way smoothing out the differences in efficiency between the fine channels. In this case there is no need for a fine-channel efficiency correction.

In the case in which a spectrum has been recorded in spectrum mode without using the stepping facility, the efficiency correction consists of three operations.
1 - Each fine-channel content is devided by its fine-channel efficiency, i.e. correction for the unequal widths of the fine-channels;

2 - The correct fine-channel content is then interpolated on to the ideal fine-channel position;

3 - The 16 fine-channel contents of a particular wire are each divided by the efficiency of that wire.

3.5.4 Energy conversion

The scattered electron energy E_f determines its fine-channel position on the focal plane. The relation between the electron energy and fine-channel number is represented by the so called dispersion polynomial

$$E_f = \Gamma B(1 + d_1(n - n_\circ) + d_2(n - n_\circ)^2 + d_3(n - n_\circ)^3 + d_4(n - n_\circ)^4) \quad (3.1)$$

with :

Γ is the conversion factor between the spectrometer magnetic field and the electron energy [MeV/T]

B is the magnetic field of the spectrometer [T]

d_1,d_2,d_3,d_4 are the coefficients of the polynomial

$n - n_\circ$ is the channel number relative to the central channel.

To determine the beam energy and the coefficients of the polynomial, the following energy-calibration procedure was pursued. First the peak positions of a number of well-known levels of ^{10}B,^{11}B,^{14}N,^{15}N, and ^{4}He were substituted in equation 3.1 and by varying the incident electron energy, E_i,$n_\circ$, and coefficients d_1 through d_4, a least square fit was made of the energies calculated in this way to the ones given by equation 2.1. A detailed description of the energy-calibration procedure can be found in [43]. The beam energies were determined with an accuracy of about 0.1% and are listed in table A.1.

3.5.5 Bin-sorting

When several spectra have been recorded under the same experimental conditions they have to be combined into one (bin-sorting). The bin-sorting procedure is performed as follows : a bin-width is chosen according to the actual resolution. This is because the energy channels or bins in the spectra are not equally wide due to the non-linearity of the dispersion polynomial. Next the

spectra are sorted in bins, the content of each bin can be expressed by

$$N_j = \sum_{k=1}^{n_s} \sum_{i=1}^{4096} \frac{O_{ijk}}{S_{ik}} n_{ik}.$$

where,

n_s is the number of sorted spectra,

O_{ijk} is overlap of bin j and fine channel i in spectrum k,

S_{ik} is the width of (fine) channel i in spectrum k, and

n_{ik} is content of (fine) channel i in spectrum k.

Finally, to each bin j an error is assigned given by :

$$\Delta N_j = (\Delta N_j)_{stat} + \Delta_{rel} N_j$$

where $(\Delta N_j)_{stat}$ is the statistical error $(\Delta N_j)_{stat} = (N_j + 1)^{1/2}$. Here, one is added to N_j to avoid the error being zero for bin content zero which may cause trouble in some fitting procedures and Δ_{rel} is the estimated relative error. The relative error was estimated from line shape fitting procedures in which it can be adjusted to achieve a chi-square near the expectation value for the best fit.

3.5.6 Normalization of spectrum

The sorted spectra are then normalized for unit collected charge and corrected for energy width of the bins and the solid angle of the spectromrter.

Each bin in the spectrum must be normalized for collected charge, because its content is not necessarily composed of contributions from all fine spectra. As a consequence each bin may have collected a different charge on which its content has to be normalized.

To make the peak-hight in the spectrum independent of the energy-width used a normalization on that energy-width is performed.

Normalization on solid angle is only necessary in case the spectra that are to be sorted were recorded with different settings of the solid-angle defining slit of the spectrometer.

These three normalizations are combined in one factor :

$$Q_j = \sum_{k=1}^{n_s} \sum_{i=1}^{4096} \frac{Q_{ijk}}{S_{ik}} q_k \Omega_k \varepsilon_i$$

where,

O_{ijk} is overlap of bin j and fine channel i in spectrum k,

q_k is the collected charge in spectrum k,

Ω_k is the solid angle of spectrum k, and

ε_i is the energy width of the bin i.

The normalized bin-content and its error are given by :

$$\overline{N_j} = N_j/Q_j, \Delta\overline{N_j} = \Delta N_j/Q_j.$$

3.6 Lineshape fitting

The bin-sorted spectra are then line shape fitted to extract the experimental cross-sections. A lineshape fitting code ALLFIT [45] was used in fitting the measured spectra. The total lineshape F(x), as a function of the electron energy loss x, consists of a sum of contributions from individual peaks in the spectrum and a background function $B(x)$.

$$F(x) = B(x) + \sum_{j \in \{peaks\}} F_j(x)$$

3.6.1 Fitting function

The lineshape for each peak, $F_j(x)$, may be described as the convolution of a resolution function R_j, a radiative response function T_j, and an intrinsic nuclear excitation function I_j. A peak whose decay width is negligible may be described by R_j and T_j alone.

The resolution function used in this analysis can be described as an asymmetric hypergausian function with tails, see equation B.1 and figure B.1 in appendix B. When the height of the lineshape on the low excitation energy or high excitation energy side of the peaks falls to the fraction f_l or f_r, respectively, of the peak height h then the lineshape is described by the tails. The left tail is exponential while the right tail has two options. If the resolution function R is convoluted with a theoretical radiative response function T, then the exponential form is used for the high excitation tail. If the convolution is treated as a single empirical function, then the inverse polynomial form is used for the high excitation tail.

The theoretical radiative response function is evaluated following the work of [47] and [48]. The total radiative response function $T(\Delta E)$ is the convolution of three contributions, the Schwinger distribution $T^{Sch}(\Delta E)$, the Bremsstrahlung distribution $T^{B}(\Delta E)$, and the Landau distribution $T^{La}(\Delta E)$. The analytic form $T(\Delta E)$ reproduces well the experimentally observed shape of the radiative tail.

It is sometimes convenient to express the convolution of R and T as a single empirical lineshape function. The chosen empirical lineshape function R in equation B.1 must smoothly join the radiative tail, with the central region of the lineshape. The empirical function used in this analysis is the same hypergausian function, equation B.1, as was in conjuction with the theoretical radiation tail, but with the right exponential tail replaced by an inverse polynomial. The parameter s ensures continuity at the match point $x = p + m_r$. Figure 3.3 shows a fit to the elastic peak of ^{15}N using empirical radiative tail.

When the decay width of a state is a significant fraction of the resolution width, as is generally the case for states above particle emission thresholds, the extracted cross section is sensitive to the form of the lineshape. In this work Lorentzian forms:

$$I_j(E) = \begin{cases} N_j \frac{1}{\pi} \frac{\Gamma_j/2}{[(E-E_T)-(E_j^\circ-E_T)^2/(E-E_T)]^2+(\Gamma_j/2)^2} & if E \neq E_T \\ 0 & if E = E_T \end{cases}$$

were used[42]. Γ_j is FWHM of I_j, E_j° is the j^{th} peak resonance energy, and E_T is the threshold energy.

3.6.2 Background

Several contributionsto the residual background are included in addition to the radiative tail. The total background function is :

$$B(x) = B_1(x) + B_2(x) \tag{3.2}$$

where,

$$B_1(x) = b_\circ + b_1 x + b_2 x^2 + b_3 x^3$$

$$B_2(x) = \begin{cases} 0 & x \leq t \\ b_1' x_1 + b_2' x_1^2 + b_3' x_1^3 & \text{where } x_1 = x - t > 0 \end{cases}$$

and t is the continuum threshold. For this analysis t was set to -10.9 MeV which is the ^{15}N alpha decay threshold.

3.6.3 Fitting procedure

Because of the limitation of the computer code, the spectra had to be analysed in two parts. The first part contains all states of less than 13.6 MeV of excitation, and the other region includes all the states with excitation energies above 13.6 MeV.

(a) The $E_{exc} \leq$ 13.6 MeV region

The lineshape parameters, asymmetry a, exponent γ, and sometimes resolution width ω (see equation B.1) for all peaks are first obtained from fitting the elastic peak region from -3 to 7 MeV and fixed at the values obtained.

The empirical radiative tails described in the previous section were used. For all the inelastic peaks the empirical tail parameter f_R, t_1, t_2 were fixed to the values obtained from the fit to the elastic peak.

^{15}N has decay thresholds at 10.2 MeV (p decay), 10.83 MeV (n decay), and 10.9 MeV (α decay). After including the empty cell spectrum in the ^{15}N fits, there remains significant ^{15}N continuum strength above 10.9 MeV. However, in examining the entire data set, it is seen that this continuum possesses considerable structure above about 10.9 MeV. For this reason, the threshold in the polynomial background(see equation 3.2) was set at 10.9 MeV. Below threshold only the constant and linear terms in the background were varied with the quadratic and cubic terms set to zero. Above threshold generally the linear term was adequate.

A typical electron scattering spectra observed in this region are displayed in figures 3.4, 3.5.

(a) The $E_{exc} \geq$ 13.6 MeV region

Because of the overwhelming number of excitations observed in the spectra, a special procedure was followed in the fitting procedure. First, the tails obtained from elastic and inelastic levels of the first part had to be fixed and extended to this region. Next, the levels in the spectra had to be identified. For this purpose a number of spectra covering a momentum transfer range from 1 to 3 fm^{-1}, were used. In this set all excitations known from the literature [16] were assigned to peaks actually observed. The relative positions of peaks in a group with at least one strong peak were locked to each other. The excita-

tion energies of peaks observed but not given by the literature was treated as free parameters. Table 3.4 summarizes the parameters of the peaks which were included in the analysis of this region, and correlates these peaks with states identified in the literature[16]. Finally, all spectra were fitted to determine the peak areas by using the same lineshape parameters as used in the first part. Figures 3.6, 3.7 and 3.8, display representative fitted ^{15}N spectra in the region from 13.6 to 21.5 MeV.

3.7 Normalization of the Cross Section

As was mentioned in section 3.2, spectra of ^{4}He and ^{1}H were recorded along with the ^{15}N measurements under the same experimental conditions. A hydrogen target was used at q-values above 2.3 fm^{-1} because the elastic form factor for helium shows a minimum in that region. A comparison between the elastic scattering cross sections extracted from these spectra with those of [49] and [50] showed a disagreement between the cross sections determined from spectra taken with a large solid angle (5.6 msr) and those determined from measurements with smaller solid angle (0.4,1.6 msr). This disagreement is attributed to the variation of the solid angle in the case of a gas target, as a function of the displacement of the scattering point from the centre of the target along the beam axis. An effective value for the large solid angle was determined (4.73 msr) by fitting the cross section obtained from spectra recorded with the large slit to those measured with the smaller ones, and a normalization factors was calculated for all q-values concerned :

$$f(q) = [\frac{d\sigma}{d\Omega}(q)]_{litt} / [\frac{d\sigma}{d\Omega}(q)]_{exp}$$

These factors have been used to correct the ^{15}N cross section caused by the difference in the target thickness. The correction factors for ^{15}N were calculated from the equation:

$$f(q)_c = \frac{P_{He,H}}{P_N} \frac{T_{He,H}}{T_N} \frac{\rho_{0He,H}}{\rho_{0N}} f(q)$$

where :

P is the gas pressure in Pa,

T is the gas temperature in K,and

ρ_0 is the specific weight of the gas at P_0,T_0 in mg/cm^3, P_0 = 101.325 kPa, T_0 = 273.15 K.

With these information the ^{15}N elastic cross sections were corrected

$$[\frac{d\sigma}{d\Omega}(q)]_N^{corr} = f(q)_c \times [\frac{d\sigma}{d\Omega}(q)]_N^{exp}.$$

From the corrected cross sections the form factors were calculated as follows

$$F^2(q) = \frac{\eta}{\sigma_M}[\frac{d\sigma}{d\Omega}(q)]_N^{corr}.$$

By comparing the corrected elastic cross sections with those of Schutz[51], at low q-values(q $\leq$ 0.6 fm^{-1}), an overall normalization of 11 % was necessary. The origin of this normalization is still not clear.

The cross sections obtained above contain a mixture of longitudinal and transverse components[equation 2.2]. In order to extract the longitudinal cross sections, the transverse data obtained previously at a scattering angle of 180° at MIT were used. The 180° data interpolated [52] to match the q-values of the forward angle data points. $(0.5 + \tan^2(\theta/2))$ times this interpolated value was then subtracted from the forward angle data to yield the longitudinal strength. This is listed in tables A in appendix A.

Table 3.4: States in ^{15}N

Selected states from compilation[16]			States included in this work	
E_x(MeV)±(keV)	$2J^\pi$	Γ(keV)	E_x(MeV)	Γ(keV)
13.608±7	$5^{(+)}$	18±4	13.61	18
(13.612±10)	(1^+)	90		
13.84±30	3^+	75	13.84	75
14.09±7	$(9^+, 7^+)$	22±6		
14.10±30	3^+	~100	14.13	50
14.16±10	$3^{(+)}$	27±6		
14.24±40	5^+	150	14.24	150
14.38±40	7^+	100	14.38	100
14.55±20		200±50	14.55	200
14.72±10		110±5	14.72	110
14.86±20		48±11	14.86	48
14.92		12±3	14.92	12
15.025±10		13±3	15.03	13
15.09±20		80±25	15.09	80
			15.27	75
15.288±10		26±6		
15.78±10			15.78	25
15.93±10		35±5	15.93	40
16.026±10		62±12		
			16.05	110
16.85±30	5	110±50	16.88	210
16.91		~350		
(17.05)			17.05	125
17.37±40		~250	17.37	250
17.58±40	3^+	450±120	17.58	450
17.72±10		48±10	17.72	48
17.95±20		167	17.95	20
18.06±10		19±4		
18.09±20		~40	18.08	40
18.27±20		235±60	18.27	235
			18.51	50
18.91±150	$3^+ + 1^+$	750±70	18.94	710
			19.36	100
19.5	3^+	~400	19.5	50
19.72±40			19.72	50
			19.80	75
			19.95	125
20.12±50			20.12	100
20.5	3^+	~400	20.5	450
			21.05	300
			21.1	50
21.82		~600	21.9	700
			22.5	700
23.19±6			23.2	350

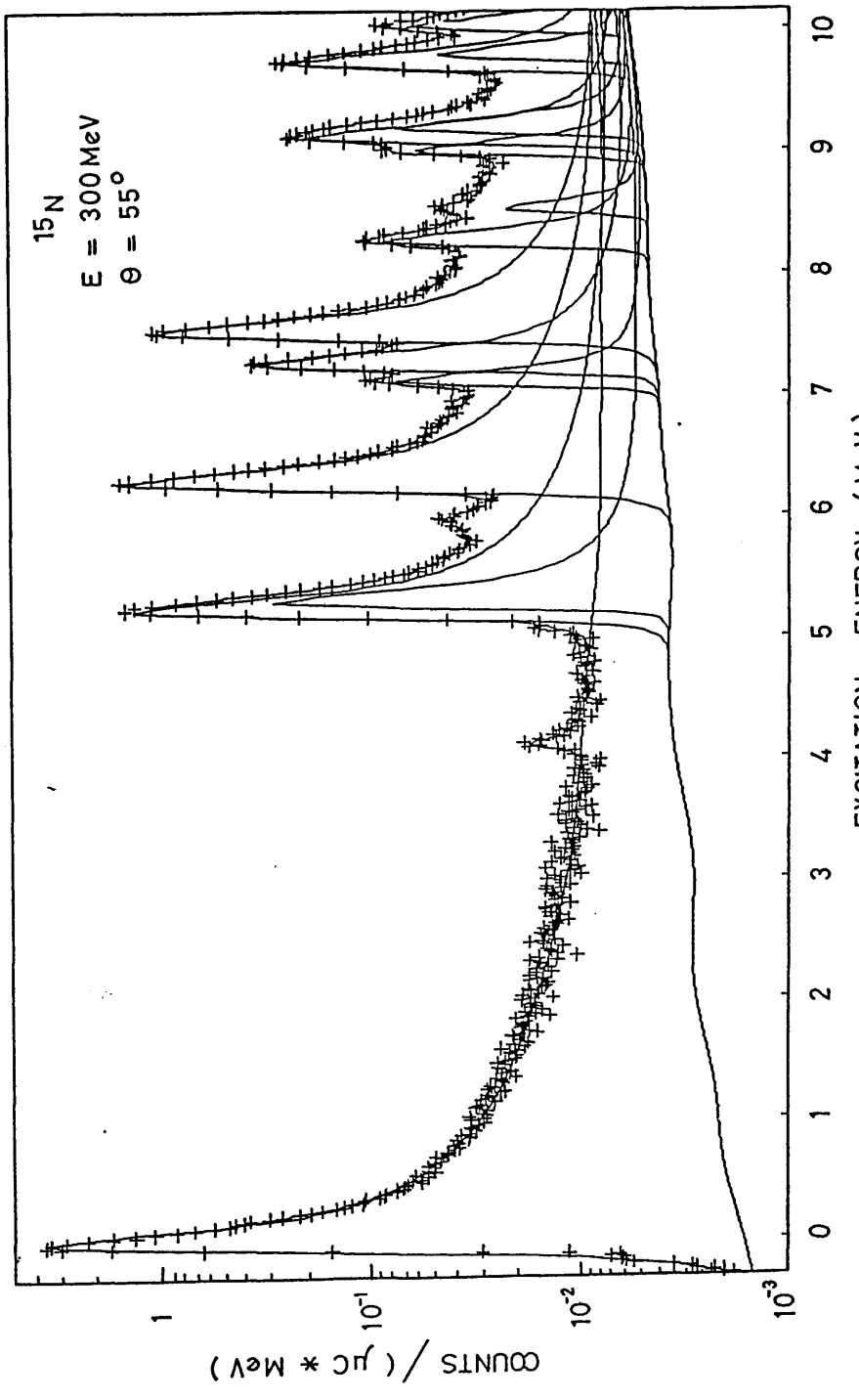

Figure 3.3: *Spectrum of elastic and inelastic scattered electrons for E_i=300 MeV and $\theta = 55°$ ($q = 1.4\ fm^{-1}$)*

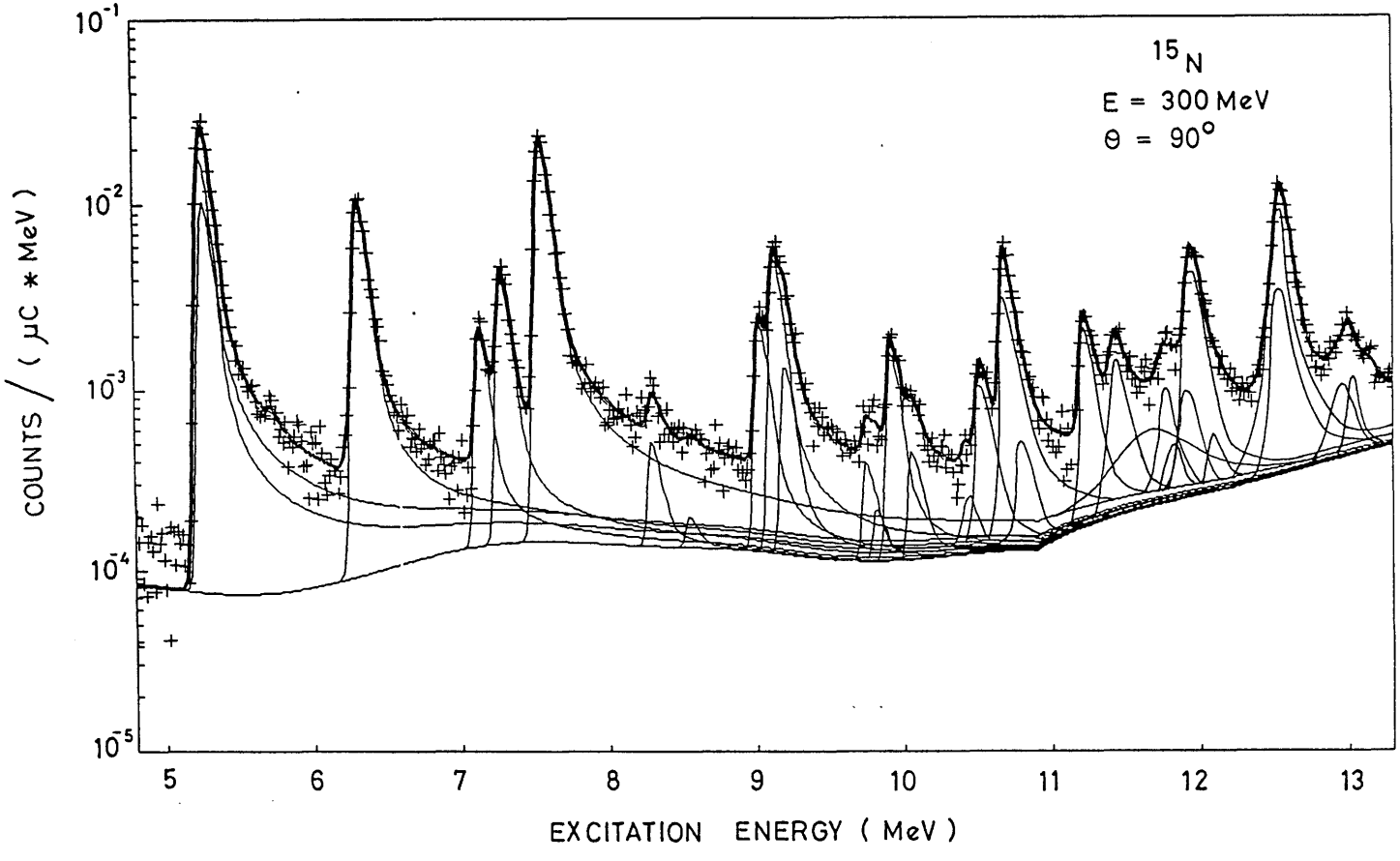

Figure 3.4: *Spectrum of inelastic scattered electrons for E_i=300 MeV and θ = 90° (q = 2.12 fm^{-1}) for $E_{exc} \leq$ 13.6 MeV region*

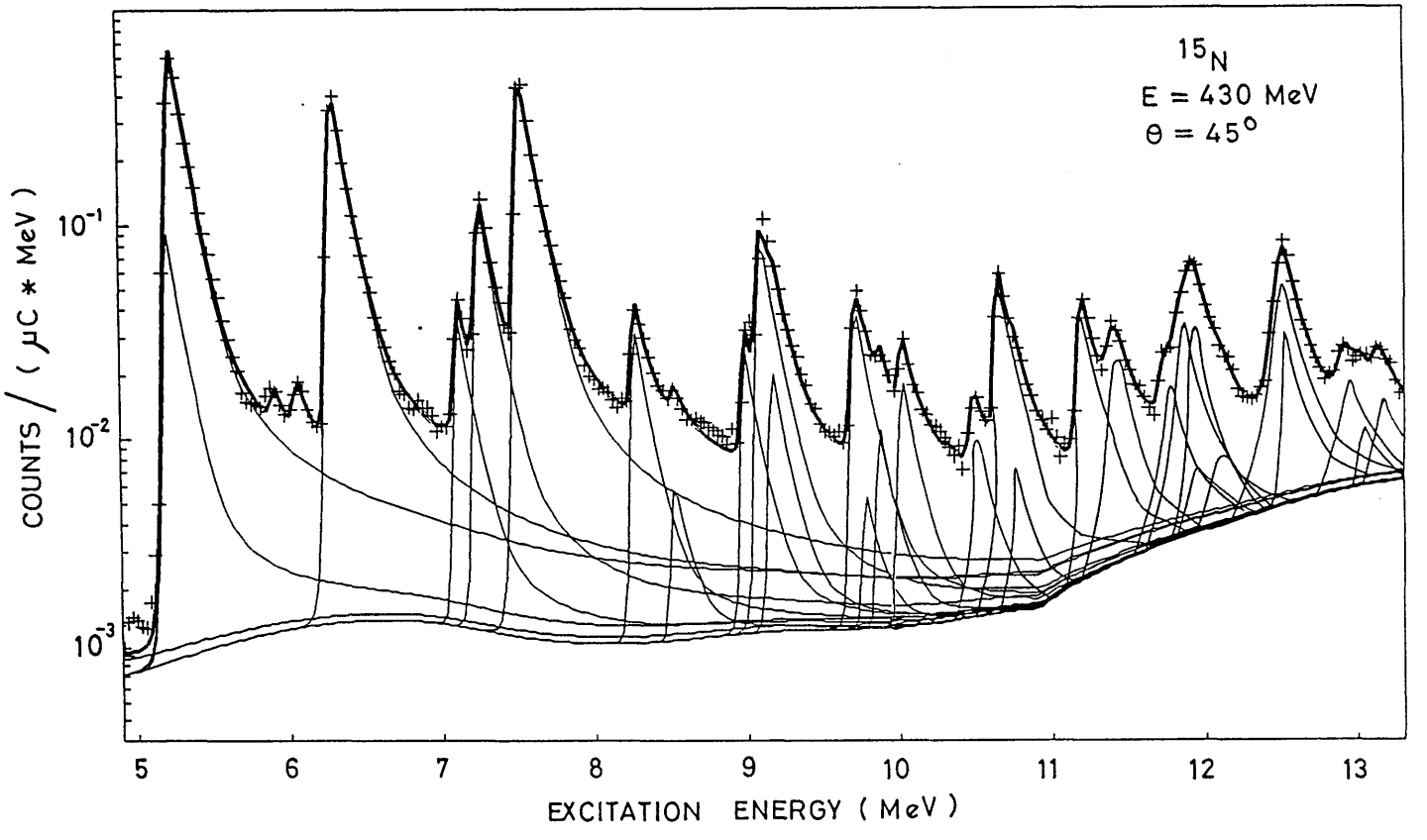

Figure 3.5: *Spectrum of inelastic scattered electrons for E_i=430 MeV and θ = 45° ($q = 1.67\ fm^{-1}$) for $E_{exc} \leq 13.6$ MeV region*

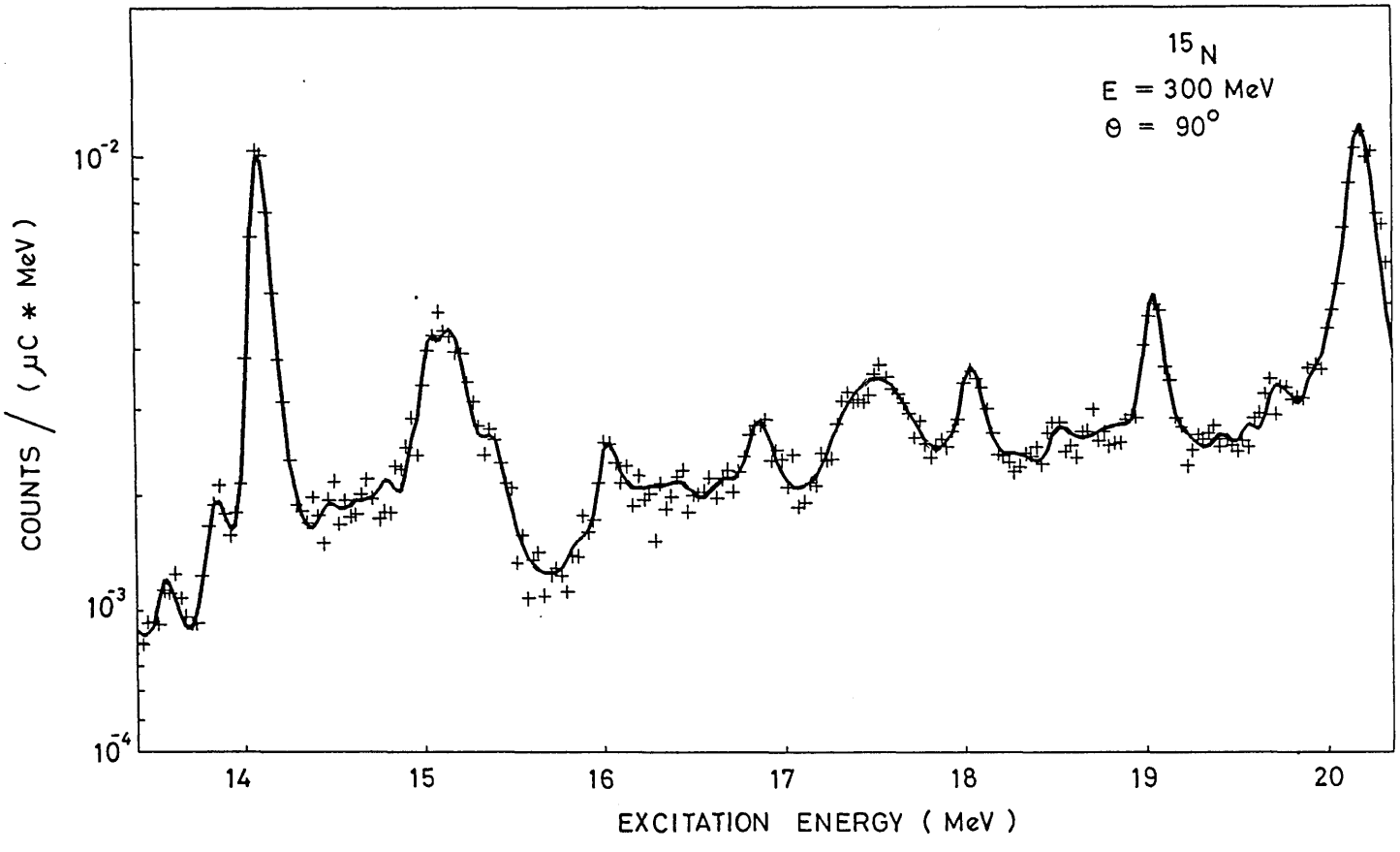

Figure 3.6: *Spectrum of inelastic scattered electrons for E_i=300 MeV and θ = 90° (q = 2.12 fm^{-1}) for $E_{exc} \geq$ 13.6 MeV region*

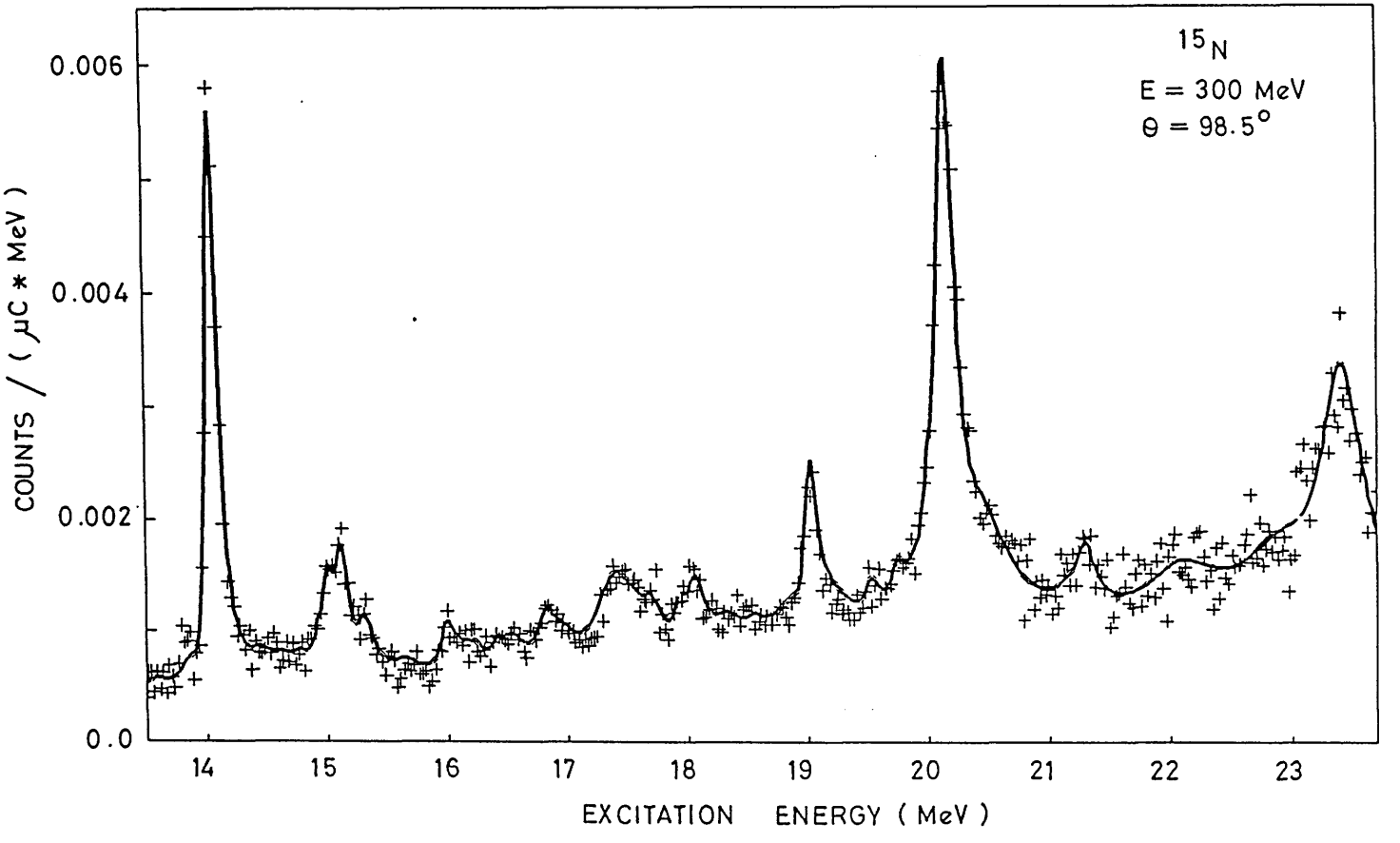

Figure 3.7: *Spectrum of inelastic scattered electrons for E_i=300 MeV and θ = 98.5° (q = 2.26 fm^{-1}) for $E_{exc} \geq$ 13.6 MeV region*

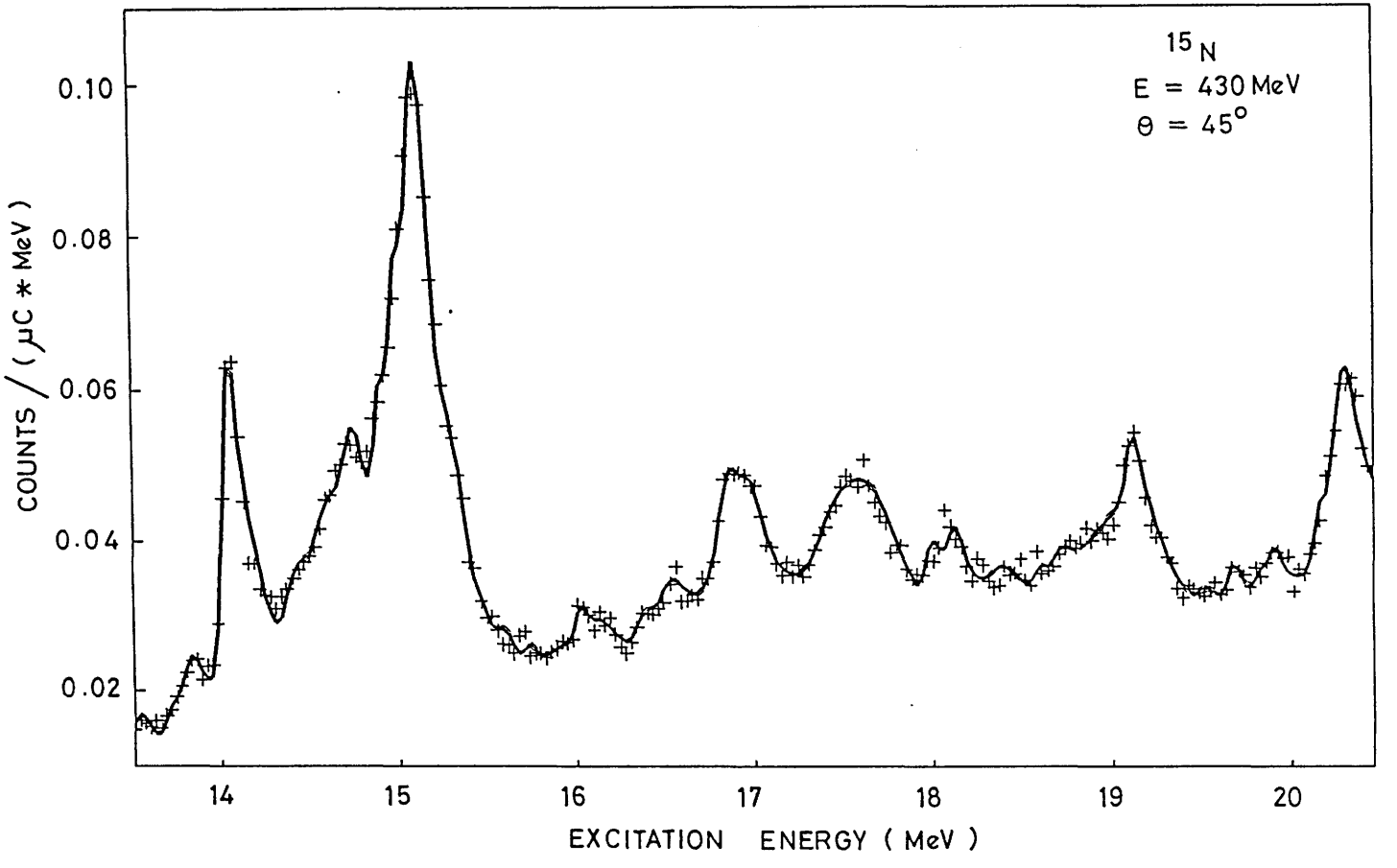

Figure 3.8: *Spectrum of inelastic scattered electrons for E_i=430 MeV and θ = 45° (q = 1.67 fm^{-1}) for $E_{exc} \geq$ 13.6 MeV region*

Chapter 4

Results and Discussion

4.1 Introduction

In chapter three the experimental measurement of the electron scattering cross sections and the determination of longitudinal and transverse form factors were discussed. The form factors for positive parity states of ^{15}N with excitation energy less than 14 MeV which were measured in this experiment are tabulated in Appendix A (tables A.1 through A.20). In addition the transverse electron scattering data for these states measured previously at MIT at the scattering angle of 180° are presented in Appendix A (tables A.21 through A.30) since these are not available elsewhere.

Form factors measured in electron scattering are Fourier transforms of corresponding nuclear transition charge and current densities ρ and $\mathbf{j}$. The transition densities represent changes in the charge, current, and magnetization distributions when the nucleus makes a transition to an excited state [31] and are determined by the wave functions of both the ground state and the excited states of the nucleus. For elastic scattering, the longitudinal form factor is simply a transform of the ground state charge distribution. In ^{15}N the ground state spin is $J^\pi = \frac{1}{2}^-$, and according to the angular momentum and parity considerations mentioned in section 2.1, for a given transition only one longitudinal multipole and in general two transverse multipoles contribute. The transition from $1/2^-$ ground state to a positive parity excited state of spin $7/2^+$, for example, will have the multipoles $\lambda^\pi = 3^-$ and 4^-. Thus the $7/2^+$ state will proceed via C3, E3 and M4 transitions. For the $1/2^+$ excited states only one transverse

multipole contibutes since in this case $1/2^+$ states will proceed via only C1 and E1.

Electron scattering data may be used in two different ways to obtain nuclear structure information. One can choose a form of the transition density and extract spectroscopic parameters for the transition. With the extended momentum transfer range of the present data, it is possible to carry out a model independent analysis which is characterized by a very large flexibility in the choice of parameters defining the transition densities. This results in somewhat larger errors on the extracted quantities but suffers only minimally by the prejudices inevitably introduced in the older methods, for example, the Tassie model[66], the Helm model[65] etc. when a well defined radial shape of the transition density was chosen.

A second way is to use the (e,e') data directly to test nuclear models. Again, because of the extended q range of the data, it is appropriate to compare the data with the predictions of a microscopic model namely the shell model. The collective models in general are too restrictive in the way they define the transition densities which is usually as derivatives of the ground state charge distributions and are not expected to be able to provide a reasonable description of the data. Moreover, the strong transverse cross sections observed for ^{15}N can only be predicted in a microscopic model.

In the following section the longitudinal form factors are analysed in a model-independent framework and provide the transition charge densities and reduced ground state transition probabilities. The comparison of the longitudinal and transverse form factors with those predicted by the shell model is discussed in section 4.3. In section 4.4 data for the $E_{exc} > 13.6$ MeV are presented.

4.2 Model Independent Analysis

The model-independent analysis was discussed in section 2.2 and was introduced with the computer code FOUBES[31]. The extracted spectroscopic information is listed in tables 4.1 and 4.2 with other experimental values obtained previously. In the following, specific details of the analysis are discussed.

As we have noted in section 2.2, the cut-off radius has to be chosen large

enough to ensure that only a negligible part of the total charge is outside that radius. However, too large a value of the cut-off radius introduces so much freedom in the choice of Fourier-Bessel coefficients that unphysical wiggles appear on the tail of the nuclear transition charge densities. To avoid these wiggles in the densities at large radii, a tail bias can be imposed as discussed in section 2.2. The radius $R_1 = 4$ fm has been used in this analysis beyond which the transition density follows such a bias in the form of a $\rho(r) \propto e^{-\alpha r}$ shape, where α is a free parameter and determines the rate of fall of $\rho(r)$ with increasing r. The cut-off radius beyond which all charge is zero has been chosen equal to 7.0 fm for all states[2].

In the Fourier Bessel analysis the A_μ coefficients (see equation 2.10) are determined mainly by the cross sections measured in the vicinity of q_μ, therefore only the coefficients A_μ for which $q_\mu < q_{max}$ can be determined by an experiment that measures cross sections up to a momentum transfer q_{max}. The data included in this analysis are extended to a maximum momentum transfer $q_{max} \leq 3.2$ fm^{-1}. Thus the data determine essentially 8 coefficients in the expansion(equation 2.10). Beyond the highest measured momentum transfer, it is necessary to assume a limiting behaviour for the form factor. This upper limit for the form factor squared was taken as Ae^{-Bq}[31], where A and B are free parameters. The limit was enforced through the use of pseudodata as specified by[31]. We assume that in this region the form factor is zero with error bars given by the upper limit envelope and spaced by $\Delta q = 1/3(q_{N+1} - q_N)$ beyond q^{eff}_{max}. Here N is the number of pseudodata points. For most of the levels 6 pseudodata points were needed. With this procedure 15 coefficients have been fitted.

The errors in the extracted transition charge densities reflect both the statistical $\Delta_{stat}(r)$ and the incompletness $\Delta_{inc}(r)$ errors introduced by the two constraints namely the extrapolated high-q behaviour and the applied tail bias. Therefore the total error $\Delta\rho_{tot}(r)$ is:

$$\Delta^2\rho_{tot}(r) = \Delta^2\rho_{stat}(r) + \Delta^2\rho_{inc}(r)$$

The variances $\Delta^2\rho_{stat}(r)$ and $\Delta^2\rho_{inc}(r)$ result from the errors in the measured

and pseudo form factors ΔF_i^{exp} ΔF_i^{pseud} with

$$\Delta^2\rho_{stat}(r) = \sum_{i=data} \Delta^2 F_i^{exp} \left(\frac{\partial\rho}{\partial F_i^{exp}}\right)^2$$

and

$$\Delta^2\rho_{inc}(r) = \sum_{i=data} \Delta^2 F_i^{pseud} \left(\frac{\partial\rho}{\partial F_i^{pseud}}\right)^2$$

where $F_i^{exp(pseud)}$ is the experimental(pseudo) form factor at q_i.

The states included in this analysis are listed in tables 4.1 and 4.2. Figures 4.1 through 4.14 show the measured longitudinal form factors with the FOUBES fit(solid line) for the $1/2^+$ states at 5.3, 8.31, 9.05 and 11.44 MeV, the $3/2^+$ states at 7.3, 8.57, 10.07, 10.8, and 11.77 MeV, the $5/2^+$ states at 5.27, 7.15, 9.15, and 10.53 MeV, and the $7/2^+$ state at 7.57 MeV. The data points displayed in these figures are the measured data recalculated for the maximum incident energy E_{max} as follows:

$$F_{rec}(E_{max}, q_{eff}) = \frac{F_1(E_{max}, q_{eff})}{F_2(E_{exp}, q_{eff})} \times F_{meas}(E_{exp}, q_{eff})$$

F_2 is the calculated form factor at the same energy as the original data from the fit. F_1 is the calculated form factor at E_{max}. The extracted transition charge densities for these states are displayed in the lower portion of figures 4.1 through 4.14. The error bands on the transition charge densities include both the statistical and incompleteness uncertainty contributions.

The large χ^2 values for states at 5.29, 11.44, 11.61, 10.8, and 5.27 are due to inconsistencies between data points. The large χ^2 values for the $5/2_1^+$ and $1/2_1^+$ levels are because these levels are the members of the doublet at 5.3 MeV which were resolved only by line-shape fitting. Most of the contribution to χ^2 for the levels at 11.44 MeV comes from the data points at high q values, because the transverse component at these values are dominant. The doublet at 9.15 MeV consists of the unresolved pair of levels at $9.152(3/2^-)$ and $9.155(5/2^+)$ MeV. According to the (γ,γ') measurements[3] the form factor at the maximum for $3/2^-$ state is $\approx 6\times10^{-5}$ and hence the contribution from this state is small. We assumed, therefore, the absence of the $3/2^-$ member in the fit of this doublet. In extracting the transition densities for the $1/2^+$(9.05 MeV), $3/2^+$(7.3 MeV),

$3/2^+$(8.57 MeV), and $3/2^+$(10.07 MeV), a lowest momentum transfer data point provided by (γ,γ') experiment[3] was also included in the fits. The form factor of this data point was calculated from the experimental B(E1) value by using the equation

$$B(EL) = \frac{Z^2}{4\pi}\frac{[(2L+1)!!]^2}{q^{2L}} \mid F_{CL} \mid^2 .$$

The B(EL) values extracted from the FOUBES fits and their uncertainties together with results from other experiments are listed in tables 4.1 and 4.2. Some experiments provided only the reduced ground state transition widths $\Gamma_\circ$. The B(EL) values for $q = \omega = E_{exc}/\hbar c$ are related to the reduced ground state transition widths $\Gamma_\circ$ by:

$$\Gamma_\circ(eV) = \frac{8\pi\alpha\hbar c}{1}10^6\frac{(L+1)}{L[(L+1)!!]^2}\left(\frac{E_{exc}}{\hbar c}\right)^{2L+1}\frac{2J_\circ+1}{2J+1}B(EL).$$

where, α=1/137 is the fine structure constant and $\hbar$c=197.3 MeV.fm. The uncertainties in some of the extracted $B(EL)$ values are rather large. It should be noted that these transition probabilities $B(EL)$ are, for most levels, extrapolated quantities and do not represent the best available information from the experiment. The fact that some of the fitted data start at momentum transfer values not lower than 0.6 fm^{-1}, introduces in the extrapolation to the photon points large uncertainties when analysed in a model independent framework. On the other hand the uncertainties in some of the $B(EL)$ values measured by (γ,γ')[3] are rather small because the $B(EL)$ value is deducible directly from the experimental data without any need of further assumptions.

It should be mentioned that the resulting $B(E1)$ values are in an overall agreement, within error, with those measured by (γ,γ') [3].

The $B(EL)$ values obtained from the theory[18] which are also displayed in the last column in tables 4.1 and 4.2 agree with the measured values for C1 transitions but disagree with those for C3 transition. This will be discussed in the following sections.

Table 4.1: B(E1) values for ^{15}N

Ex (MeV)	$2J^{\pi}$	Present $e^2.f^2$	χ^2	Others $e^2.f^2$	Theory $e^2.f^2$
5.29	1_1^+	0.004(0.013)	9.0	0.007[a] 0.014(0.04)[b]	5.03E-05
8.31	1_2^+	5.02(11)E-04	1.1	4.99(3.3)E-04[c]	4.33E-04
9.05	1_3^+	1.625(0.3)E-03	1.5	1.55(0.25)E-03[c]	1.0E-03
11.44	1_4^+	1.51(6.4)E-04	10.5		
11.61	1_5^+	5.37(2.0)E-02	9.64		
7.30	3_1^+	6.11(0.58)E-03	2.3	5.3(0.4)E-03[c] 0.123(0.03)[a]	5.0e-03
8.57	3_2^+	1.66(0.9)E-03	1.2	7.45(7.4)E-03[c]	1.24E-03
10.07	3_3^+	1.46(0.16)E-02	4.5	1.2(0.07)E-02[c]	1.0E-02
10.8	3_4^+	5.05(7.7)E-04	5.2		
11.77	3_5^+	1.33(0.32)E-02	3.4		

[a] Reference [20].
[b] Reference [21].
[c] Reference [3].

Table 4.2: B(E3) values for ^{15}N

Ex (MeV)	$2J^{\pi}$	Present $e^2.f^6$	χ^2	Others $e^2.f^6$	Theory $e^2.f^6$
5.27	5_1^+	264.6(96.5)	18.7	189(6)[a] 293(20)[b]	160
7.155	5_2^+	12.2(1.1)	0.43	7.1(8)[b]	0.122
9.15	5_3^+	67.8(8.5)	1.4		6.8
10.5	5_4^+	2.65(0.6)	1.8		
12.5	5_7^+	53.6(13)	5.5		
13.61	5_9^+	3.9(1.2)	2.0		
7.57	7_1^+	203(13)	1.9	136(12)[b]	54

[a] Reference [20].
[b] Reference [21].

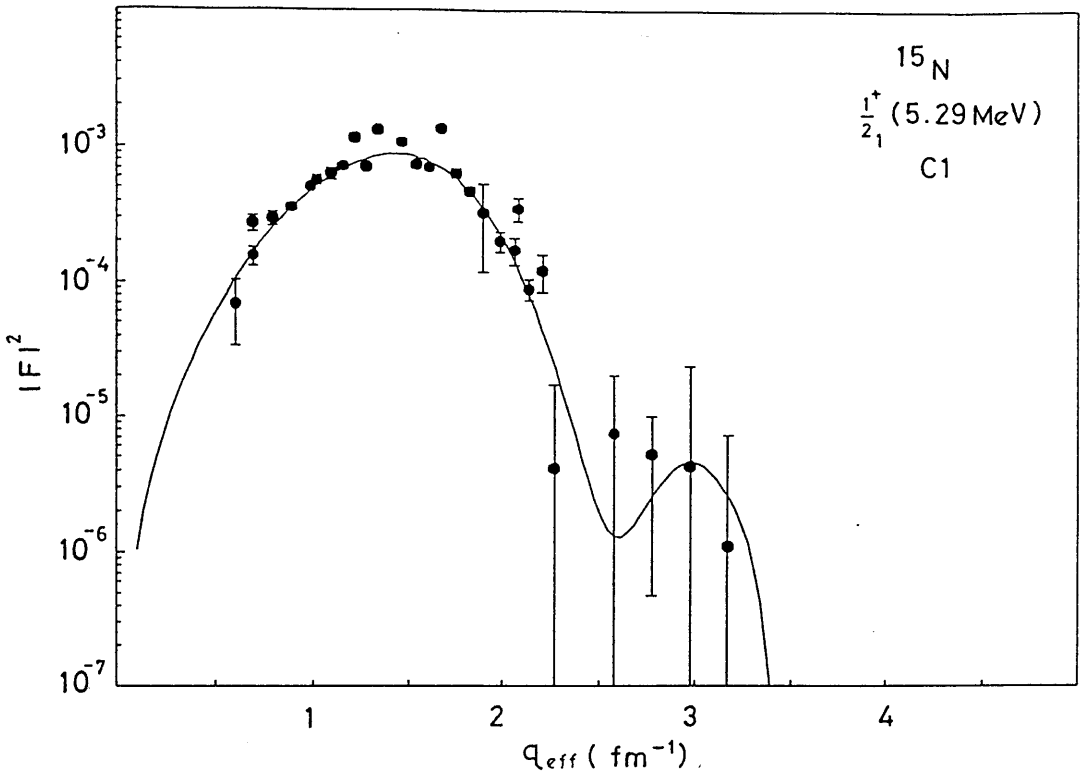

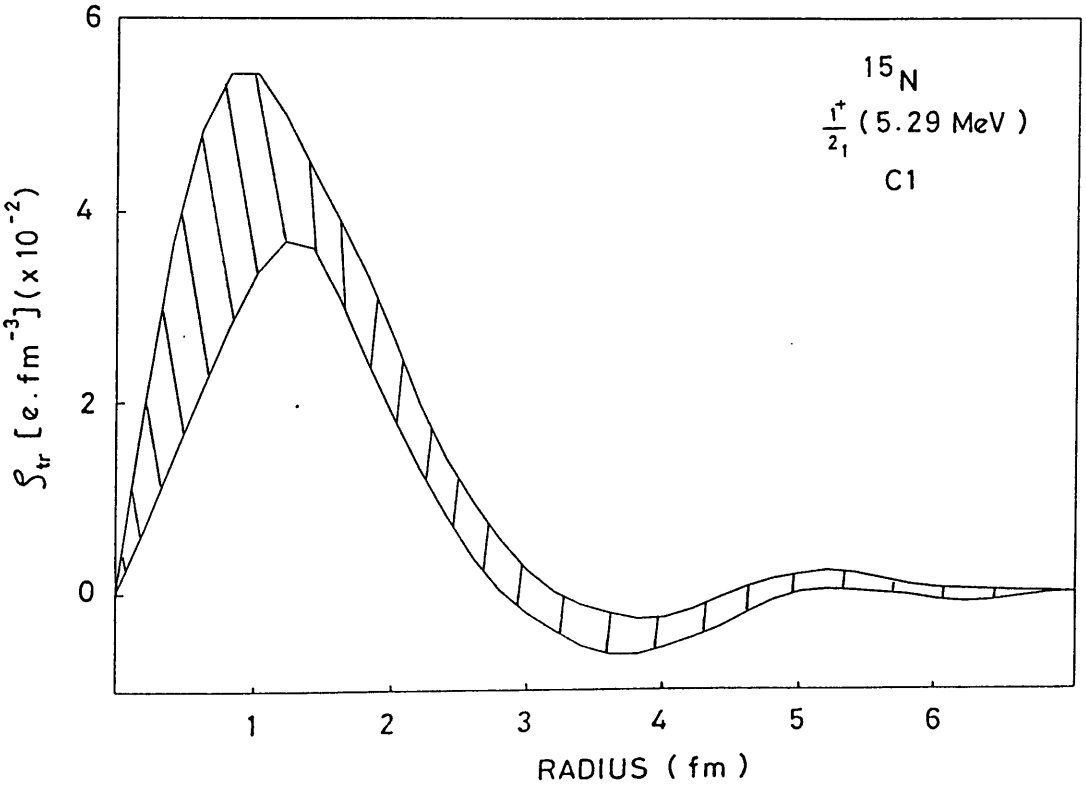

Figure 4.1: *Measured form factor for $1/2_1^+$ at 5.29 MeV and extracted charge density.*

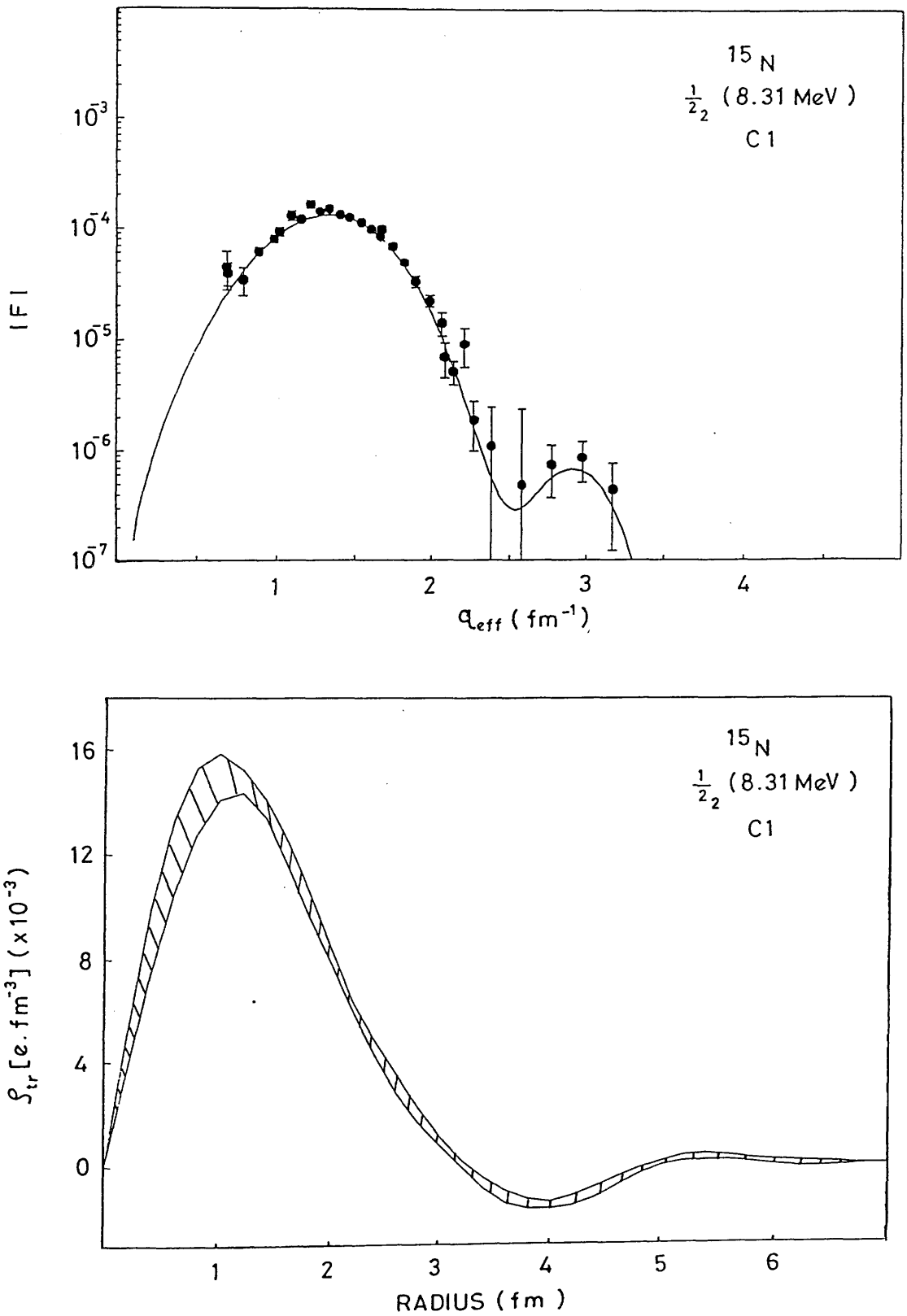

Figure 4.2: *Measured form factor for $1/2_2^+$ at 8.31 MeV and extracted charge density.*

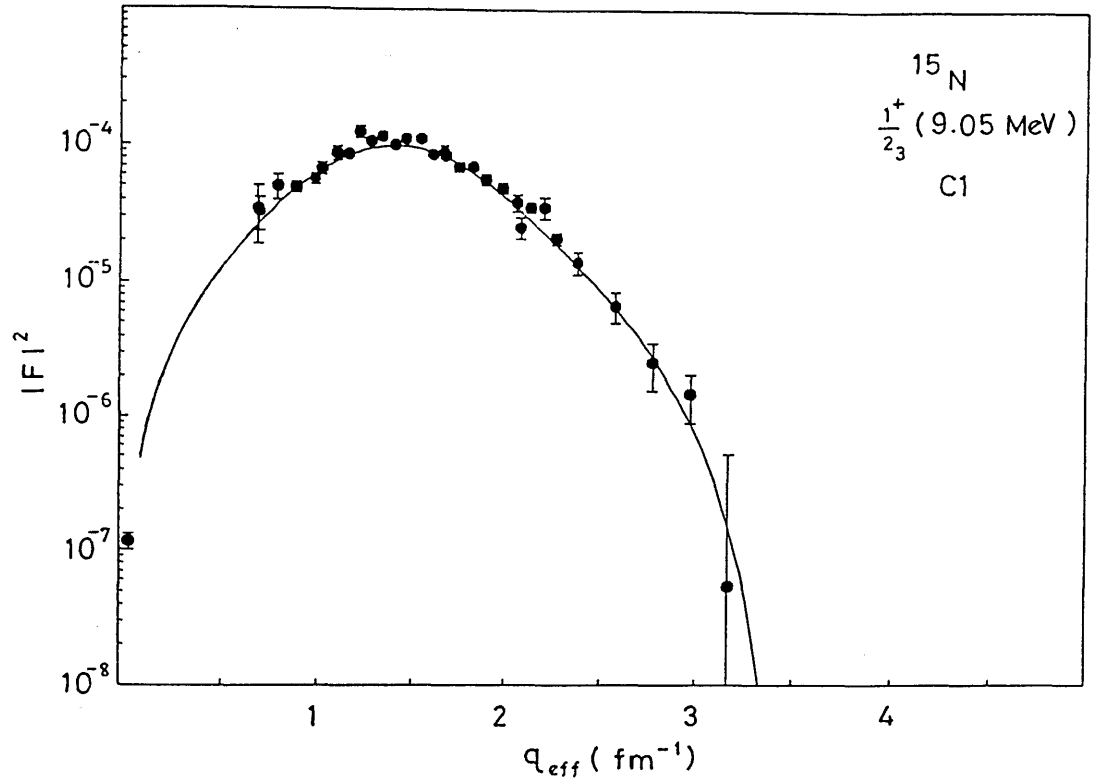

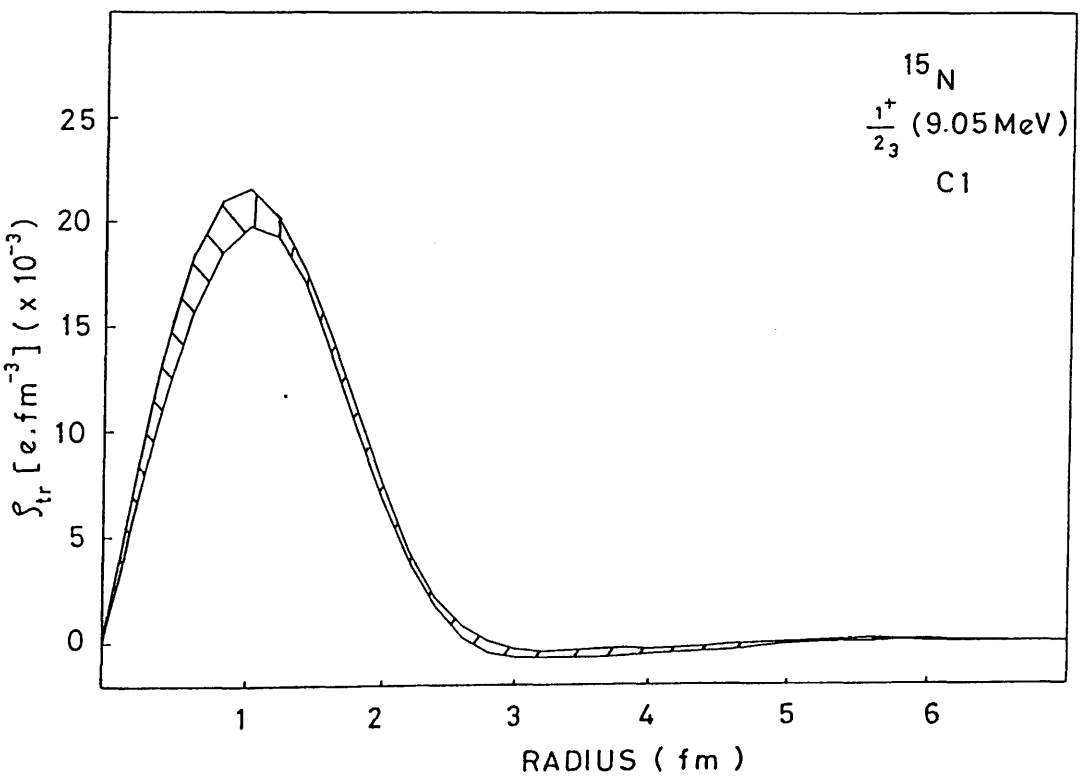

Figure 4.3: *Measured form factor for $1/2_3^+$ at 9.05 MeV and extracted charge density.*

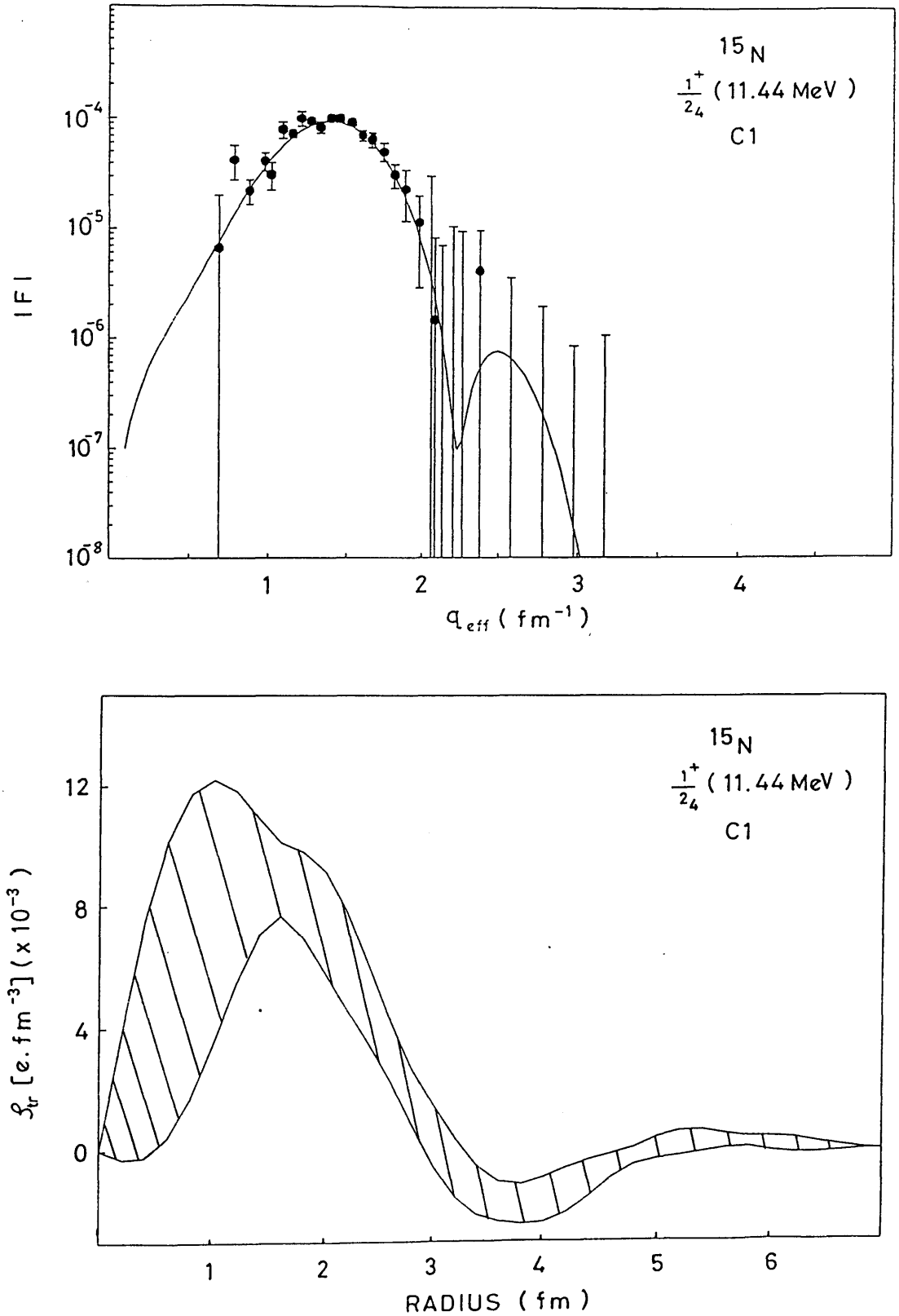

Figure 4.4: *Measured form factor for $1/2_4^+$ at 11.44 MeV and extracted charge density.*

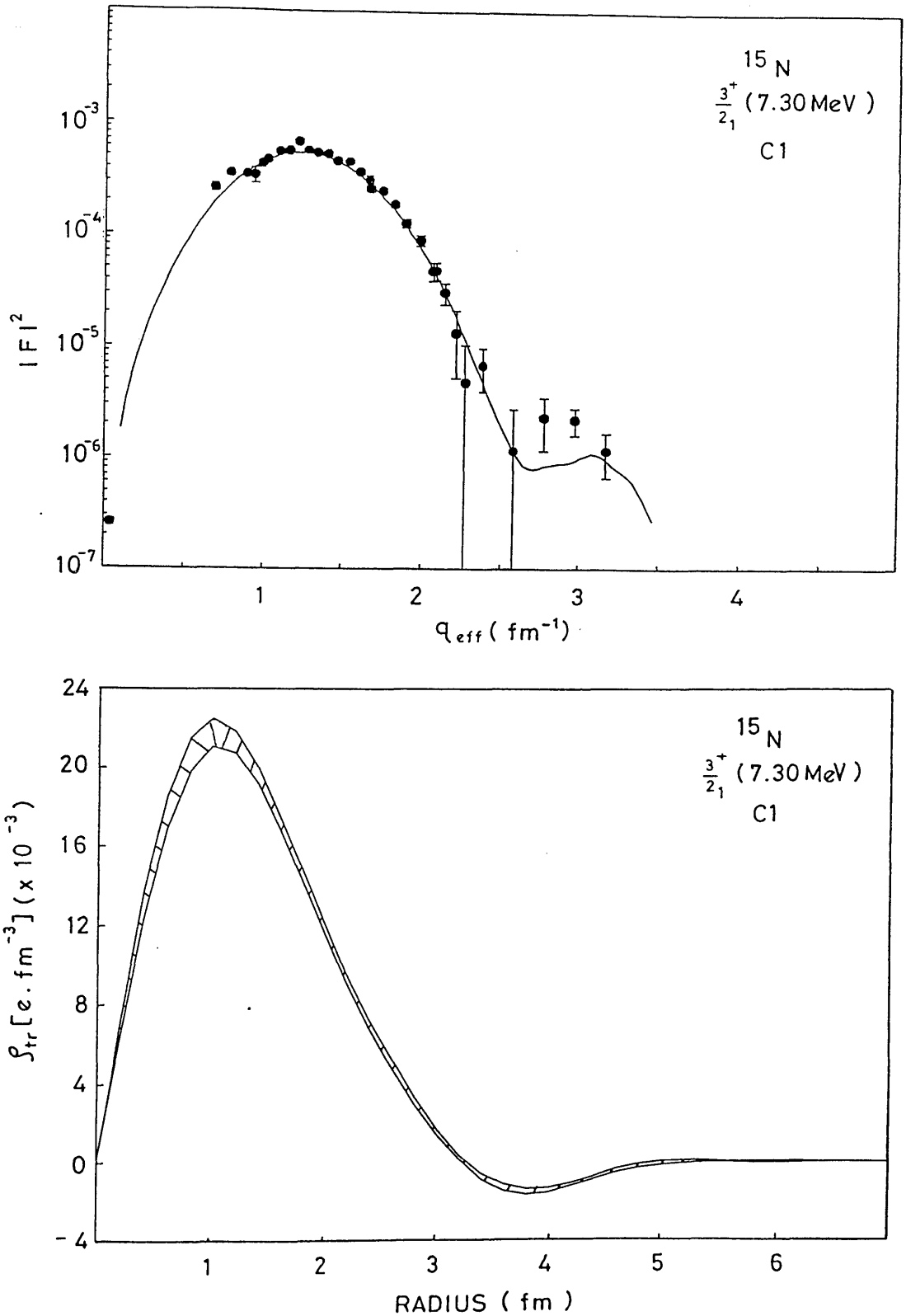

Figure 4.5: *Measured form factor for $3/2_1^+$ at 7.30 MeV and extracted charge density.*

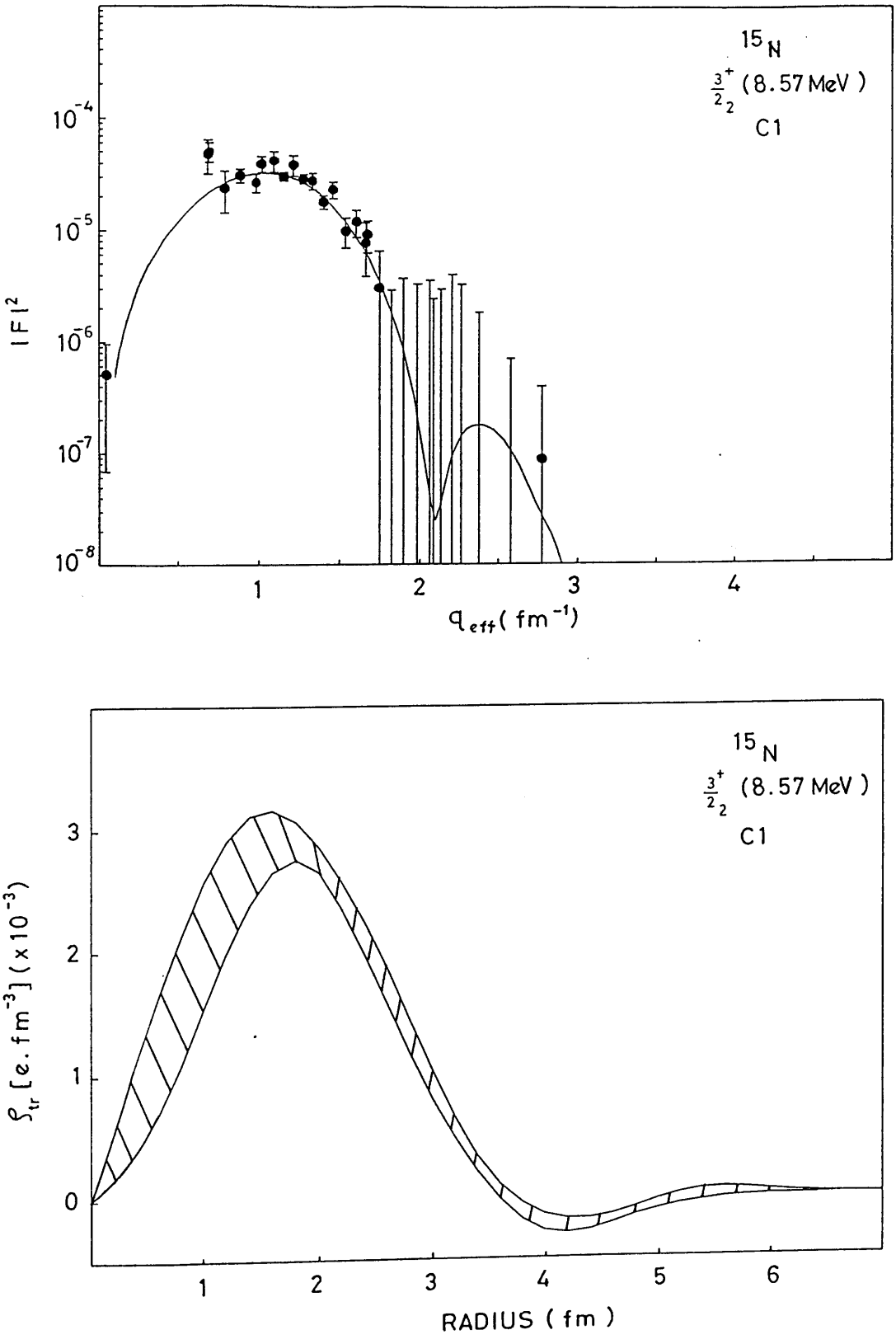

Figure 4.6: *Measured form factor for $3/2_2^+$ at 8.57 MeV and extracted charge density.*

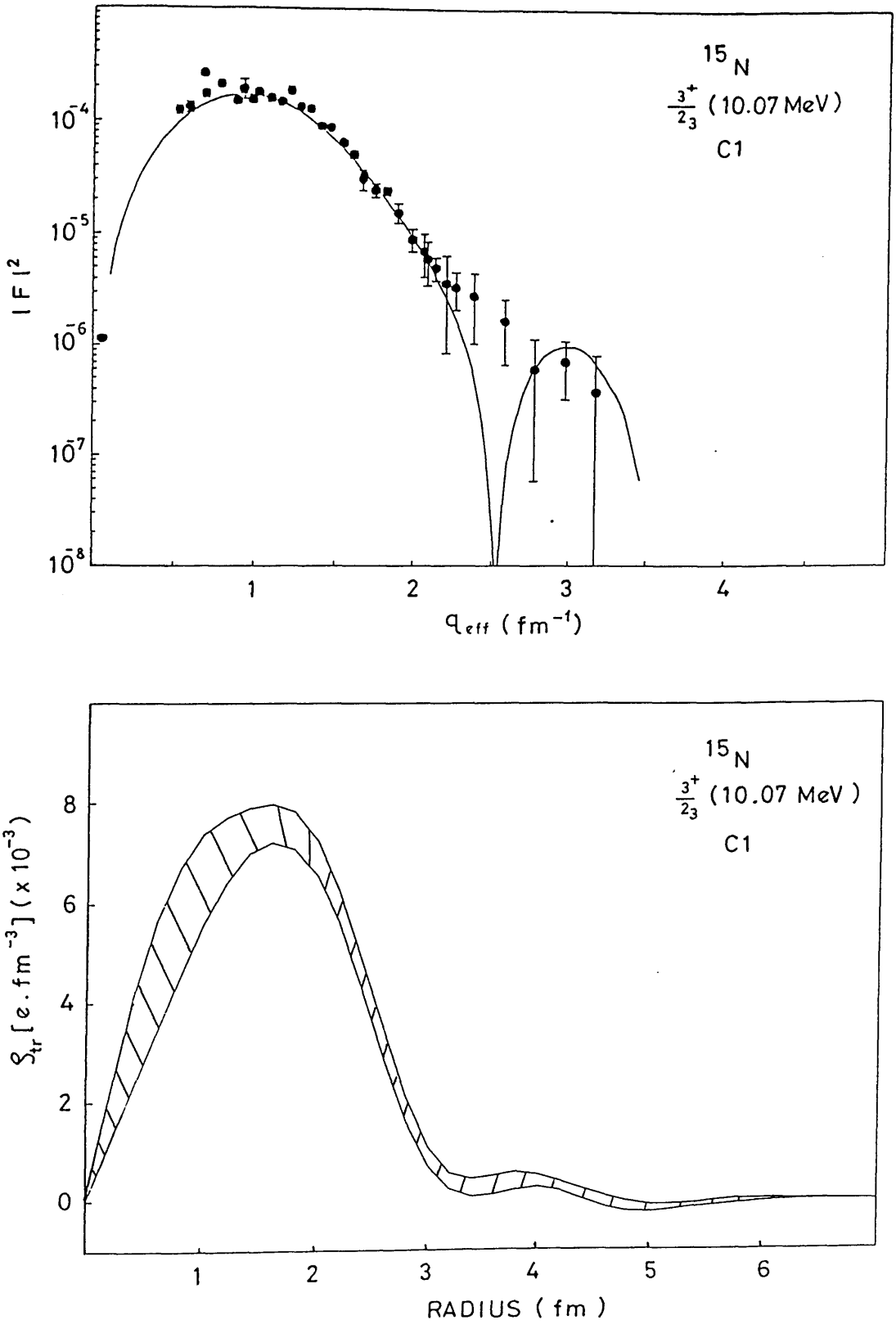

Figure 4.7: *Measured form factor for $3/2^+_3$ at 10.07 MeV and extracted charge density.*

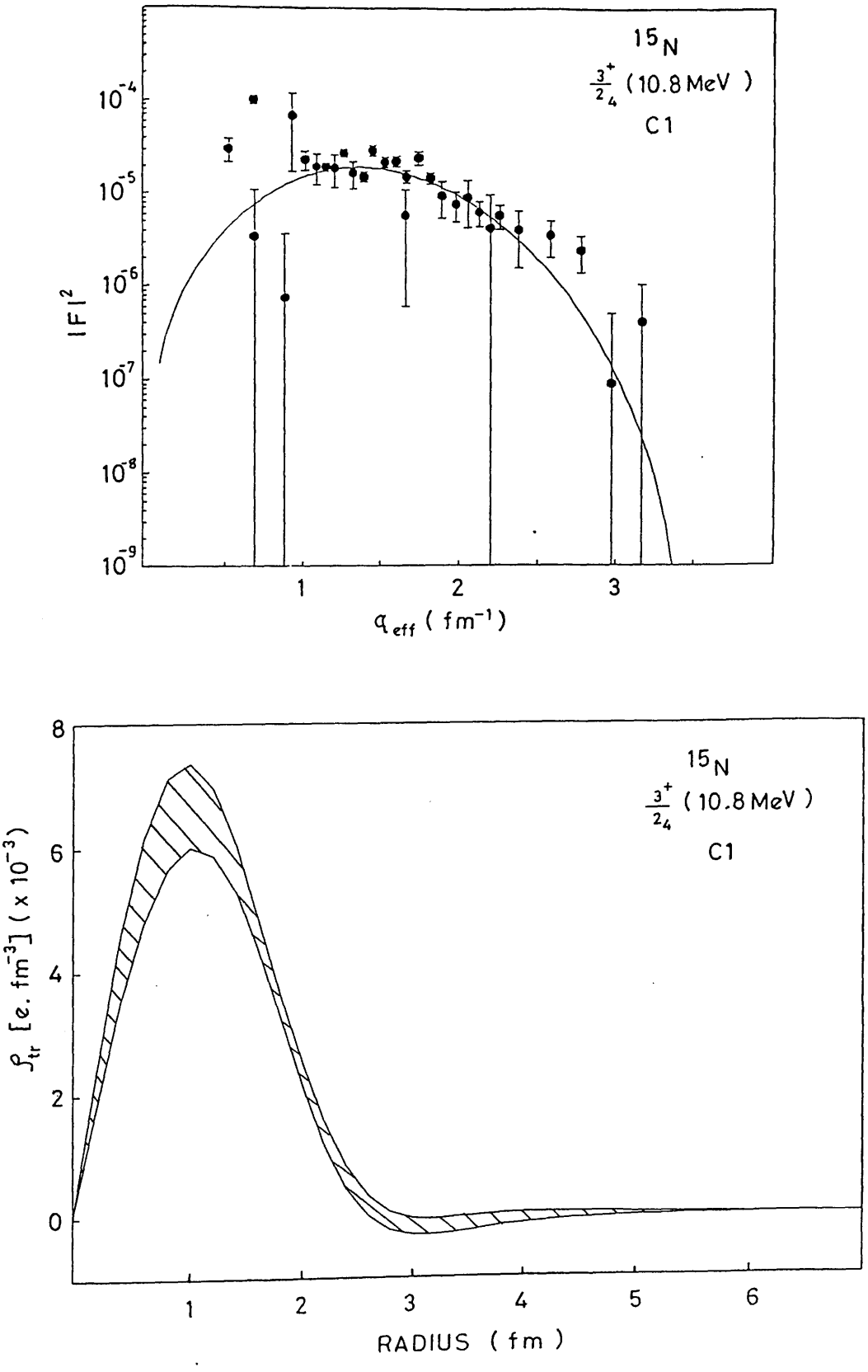

Figure 4.8: *Measured form factor for $3/2_4^+$ at 10.8 MeV and extracted charge density.*

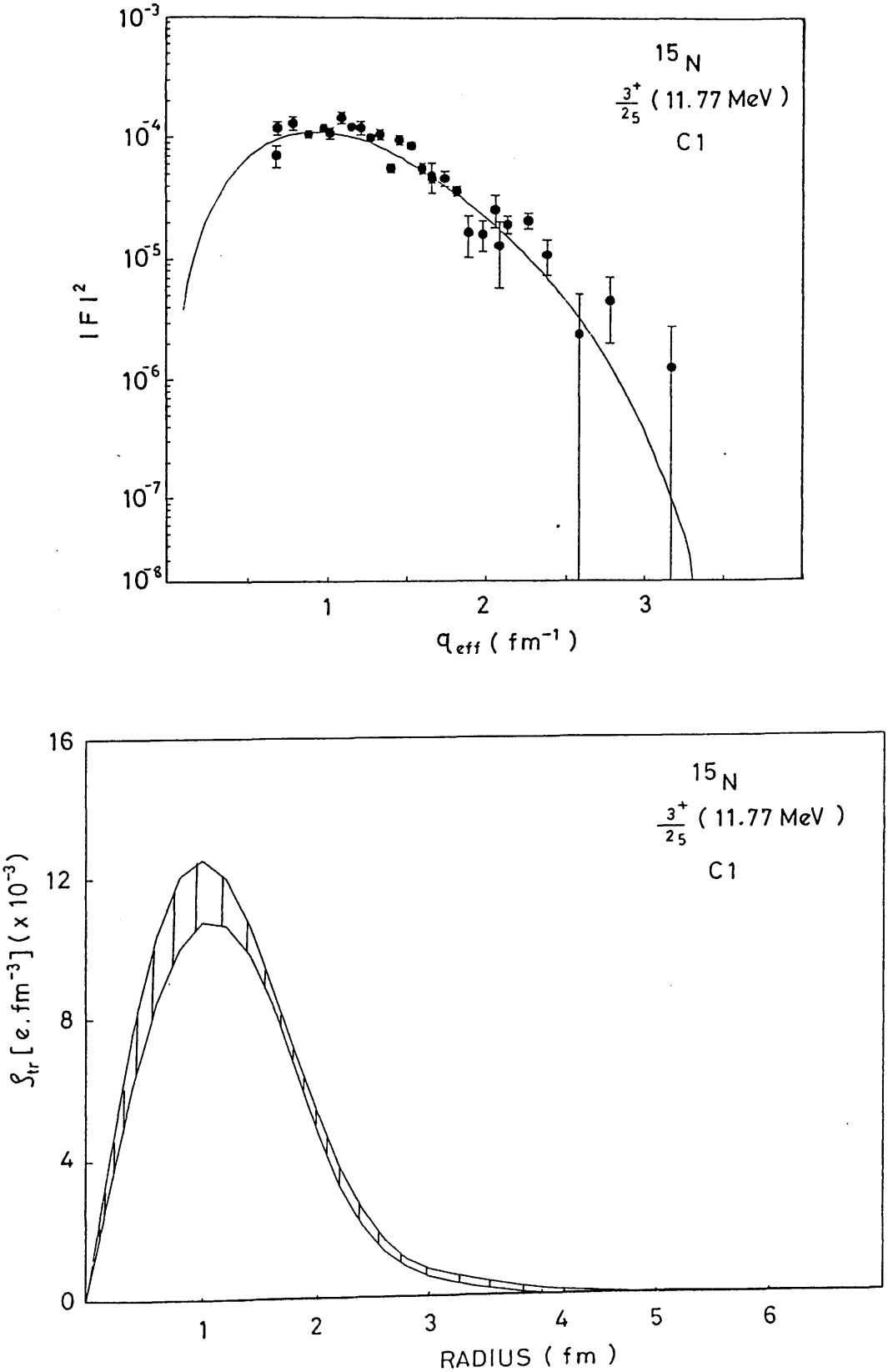

Figure 4.9: *Measured form factor for $3/2^+_5$ at 11.77 MeV and extracted charge density.*

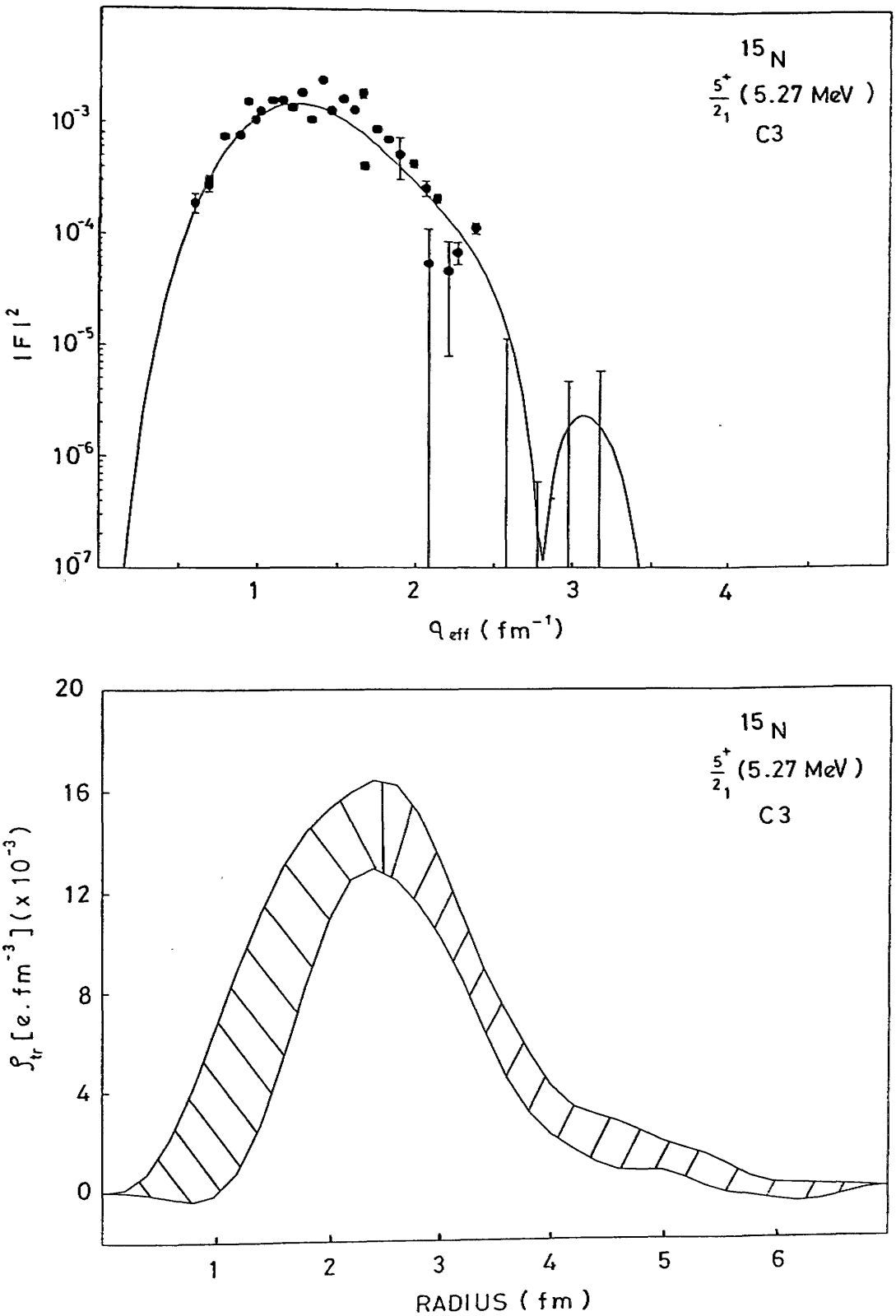

Figure 4.10: *Measured form factor for $5/2_1^+$ at 5.27 MeV and extracted charge density.*

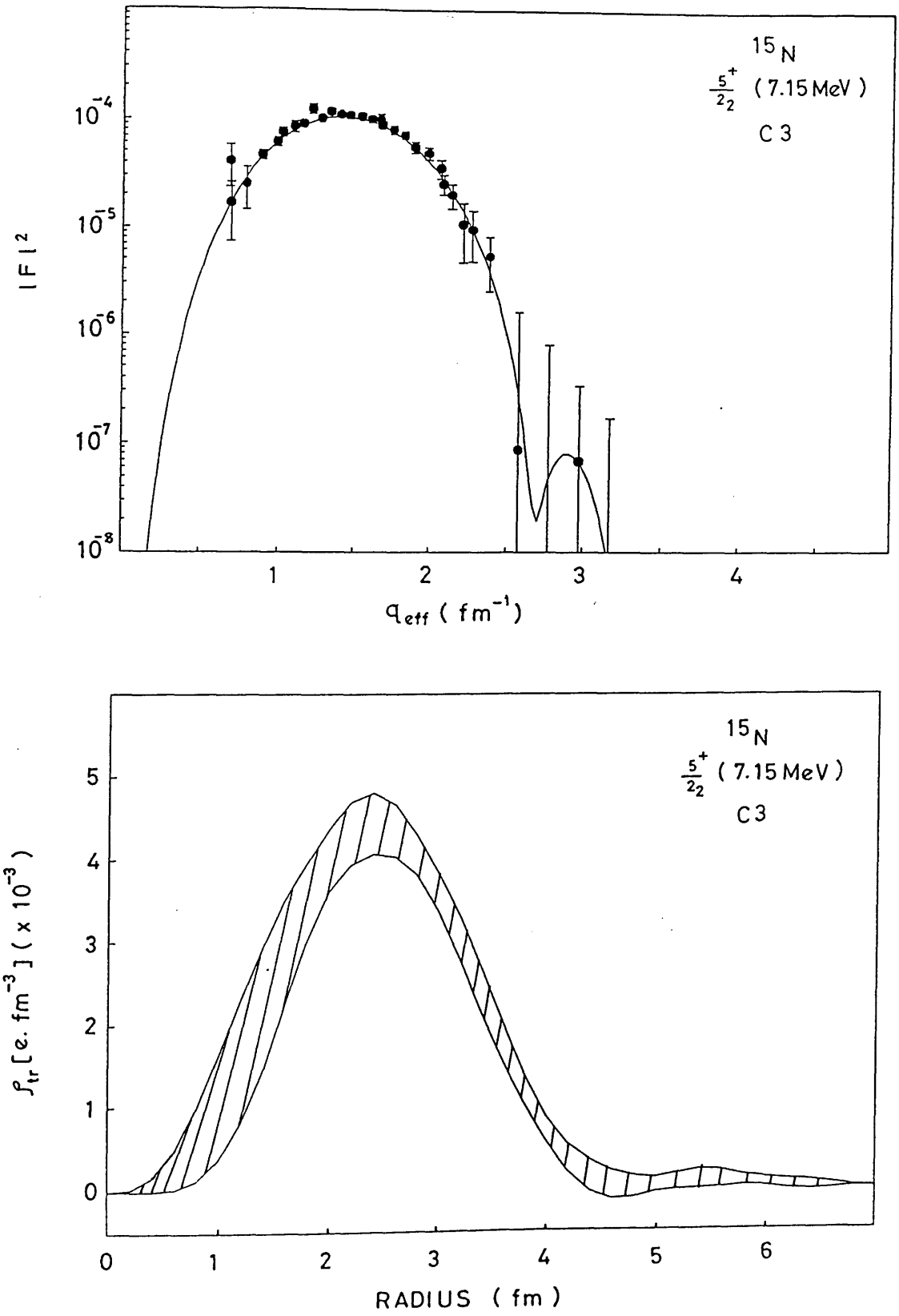

Figure 4.11: *Measured form factor for $5/2_2^+$ at 7.15 MeV and extracted charge density.*

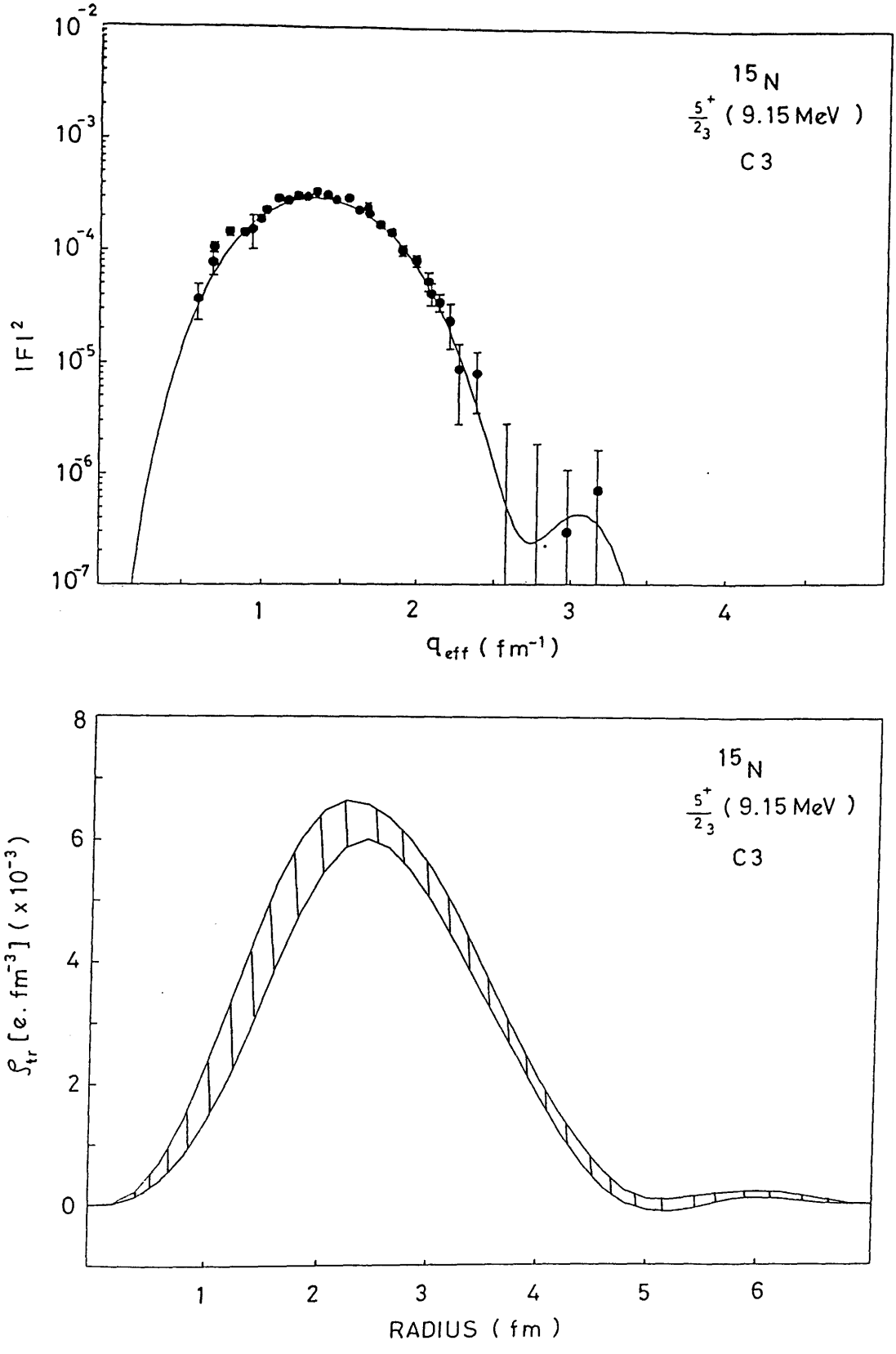

Figure 4.12: *Measured form factor for $5/2_3^+$ at 9.15 MeV and extracted charge density.*

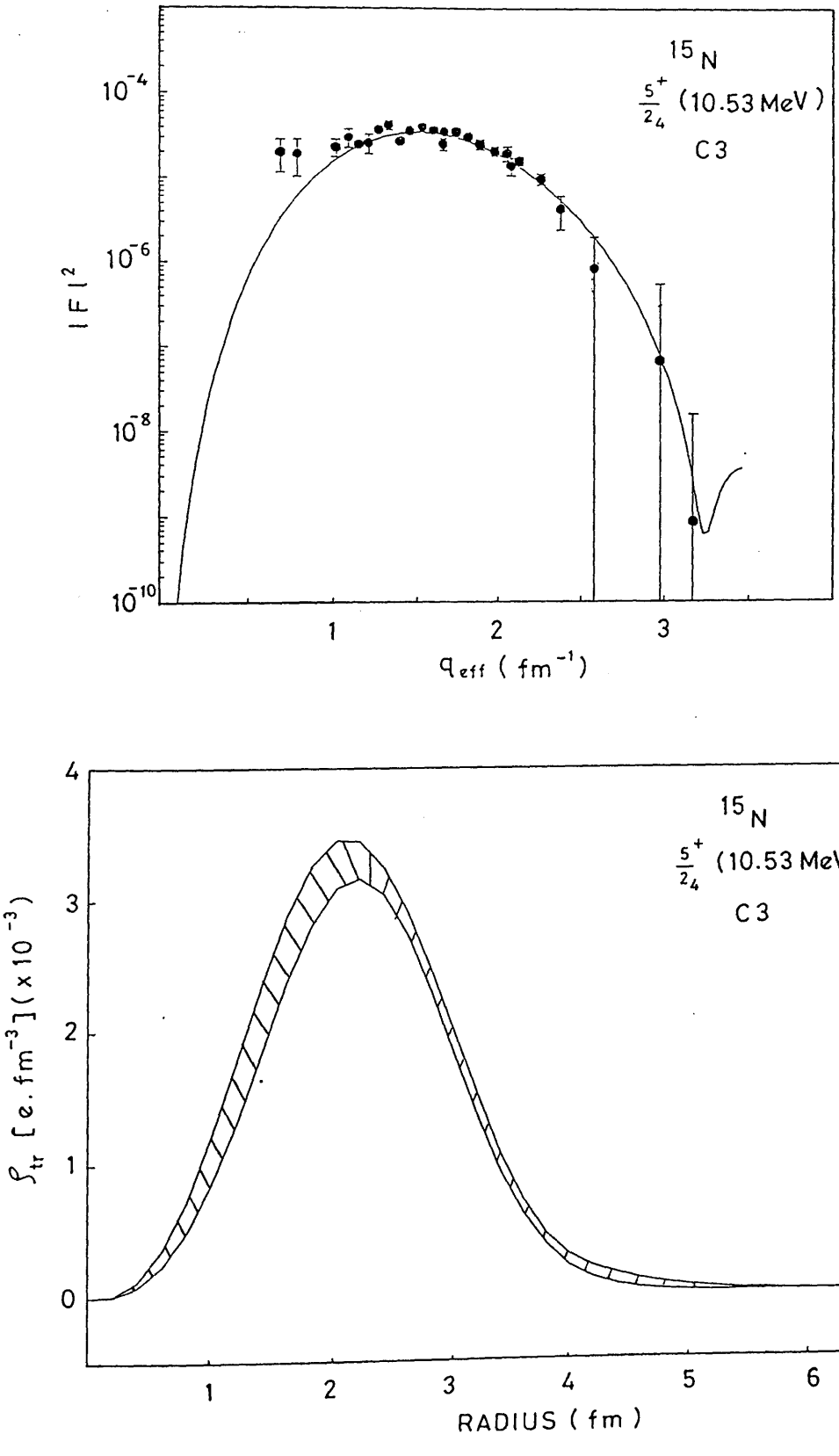

Figure 4.13: *Measured form factor for $5/2_4^+$ at 10.5 MeV and extracted charge density.*

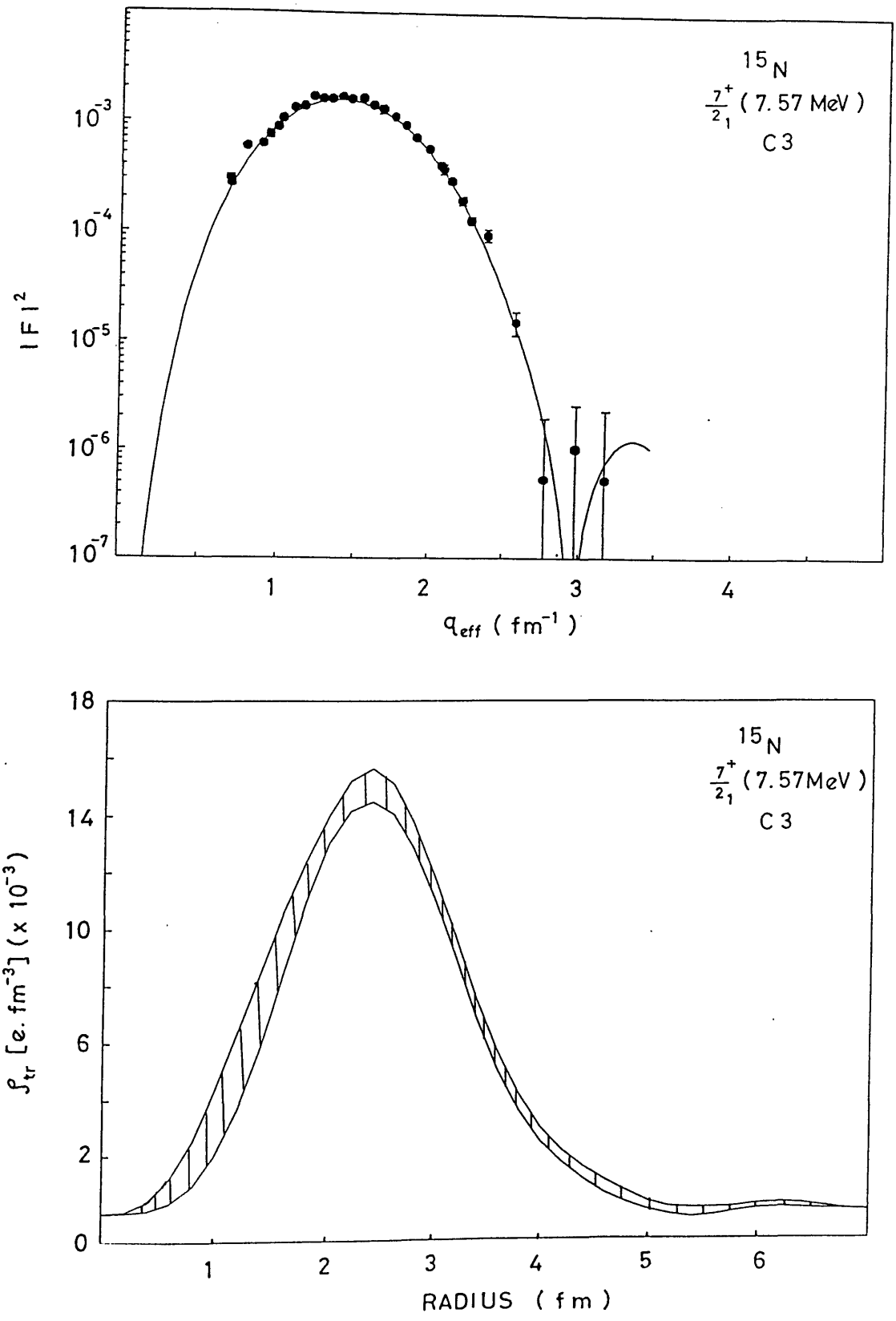

Figure 4.14: *Measured form factor for $7/2_1^+$ at 7.57 MeV and extracted charge density.*

4.3 Shell Model

In the previous section the experimental longitudinal form factors were discussed in terms of a model independent analysis. These form factors and those measured at 180° will now be compared with the predictions of the nuclear shell model. Shell model calculations used in this analysis were performed in a $(1+3)\hbar\omega$ space for the positive parity states in ^{15}N by Millener[12] and are the most extensive available at present. The ground state was confined to the p-shell, and the excited states were formed by promoting one or more nucleons into the sd-shell through the fp-shell. This allows the following configurations: s^{-1}; $p^{-2}(sd)^1$; $p^{-4}(sd)^3$; $p^{-3}(sd)^1(pf)^1$; $s^{-1}p^{-2}(sd)^2$. The effective interactions used were those of Cohen and Kurath[68] for the p shell, of Kuo-Brown[69] for the sd shell, and of Millener and Kurath[70] for the particle-hole interaction. The Utrecht group of Glaudemans[71] has also carried out a shell model calculation in a $3\hbar\omega$ model space for ^{15}N. The interactions used in this calculation are derived from the Reid soft-core potential and the Sussex matrix elements. The results of this calculations are also compared with the data. The theoretical form factors were calculated in the PWBA. This approximation is adequate for a light nucleus like ^{15}N ($Z\alpha \ll 1$) where the Coulomb distortion effects are small and can be accounted mainly by the construction of an effective momentum transfer as discussed in subsec. 2.1.4. Therefore, comparisons with experiment are made by plotting the experimental form factors vs q_{eff} and the calculated form factors vs q. The effective momentum transfer q_{eff} is given in subsec. 2.1.4.

The radial wave functions required for the single nucleon transition densities were calculated both for the harmonic oscillator(HO) and Woods-Saxon (WS) potentials. In HO, the oscillator length parameter b = 1.7 fm was chosen to reproduce the root mean square (r.m.s) charge radius of 2.611 fm for ^{15}N obtained from an analysis of the elastic electron scattering cross sections measured in this experiment [2]. The WS potential parameters were those of Gamba et.al.[53]. Comparison between the HO and WS wave functions shows no appreciable difference, figure 4.26, and for reasons mentioned in subsec. 2.2.2, we have used

the HO wave function in our analysis.

Two corrections must be applied to the calculated form factors to convert them into a representation appropriate for comparison with experimental form factors, see subsec. 2.2.2. These corrections are accomplished by multiplying the form factors by factors corresponding to corrections for the center-of-mass motion of the nucleons and the finite size of the nucleon.

Generally the B(EL,ω) values and the longitudinal form factors obtained in the shell model calculations are too small compared with the experimental data. This is particularly true for the so called collective transitions. Conventionally the discrepancy between the experimental and theoretical form factor is explained by the introduction of an additive effective charge defined as:

$$e = e_i + \delta e$$

where e_i is the charge of the free nucleon(e_p=1, e_n=0) and δe is the effective charge. Some flexibility in the choice of different values of δe for the neutron and the proton has been found to provide a better description of the experimental data. This approach was investigated by Brown et al.[55] for nuclei near ^{16}O and they found effective charges for the neutron δ_n=0.34 and for proton δ_p=0.0. For octupole transitions it has been found that the δ_n that is bigger than the δ_p explained the experimental data very well[63], [64]. Millener has suggested that the octupole transitions in ^{15}N can be explained by δ_n=0.385, δ_p=0.095[18]. The present data are extended to a high momentum transfer(q=3.2 fm^{-1}) and are useful for tests of these observations.

In the following subsections we investigate the electric dipole, octupole and M4 transitions in terms of the shell model predictions.

4.3.1 Electric Dipole Transitions

Since ^{15}N has a J^π=1/2$^-$ ground state, all the states of J^π=1/2$^+$ or 3/2$^+$ yield longitudinal C1 scattering and transverse E1 scattering. For the 3/2$^+$ excited states transverse M2 multipoles also contribute. The longitudinal form factors for these transitions were presented in the previous section in the frame work of a model independent analysis. Both longitudinal and transverse form factors are now compared with the shell model predictions.

These transitions include the $1/2^+$ states at 5.29, 8.31, 9.05, and 11.44 MeV and $3/2^+$ states at 7.30, 8.57, 10.07, 10.8, and 11.78 MeV. We first concentrate not on any individual level but on the general features of the experimental and theoretical form factors. The longitudinal and transverse form factors for these states are presented in figures 4.15 through 4.23 along with the shell model predictions of Millener(solid line) and Utrecht group(dashed line). We have chosen to present the calculations for all of these form factors using no effective charges in longitudinal component and using the free-nucleon orbital and spin g factors. These comparisons reveal several features: the theoretical longitudinal form factor is always smaller than the data. The theoretical transverse form factor shows the opposite behaviour to the longitudinal one and is always larger than the data. Further, both longitudinal and transverse theoretical form factors, generally, do not appear to have the correct shape to give a good description of the data. Finally, the theoretical form factor calculated by Millener provide a better description of the data than those calculated by the Utrecht group. Therefore, we will discuss the data in terms of Millener calculations.

In this first pass over our longitudinal and transverse form factors, we have examined the general aspects of the shell model predictions. We now turn to detailed examinations of the individual form factors.

As we have mentioned previously in this section, the discrepancy between the experimental and theoretical form factor is conventionally explained by a constant additive effective charge. Two sets of effective charges have been used. These values are as follows: $\delta e_p=\delta e_n=0.37$ for $1/2^+$ states and $\delta e_p=\delta e_n=0.25$ for $3/2^+$ states. For the transverse form factor case a downward normalisation factor of 1.6 has been used. These values are the optimum values that can be used to describe the data without invalidating the use of a constant effective charge. We will discuss first the longitudinal form factors in terms of the shell model predictions calculated with these effective charges and afterwards return to the transverse data.

The longitudinal data and shell model calculations for $1/2^+$ states at 5.3, 8.31, 9.05, and 11.44 MeV are shown in figures 4.15 through 4.18 and the dot-dashed curves represent the shell model predictions. The most significant

form factor associated with these levels is the first $1/2^+$ state at 5.29 MeV. The predicted C1 form factor gives a good fit to these data, even though the experimental B(E1)(q=0) value is very much larger than theory (see table 4.1). The higher $1/2^+$ levels have form factors which disagree in various ways with the predictions. In comparison to the theory, the longitudinal data for 8.31 and 9.05 MeV levels are large while they are smaller for the 11.44 MeV level. The experimental B(E1) values for these states are in overall agreement with theory and with those measured by (γ, γ')[3] (see table 4.1).

The longitudinal data and the predictions for the $3/2^+$ states at 7.30, 8.57, 10.07, 10.8 and 11.78 MeV are shown in figures 4.19 throgh 4.23. Again, the dot-dashed curves represent the shell model calculations. The predictions for the first two $3/2^+$ states at 7.30 and 8.57 MeV are in reasonable agreement with the data. However, the experimental shapes for these states disagree with theory at larger values of momentum transfer. The data for the $3/2^+$ level at 10.07 MeV is in agreement with C1 predictions at larger values of momentum transfer but the predicted strength in the vicinity of the maximum of the form factor is low. The C1 predictions for the $3/2^+$ states at 10.8 and 11.78 MeV are those calculated by Utrecht group since Millener calculations are not available. The form factors for these levels are different from the predictions. The experimental B(E1) values for the $3/2^+$ states are in good agreement with theory and those measured by (γ, γ')[3] (see table 4.1).

As we have mentioned previously at the beginning of this section that some flexibility in the prescription of different values of δe for the neutron and the proton has been found to provide a better description of the experimental data. This approach has been used to explain the experimental C1 form factors. For example, we present the data in figure 4.24 for $1/2^+$ level at 9.05 MeV with shell model prediction calculated by given δe for proton and neutron as follows: $\delta e_p = 0.5$, $\delta e_n = 1.1$. Unfortunately, it was not possible to use a constant set for δe which can describe the data.

In an attempt to improve the comparison with the shell model a phenomenological approach was used. In this approach shell model wave functions were mixed with configurations which are outside of the model space considered by

the shell model. Such configurations will in general be expected to have a q-dependence which is different from that of the shell model form factors. The shapes of C1 form factors for these configurations are displayed along with the observed form factor for the 7.30-MeV level as an example in figure 4.25 and provide a very large variety of momentum transfer dependences. However, the shapes of these configurations are quite different from the observed C1 form factors and it was not possible to explain the experimental C1 form factors by reasonably small admixture amplitudes to the shell model densities.

In the case of the transverse form factors, the comparison with the shell model predictions for $1/2^+$ and $3/2^+$ states are displayed in figures 4.15 through 4.23. A remakably good description of the experimental form factor for the $3/2^+$ level at 7.30 MeV is provided by the shell model calculations. For the 5.30-MeV state the comparison with the shell model is somewhat less complete due to the contributions from the the $5/2^+$ at 5.27 MeV which was not resolved in the 180° experiment. The transverse multipoles which are involved in these transitions are E1, E3, and M2. The dominant contributions to the form factor are predicted to come from the E1 form factor. No strong peaks are excited at 8.31 and 9.05 MeV. However, few data points are observed at low q for the 8.31-MeV level and E1 prediction seems to work well. The other transverse form factors disagree in various ways with the shell model predictions but the overall agreement with the theoretical predictions is reasonably satisfactory.

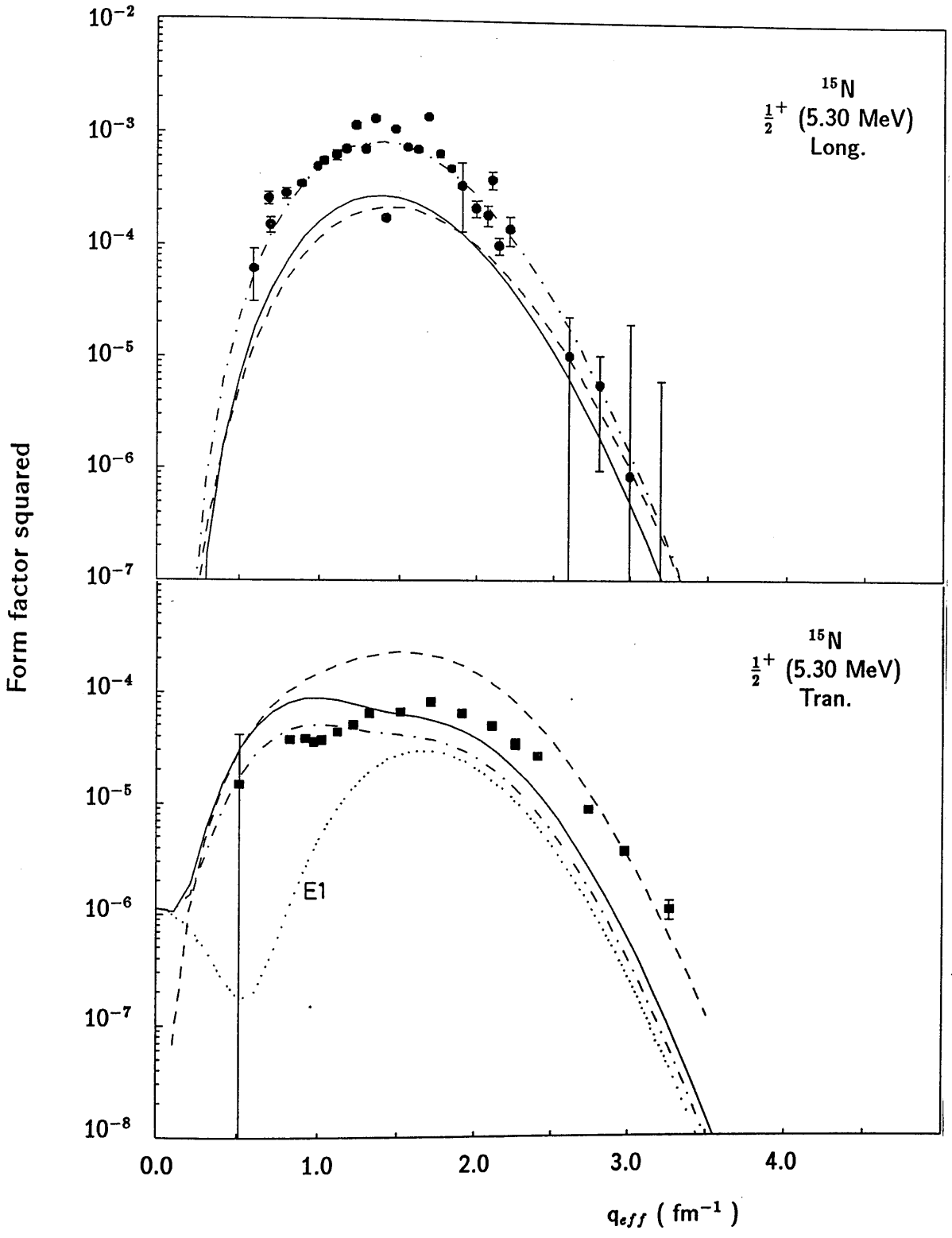

Figure 4.15: *Comparison between the experimental longitudinal and transverse form factors and the shell model predictions of Millener(solid lines) and of Utrecht group(dashed lines). The dot-dashed curves represent the predictions calculated with δe.*

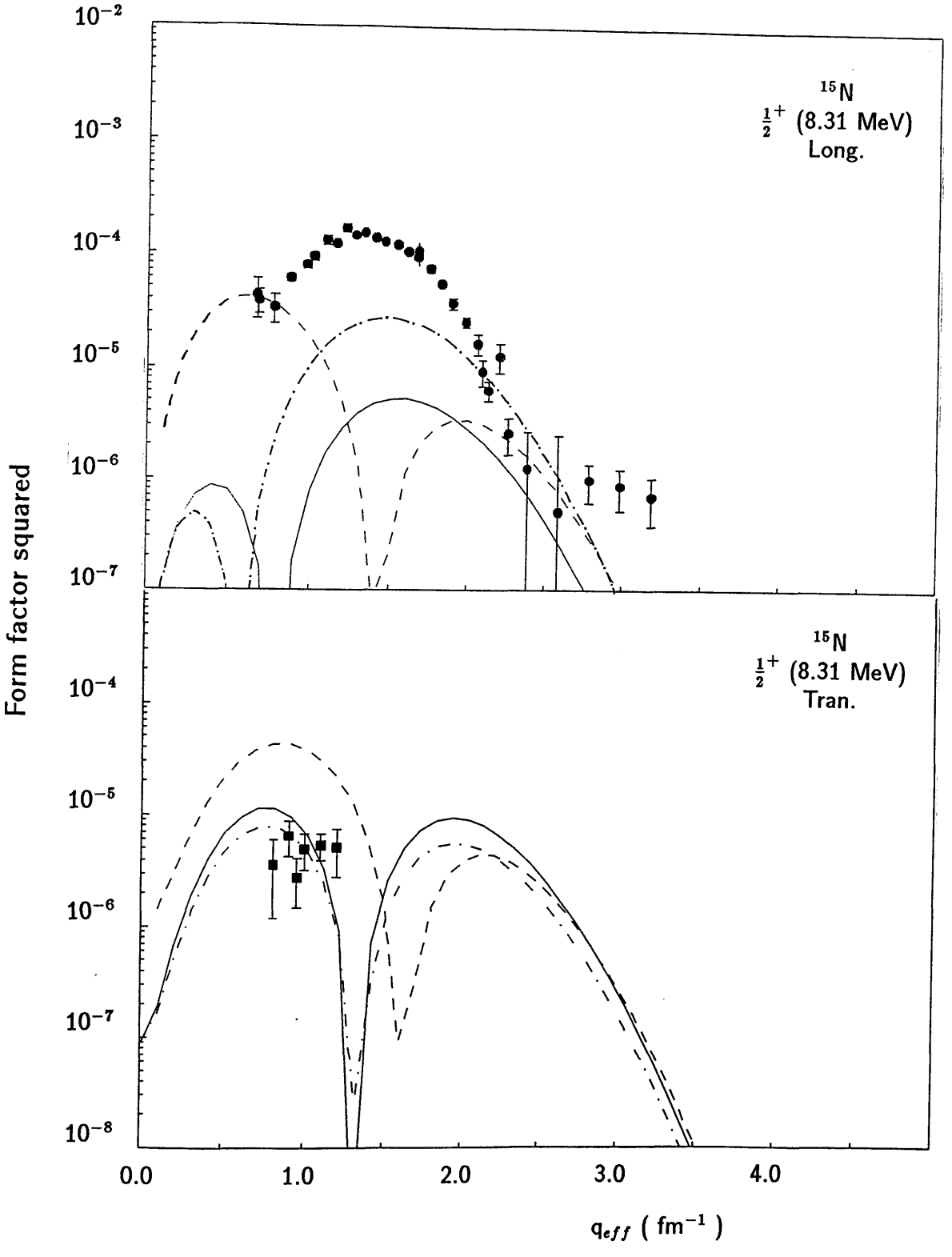

Figure 4.16: *Comparison between the experimental longitudinal and transverse form factors and the shell model predictions of Millener(solid lines) and of Utrecht group(dashed lines). The dot-dashed curves represent the predictions calculated with δe.*

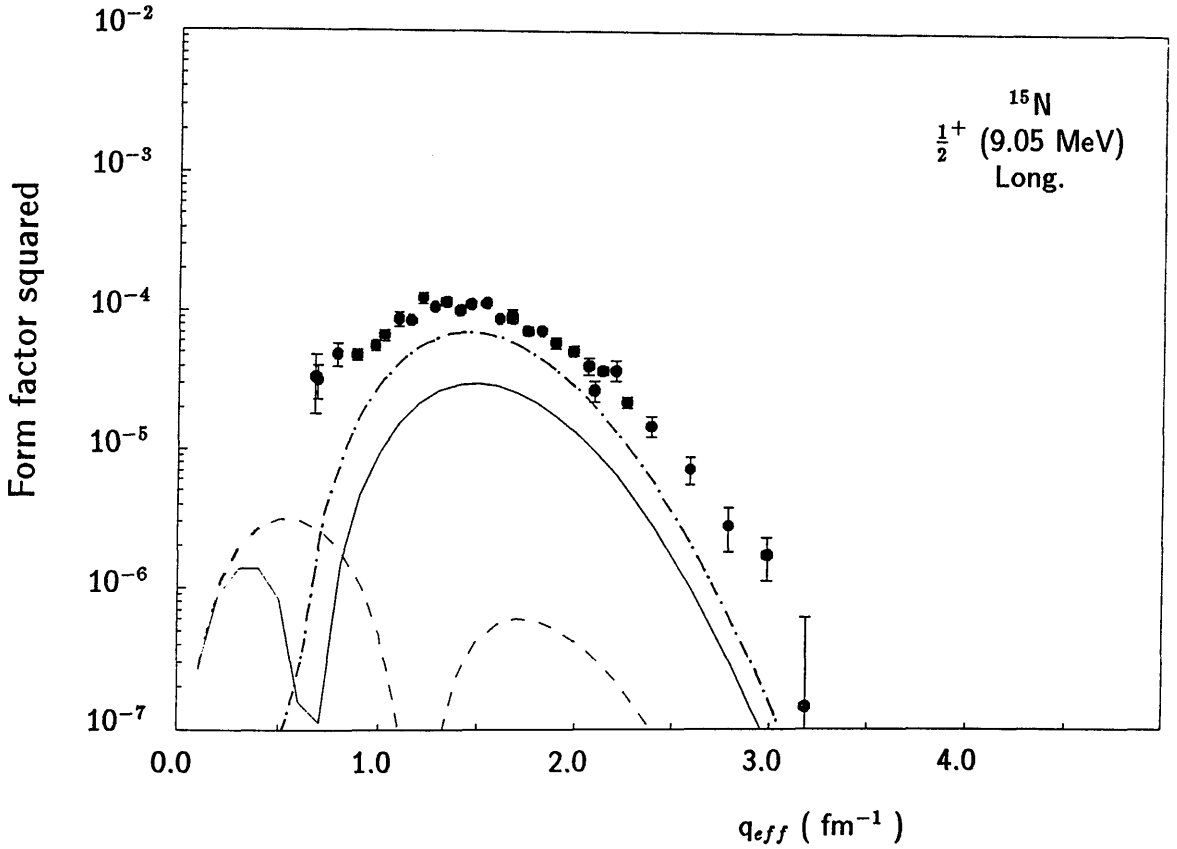

Figure 4.17: *Comparison between the experimental longitudinal form factors and the shell model predictions of Millener(solid lines) and of Utrecht group(dashed lines). The dot-dashed curve represents the prediction calculated with δe.*

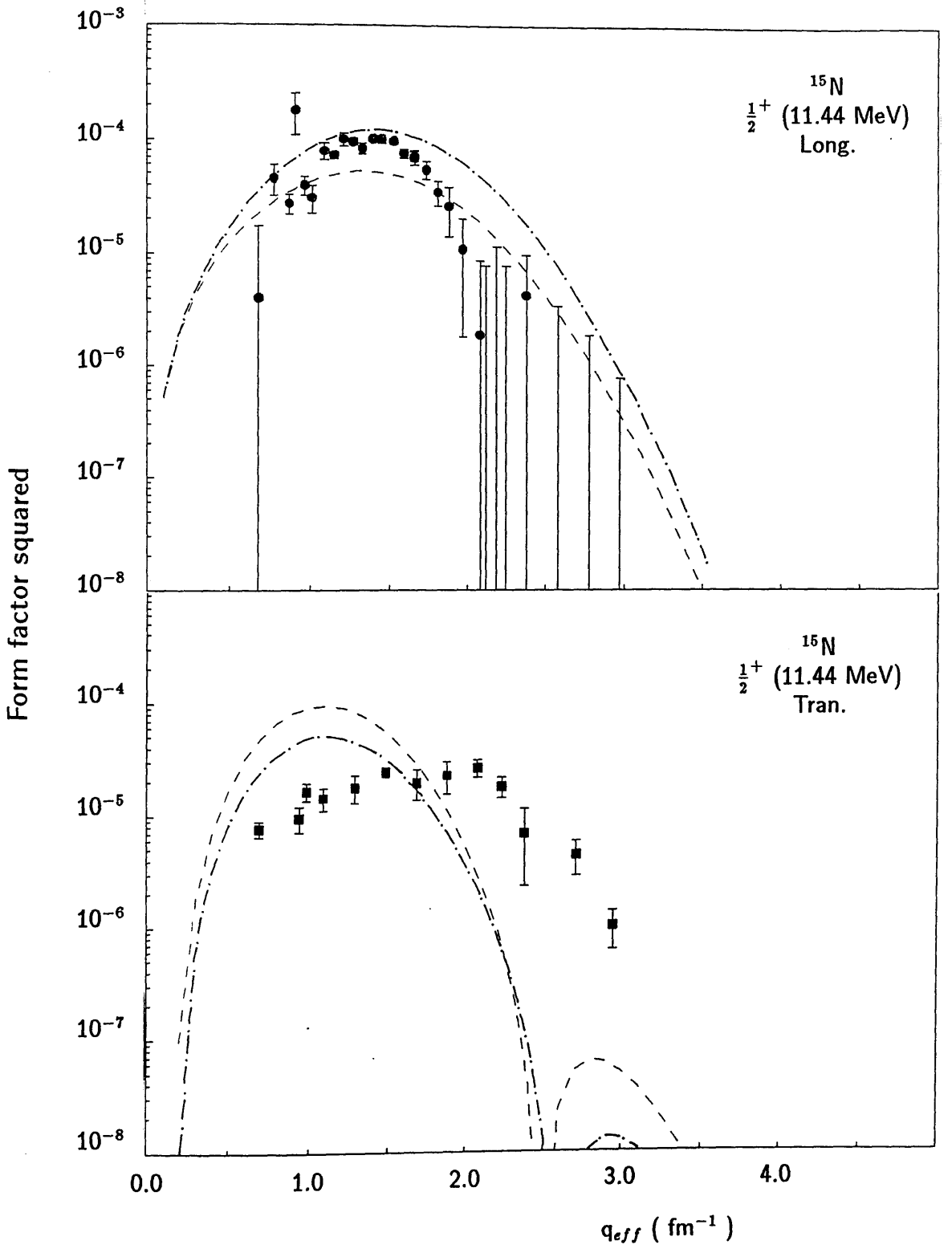

Figure 4.18: *Comparison between the experimental longitudinal and transverse form factors and the shell model predictions of Utrecht group(dashed lines). The dot-dashed curve represents the predictions calculated with δe.*

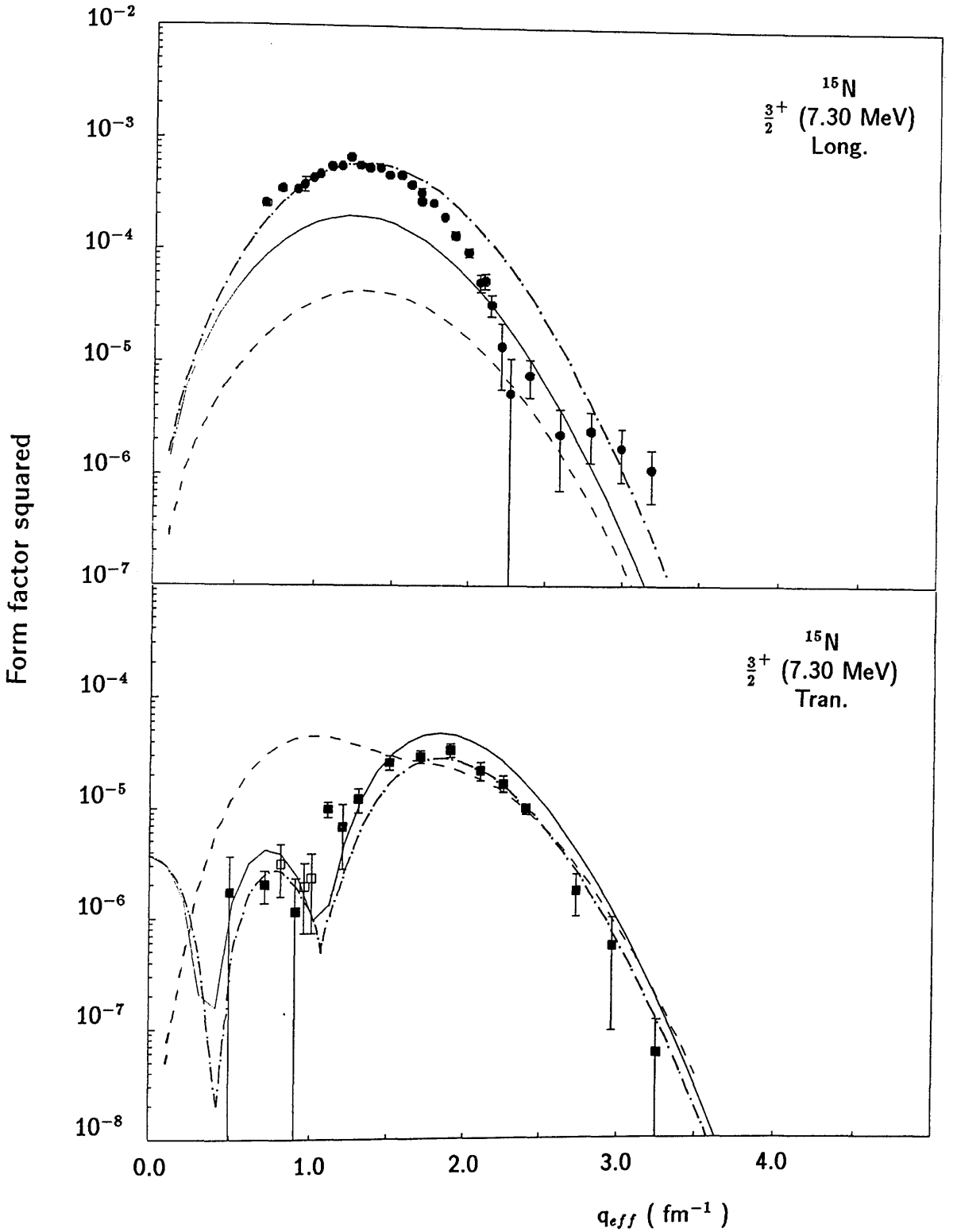

Figure 4.19: *Comparison between the experimental longitudinal and transverse form factors and the shell model predictions of Millener(solid lines) and of Utrecht group(dashed lines). The dot-dashed curves represent the predictions calculated with δe.*

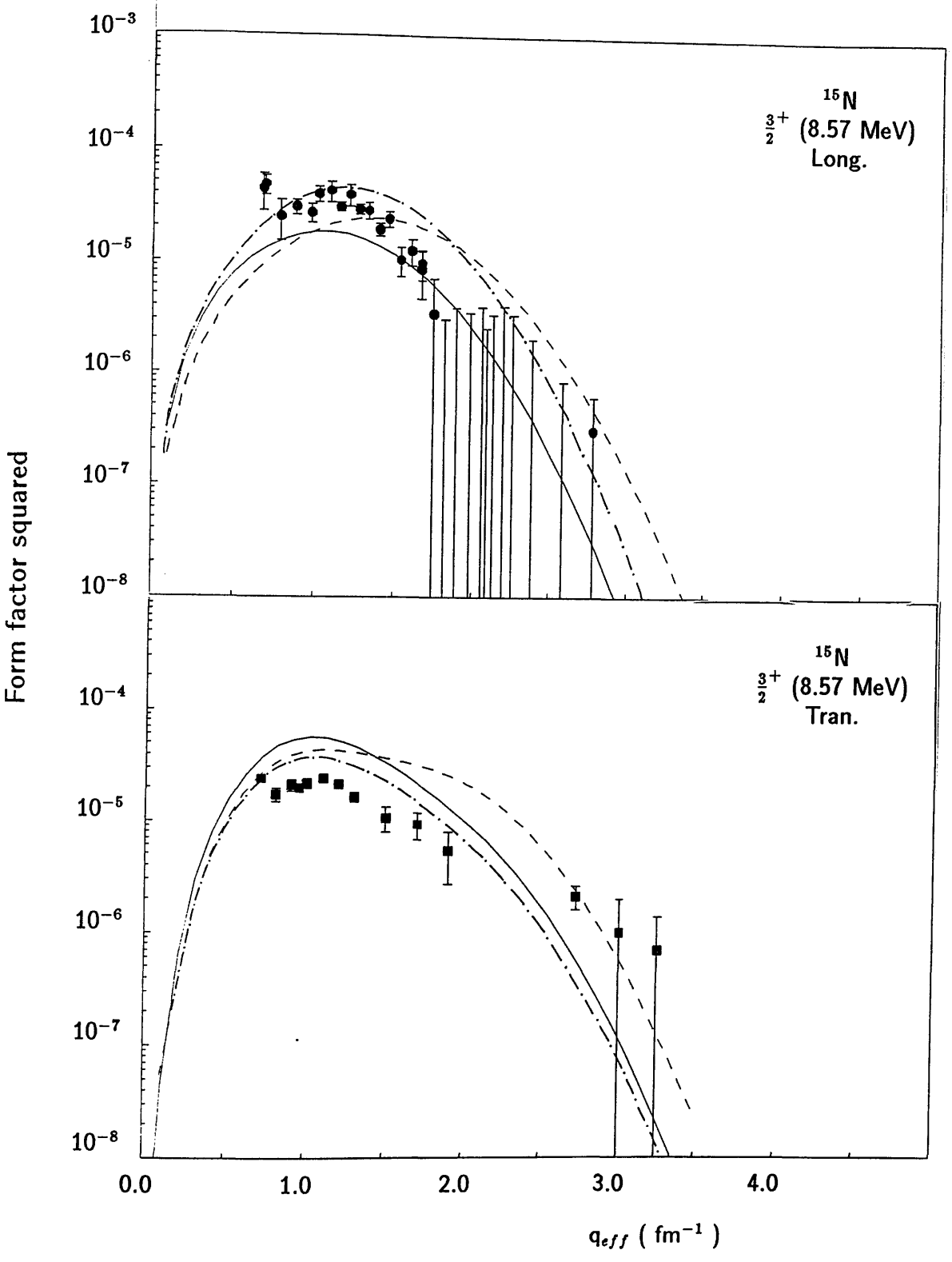

Figure 4.20: *Comparison between the experimental longitudinal and transverse form factors and the shell model predictions of Millener(solid lines) and of Utrecht group(dashed lines). The dot-dashed curves represent the predictions calculated with δe.*

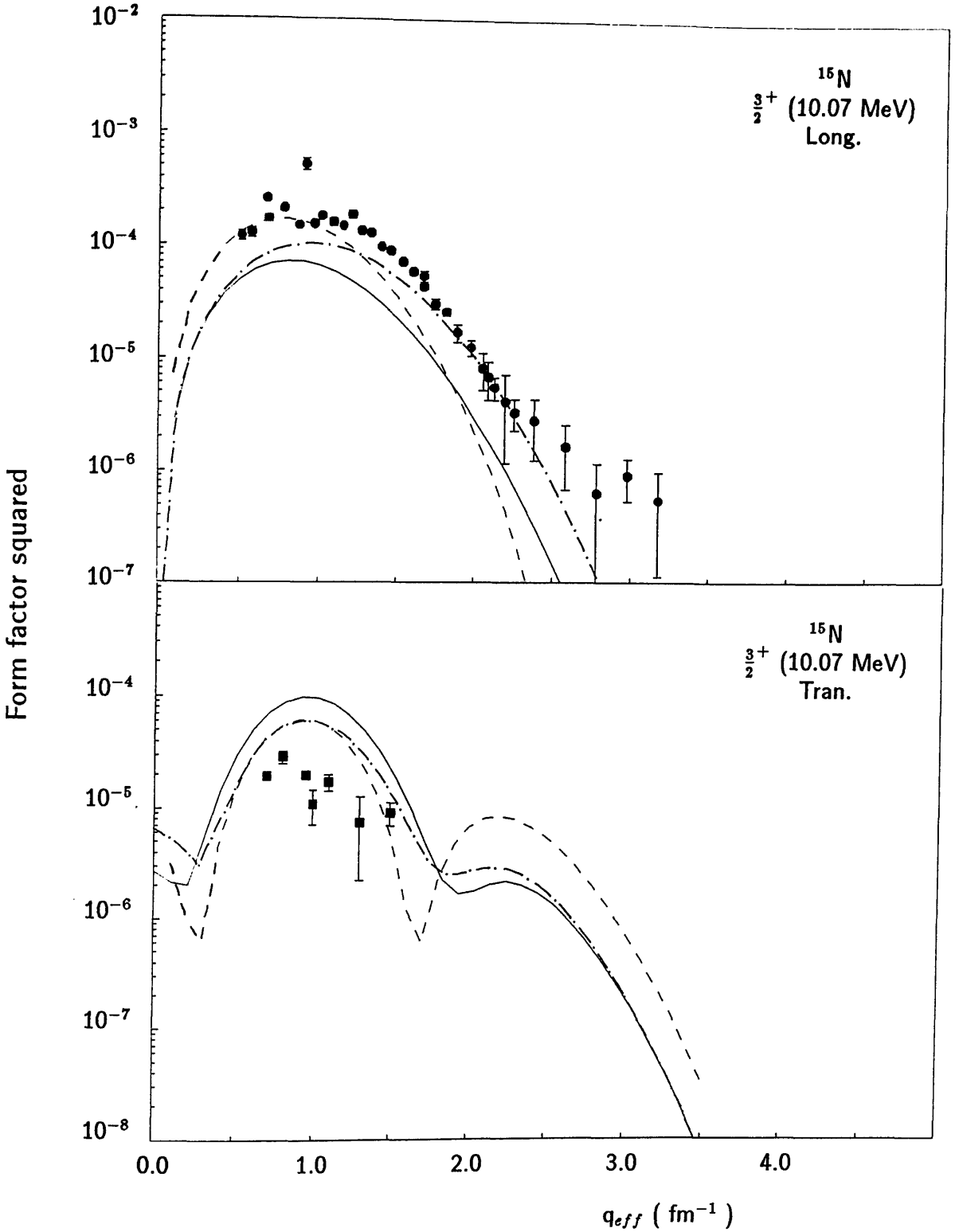

Figure 4.21: *Comparison between the experimental longitudinal and transverse form factors and the shell model predictions of Millener(solid lines) and of Utrecht group(dashed lines). The dot-dashed curves represent the predictions calculated with δe.*

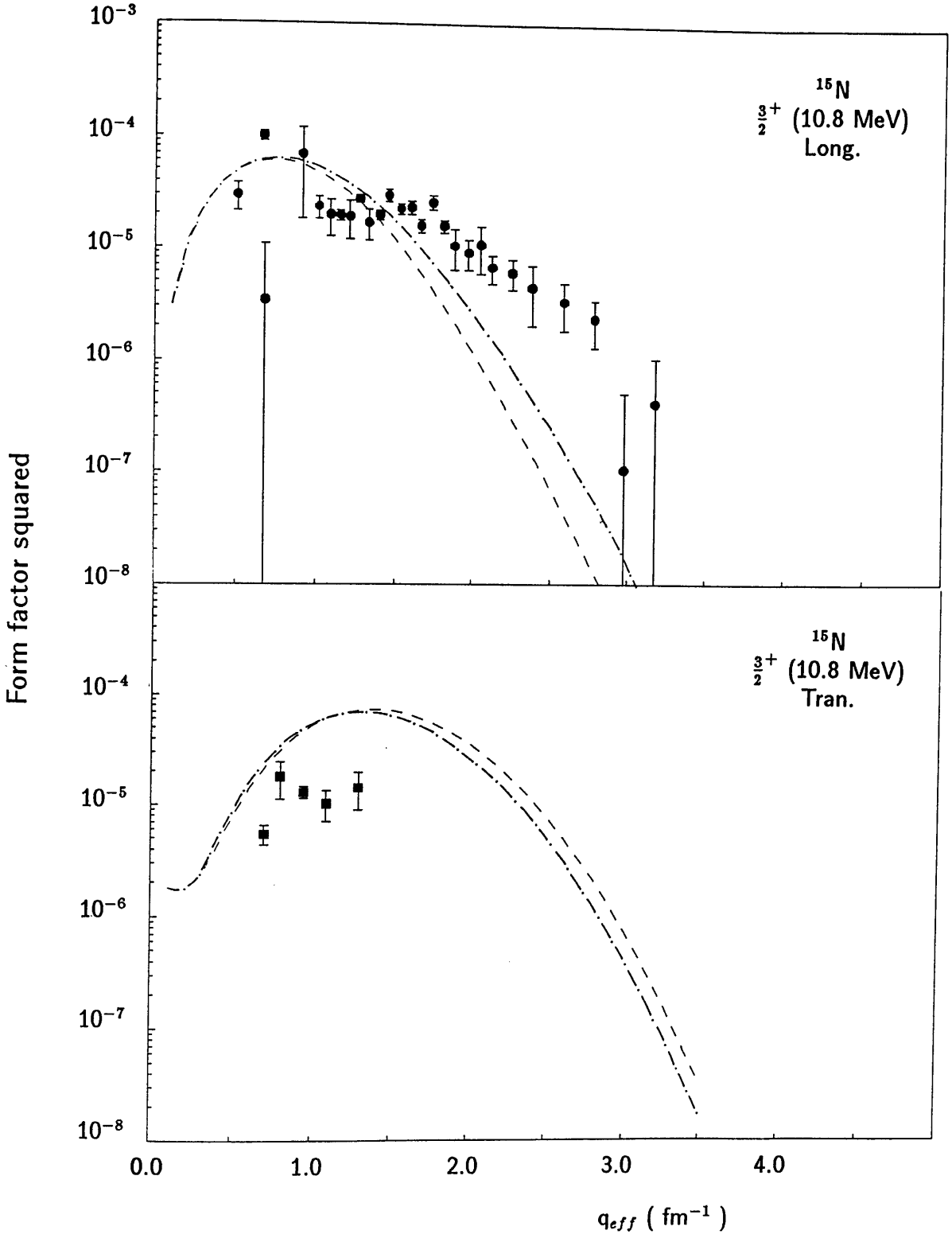

Figure 4.22: *Comparison between the experimental longitudinal and transverse form factors and the shell model predictions of Utrecht group(dashed lines). The dot-dashed curves represent the predictions calculated with δe.*

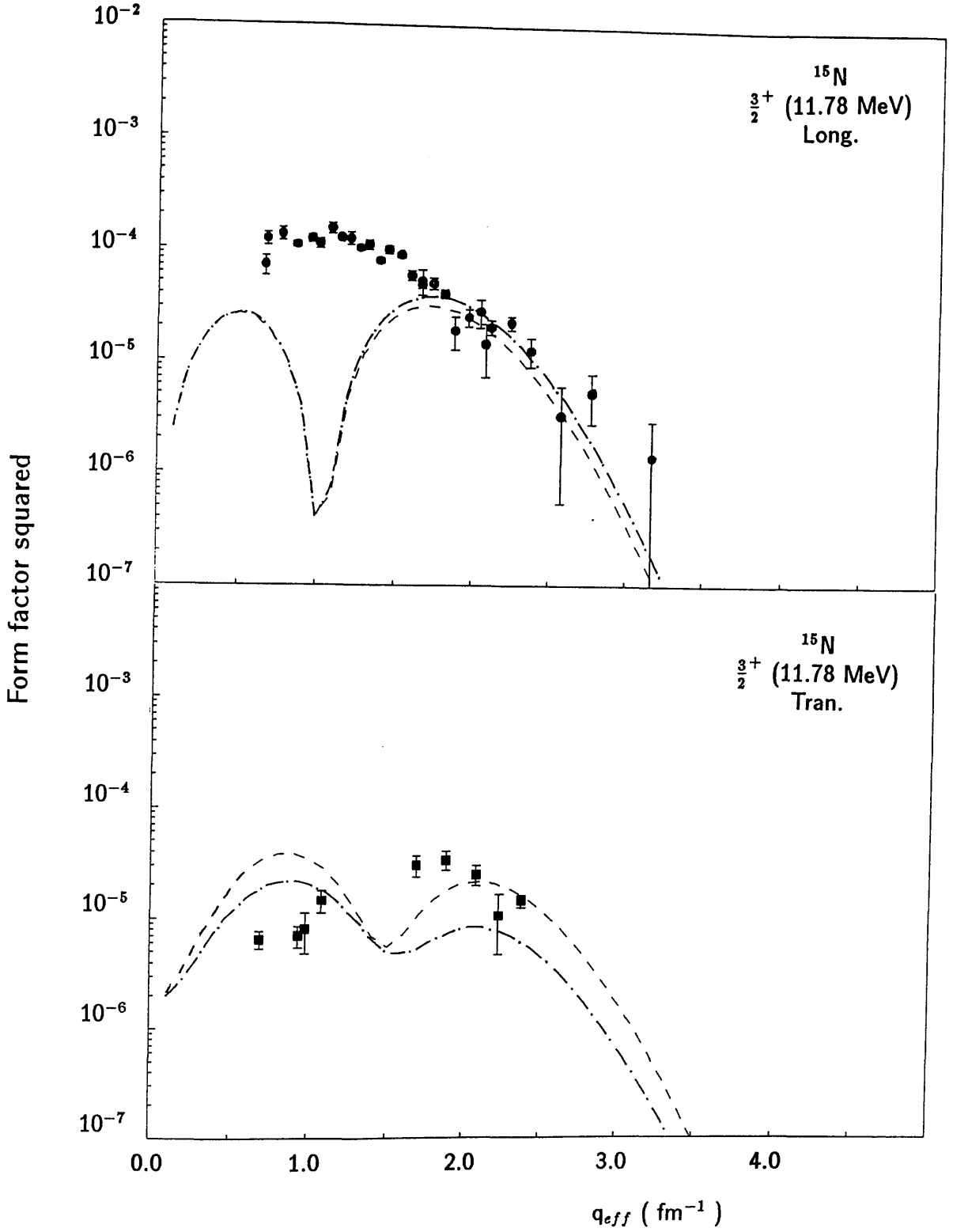

Figure 4.23: *Comparison between the experimental longitudinal and transverse form factors and the shell model predictions of Utrecht group(dashed lines). The dot-dashed curves represent the predictions calculated with δe.*

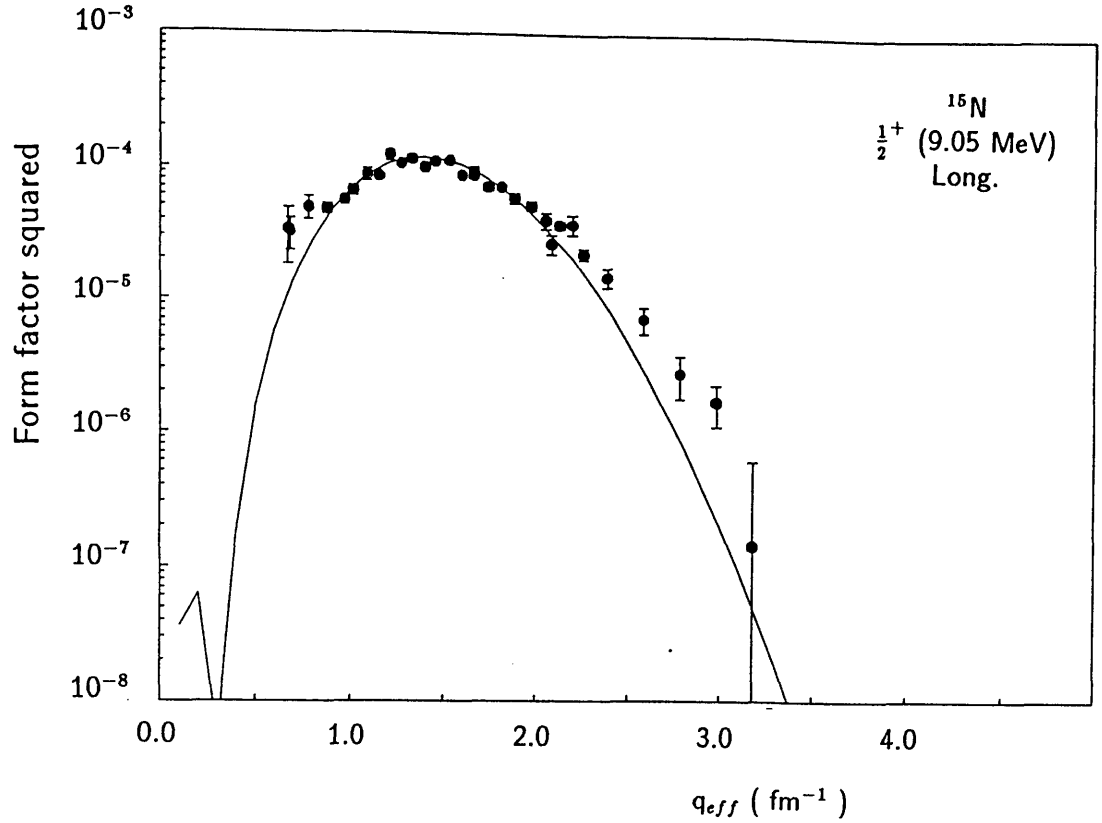

Figure 4.24: *Comparison between the experimental longitudinal form factors and the shell model prediction calculated by unequal values of δe_p and δe_n.*

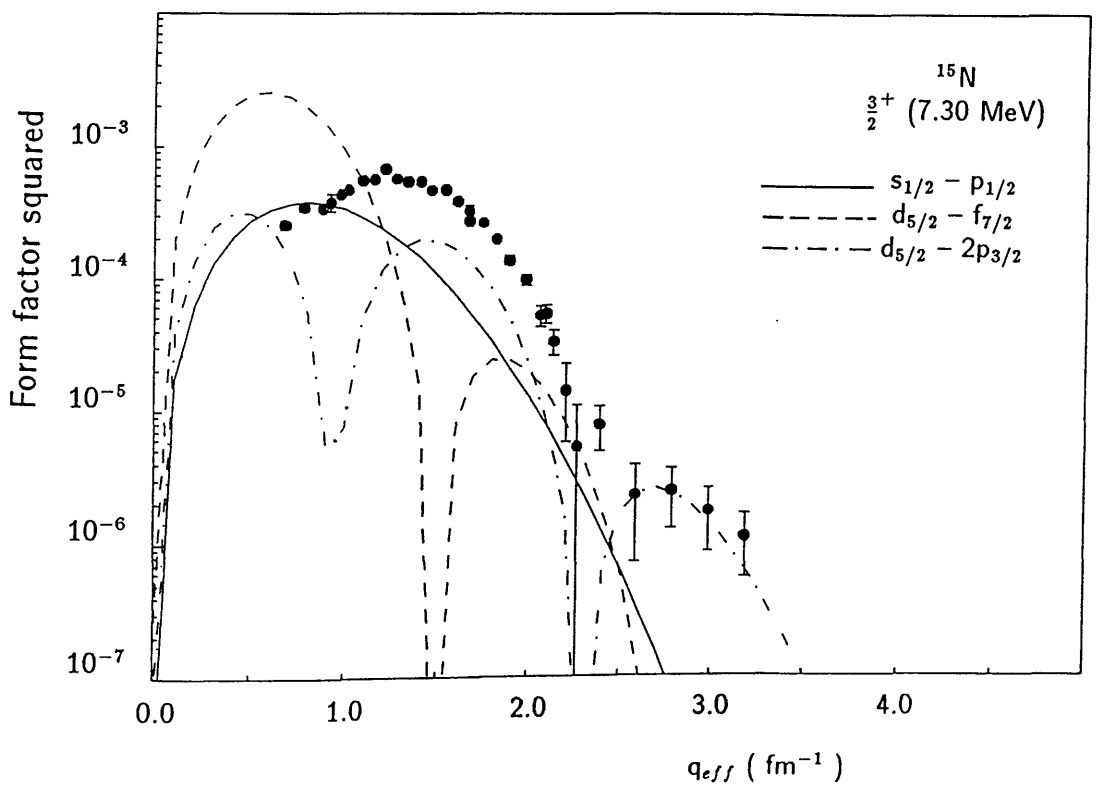

Figure 4.25: *Possible C1 form factors for different configurations in comparison with the observed C1 form factor for the $3/2^+$ state at 7.3 MeV.*

4.3.2 Electric Octupole Transitions

The octupole transitions in ^{15}N are of particular interest for a combination of related reasons. In the simplest shell model, the ^{15}N ground states is a single proton hole in a doubly closed 1p shell. Within the approximation of the $1\hbar\omega$ shell model, the configurations leading to the formation of positive parity states correspond to a single-particle in the 2s-1d shell coupled to two holes in the p-shell. In this picture the C3 transitions will then proceed via $1p_{1/2}$ or $1p_{3/2}$ particle excitation to the $1d_{5/2}$ or $1d_{3/2}$ orbital and will have a unique radial shape, see figure 4.26. The use of a $3\hbar\omega$ model-space is found to give little modification to the shape of the octupole transitions. In figure 4.26 the form factor for the $7/2^+$ level at 7.57 MeV as calculated in the $3\hbar\omega$ model-space(solid line) is compared with the experimental C3 form factor. Woods-Saxon wave functions do not change the q-dependence in any significant way and the use of harmonic-oscillator wave functions to define the radial shape of basis states is justified. Comparison between the form factors calculated with Woods-Saxon and that with harmonic-oscillator wave functions is also displayed in figure 4.26.

The octupole transitions discussed in this section are those for the first three $5/2^+$ states at 5.27, 7.15 and 9.15 MeV, and the $7/2^+$ state at 7.57 MeV. The $5/2^+_1$, $5/2^+_2$ and $7/2^+_1$ states were measured previously by Dally et al.[20] and Kim et al[21]. These data are displayed in figures 4.27 and 4.28 with the corresponding results measured in the present experiment. The Stanford data[20] suffer from poor resolution with FWHM of 700 keV and an uncertain normalization of the order of 20% due to use of a liquid ammonia target. The more serious limitation of these data is that no longitudinal transverse separation was carried out which is particularly important for $q > 2$ fm^{-1} where the transverse form factor has significant contributions. The data were analysed with the use of the independent particle shell model, and values of the nuclear transition probabilities were given, see table 4.2. The Saskatoon data[21] include the doublet at 5.3 MeV, the unresolved levels at 7.15 and 7.30 MeV, and the level at 7.57 MeV. Longitudinal transverse separation were performed but because of the poor statistics associated with the backward angle runs at low momentum transfers, only three data points of the transverse form factor were obtained.

They attributed the transverse form factors of the doublet at 5.3 MeV to M2 while this transverse should include a mixture of E1, M2 and E3. The M2 form factor calculated in the Helm model [65] is very different from that predicted by Millener's large-basis shell model calculation and must be viewed with caution. Again the transverse form factor at the unresolved levels at 7.15 and 7.3 MeV that would have contributions from E1, M2 and E3 multipoles was analysed as an M2 form factor arising from the transition to the 7.15-MeV level. This is a very unreliable assumption. The resulting reduced transition probabilities were discussed in terms of the weak coupling models and neither level was reasonably accounted for by these models. The measured B(E) values may be found in table 4.2.

Comparison between the shell model predictions for the C3 transitions and the measured longitudinal form factors are presented in figures 4.29 and 4.30. It should be noted, here, that the doublet at 9.15 MeV consists of the unresolved pair of levels at 9.152 MeV($3/2^-$) and 9.155 MeV($5/2^+$). As we have mentioned in section 4.2, the $3/2^-$ transition strength is quite small according to the the (γ, γ') experiment. We present in figure 4.30 the predicted C2 from factor calculated by Utrecht shell model for the $3/2^-$ level. We can see that the C2 form factor has a minimum at the measured form factor peak confirming that the contribution from C2 form factor is small. The following observations are obvious from the comparison with the shell model predictions: the shell model form factor is always smaller than the experimental form factor, the shell model form factors do not have the correct q-dependence tending to be too broad relative to the experimental data and it is not possible to normalize the calculated curves by the same constant factor to obtain agreement with the experimental data thus invalidating the hypothesis of a constant effective charge. In fact the effective charge needed to reproduce the strength at the maximum of the form factors varies from 0.1 for the $5/2_1^+$ to $\sim$ 2.2 for $5/2_2^+$ with other transitions requiring intermediate values. The effective charge values are presented in table 4.4. In figures 4.29 and 4.30 the solid curves represent the shell model predictions with no effective charges, while the dashed curves are those with effective charges. It should be noted that the predicted C3 form factors with

the effective charges chosen to reproduce the maximum of the experimental form factor can also be obtained by choosing different values for the effective charges for protons and neutrons. However, the neutron effective charge required is larger than the proton effective charge. For example, for the $7/2_1^+$ form factor, $\delta e_n = 0.385$, $\delta e_p = 0.095$ were required to reproduce the experimental strength. The predicted C3 form factor with these effective charges is shown with the experimental form factor in figure 4.31.

The major inadequacy of the shell model is the neglect of mixing with configurations outside the restricted model space. However, significant extension of the shell model basis requires knowledge of many more two-body interaction matrix elements and even if these were known the size of such a calculation would rapidly become prohibitive. Although the shell model description of the C3 transitions is not consistently good in terms of the predicted strength, from the comparisons it would appear that the model wave function is missing only a small contribution from configurations not included in the shell model space.

It is possible to utilize the experimental data to obtain some feeling for the reasons of this contribution by writing the physical transition density as follows:

$$\rho_{tr}(r) = \rho_{SM}(r) + \alpha\rho_{add}(r) \tag{4.1}$$

Here α is an adjustable parameter and $\rho_{add}(r)$ is the contribution from configurations which are outside of the model space considered by the shell model. Such configurations will in general be expected to have a q-dependence which is different from that of the shell model form factors. These configurations may be found in the diagram shown in figure 4.32 and the shapes are displayed in figure 4.33. The C3 form factor shapes for transitions which proceed via 2s$\rightarrow$ f, d$\rightarrow$ 2p and p$\rightarrow$ g transitions are different from those of the shell model, while the form factor shape for the s$\rightarrow$ f transition are similar to that of shell model. These configurations were mixed to the shell model form factors by varying α to reproduce the experimental form factor. With this model space it was not possible to give a description of all the octupole transitions. In figure 4.33 we present one of these attempts for the $7/2_1^+$ state. While the mixing with the form factor produced by s$\rightarrow$ f transition looks good when compared to the data,

the value of α needed is very large($\approx$ 2) and it is unresonable to assume that the shell model wave functions will require modification of such extent.

An alternative choice for $\rho_{add}(r)$ as that of a collective vibrational state, however, can provide an overall satisfactory agreement for all the four states with very significant improvements in both the shape and strength of the predicted form factors. This procedure has some theoretical [57,58] and experimental [56,22] justification even though the application to explain octupole transition data in this way has not been attempted so far. However, the existence of low-lying octupole collective states is well established and considerable evidence for the existence of a giant octupole resonance(GOR) at an excitation energy of $\sim 110/A^{1/3}$ MeV [59] has accumulated in recent years.

The radial shape of the collective state to be used in equation 4.1 was chosen as

$$\rho_{add}(r) = Nr\rho'_{g.s}(r) \tag{4.2}$$

where N is adjusted to give the strength required by the sum rule[57] and $\rho'_{g.s}(r)$ is the radial derivative of the ground state charge distribution of the nucleus which was obtained in this experiment[2] in terms of a Fourier-Bessel series

$$\begin{aligned} \rho_{g.s}(r) &= \textstyle\sum_\mu A_\mu j_0(q_\mu r) \quad r < R_c \\ &= 0 \qquad\qquad\qquad\quad r \geq R_c \end{aligned} \tag{4.3}$$

The values $q_\mu R_c$ gives the μ^{th} zero of the spherical Bessel function: $j_0(q_\mu R_c)$=0, where, R_c = 7 fm, is the cut-off radius (see section 4.2) and A_μ are the Fourier-Bessel coefficients obtained from the analysis and are listed in table 4.3. The description of ρ_{add}(r) in equation 4.2 was then used in equation 4.1 and α was treated as an adjustable parameter for each transition studied. In ρ_{SM}(r), no effective charges were used. The results are presented in table 4.4 and figures 4.34 and 4.35. The admixture is always such that the strength of the transition is enhanced. Considerable improvement in the q-dependence of all the transitions studied is observed for values of α which are needed to reproduce the experimentally observed form factor maxima.

Table 4.3: Fourier Bessel coefficients for the ground state of ^{15}N.

μ	$100 \times A_\mu$	$100 \times \Delta A_\mu$
1	2.549	0.003
2	5.063	0.017
3	2.984	0.019
4	-0.553	0.015
5	-1.59	0.03
6	-0.77	0.03
7	-0.23	0.05
8	-0.04	0.07

For the transverse form factors, the comparison with the shell model for the 5.27 MeV and 9.15 MeV, $5/2^+$ states is somewhat less complete due to the contributions from the $1/2^+$ state at 5.30 MeV and the $3/2^-$ state at 9.15 MeV which were not resolved in the 180° experiment. The measured transverse form factors of the doublet at 5.30 MeV are shown in comparison with the shell model predictions in figure 4.15 and has been already discussed in the previous section. The transverse form factors of the doublet at 9.15 MeV are shown in comparison with the predictions of the corresponding states in figure 4.36. The multipolarities which are involved in this transition are E3, M2, M1, E2. The predicted transverse form factors for these transitions show the opposite behaviour with respect to other predicted transverse form factors which are always larger than the observed strength. The form factors of the 7.15 MeV $5/2^+$ and the 7.57 MeV $7/2^+$ states and the shell model predictions are presented in figure 4.37. The theoretical transverse form factor is dominated by E3 component in both states and a downward normalization by a factor of 1.6 is required to obtain agreement with the measured strength. This observation is similar to that for the transverse transitions leading to the other states in ^{15}N[60] and ^{13}C[72]. However, transverse transition in nuclei in the bottom half of the 1p-shell, namely ^{7}Li [10], ^{10,11}B [11] are extremely well described by similar shell model calculations without the use of any normalization. At the present time, there is no theoretical model which can consistently explain these observations[60].

Table 4.4: Collective state mixing parameters

Transitions	Excitation Energy (MeV)	δe	α
$5/2^+$	5.27	0.1	0.004 ± 0.0004
$5/2^+$	7.15	2.2	0.006 ± 0.0006
$7/2^+$	7.57	0.27	0.013 ± 0.001
$5/2^+$	9.15	1.2	0.006 ± 0.0006

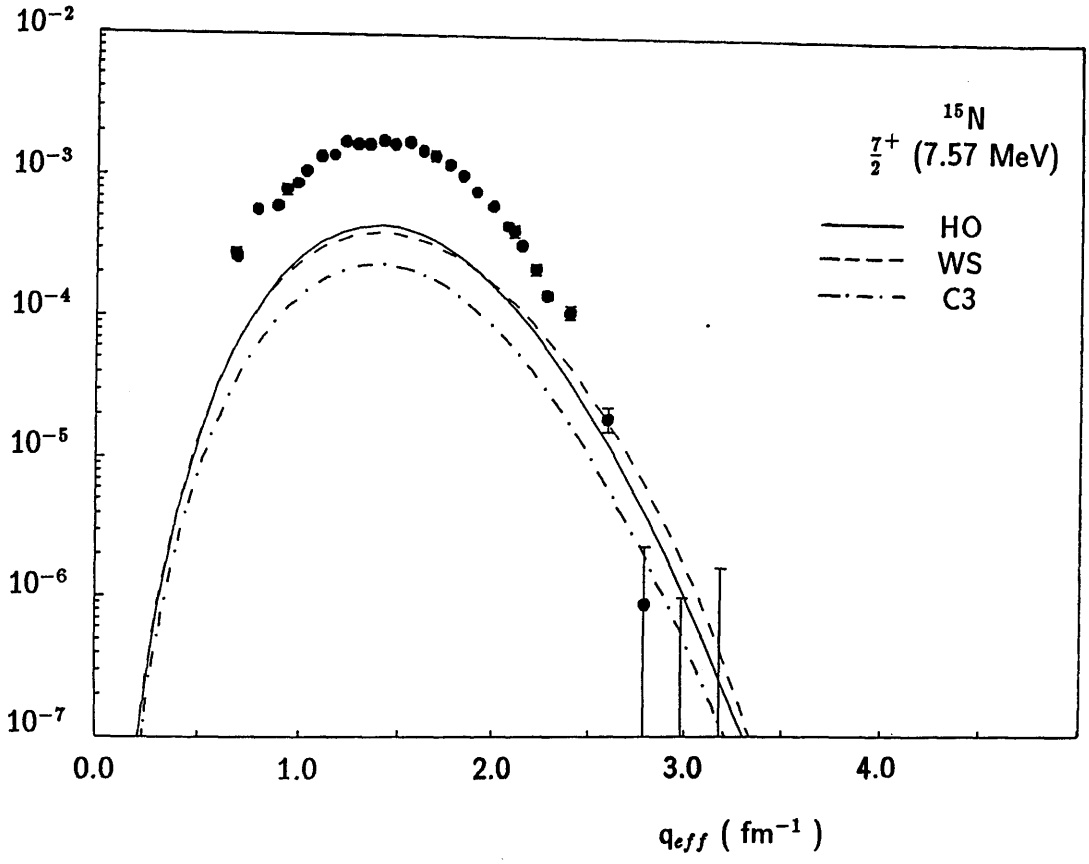

Figure 4.26: *Experimental longitudinal form factor for the $7/2_1^+$. The solid curve represents the shell model prediction calculated with harmonic oscillator wave function while the dashed curve is that with Woods-Saxon wave function. The dot-dashed curve represents the C3 form factor shape for the configuration* $p_{3/2} \rightarrow d_{5/2}$ *for HO wave function.*

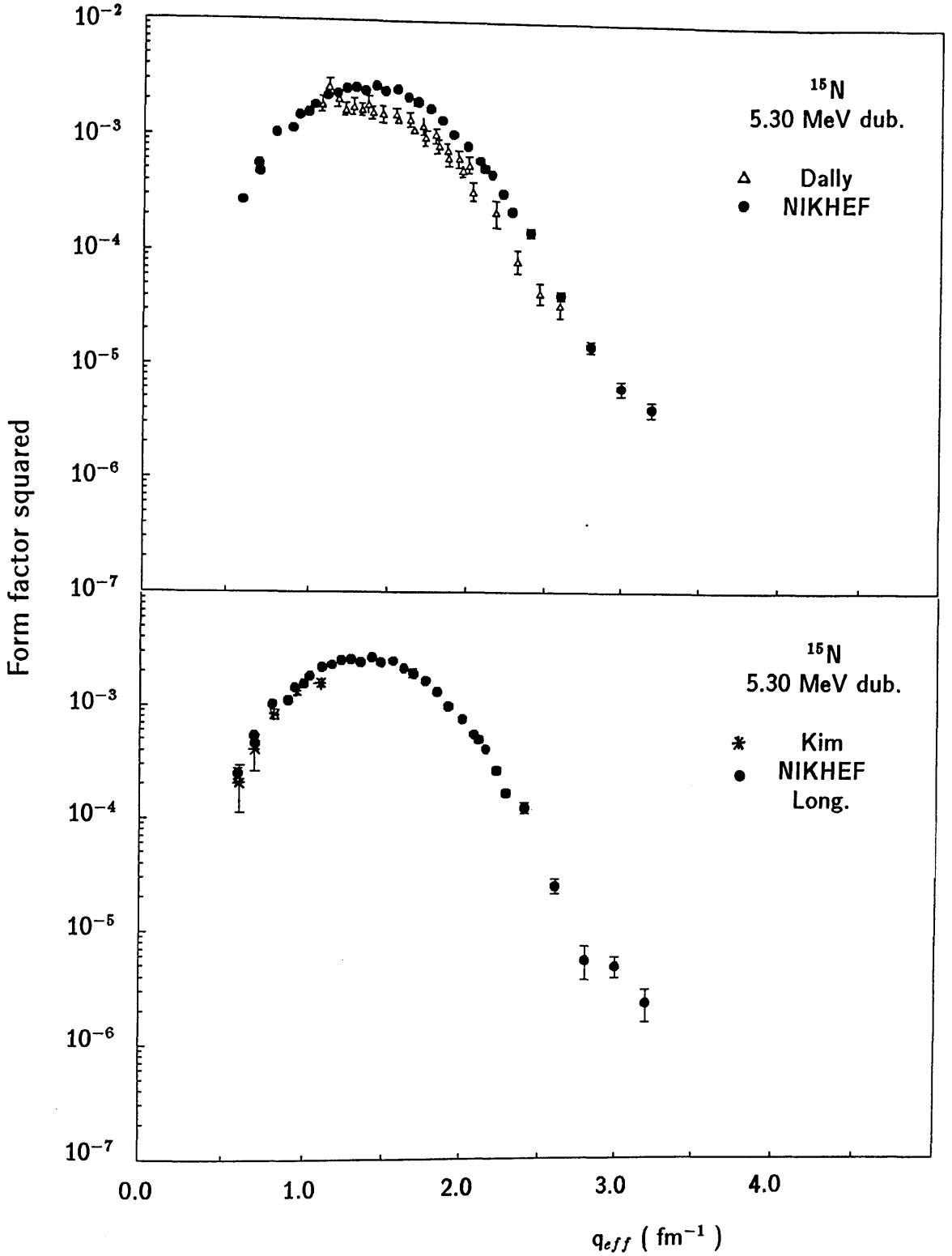

Figure 4.27: *The experimental form factors for the doublet at 5.3 MeV with those measured by Dally et al.[20] (triangle symbols) and those measured by Kim et al.[21] (cross symbols).*

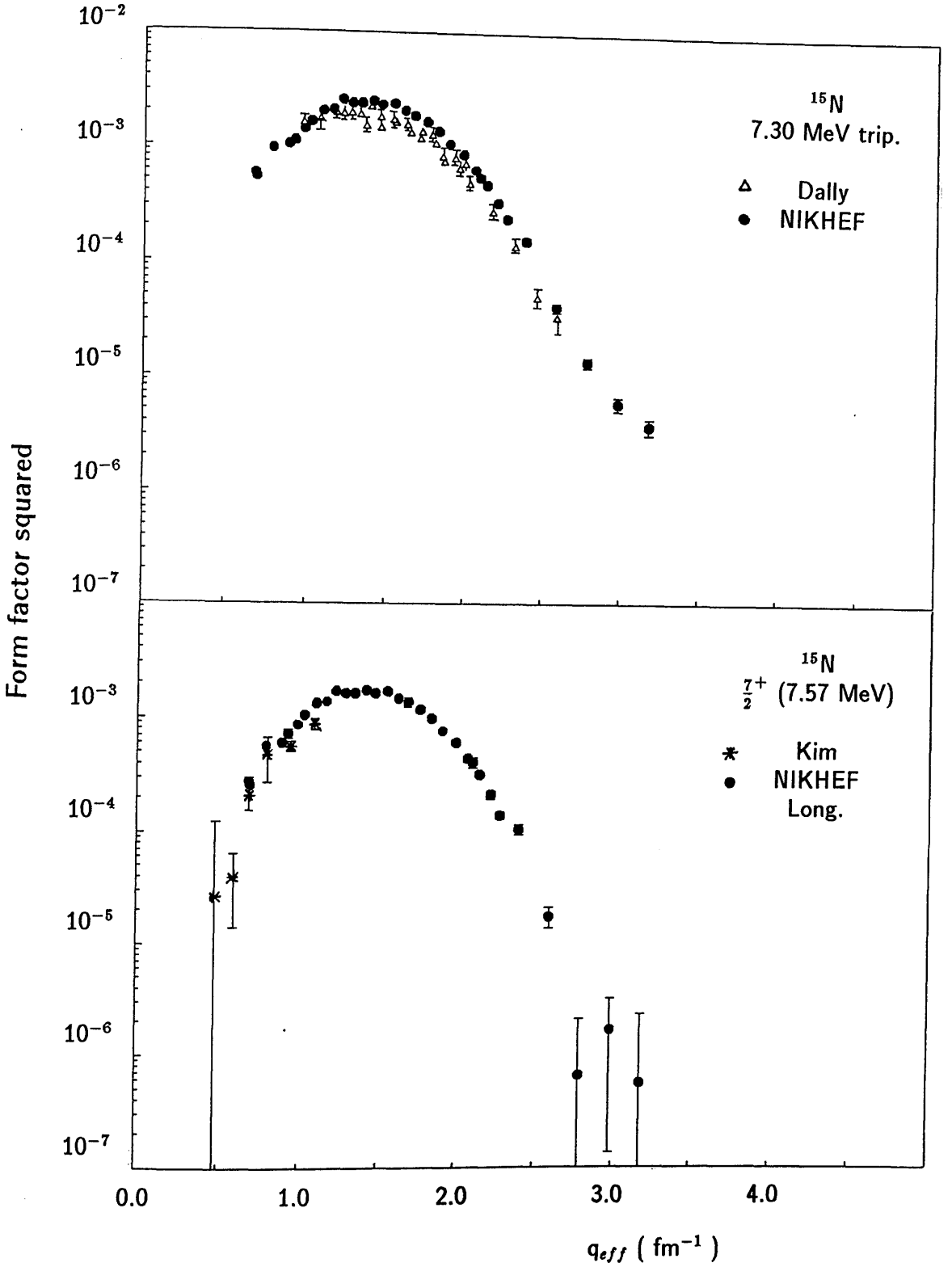

Figure 4.28: *The experimental form factors for the triplet at 7.3 MeV with those measured by Dally et al.[20] (triangle symbols) and those measured by Kim et al.[21] (cross symbols) for the 7.57-MeV level.*

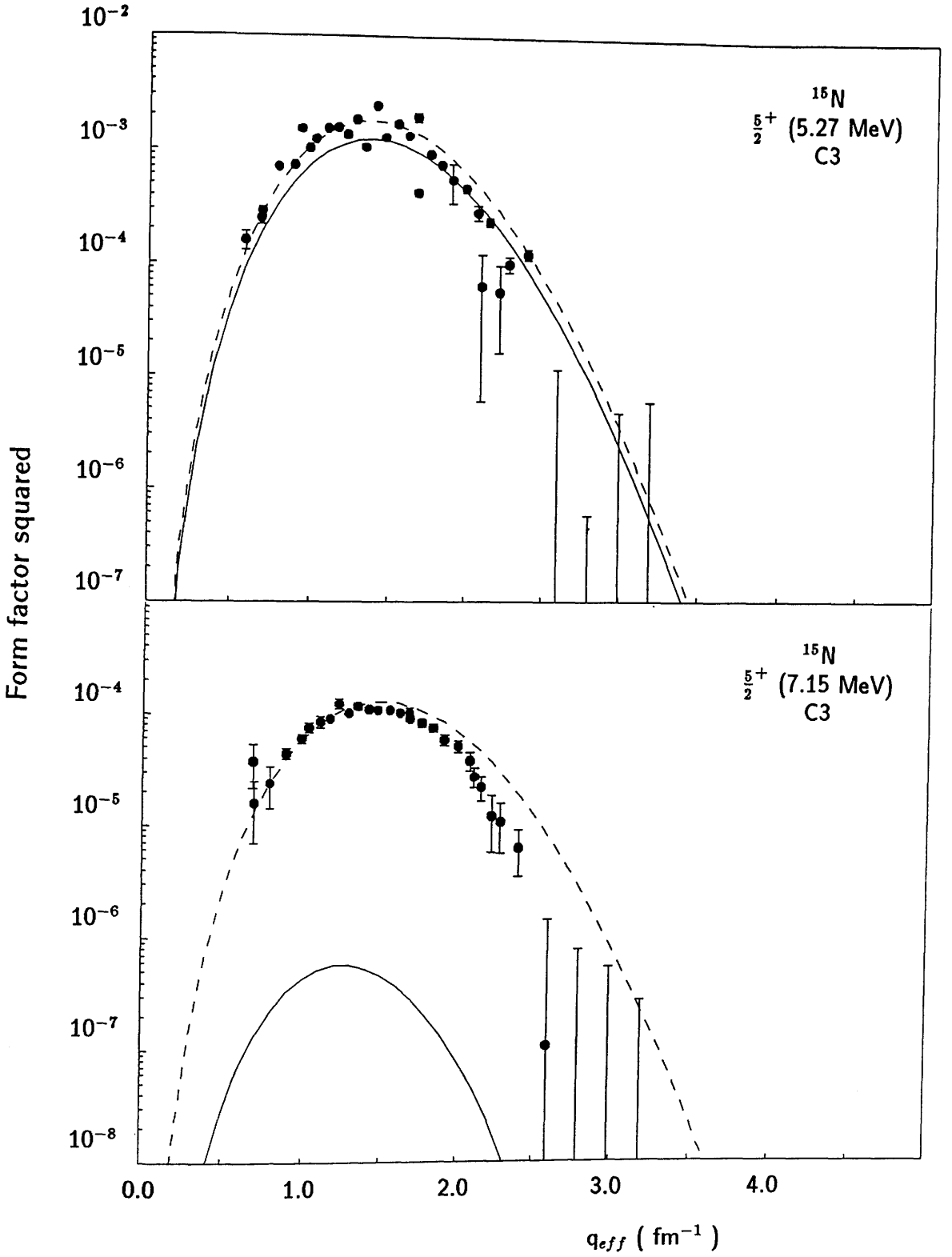

Figure 4.29: *Experimental and theoretical longitudinal form factors for the 5.27 and the 7.15-MeV levels. The solid curve is the prediction of the shell model. The dashed curve is that with δe chosen to reproduce the maximum of the experimental form factor.*

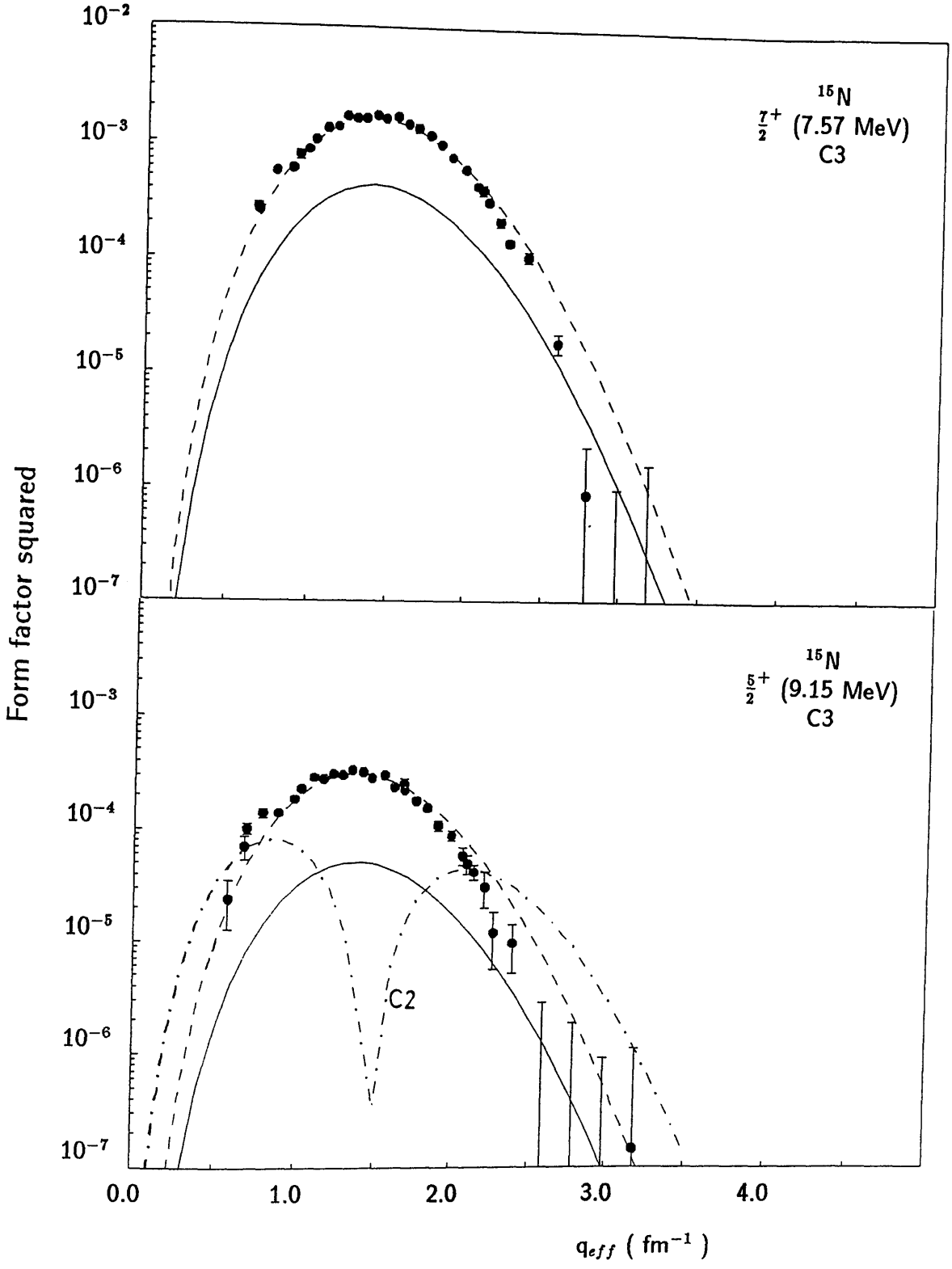

Figure 4.30: *Experimental and theoretical longitudinal form factors for the 7.57 and the 9.15-MeV levels. The solid curve is the prediction of the shell model. The dashed curve is that with δe chosen to reproduce the maximum of the experimental form factor. The dot-dashed curve represents the shell model C2 prediction.*

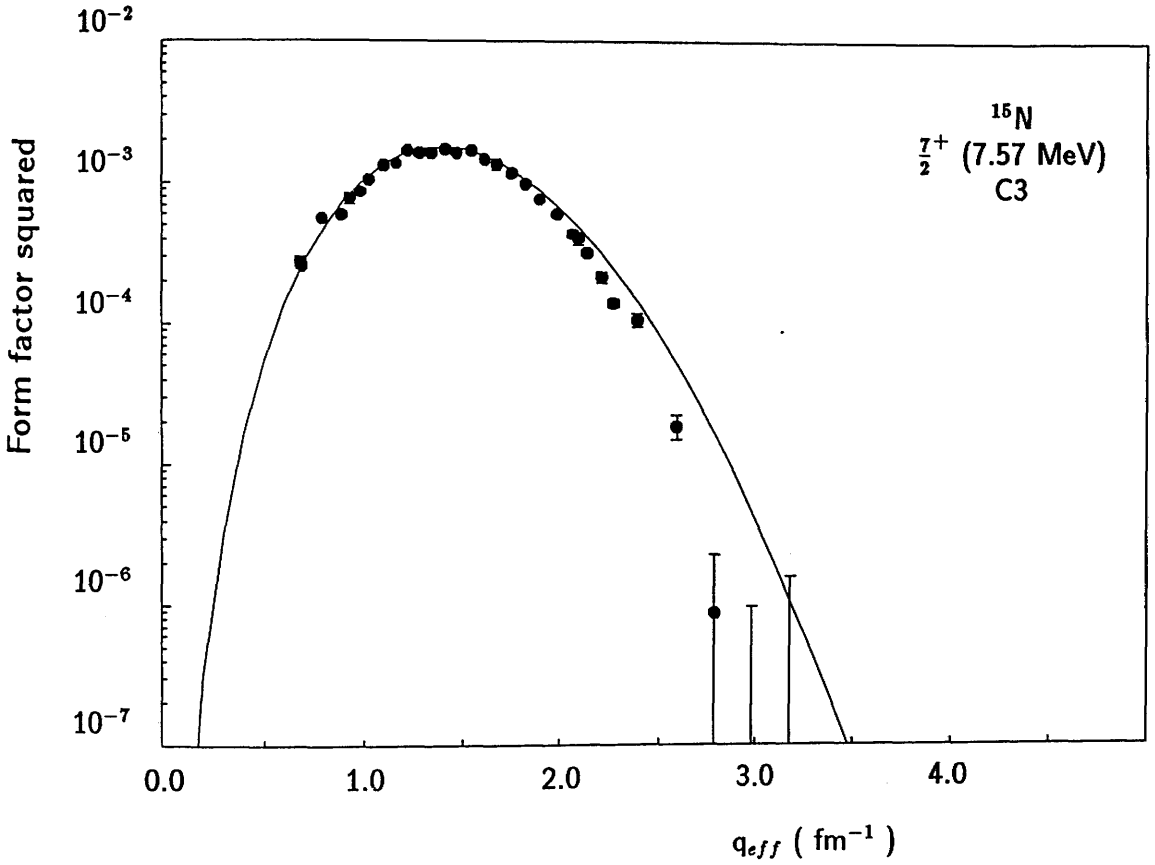

Figure 4.31: *Experimental and theoretical longitudinal form factors for the 7.57-MeV level calculated with unequal values of δe_p and δe_n.*

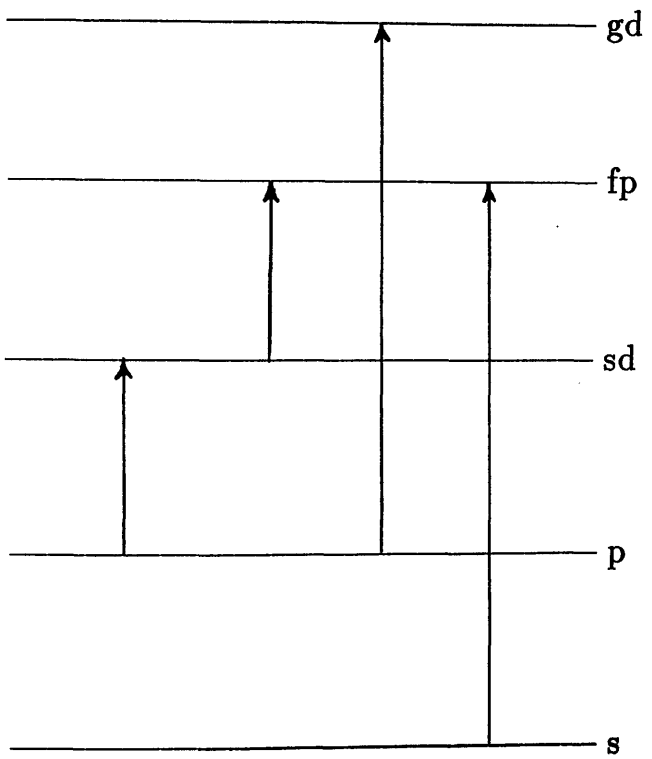

Figure 4.32: *Possible C3 transitions for different configurations.*

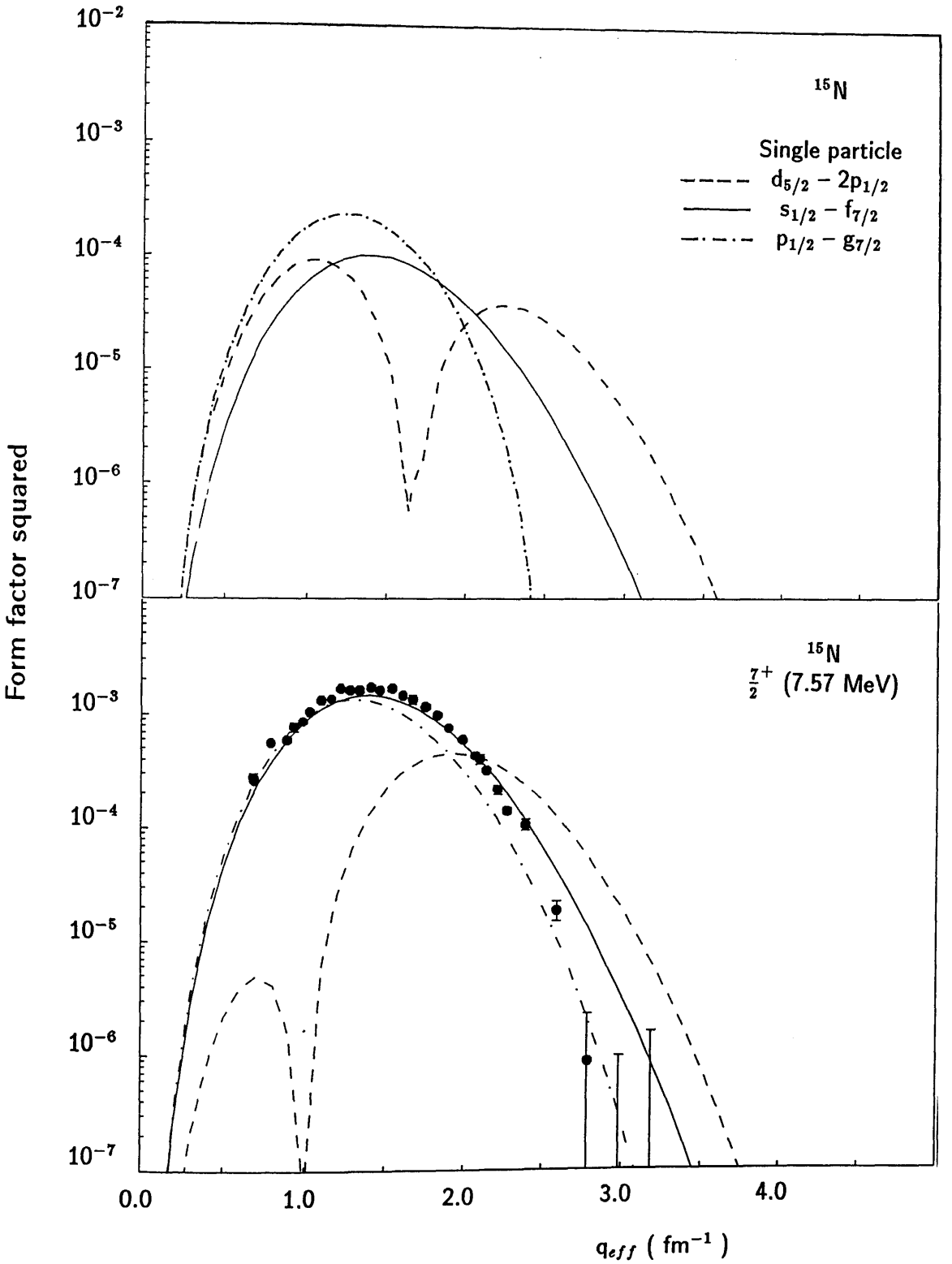

Figure 4.33: *Possible C3 form factors calculated from different configurations, in the upper. In the lower, Comparison between data and theory for the 7.57-MeV level. The curves are predictions of the shell model mixed with the configurations shown above as defined in equation 4.1.*

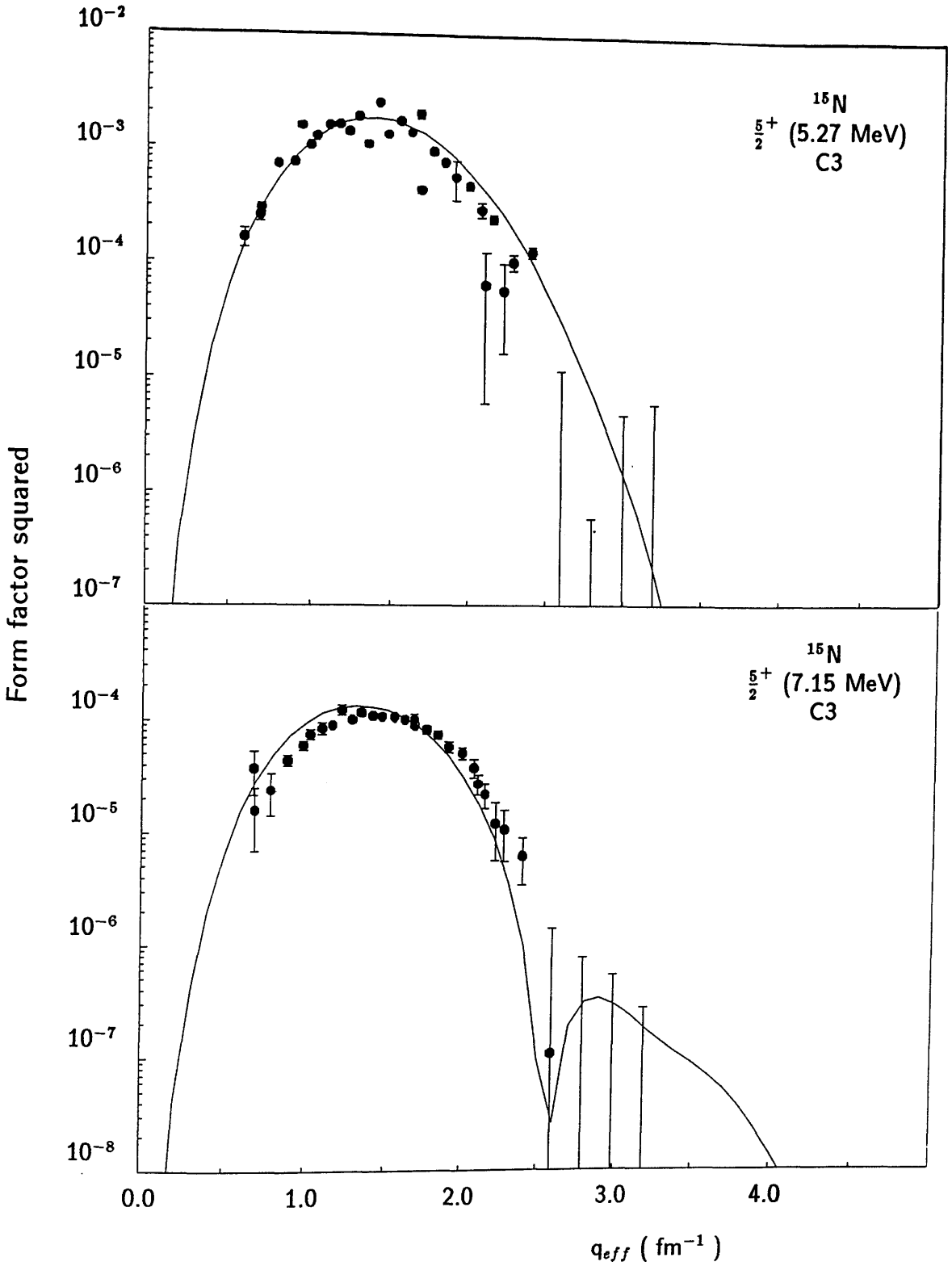

Figure 4.34: *The experimental longitudinal form factor for the 5.27 and 7.15-MeV levels. The curves are the predictions of the model defined in equations 4.1 and 4.2.*

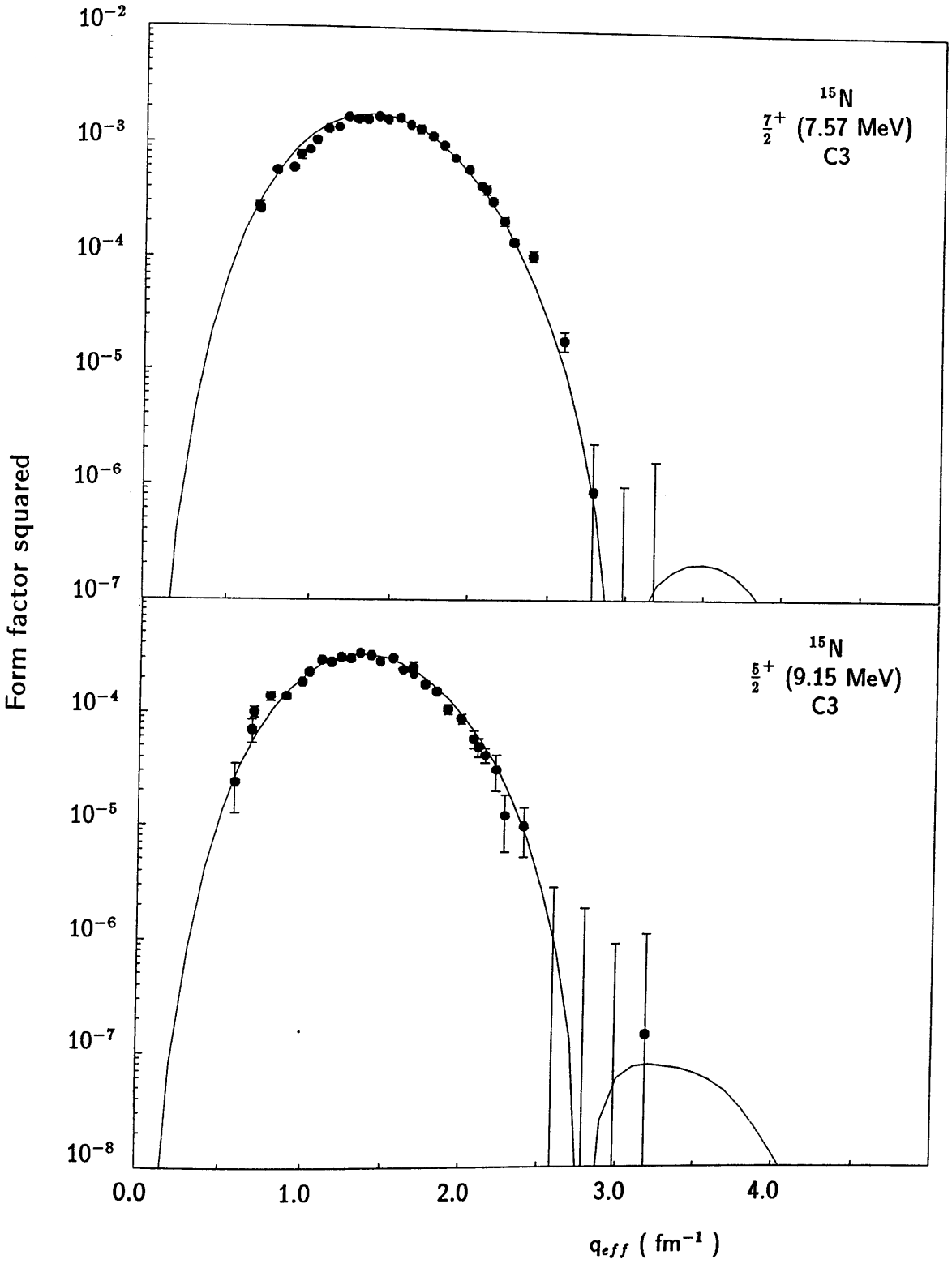

Figure 4.35: *The experimental longitudinal form factor for the 7.57 and 9.15-MeV levels. The curves are the predictions of the model defined in equations 4.1 and 4.2.*

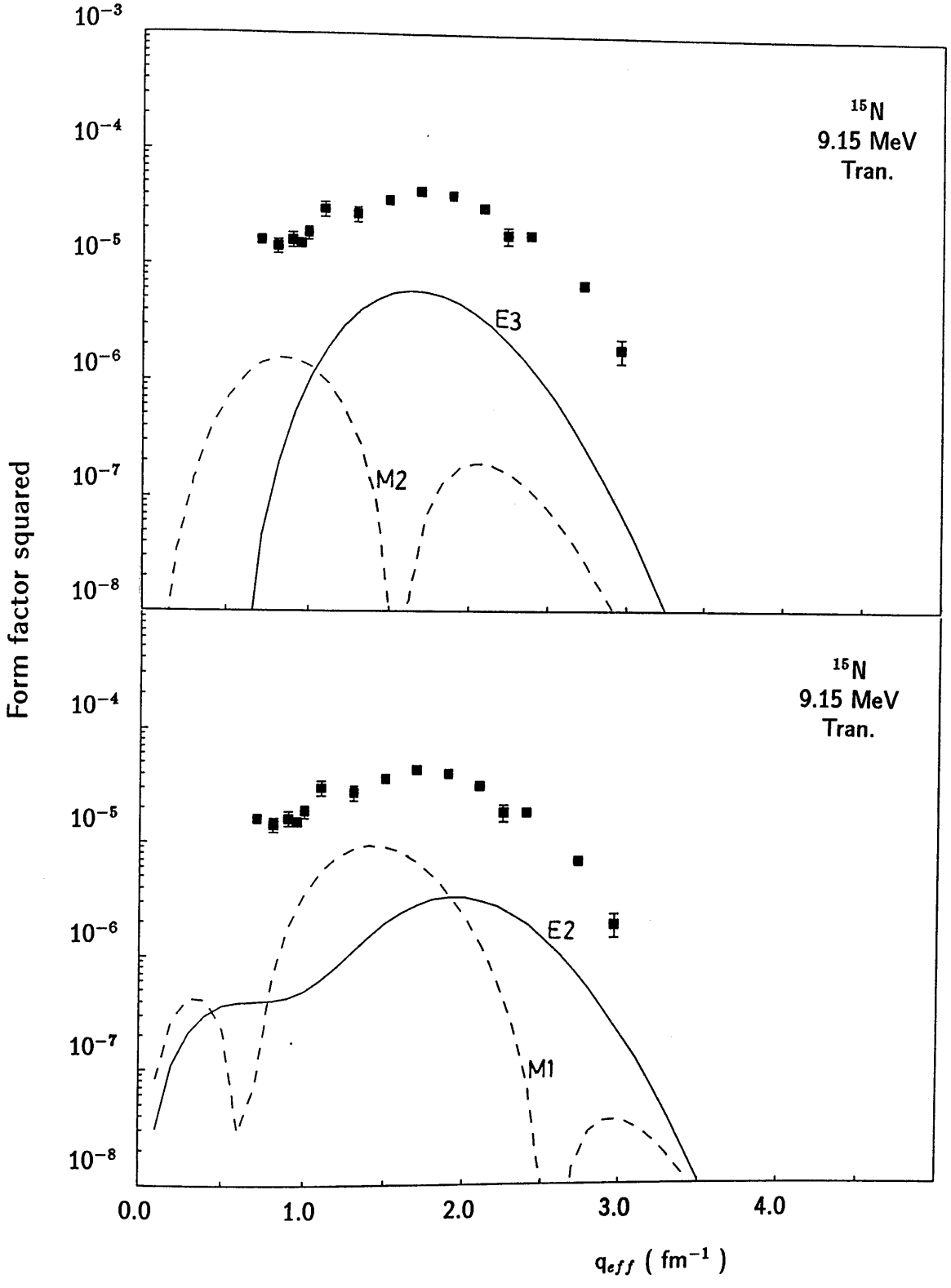

Figure 4.36: *Experimental and theoretical transverse form factors for the 9.15-MeV level. The curves are the multipoles involved in this transition which are arising from the $5/2_3^+$ and $3/2_2^-$ states.*

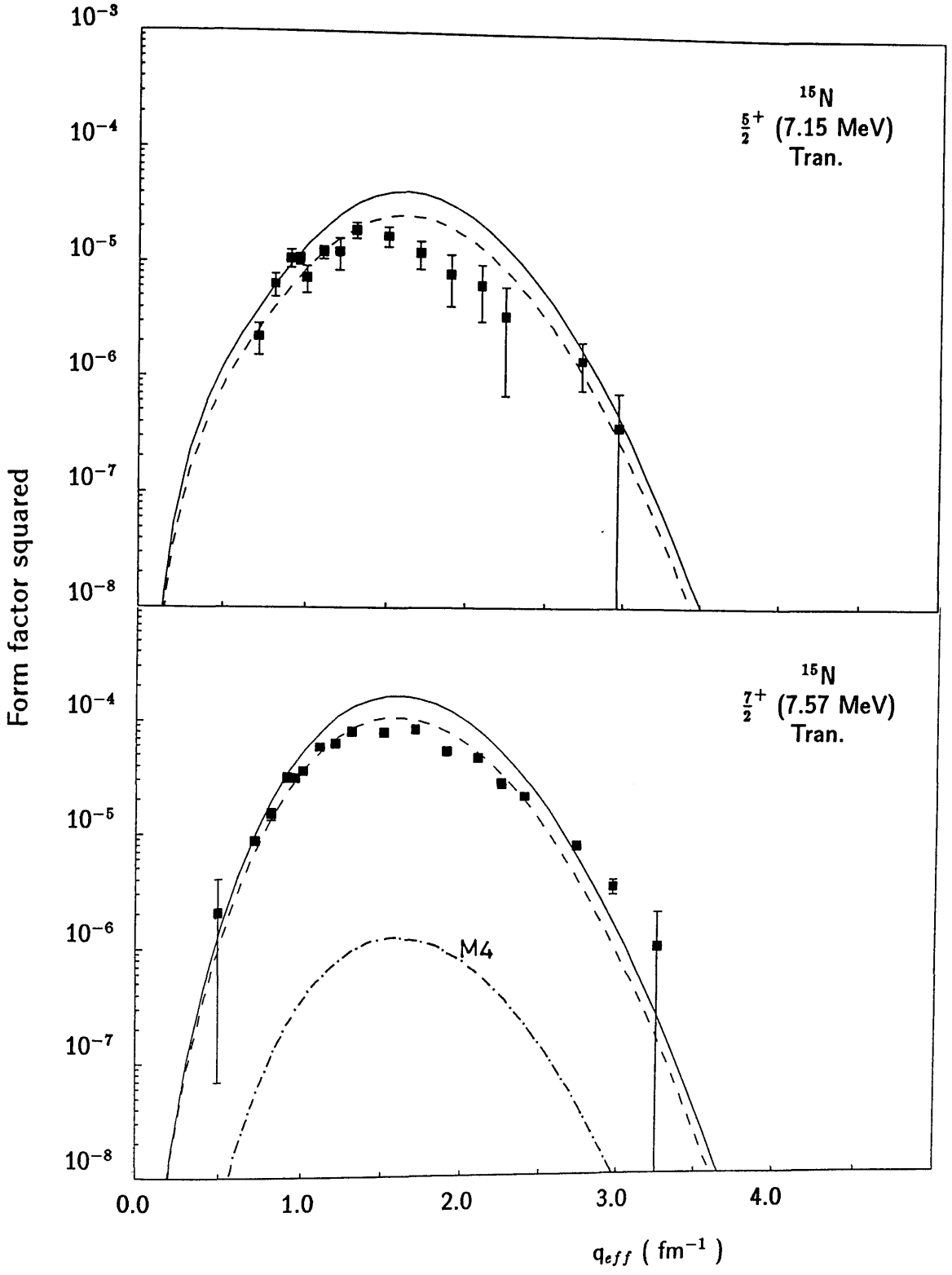

Figure 4.37: *Experimental and theoretical transverse form factors for the 7.15 and 7.57-MeV levels. The solid curves are the predictions of the shell model with free proton and neutron magnetic moments, while the dashed curves are those normalized downward by a factor of 1.6. The dot-dashed curve is the predicted M4 contribution.*

4.3.3 M4 Transitions

The states that can be reached by M4 transitions are particularly interesting for nuclei in the upper half of 1p-shell since there is only one possible configuration for such a transition: $[\ 1d_{5/2} \otimes 1p_{3/2}^{-1}\ ]_{4^-}$. Such a configuration is called stretched because the spin and orbital angular momentum transfer add together maximally i.e. the total angular momentum transfer ΔJ is one unit greater than the sum of the orbital angular momenta of the particle l_p and hole l_h, $\Delta J = l_p + l_h + 1$. The total orbital angular momentum transfer ΔL is given by $\Delta L = l_p + l_h$ and therefore a spin transfer $\Delta S = 1$ is required to meet the condition that $\Delta J = \Delta L + \Delta S$[61]. Such states are interesting because the electron scattering form factor obtains contributions from only the magnetisation density while the convection currents do not contribute.

The electron scattering data measured at 180° have observed strongly excited states at 10.7, 12.5, 14.1, 20.1 and 23.2 MeV. The states at 10.7 and 12.5 MeV have, previously, been identified as having $J^\pi=9/2^+$ [16]. The cross sections for the states at 10.7, 12.5, 14.1, 17.2, 20.1 and 23.2 MeV have been measured recently with pion inelastic scattering by Morris et al.[61] and were found to contain significant M4 strength. For the M4 transitions in the p-shell nuclei, the $[\ 1d_{5/2} \otimes 1p_{3/2}^{-1}\ ]_{4^-}$ matrix element is energetically favourable. If M4 form factors from other particle-hole configurations were possible, the resultant M4 form factors would have shapes significantly different from the observed M4 shape as shown in figure 4.38. In this figure, the $(d_{5/2},p_{3/2}^{-1})$ configuration produces an M4 form factor shape which is consistent with the experimental M4 shape for the 10.7 MeV state. We compare in figures 4.41 and 4.42 the M4 form factor produced by such a configuration (solid lines) with the observed M4 form factor data.

The experimental transverse form factors for the 7.57, 10.7, 12.5, 14.0, 20.1 and 23.2 MeV states are now discussed in terms of the shell model predictions. The measured transverse form factor for the first $7/2^+$ level at 7.57 MeV is shown in comparison with the predictions of the shell model in figure 4.37. The transverse components involved in this transition are E3 and M4. The theoretical transverse form factor is dominated by the E3 component. It agrees

in shape with the experimental form factor and a downward normalization by a factor of 1.6 is required to obtain agreement with the measured strength. There is only 2.5% M4 strength predicted in this transition. The longitudinal form factor for this state is shown with the predicted C3 in figure 4.30 and has already been discussed in the previous section.

Since the 10.7 MeV $3/2^-$ state lies very close to the $9/2^+$ level at 10.69 MeV, see figure 1.1, this doublet would have a mixture of M4, E5, E2 and M1 multipoles. The measured and theoretical transverse form factors of this level are displayed in figure 4.39. It is clear that the predicted E2, M1 and E5 form factor strength are very small compared to that of M4. Therefore we attribute the observed transverse form factor at 10.7 MeV to M4 transition. However, there is some excess strength in the experimental form factor at q > 2.2 fm^{-1}. This feature is more pronounced for the other M4 transitions to higher lying excited states which are discussed below. The longitudinal form factor for this doublet include a mixture of C2 and C5 arising from the $3/2^-$ and $9/2^+$ states respectively. The largest multipolarity which is consistent with the sd-shell model space is M4. Thus, C5 strength is expected to be small due to the lack of available configurations which can produce $\Delta J^\pi = 5^-$. We compare the longitudinal data to the corresponding calculated form factor in figure 4.40. We see that the predicted C5 is very small and is consistent with the experimental data which obviously receives its observed strength from the C2 form factor due to the excitation of the $3/2^-$ state at 10.7 MeV.

The unresolved levels at 12.5 MeV $5/2^+$, 12.52 MeV $5/2^+$ and at 12.55 MeV $9/2^+$ include complicated mixtures of E3, M2, M4 and E5 multipoles. The shell model predictions of M4 and E5 strength are compared with the transverse form factor at 12.5 MeV in figure 4.41 and accounts for about 80% of the M4 strength observed in these levels. However, the experimental form factor is augmented by contributions from other neighbouring levels and a definite conclusion is difficult to draw from this comparison. The data for the levels at 14.0, 20.1, and 23.2 MeV have a form factor with M4 like q-dependence. The shell model predictions also show significant M4 strength in these states. These are displayed in figures 4.41 and 4.42. The large M4 strength observed

in the obove transitions is in agreement with the results of the pion scattering experiment[61].

In a pion scattering experiment the ratios of the measured cross sections for π^+ and π^- scattering can be used to extract the isoscalar and isovector spectroscopic amplitudes Z_0 and Z_1. The Z_0 and Z_1 amplitudes are defined to be the same as the one-body density-matrix element in a shell model calculation[62], which are equal to unity for a pure particle-hole transition. The corresponding proton and neutron spectroscopic amplitudes Z_p and Z_n are related to these by

$$Z_p = \frac{(Z_0 - Z_1)}{\sqrt{2}}$$

$$Z_n = \frac{(Z_0 + Z_1)}{\sqrt{2}}$$

The values of Z_0 and Z_1 may be obtained from the experimental cross sections by solving the following simultaneous equations[61]

$$\begin{aligned} Z_1 &= 2Z_0 \pm 2\sqrt{N^+} \\ Z_1 &= -2Z_0 \pm 2\sqrt{N^-} \end{aligned} \tag{4.4}$$

Here N^+ and N^- are factors needed to normalize the calculated π^+ and π^- angular distributions in DWBA to the measured π^+ and π^- angular distributions[61]. However, these equations yield two independent solutions for Z_0 and Z_1. This ambiguity can often be resolved by comparing the pion results with those from electron scattering, since the transverse form factor is proportional to $(Z_1 - 0.187Z_0)$ [72], i.e.

$$Z_1 = 0.187Z_0 \pm C, \tag{4.5}$$

where C is the strength of the electron scattering form factor in units of the single particle isovector form factor, F_{M4}. The M4 form factor for the $(d_{5/2},p_{3/2})_{M4,\Delta T=1}$ matrix element in the PWBA and with harmonic oscillator radial wave function, is given by[73]

$$\mid F_{M4}(q) \mid^2 = \left(\frac{2J_f+1}{2J_i+1}\right)\left(\frac{1}{Z^2}\right)\frac{32}{63}y^4e^{-2y}b^{-2}\left(\frac{\hbar c}{2Mc^2}\right)^2(\mu_p - \mu_n)^2 f_{CM}^2 f_{SN}^2, \tag{4.6}$$

where $y = (bq/2)^2$, b=1.7 fm and f_{CM}^2 and f_{SN}^2 are the centre-of-mass and nucleon finite size terms and are found in section 2.2. By comparing the value

at the maximum of the experimental M4 form factor with the form factor defined by equation 4.6 the values of C can be determined for the observed states. These are displayed in table 4.5 along with N^+ and N^- values from the pion scattering experiment.

A graphical analysis of the combined (π, π') and (e,e') data can now provide a useful way of obtaining unique set of Z_0 and Z_1 values[61]. One plots the Z_1 and Z_0 values as shown in figure 4.43 such that equation 4.5 provides two parallel lines with intercepts on the Z_1 axis equal to +C and -C. These lines which are labled (e,e') then represent allowed combinations of Z_1 and Z_0 values. Similarly, pion scattering data gives two parallel lines (labeled σ^+/σ^{DW}) for π^+ scattering with intercepts $\pm 2\sqrt{N^+}$ and two parallel lines (labeled σ^-/σ^{DW}) for π^- scattering with intercepts $\pm 2\sqrt{N^-}$. The widths of the bands are due to the statistical errors in σ^+ and σ^-. In the absence of (e,e') data, the pion scattering data gives two acceptable solutions represented by the two points of intersections, X and Y on the figure. With the (e,e') data included for example for the 10.7 MeV state, only solution X is consistent with all measurements; solution Y being obviously unrepresentative of the (e,e') data. Thus, it is possible to obtain unique value of spectroscopic amplitudes for a given M4 transition with the combined analysis. The results of such an analysis for the other states are shown in figures 4.43 and 4.44

The (e,e') data for the state at 12.5 MeV is an upper limit for the M4 strength since the $\Delta T=3/2, 5/2^+$ level at 12.52 MeV is expected to be strongly excited by an E3 transition[18]. Therefore the second solution can be ruled out and the first solution is prefered for this level. For the 14-MeV level, the agreement between the amplitudes extracted from pion scattering and the (e,e') data favours the second solution. No strong peak is observed in the (e,e') spectrum for the 17.2-MeV level and the peak value of the form factor is estimated to be less than 10% that for the 14.0-MeV state. For the 20.1 and 23.2 MeV states, there is good agreement between the second solution and (e,e') data.

Table 4.5: Combined analysis of the (π, π') and (e,e') data

E_{ex} (MeV)	$2\sqrt{N^+}$	$2\sqrt{N^-}$	C
10.7	0.73±0.04	0.224±0.04	0.322±0.01
12.5	0.922±0.06	0.254±0.06	0.508±0.01
14.0	0.631±0.06	0.433±0.06	0.432±0.01
17.2	1.074±0.06	1.262±0.06	0.147±0.01
20.1	0.586±0.07	0.554±0.07	0.56±0.01
23.2	0.774±0.16	0.39±0.16	0.522±0.02

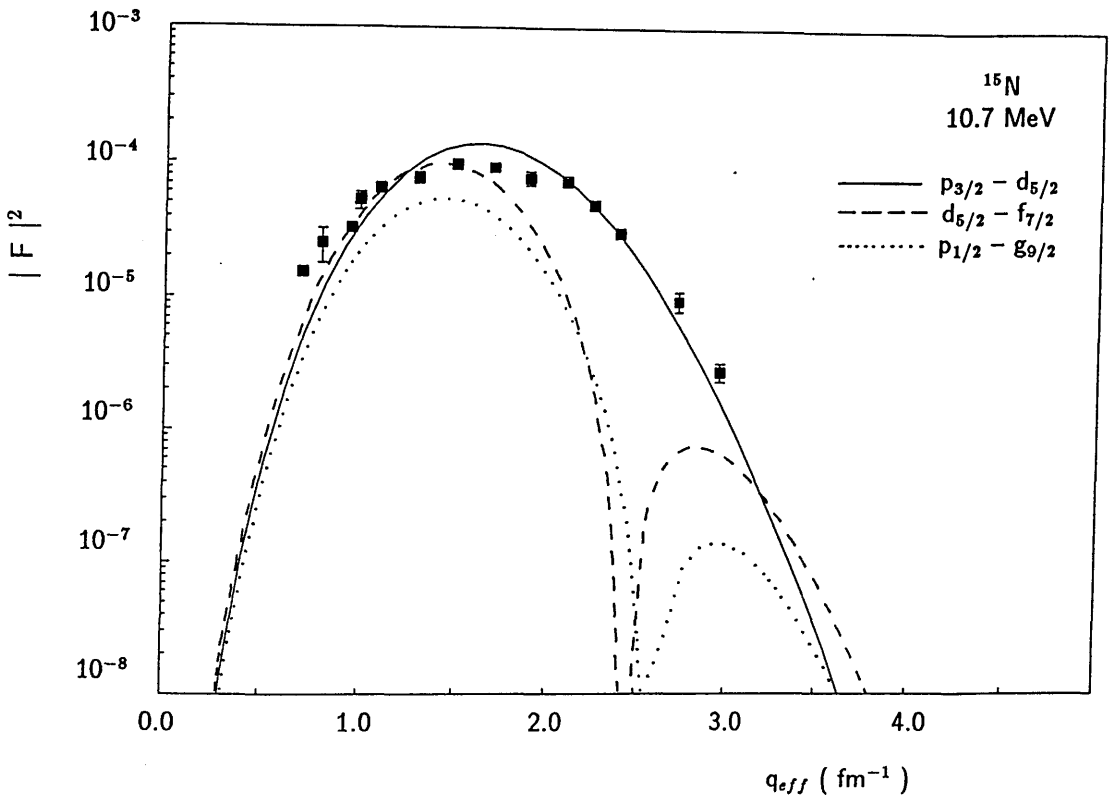

Figure 4.38: *Possible M4 form factors for different configurations calculated with harmonic oscillator wave function, b=1.7 fm*

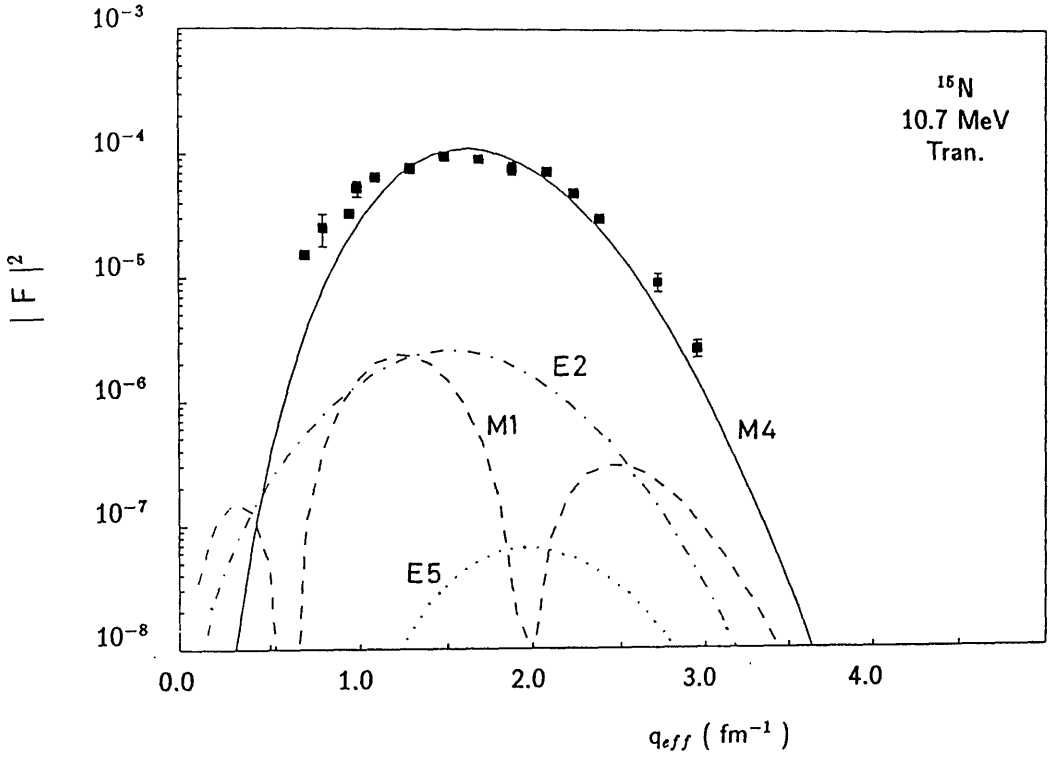

Figure 4.39: *The 10.7 MeV experimental transverse form factor with the shell model predictions for different multipoles.*

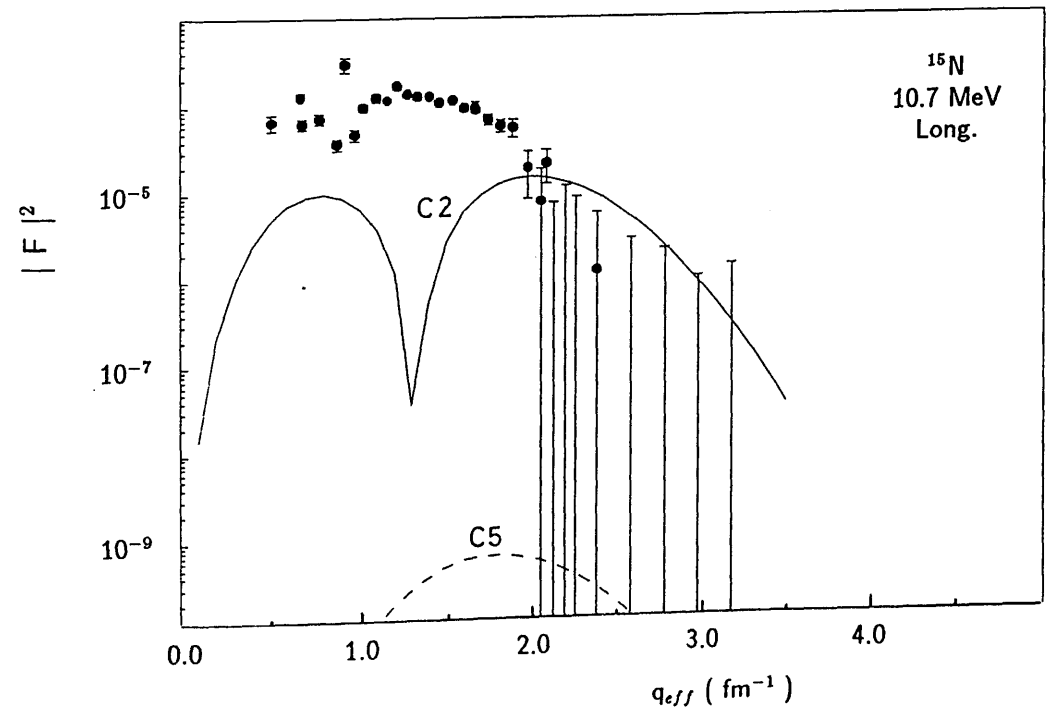

Figure 4.40: *The 10.7 MeV experimental longitudinal form factor with the C2 and C5 shell model predictions.*

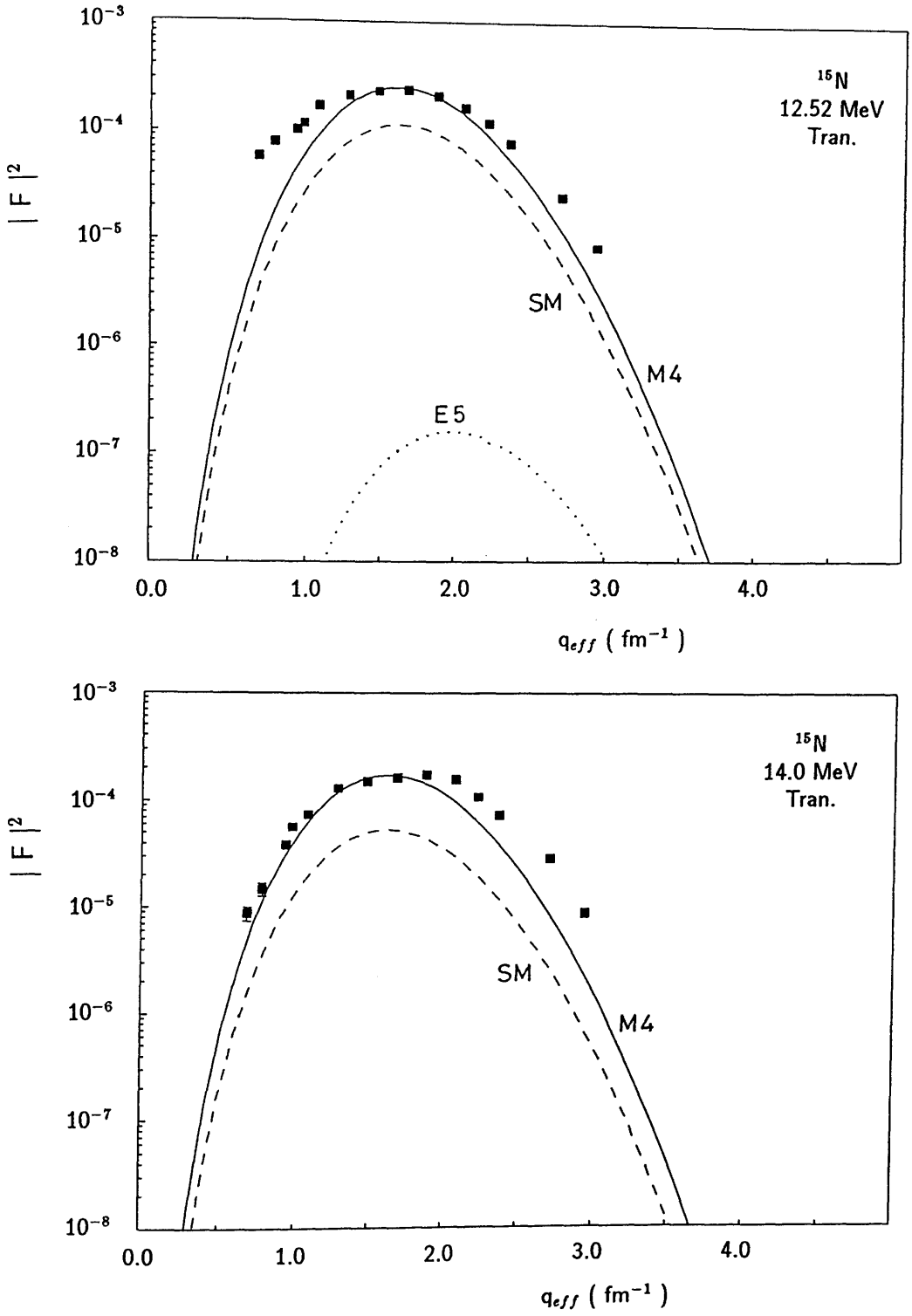

Figure 4.41: *Transverse experimental and theoretical form factor for the levels at 12.5 and 14 MeV. The solid curves are the M4 form factor produced by the* $(d_{3/2}, d_{5/2})$ *configuration. The dashed and doted curves are the M4 and E5 shell model predictions, respetively.*

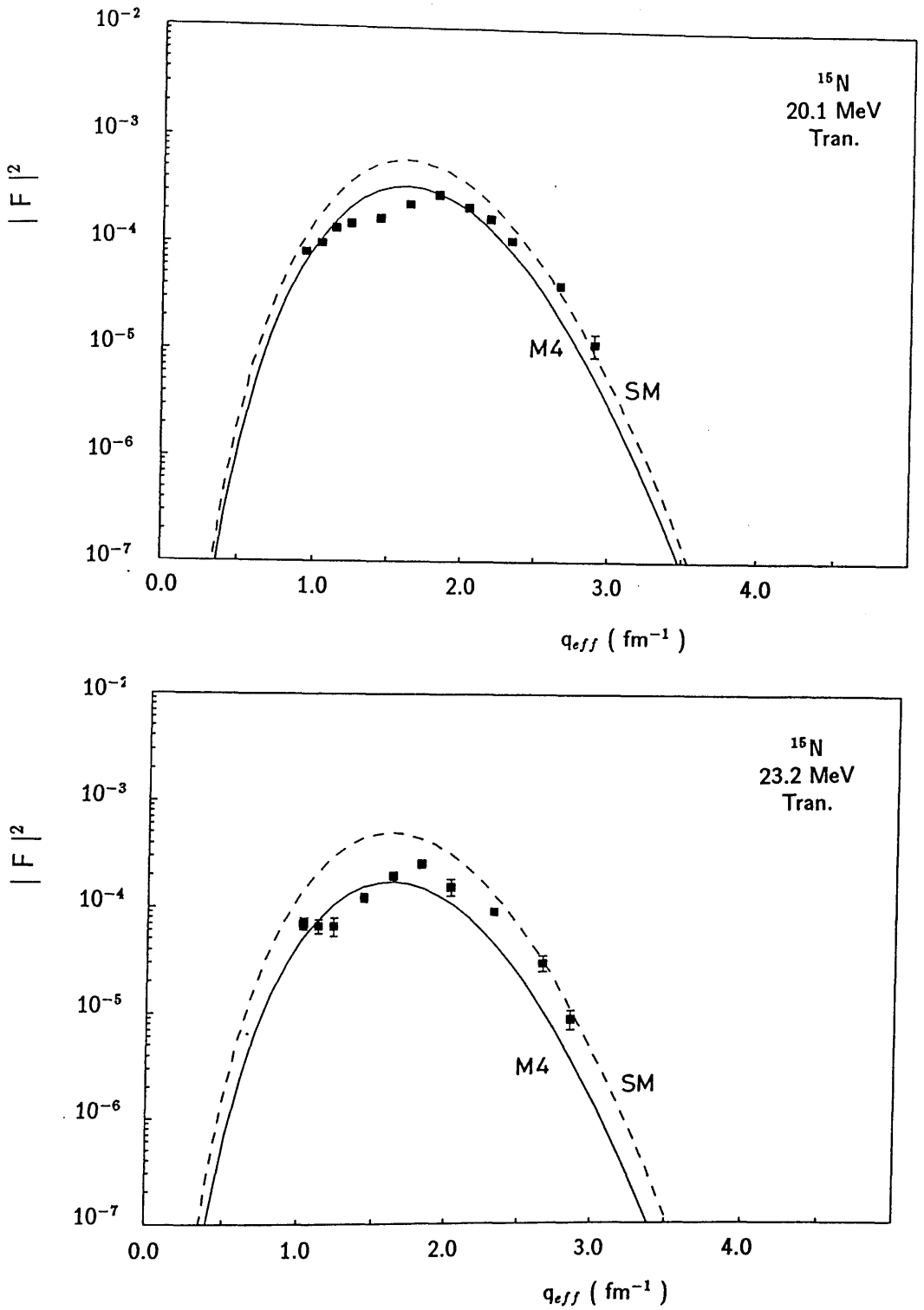

Figure 4.42: *Transverse experimental and theoretical form factor for the levels at 20.1 and 23.2 MeV. The solid curves are the M4 form factor produced by the* $(d_{3/2}, d_{5/2})$ *configuration. The dashed curves are the M4 shell model predictions.*

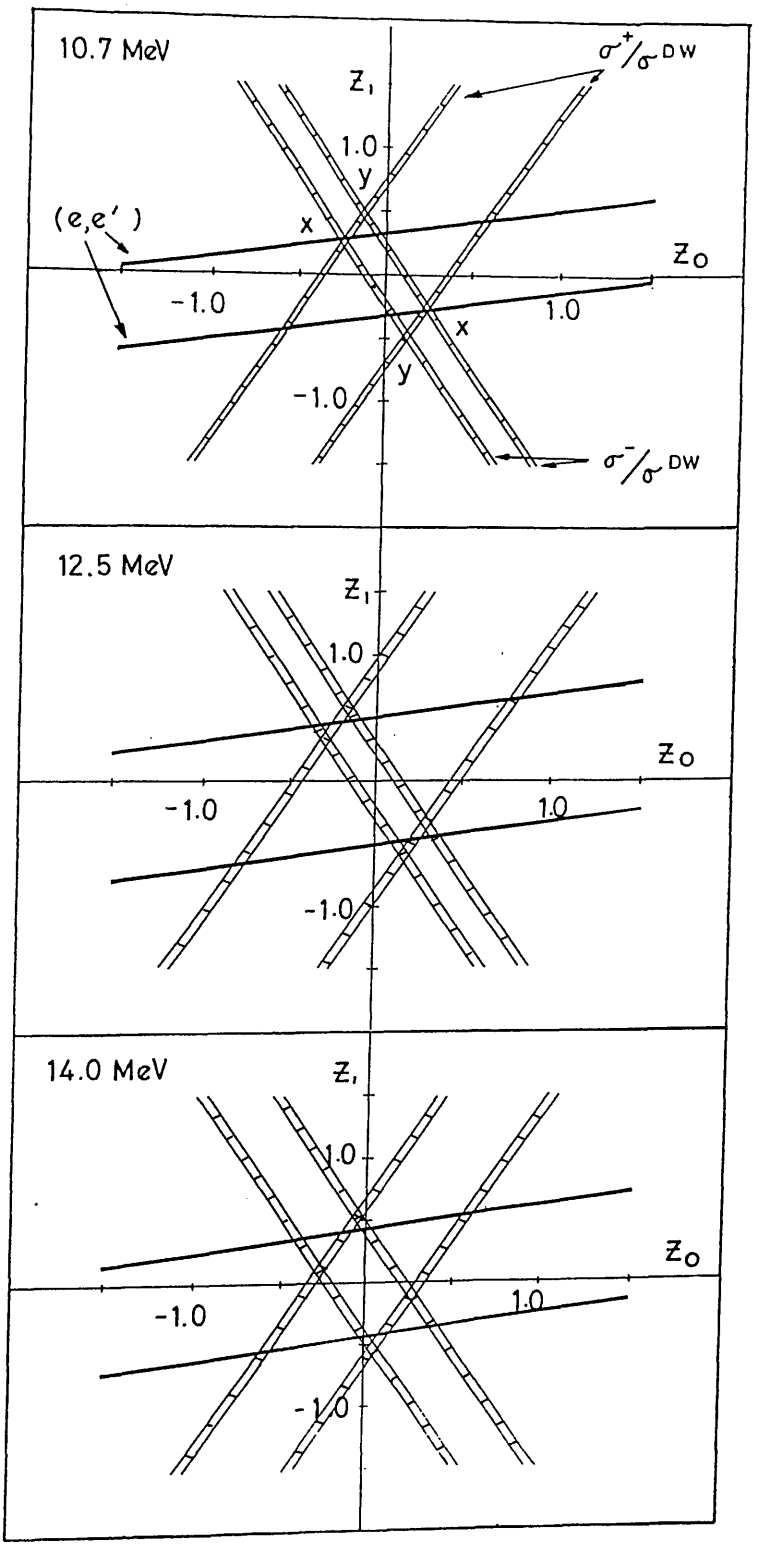

Figure 4.43: *Isovector versus isoscalar spectroscopic amplitudes. The intersections of the bands labeled* σ^+/σ^{DW} *and* σ^+/σ^{DW} *represent the two solutions for* Z_0 *and* Z_1 *from the* (π,π') *data. The lines labeled (e,e') correspond to the values of* Z_0 *and* Z_1 *consistent with the electron scattering data.*

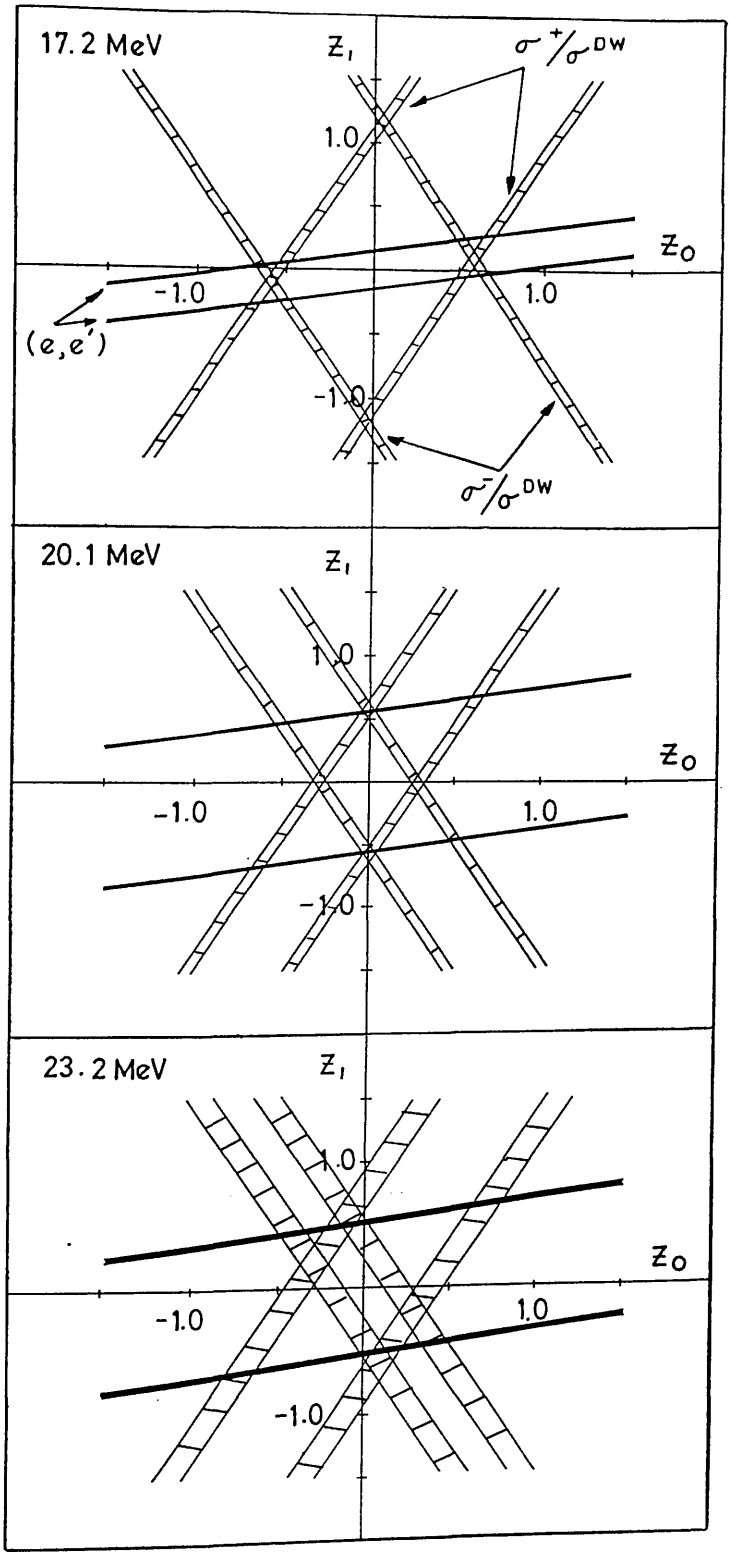

Figure 4.44: *Isovector versus isoscalar spectroscopic amplitudes. The intersections of the bands labeled* σ^+/σ^{DW} *and* σ^+/σ^{DW} *represent the two solutions for* Z_0 *and* Z_1 *from the* (π,π') *data. The lines labeled (e,e') correspond to the values of* Z_0 *and* Z_1 *consistent with the electron scattering data.*

4.4 The $E_{exc} > 13.6$ MeV region

In the present experiment the form factor of many states in the $E_{exc} > 13.6$ MeV region are obtained. The experimental form factors for these states are presented in this section without comparison with theory since no theoretical calculations are available. All of the states below 13.6 MeV excitation have already been presented and discussed in this chapter except those at 11.61 12.52, 12.93, 13.16, 13.39 and 13.6 MeV. The form factors for these states are displayed in figure 4.45 and 4.46. The longitudinal form factors for the states at 12.52 MeV are shown in figure 4.45. The transverse form factors are shown in figure 4.41 and compared with the shell model predictions in the previous section.

For excited states beyond 13 MeV the spin parity assignements are not very extensive. There are a number of $1/2^{\pm}$, $3/2^{\pm}$, $5/2^{\pm}$ states in this region and we do observe form factors which represent a wide variety of q-dependences. However, a detailed interpretation of these form factors requires more theoretical understanding and we have presented the form factors in figures 4.47 through 4.58. In the region beyond 18 MeV we have identified several new states and obtained a width parameter for these. These results have been presented in table 3.4.

The giant resonance region (GR) of ^{15}N has been studied previously by inelastic electron scattering[15] in a momentum transfer range 0.36 - 1.25 fm^{-1}. In the present experiment we have extended the work of Ansaldo et al.[15] up to much higher momentum transfer(3.2 fm^{-1}). Following the work of Ansaldo, the longitudinal and transverse form factors for the states in the excitation energy region between 14 and 18.5 MeV were integerated. The momentum transfer dependence of the form factors for this region along with those of Ansaldo is shown in figure 4.59. There is good agreement between the two experiments. The solid and dashed lines represent the C1 and C2 contributions calculated with the Helm model[65] with parameters R=2.58 fm and g=1.05 fm[15]. It is clear that the excess strength in the q > 1 fm^{-1} region is observed suggesting that a higher multipolarity might be contributing in these excitations. The dot-

dashed line represents the C3 contribution. The transverse form factor strength is displayed along with those of Ansaldo in figure 4.59. Again, the agreement between the two experiments is satisfactory.

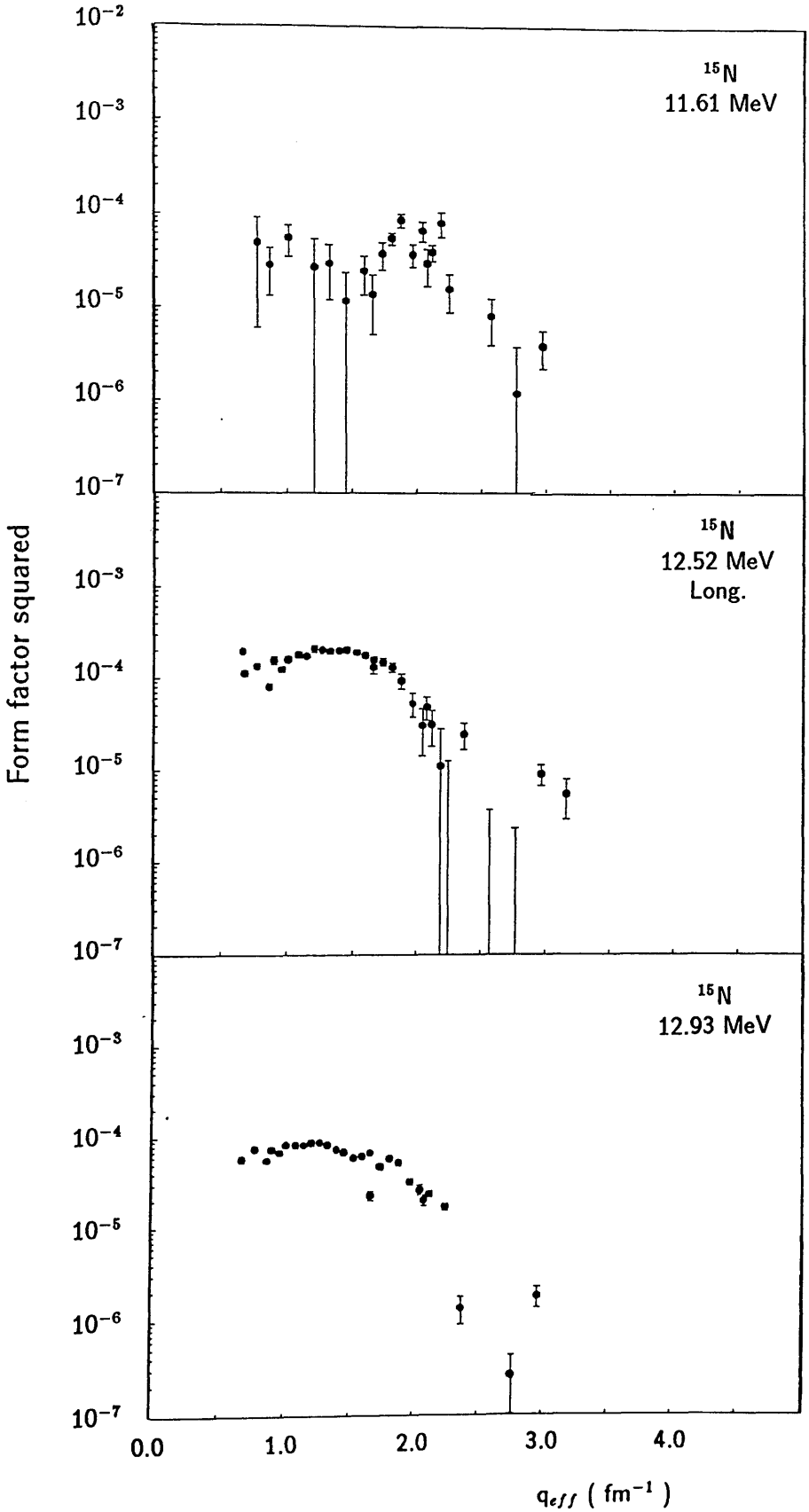

Figure 4.45: *The experimental form factors for the states at 11.61, 12.52 and 12.93 MeV.*

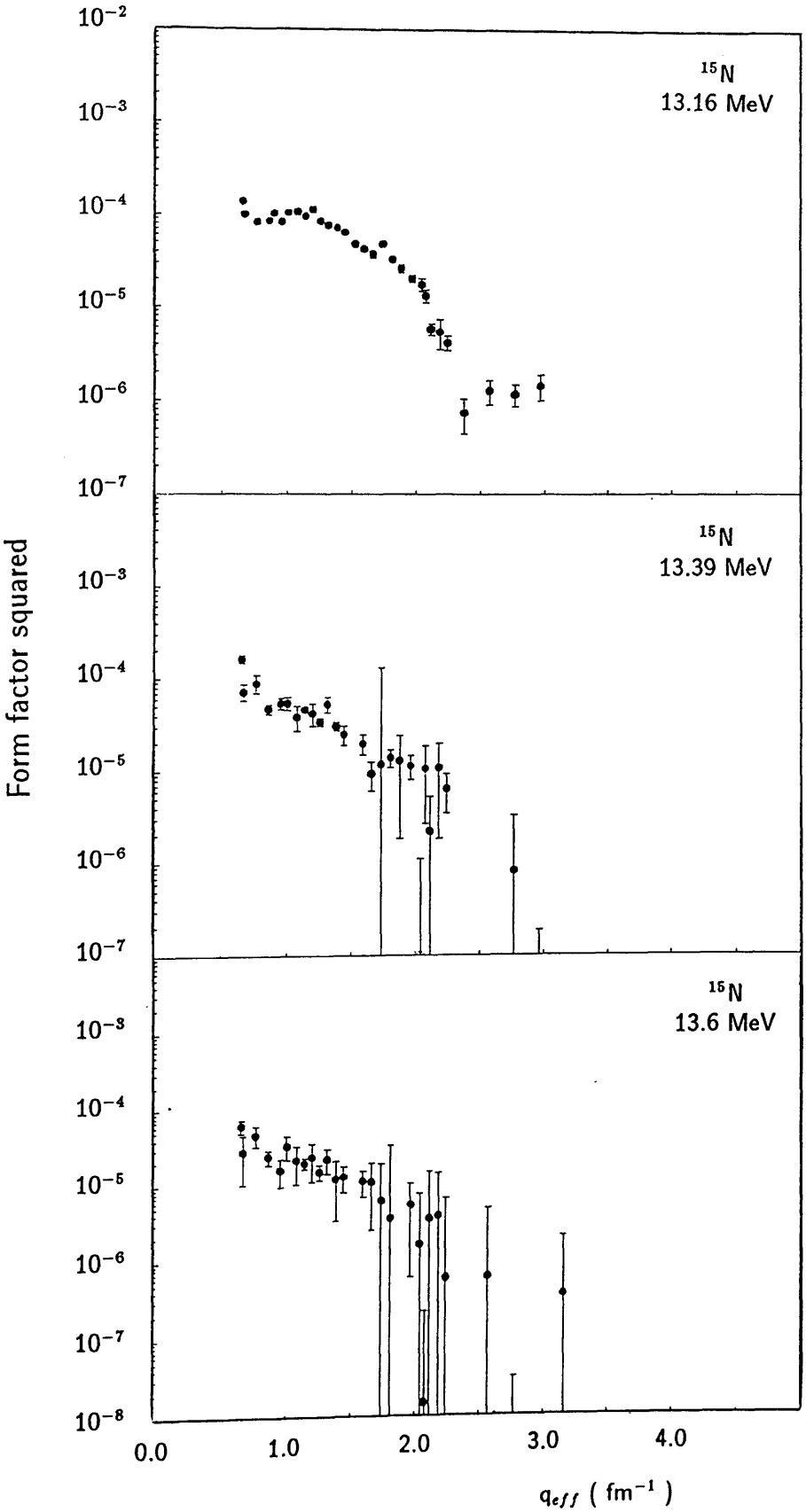

Figure 4.46: *The experimental form factors for the states at 13.16, 13.39 and 13.6 MeV.*

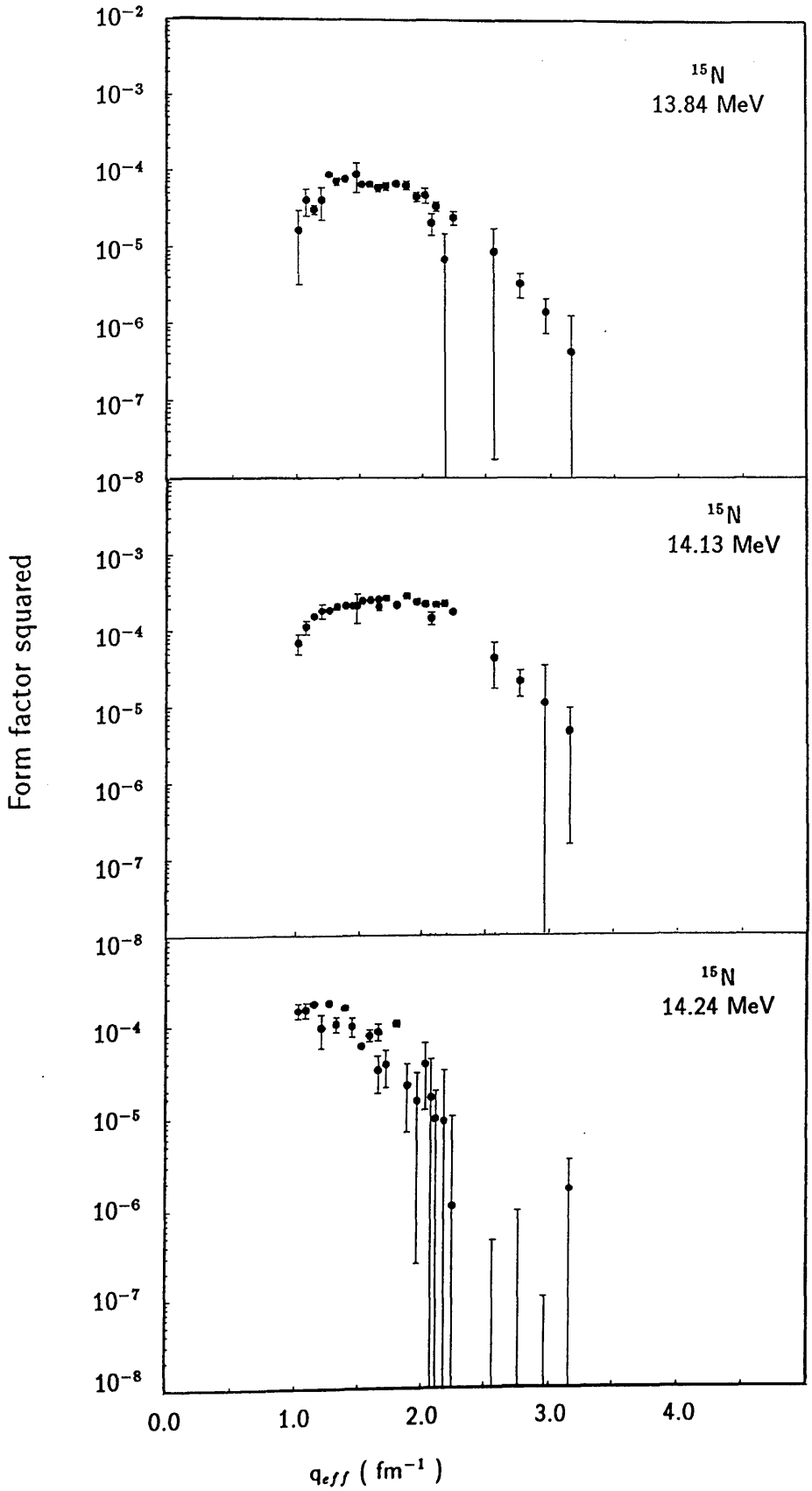

Figure 4.47: *The experimental form factors for the states at 13.84, 14.13 and 14.24 MeV.*

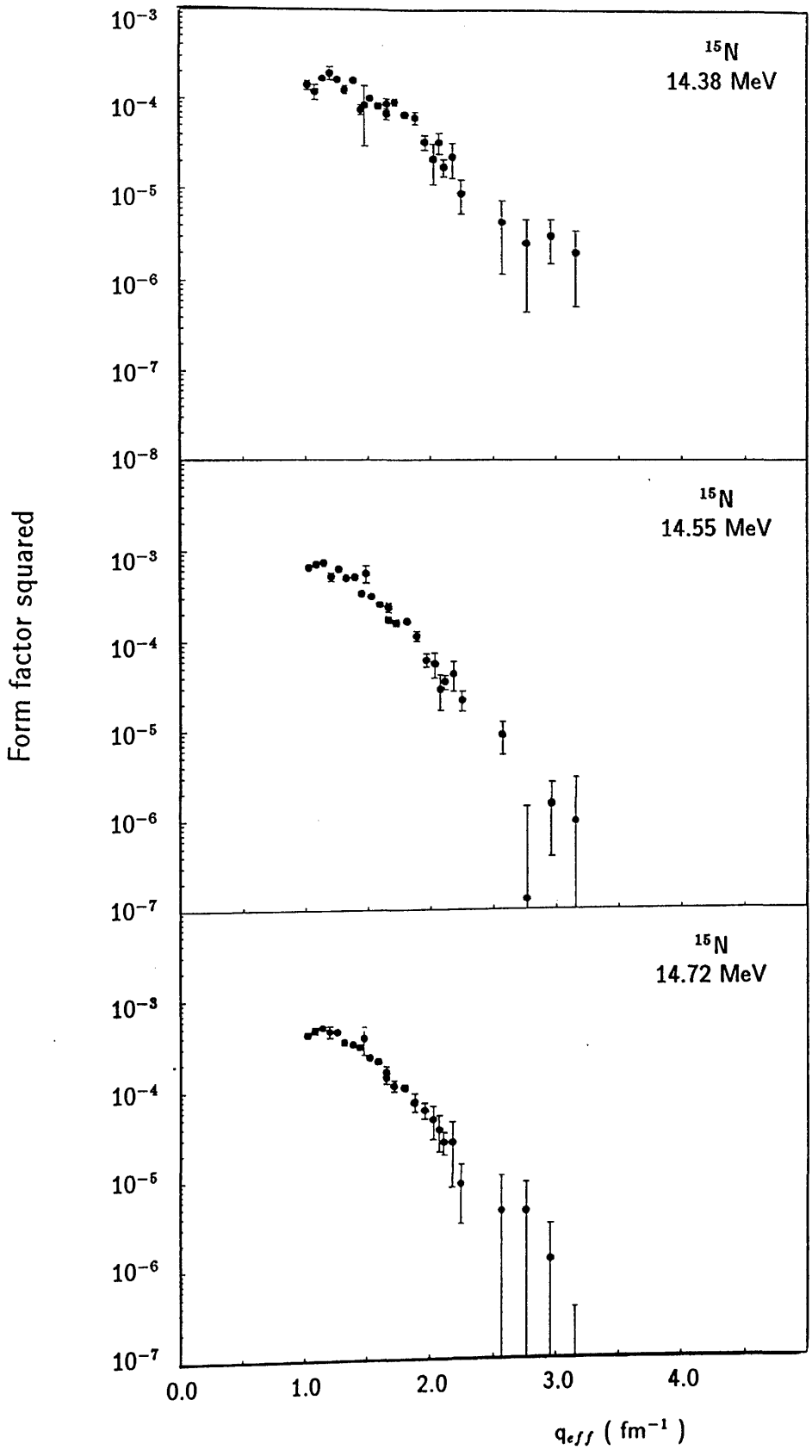

Figure 4.48: *The experimental form factors for the states at 14.38, 14.55 and 14.72 MeV.*

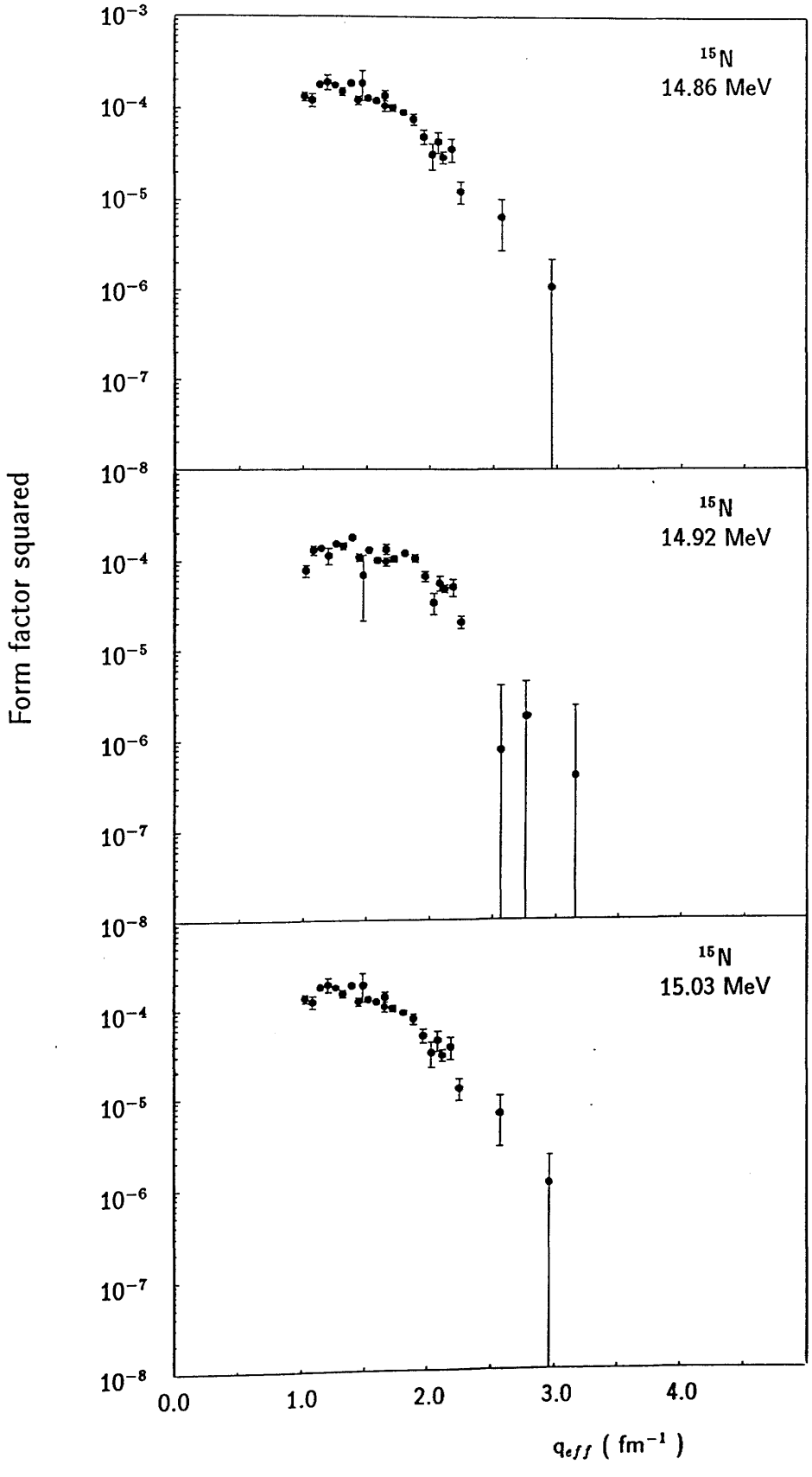

Figure 4.49: *The experimental form factors for the states at 14.86, 14.92 and 15.03 MeV.*

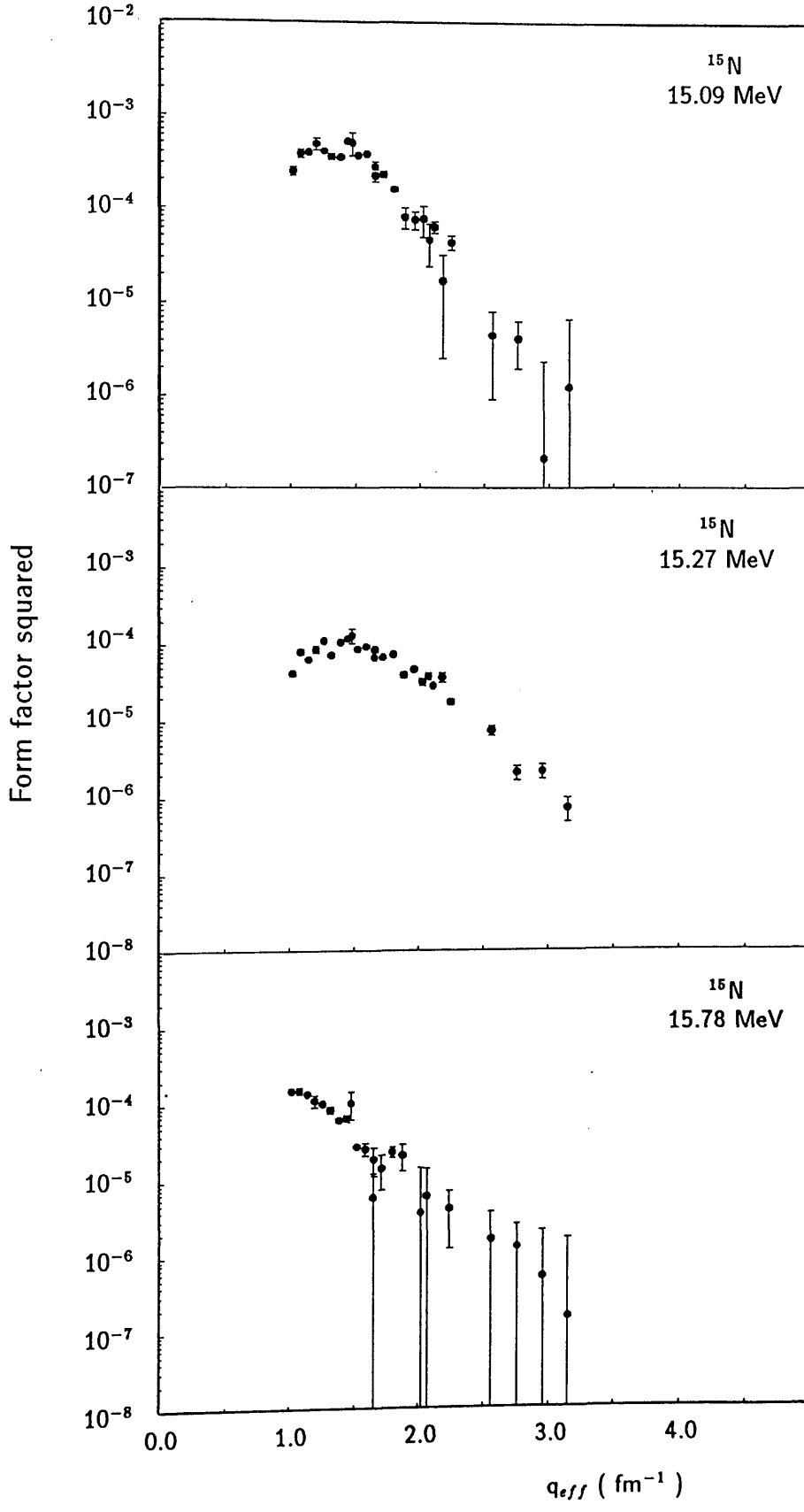

Figure 4.50: *The experimental form factors for the states at 15.09, 15.27 and 15.78 MeV.*

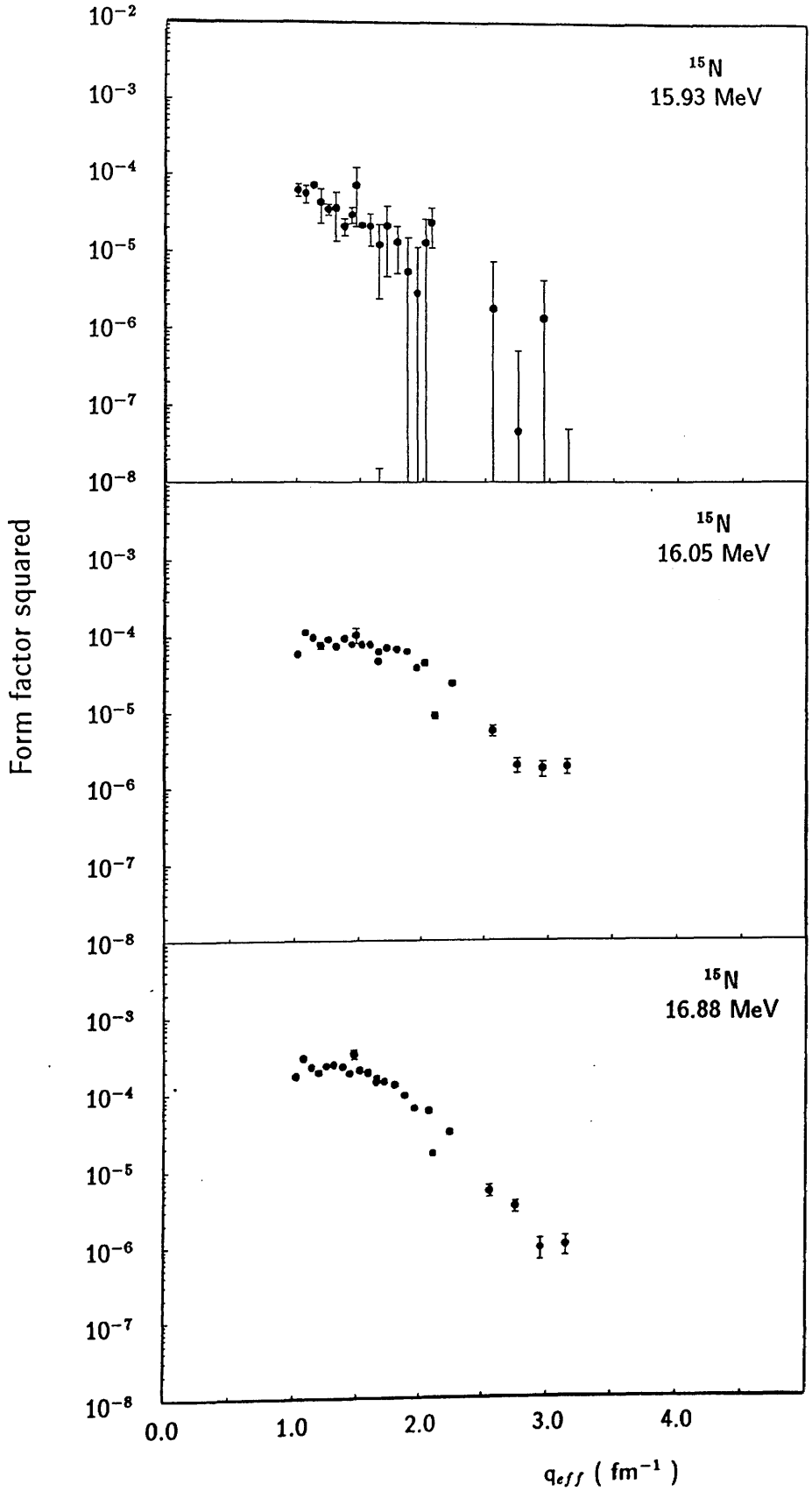

Figure 4.51: *The experimental form factors for the states at 15.93, 16.05 and 16.88 MeV.*

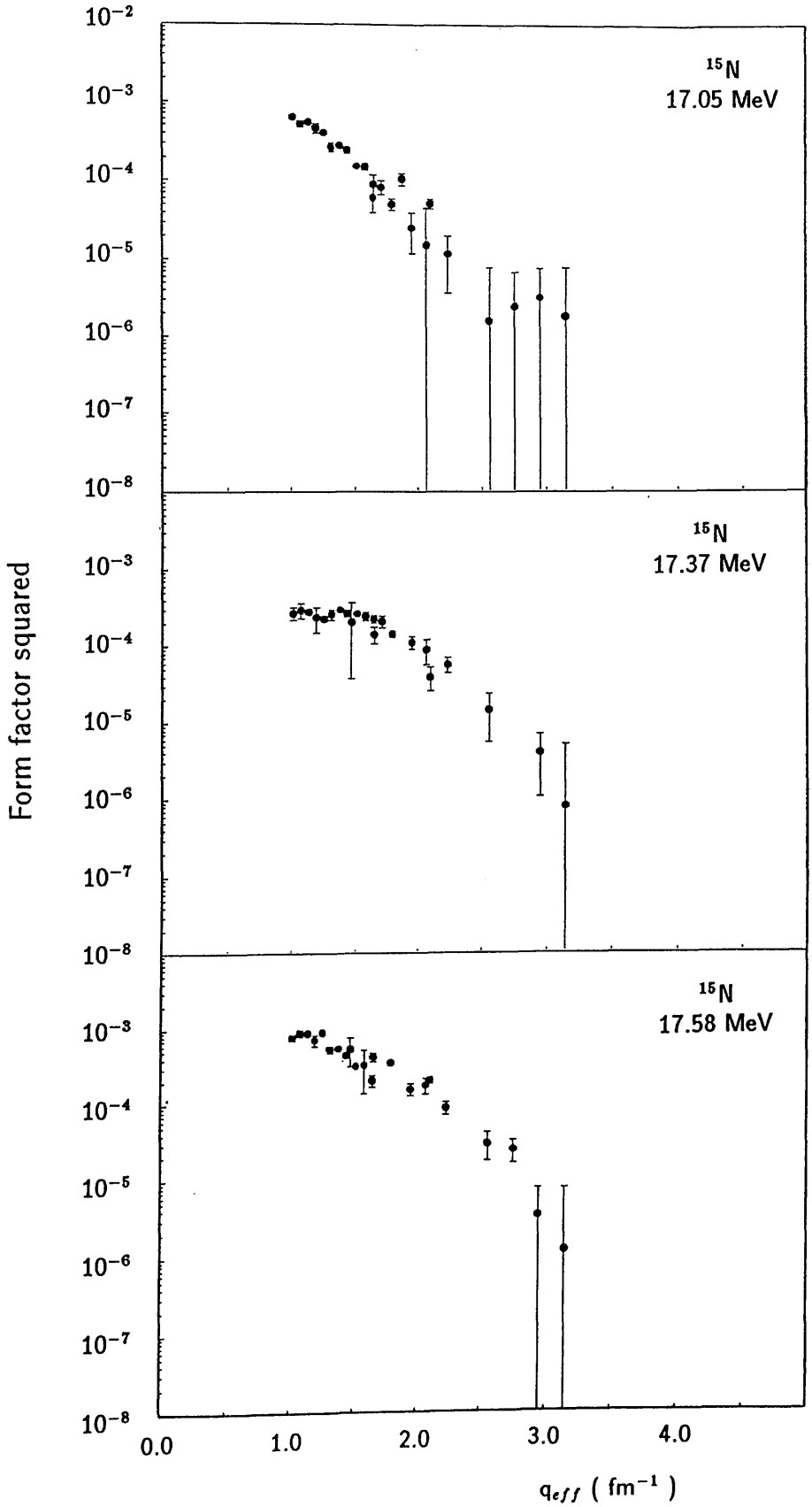

Figure 4.52: *The experimental form factors for the states at 17.05, 17.37 and 17.58 MeV.*

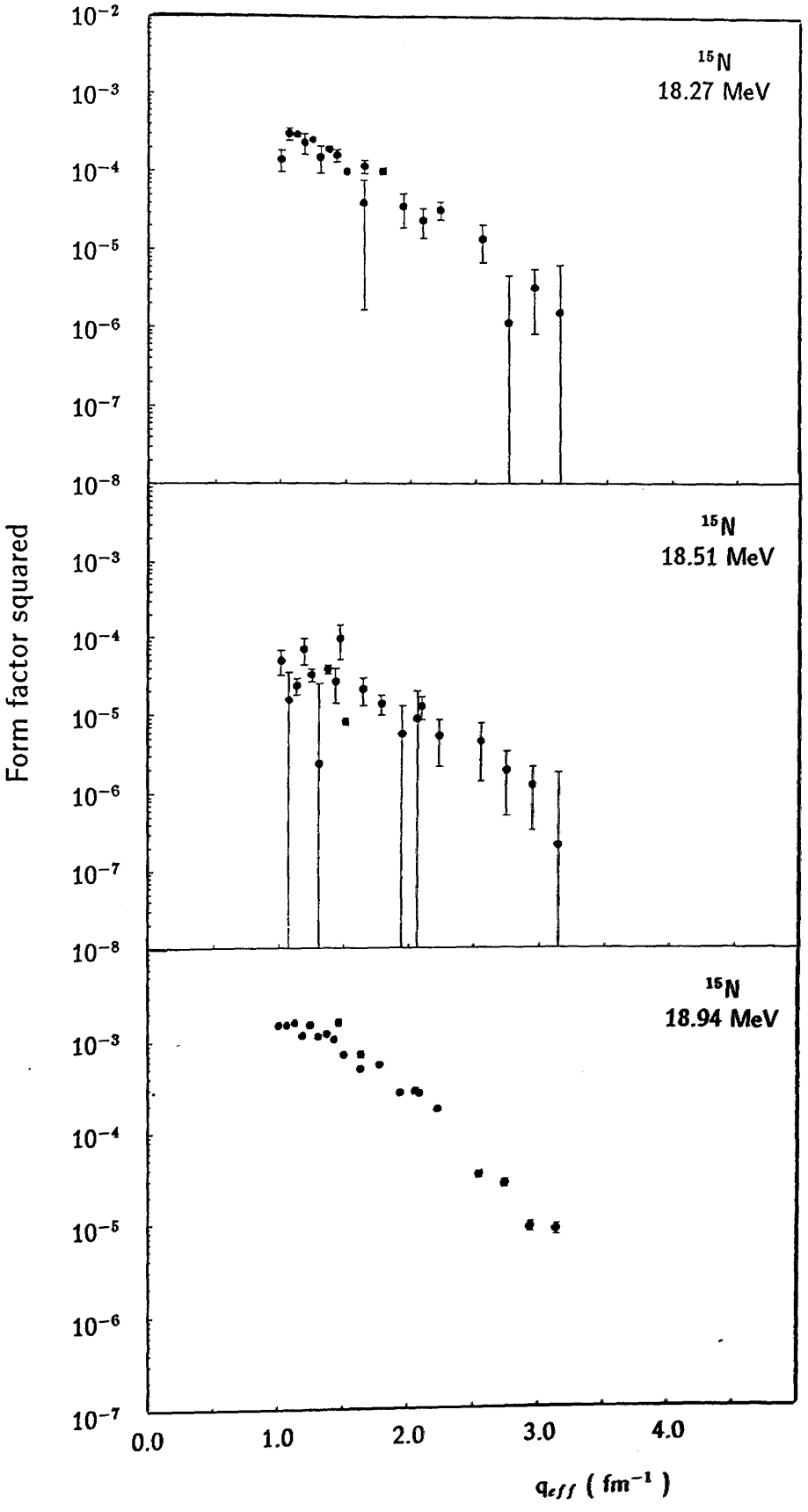

Figure 4.54: *The experimental form factors for the states at 18.27, 18.51 and 18.94 MeV.*

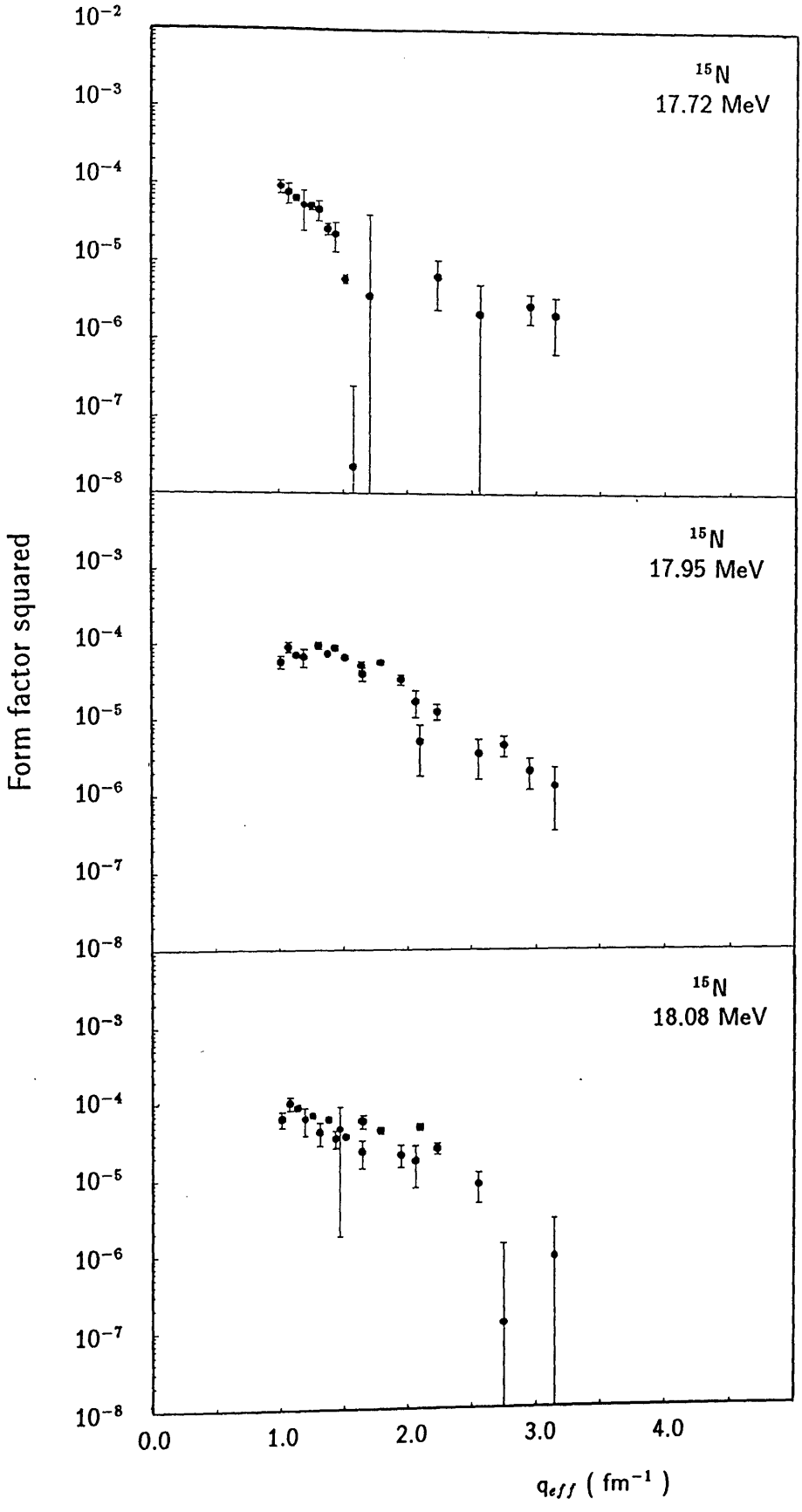

Figure 4.53: *The experimental form factors for the states at 17.72, 17.95 and 18.08 MeV.*

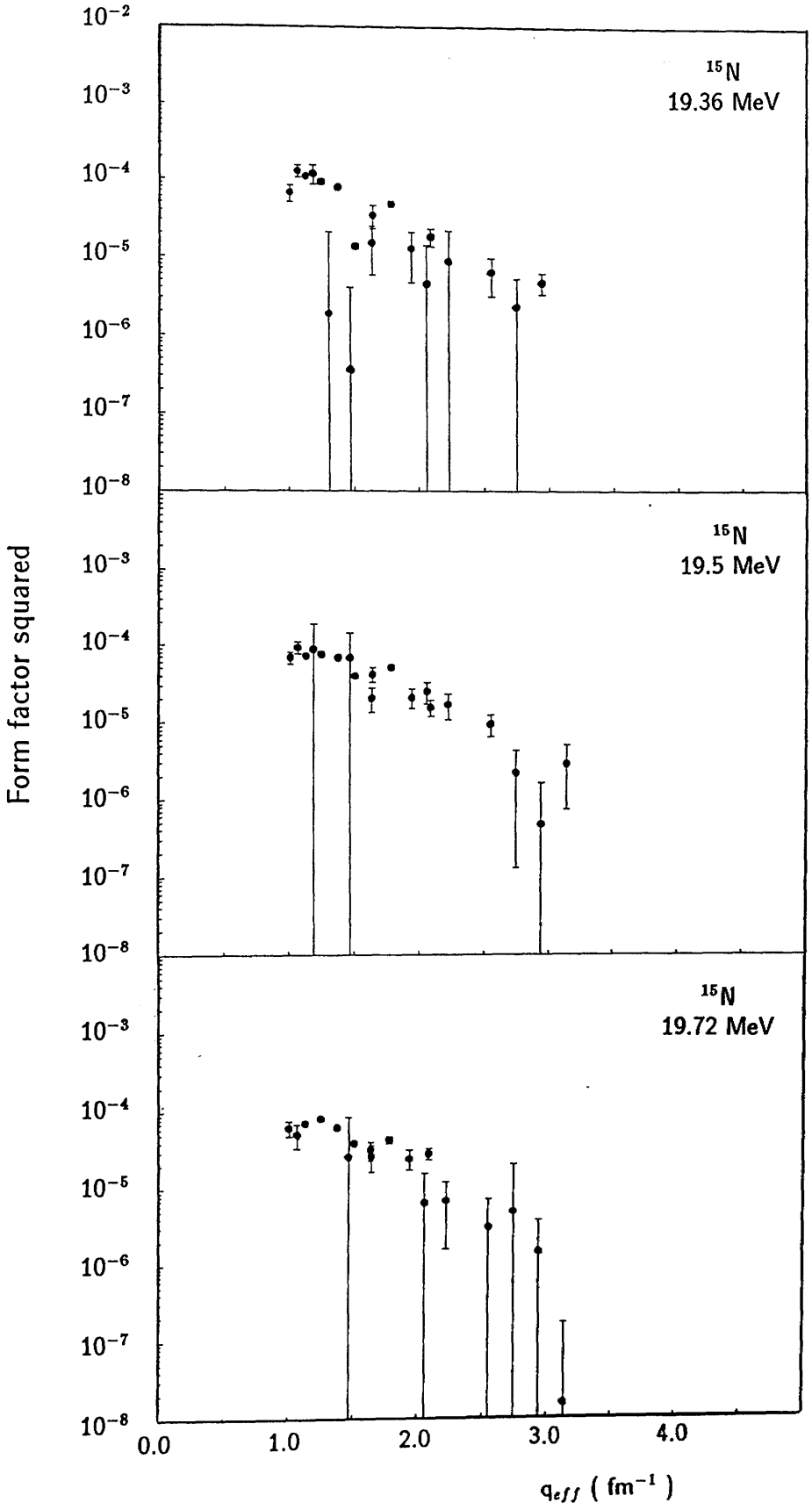

Figure 4.55: *The experimental form factors for the states at 19.36, 19.5 and 19.72 MeV.*

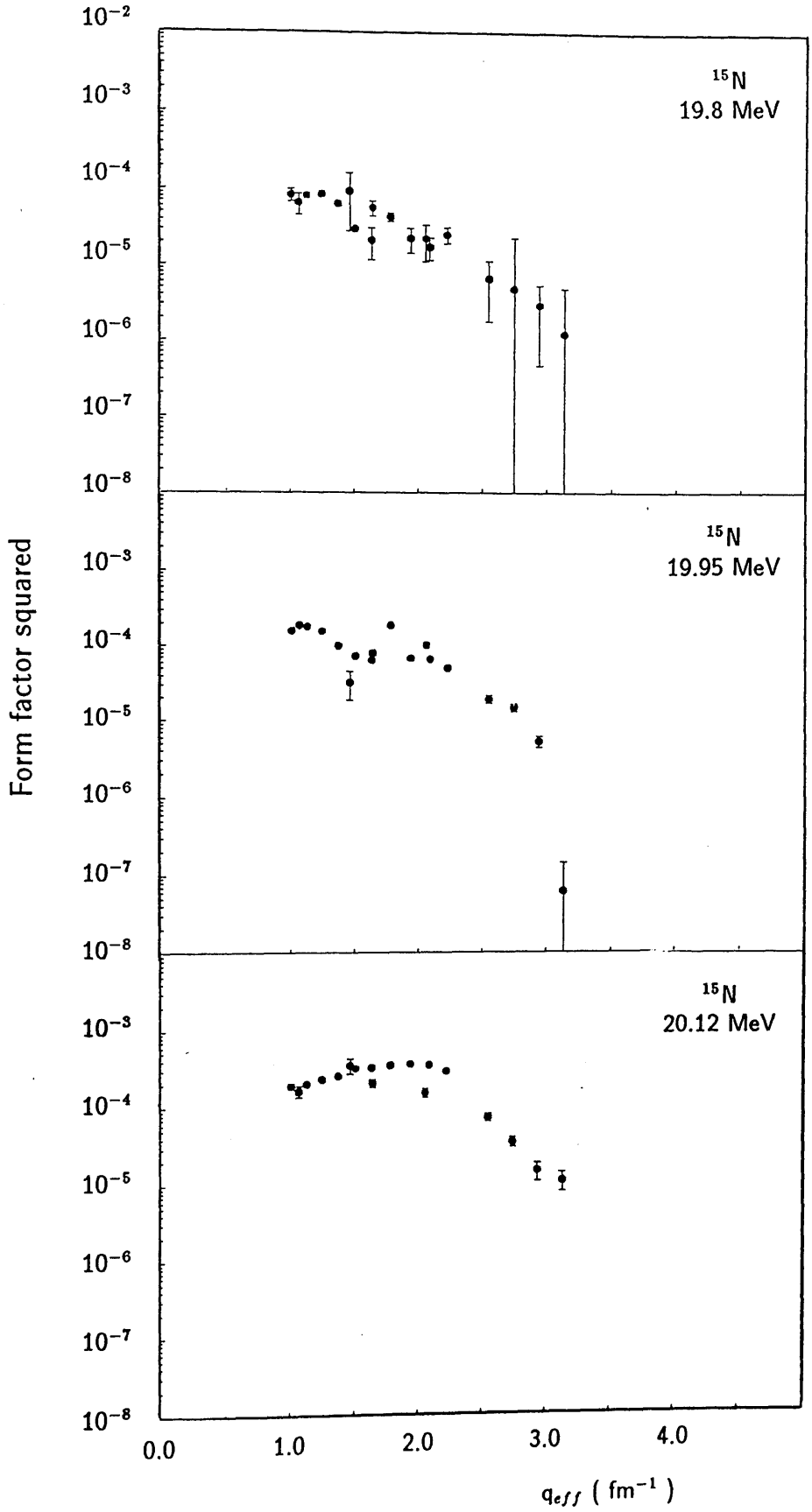

Figure 4.56: *The experimental form factors for the states at 19.8, 19.95 and 20.12 MeV.*

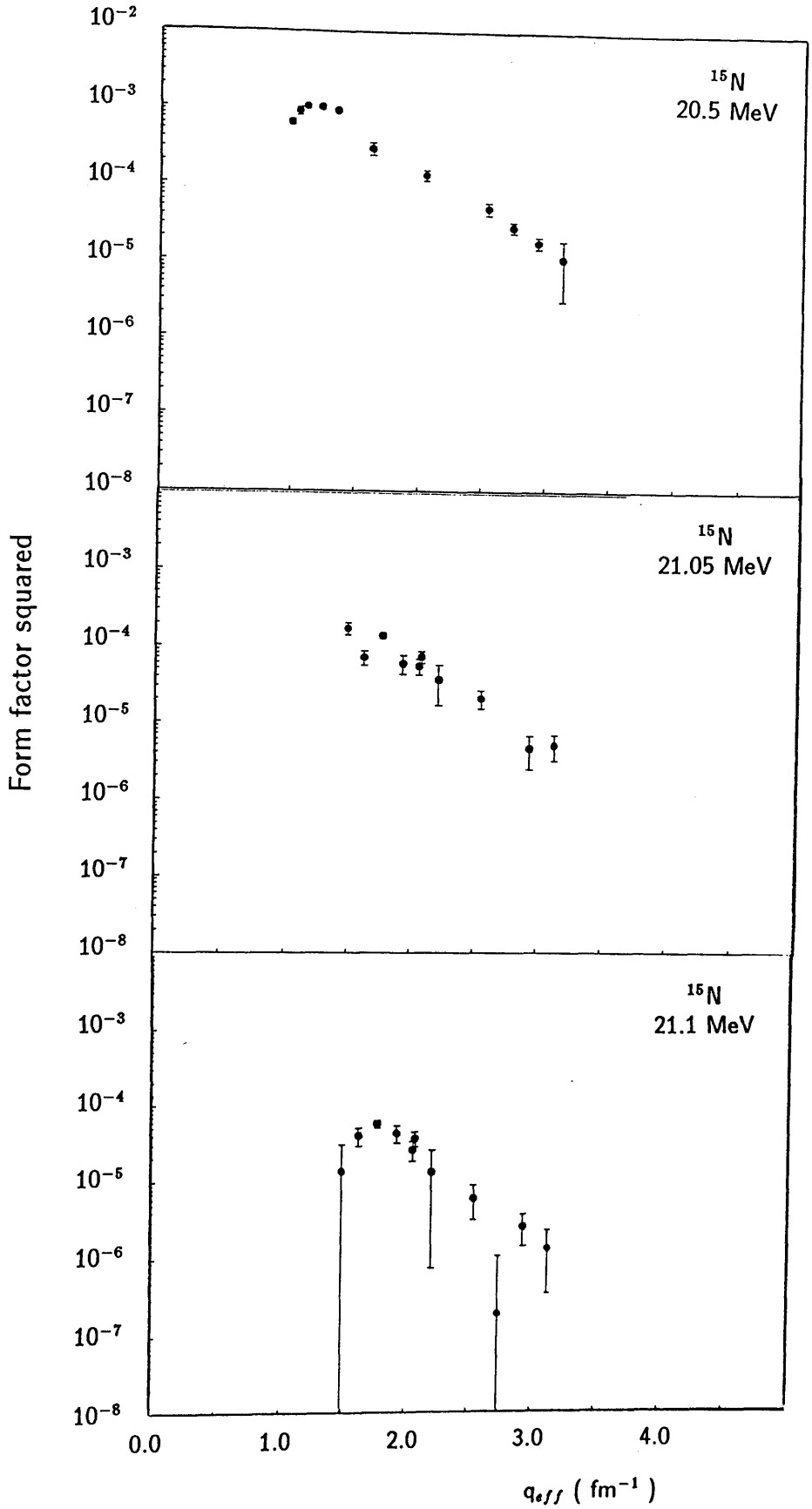

Figure 4.57: *The experimental form factors for the states at 20.5, 21.05 and 20.1 MeV.*

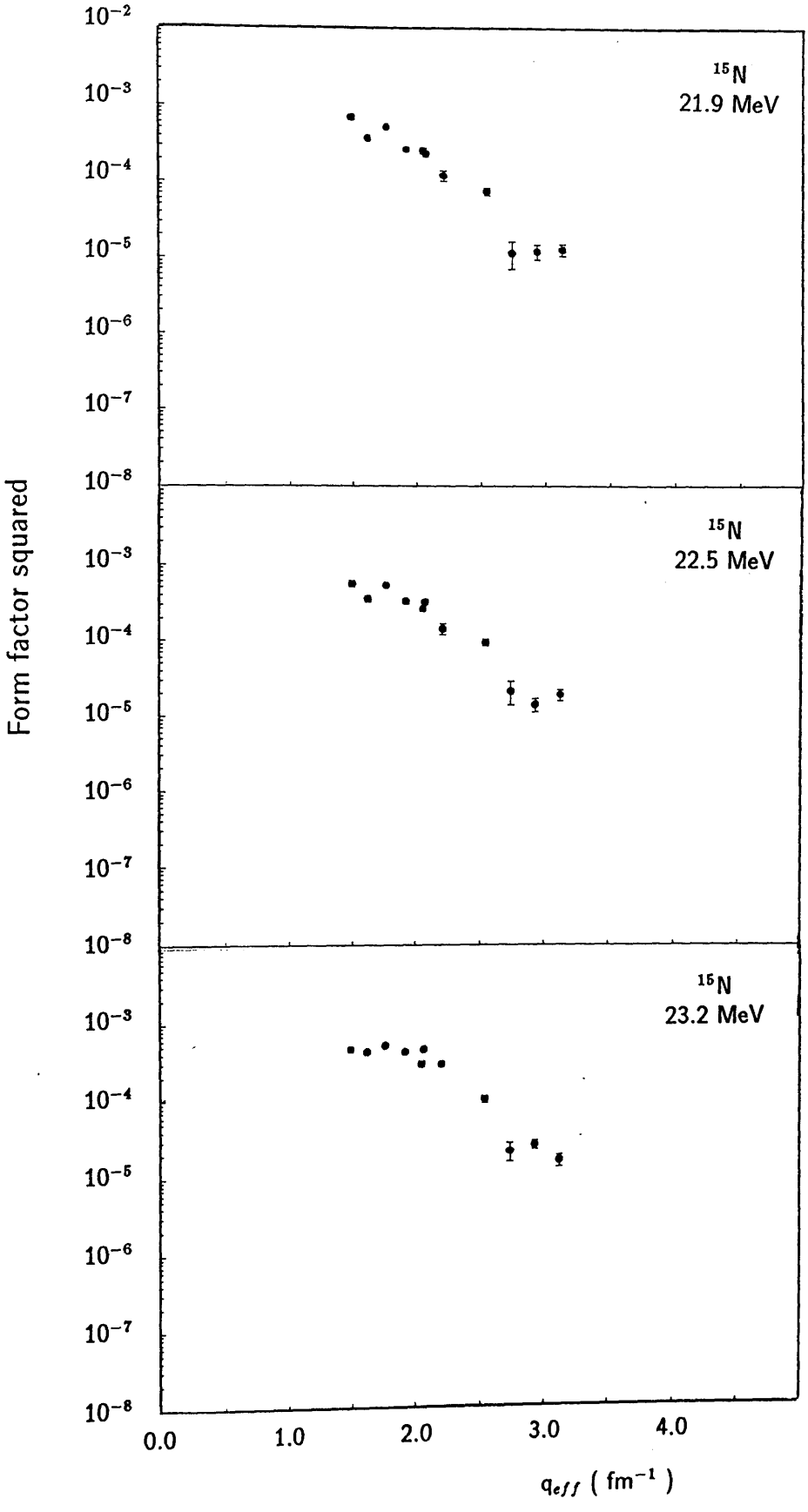

Figure 4.58: *The experimental form factors for the states at 21.9, 22.5 and 23.2 MeV.*

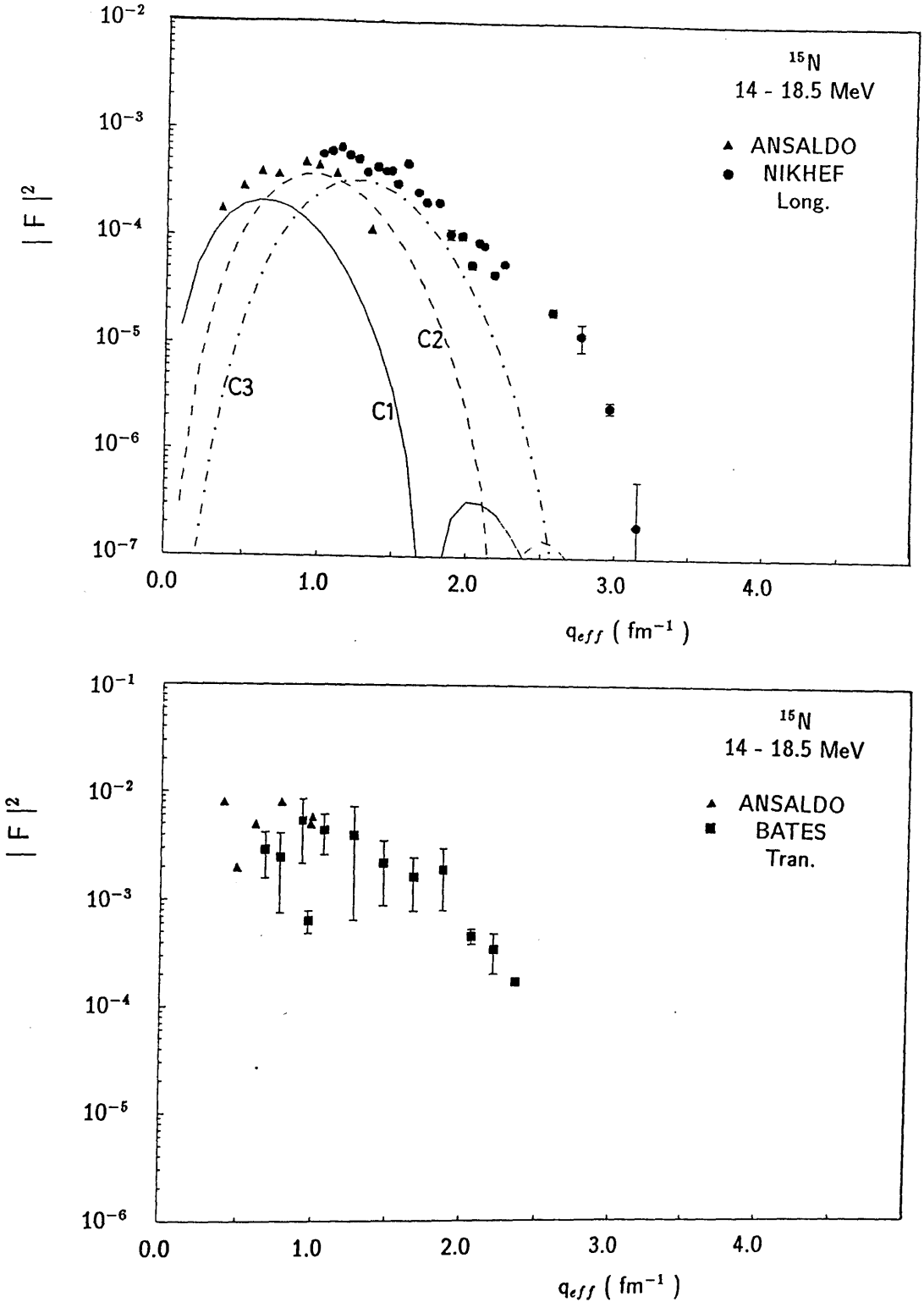

Figure 4.59: *The integrated longitudinal (upper) and transverse (lower) form factors for the region between 14-18.5 MeV with those of Ansaldo[15](solid triangles). The curves represent the Helm model C1, C2 and C3 components.*

Chapter 5

Conclusions

In this thesis, measurements of electron scattering form factors for many transitions in ^{15}N have been presented. The measurements were carried out at 70, 130, 300, and 430 MeV incident electron energy with an angular range from 40° to 98.5° covering a momentum transfer region between 0.5 and 3.2 fm^{-1}. The primary reason of this project was to study the structure of the positive parity states of the nucleus ^{15}N. The formation of such states includes 1p-2h and/or 3p-4h configurations and the amplitudes are sensitive to the particular choice of the effective interaction used in the shell model description.

The data of the present experiment together with the existing data obtained at scattering angle of 180° were used to obtain the longitudinal and transverse components of the form factors for most of the observed excitations.

The experimental longitudinal form factors were used in a DWBA model independent analysis to extract the transition charge densities for most of the positive parity states below 12 MeV of excitations. The extracted reduced transition probabilities were compared with those measured by (γ, γ')[3] for the dipole transitions. The B(EL) values for dipole transitions are found in general agreement with those measured by (γ, γ').

The longitudinal and transverse form factors were compared with the predictions of a nuclear shell model calculation performed in a $3\hbar\omega$ space. From this comparison, the following features have been revealed: the predicted form factor is always smaller than data although the experimental B(EL) values agree with theory for the C1 transitions. The shell model calculations with additive effective charge of δe_p=δe_n=0.37 for $1/2^+$ states and δe_p = δe_n=0.25 for $3/2^+$

states are only able to reproduce the longitudinal form factors for $1/2_1^+$, $3/2_1^+$ and $3/2_2^+$. A combination of effective charges for proton and neutron was also used. It was obvious that $\delta e_n > \delta e_p$. For the $7/2^+$ level at 7.57 MeV δe_n=0.385 and δe_p=0.01 were required to reproduce the experimental form factor. This approach is also not able to describe all the data. The shell model predictions for some states were found completely different from the experiment. These states are the $1/2^+$ level at 8.31 MeV, the $3/2^+$ level at 10.8 MeV and the $3/2^+$ level at 11.78. Arbitrary extension of model space by mixing with configurations which are outside of model space does not help too much. However, for the octupole transitions, a very satisfactory explanation is obtained by mixing contributions from a collective state. It is tempting to identify this state with the giant octupole transition. For the transverse form factors, the shapes are generally satisfactory compared to the data but strengths are mostly too large by a factor of 1.6.

The M4 transitions have been studied by Morris et al.[61] using (π, π') in ^{15}N. The M4 transitions identified by this experiment were those at 10.7, 12.5, 14.1, 17.2, 20.1, and 23.2 MeV. These states were excited in the present experiment except the one at 17.2 MeV. The (e,e') data were used to remove one of the two possible solutions of the spectroscopic amplitudes in the (π, π') analysis and thus better identify the nature of these states.

A large number of states beyond 13 MeV of excitation were observed in this experiment and the form factors of these states have been obtained. In the region beyond 18 MeV several new states were identified and width parameters for these states have been given.

The giant resonance region of ^{15}N has been studied with electron scattering by Ansaldo et al.[15]. The form factors of giant dipole and octupole resonances at low q($\leq$ 0.97 fm^{-1}) were obtained. In our experiment we have extended the work of Ansaldo to much higher values of momentum transfer.

The resolution in the present experiment was one of the most serious limitations. It is possible to improve resolution in (e,e') by using a thin solid target.

The high resolution coincidence (e,e'x) experiments provide an ideal probe for identification of the overlapping levels in the giant resonance region and be-

low. The x refers to a suitable decay product such as a γ-ray, proton, or alpha particle. The (e,e'γ) coincidence, in particular, can provide increased resolution over that obtained in inclusive electron scattering[74]. One example of a closely-lying doublet is of the $1/2_1^+$ and $5/2_1^+$ states. Such levels can be resolved by (e,e'γ), since the angular distribution for reaction with J=$1/2^+$ must be different from the angulardistribution function for the excitation of the $5/2^+$ state. The 9.152 MeV $3/2^-$ state lies very close to a $5/2^+$ level at 9.155 MeV so practical considerations would suggest that measurement of the electroexcitation of that level would be difficult. However, the 9.155 MeV level does not γ-decay strongly to the ground state so the two levels may be resolvable with the (e,e'γ) reaction. It should be noted that in the (e,e') experiments only two observables can in principle be extracted, F_L^2, F_T^2, and so any additional information from (e,e'γ) studies will be a step forward in trying to analyse a given electromagnetic transition into its underlying multipoles. Thus, it seems that the (e,e'γ) reaction has great potential as a tool for nuclear structure studies.

Appendix A

Data Tables

Table A-1 list the ^{15}N run parameters. Run numbers between 1 and 37 represent the parameters for the data measured at forward angles, $\theta \leq 98.5°$(NIKHEF). Run numbers from 38 to 55 are those for data measured at scattering angle of 180°(BATES). Tables A-2 through A-20 list total and longitudinal measured cross sections. The transverse form factors are listed in tables A-21 through A-30.

The total form factors were obtained from the measured cross sections according to equation 2.2. The effective momentum transfer q_{eff} was calculated using the formula given in subsec. 2.1.4.

Table A-1: ^{15}N run parameters.

Run No.	E_o(MeV) NIKHEF	Theta Deg.	q (fm^{-1})	Run No.	E_o(MeV) BATES	Theta Deg.	q (fm^{-1})
1	68.75	60.00	0.348	38	49.2	178.0	0.497
2	68.75	80.00	0.447	39	70.4	178.0	0.710
3	92.17	68.50	0.525	40	80.2	178.0	0.808
4	92.17	78.50	0.590	41	89.6	178.0	0.902
5	129.70	62.50	0.680	42	94.9	178.0	0.955
6	171.98	46.50	0.687	43	99.3	178.0	0.999
7	171.98	53.60	0.784	44	109.4	178.0	1.100
8	171.98	61.00	0.882	45	119.5	178.0	1.201
9	129.70	90.00	0.925	46	129.5	178.0	1.300
10	171.98	68.59	0.978	47	149.6	178.0	1.500
11	298.19	39.96	1.030	48	169.4	178.0	1.696
12	298.19	42.44	1.091	49	189.2	178.0	1.892
13	298.19	45.00	1.153	50	208.9	178.0	2.086
14	298.19	47.45	1.212	51	224.2	178.0	2.236
15	298.19	50.00	1.272	52	239.1	178.0	2.383
16	298.19	52.50	1.331	53	273.4	178.0	2.718
17	298.19	55.50	1.401	54	297.8	178.0	2.956
18	298.19	58.00	1.458	55	326.7	178.0	3.236
19	430.33	40.00	1.486				
20	298.19	61.50	1.537				
21	298.19	64.51	1.603				
22	430.33	45.09	1.665				
23	298.19	67.50	1.668				
24	298.19	71.04	1.743				
25	298.19	74.52	1.816				
26	298.19	78.52	1.896				
27	298.19	82.51	1.975				
28	298.19	86.54	2.051				
29	430.33	57.44	2.081				
30	298.19	90.54	2.124				
31	298.19	94.51	2.194				
32	298.19	98.52	2.262				
33	406.84	71.18	2.376				
34	430.33	73.34	2.577				
35	430.33	80.22	2.775				
36	430.33	87.51	2.973				
37	430.33	95.33	3.171				

Table A-2: Form factors for $\frac{1}{2}^+_1$ (5.30 MeV).

Run No.	q_{eff} (fm^{-1})	σ (fm^2/st)	$\mid FF \mid^2$ *Tot.*	Err (%)	$\mid FF \mid^2$ *Long.*	Err (%)
4	0.587	1.145E-10	8.702E-05	24.46	6.152E-05	49.19
5	0.681	5.589E-11	2.848E-04	11.67	2.587E-04	13.25
6	0.690	6.219E-10	1.719E-04	13.20	1.509E-04	15.59
7	0.788	2.764E-09	3.147E-04	10.10	2.877E-04	11.10
8	0.886	5.527E-09	3.844E-04	4.93	3.519E-04	5.40
10	0.983	3.818E-08	5.336E-04	5.16	4.991E-04	5.55
11	1.024	3.687E-10	5.875E-04	7.23	5.645E-04	7.53
12	1.099	6.014E-10	6.610E-04	9.15	6.338E-04	9.55
13	1.161	4.438E-09	7.480E-04	3.87	7.176E-04	4.04
14	1.221	8.461E-09	1.187E-03	6.10	1.152E-03	6.29
15	1.282	3.965E-09	7.559E-04	4.30	7.137E-04	4.57
16	1.341	2.200E-09	1.370E-03	4.56	1.322E-03	4.73
17	1.411	9.133E-10	2.262E-04	4.32	1.767E-04	5.79
18	1.469	2.634E-09	1.132E-03	4.13	1.080E-03	4.34
20	1.548	8.456E-10	8.111E-04	4.65	7.517E-04	5.03
21	1.615	7.796E-11	7.911E-04	4.56	7.217E-04	5.02
23	1.680	1.401E-09	1.475E-03	3.61	1.399E-03	3.82
24	1.756	9.684E-09	7.459E-04	6.13	6.660E-04	6.89
25	1.829	1.350E-09	5.722E-04	4.62	4.938E-04	5.45
26	1.900	1.088E-13	4.258E-04	50.14	3.487E-04	61.26
27	1.989	4.524E-09	2.950E-04	12.28	2.184E-04	16.71
28	2.066	2.413E-10	2.670E-04	15.25	1.919E-04	21.31
29	2.096	3.479E-09	4.352E-04	15.50	3.939E-04	17.13
30	2.140	1.087E-13	1.730E-04	9.76	1.020E-04	17.10
31	2.211	3.781E-09	2.082E-04	19.71	1.432E-04	28.98
32	2.270	3.556E-09	6.656E-05	18.74	4.795E-06	295.25
34	2.595	2.774E-09	2.675E-05	48.37	1.049E-05	123.64
35	2.794	8.709E-09	1.499E-05	31.90	5.777E-06	83.37
36	2.994	8.677E-13	5.957E-06	330.28	8.543E-07	300.00
37	3.193	1.087E-13	3.085E-06	202.06	7.738E-08	300.00

Table A-3: Form factors for $\frac{1}{2}^+_2$ (8.31 MeV)

Run No.	q_{eff} (fm^{-1})	σ (fm^2/st)	$\mid FF \mid^2$	Err (%)
5	0.673	1.145E-10	4.286E-05	38.51
6	0.684	5.589E-11	3.831E-05	23.45
7	0.780	1.544E-10	3.337E-05	28.50
8	0.878	6.577E-11	6.009E-05	7.04
9	0.915	8.916E-15	1.688E-05	263.85
10	0.974	7.172E-11	7.848E-05	7.04
11	1.019	1.135E-10	9.291E-05	7.85
12	1.093	1.397E-10	1.292E-04	8.84
13	1.155	2.994E-07	1.197E-04	3.74
14	1.214	1.018E-07	1.643E-04	7.72
15	1.275	1.388E-06	1.427E-04	3.68
16	1.334	8.562E-07	1.510E-04	5.40
17	1.404	2.826E-07	1.350E-04	3.57
18	1.461	3.186E-09	1.263E-04	4.74
20	1.540	2.963E-07	1.182E-04	4.04
21	1.607	4.138E-09	1.025E-04	4.81
22	1.670	1.548E-07	9.187E-05	84.22
23	1.672	7.661E-07	1.041E-04	5.71
24	1.747	1.618E-12	7.339E-05	6.49
25	1.820	5.548E-11	5.375E-05	5.02
26	1.890	4.580E-07	3.676E-05	10.98
27	1.979	1.501E-07	2.515E-05	10.53
28	2.056	3.741E-07	1.637E-05	20.66
29	2.088	3.474E-12	9.247E-06	25.67
30	2.129	3.033E-07	6.292E-06	20.11
31	2.199	6.892E-07	1.266E-05	29.10
32	2.259	6.180E-07	2.564E-06	36.32
33	2.384	1.610E-08	1.238E-06	115.06
34	2.585	2.043E-07	5.040E-07	300.00
35	2.784	9.703E-09	9.796E-07	37.64
36	2.983	5.202E-08	8.666E-07	40.97
37	3.182	9.308E-07	6.930E-07	46.16

Table A-4: Form factors for $\frac{1}{2}^{+}_{3}$ (9.05 MeV)

Run No.	q_{eff} (fm^{-1})	σ (fm^2/st)	$\mid FF \mid^2$	Err (%)
5	0.671	1.145E-10	3.338E-05	45.18
6	0.682	5.589E-11	3.180E-05	26.76
7	0.779	1.544E-10	4.895E-05	19.65
8	0.876	6.577E-11	4.808E-05	8.19
9	0.912	8.916E-15	5.711E-06	300.00
10	0.972	7.172E-11	5.602E-05	8.66
11	1.017	1.135E-10	6.634E-05	9.75
12	1.092	3.468E-11	8.716E-05	11.11
13	1.154	4.231E-15	8.528E-05	4.17
14	1.213	2.914E-11	1.243E-04	9.14
15	1.274	3.438E-07	1.063E-04	4.04
16	1.332	8.562E-07	1.157E-04	6.52
17	1.402	2.826E-07	1.009E-04	3.85
18	1.459	3.186E-09	1.116E-04	5.20
20	1.538	2.963E-07	1.126E-04	4.25
21	1.605	4.138E-09	8.789E-05	5.21
22	1.669	1.548E-07	9.227E-05	10.80
23	1.670	7.661E-07	8.646E-05	4.67
24	1.745	1.618E-12	7.131E-05	6.90
25	1.817	5.548E-11	7.201E-05	4.70
26	1.888	4.580E-07	5.883E-05	9.02
27	1.976	1.501E-07	5.117E-05	7.90
28	2.053	3.741E-07	4.008E-05	13.32
29	2.086	3.474E-12	2.671E-05	16.45
30	2.126	3.033E-07	3.696E-05	7.21
31	2.196	6.892E-07	3.727E-05	16.84
32	2.256	6.180E-07	2.213E-05	9.66
33	2.382	1.610E-08	1.490E-05	17.13
34	2.583	2.043E-07	7.231E-06	23.34
35	2.782	9.703E-09	2.822E-06	35.39
36	2.980	5.202E-08	1.725E-06	34.30
37	3.179	9.308E-07	1.446E-07	300.00

Table A-5: Form factors for $\frac{1^+}{24}$ (11.44 MeV)

Run No.	q_{eff} (fm^{-1})	σ (fm^2/st)	$\mid FF \mid^2$ *Tot.*	Err (%)	$\mid FF \mid^2$ *Long.*	Err (%)
5	0.664	1.145E-10	1.037E-05	126.57	3.886E-06	300.00
6	0.677	5.589E-11	1.157E-05	113.67	6.392E-06	206.06
7	0.773	1.544E-10	4.693E-05	29.06	4.065E-05	33.67
8	0.869	6.577E-11	2.893E-05	18.04	2.125E-05	25.84
9	0.903	8.916E-15	3.902E-05	130.57	2.502E-05	204.01
10	0.965	7.172E-11	5.128E-05	13.41	3.965E-05	18.48
11	1.013	1.135E-10	4.067E-05	20.32	3.049E-05	27.83
12	1.087	3.468E-11	8.790E-05	14.67	7.830E-05	16.70
13	1.149	4.231E-15	8.232E-05	4.99	7.191E-05	6.71
14	1.208	7.236E-12	1.105E-04	11.98	9.902E-05	13.69
15	1.268	6.526E-11	1.070E-04	4.56	9.447E-05	6.26
16	1.327	2.026E-13	9.729E-05	8.96	8.316E-05	11.22
17	1.396	7.469E-19	1.184E-04	4.06	1.018E-04	5.48
18	1.453	7.145E-11	1.192E-04	5.81	1.005E-04	7.29
20	1.532	2.842E-13	1.158E-04	4.63	9.553E-05	6.26
21	1.598	2.743E-11	9.393E-05	6.50	7.397E-05	9.76
22	1.664	6.740E-15	8.278E-05	11.29	6.888E-05	14.58
23	1.663	8.643E-12	8.970E-05	5.05	7.010E-05	9.79
24	1.738	6.405E-14	7.516E-05	9.61	5.426E-05	17.76
25	1.810	1.053E-10	5.796E-05	6.05	3.439E-05	23.72
26	1.880	2.099E-11	5.251E-05	16.18	2.598E-05	46.18
27	1.968	1.391E-14	4.465E-05	10.36	1.341E-05	69.25
28	2.044	2.282E-13	2.417E-05	136.75	1.000E-10	300.00
29	2.080	2.071E-10	2.339E-05	24.09	1.987E-06	300.00
30	2.117	3.537E-07	3.113E-05	12.22	1.000E-10	300.00
32	2.246	6.180E-07	1.849E-05	16.66	1.000E-10	300.00
33	2.375	1.610E-08	1.168E-05	25.81	4.186E-06	132.36
34	2.576	2.043E-07	3.616E-06	55.38	1.000E-10	300.00

Table A-6: Form factors for $\frac{1}{2}^{+}_{5}$ (11.61 MeV)

Run No.	q_{eff} (fm^{-1})	σ (fm^2/st)	$\mid FF \mid^2$	Err (%)
5	0.664	1.145E-10	7.305E-04	6.49
6	0.677	5.589E-11	2.282E-04	18.84
7	0.772	1.544E-10	4.903E-05	87.65
8	0.869	6.577E-11	2.820E-05	52.88
10	0.964	8.916E-15	6.039E-11	300.00
11	1.013	7.172E-11	5.509E-05	37.40
12	1.087	1.135E-10	3.213E-13	300.00
13	1.149	3.468E-11	2.323E-20	0.00
14	1.208	4.231E-15	2.670E-05	101.61
15	1.268	7.236E-12	2.881E-09	300.00
16	1.326	6.526E-11	2.941E-05	59.32
17	1.396	2.026E-13	3.532E-20	0.00
18	1.453	7.469E-19	1.169E-05	101.43
20	1.531	7.145E-11	4.164E-09	300.00
21	1.598	2.842E-13	2.453E-05	44.64
23	1.662	2.743E-11	1.376E-05	62.28
24	1.737	6.740E-15	3.747E-05	32.97
25	1.809	8.643E-12	5.505E-05	15.20
26	1.879	6.405E-14	8.694E-05	16.76
27	1.968	1.053E-10	3.720E-05	27.02
28	2.044	2.099E-11	6.662E-05	25.03
29	2.080	1.391E-14	2.965E-05	43.29
30	2.117	2.282E-13	3.919E-05	19.91
31	2.187	5.142E-11	8.136E-05	29.67
32	2.246	1.579E-12	1.579E-05	44.18
34	2.575	3.556E-09	8.163E-06	51.84
35	2.773	2.774E-09	1.193E-06	218.40
36	2.971	8.709E-09	3.939E-06	43.85
37	3.169	8.677E-13	7.835E-09	300.00

Table A-7: Form factors for $\frac{3}{21}^{+}$ (7.30 MeV)

Run No.	q_{eff} (fm^{-1})	σ (fm^2/st)	$\mid FF \mid^2$ *Tot.*	Err (%)	$\mid FF \mid^2$ *Long.*	Err (%)
5	0.676	1.145E-10	2.573E-04	8.39	2.556E-04	8.46
6	0.686	5.589E-11	2.563E-04	5.70	2.550E-04	5.74
7	0.783	1.544E-10	3.477E-04	5.09	3.456E-04	5.13
8	0.881	6.577E-11	3.429E-04	3.55	3.412E-04	3.59
9	0.919	8.916E-15	3.409E-04	15.56	3.391E-04	15.65
10	0.977	2.889E-10	4.325E-04	3.61	4.306E-04	3.64
11	1.020	4.387E-07	4.683E-04	3.92	4.666E-04	3.94
12	1.095	1.018E-09	5.595E-04	4.53	5.542E-04	4.58
13	1.158	2.994E-07	5.634E-04	3.16	5.575E-04	3.21
14	1.217	1.018E-07	6.803E-04	4.45	6.755E-04	4.50
15	1.277	1.388E-06	5.759E-04	3.13	5.688E-04	3.20
16	1.336	8.562E-07	5.493E-04	3.75	5.393E-04	3.84
17	1.406	2.826E-07	5.551E-04	3.19	5.409E-04	3.32
18	1.464	3.186E-09	4.840E-04	3.51	4.661E-04	3.70
20	1.543	2.963E-07	4.935E-04	3.23	4.709E-04	3.45
21	1.610	4.138E-09	4.080E-04	3.52	3.832E-04	3.85
22	1.672	1.548E-07	3.449E-04	9.02	3.256E-04	9.59
23	1.675	7.661E-07	3.014E-04	4.59	2.743E-04	5.21
24	1.750	1.618E-12	2.967E-04	3.98	2.663E-04	4.68
25	1.823	5.548E-11	2.360E-04	3.53	2.019E-04	4.72
26	1.894	4.580E-07	1.756E-04	5.29	1.373E-04	7.80
27	1.982	1.501E-07	1.337E-04	5.22	9.668E-05	9.32
28	2.059	3.741E-07	8.590E-05	8.41	5.186E-05	18.02
29	2.091	3.474E-12	7.210E-05	10.74	5.396E-05	15.63
30	2.133	3.033E-07	6.502E-05	5.54	3.333E-05	20.81
31	2.203	6.892E-07	4.536E-05	13.71	1.448E-05	57.33
32	2.263	6.180E-07	3.514E-05	7.56	5.277E-06	107.71
33	2.387	1.610E-08	1.855E-05	14.15	7.767E-06	37.62
34	2.588	2.043E-07	7.025E-06	18.35	1.316E-06	121.15
35	2.787	9.703E-09	4.223E-06	20.18	2.401E-06	48.88
36	2.987	5.202E-08	2.508E-06	24.29	2.423E-06	25.39
37	3.186	9.308E-07	1.433E-06	34.41	1.331E-06	37.84

Table A-8: Form factors for $\frac{3}{2}^+_2$ (8.57 MeV)

Run No.	q_{eff} (fm^{-1})	σ (fm^2/st)	$\mid FF \mid^2$ *Tot.*	Err (%)	$\mid FF \mid^2$ *Long.*	Err (%)
5	0.672	1.145E-10	7.054E-05	22.70	4.694E-05	34.13
6	0.683	5.589E-11	6.750E-05	14.12	4.941E-05	19.32
7	0.780	1.544E-10	3.864E-05	24.45	2.362E-05	40.48
8	0.877	6.577E-11	4.748E-05	8.27	3.081E-05	14.46
10	0.973	7.172E-11	4.638E-05	10.05	2.674E-05	18.29
11	1.018	1.135E-10	5.341E-05	11.35	3.947E-05	15.73
12	1.093	3.468E-11	5.786E-05	14.79	4.226E-05	20.40
13	1.155	1.704E-14	4.581E-05	5.33	3.028E-05	8.87
14	1.214	1.018E-07	5.373E-05	15.23	3.889E-05	21.32
15	1.275	1.388E-06	4.196E-05	5.86	2.879E-05	9.59
16	1.333	8.562E-07	3.978E-05	11.46	2.798E-05	16.95
17	1.403	2.826E-07	2.955E-05	6.04	1.879E-05	12.92
18	1.460	3.186E-09	3.337E-05	9.47	2.353E-05	15.78
20	1.539	2.963E-07	1.951E-05	10.20	1.053E-05	28.65
21	1.606	4.138E-09	2.188E-05	10.99	1.283E-05	26.18
22	1.670	1.548E-07	1.519E-05	22.93	8.699E-06	44.68
23	1.671	7.661E-07	1.908E-05	9.31	9.952E-06	30.22
24	1.746	1.618E-12	1.204E-05	21.08	3.339E-06	108.37
25	1.819	5.548E-11	5.919E-06	20.51	1.000E-10	300.00
26	1.889	4.580E-07	5.628E-06	42.33	1.000E-10	300.00
27	1.978	1.501E-07	3.656E-06	40.75	1.000E-10	300.00
28	2.055	3.741E-07	3.163E-06	71.92	1.000E-10	300.00
29	2.088	3.474E-12	3.251E-06	55.73	1.000E-10	300.00
30	2.128	3.033E-07	1.064E-06	87.36	1.000E-10	300.00
31	2.198	6.892E-07	2.819E-06	85.80	1.000E-10	300.00
32	2.258	6.180E-07	2.085E-06	39.42	1.000E-10	300.00
33	2.384	1.610E-08	2.019E-06	73.50	1.000E-10	300.00
34	2.585	2.043E-07	4.006E-07	114.02	1.000E-10	300.00
35	2.783	9.703E-09	5.442E-07	56.42	5.433E-07	56.51
36	2.982	5.202E-08	2.496E-12	300.00	1.000E-10	105.25
37	3.181	9.308E-07	8.454E-11	300.00	1.000E-10	300.00

Table A-9: Form factors for $\frac{3}{23}^+$ (10.07 MeV)

Run No.	q_{eff} (fm^{-1})	σ (fm^2/st)	$\mid FF \mid^2$	Err (%)
3	0.507	1.145E-10	1.195E-04	9.30
4	0.570	5.589E-11	1.280E-04	9.89
5	0.668	1.544E-10	2.574E-04	4.95
6	0.680	6.577E-11	1.708E-04	6.99
7	0.776	8.916E-15	2.097E-04	6.53
8	0.873	7.172E-11	1.488E-04	4.41
9	0.908	1.135E-10	1.941E-04	19.14
10	0.969	3.468E-11	1.531E-04	4.94
11	1.015	4.231E-15	1.795E-04	5.50
12	1.090	7.236E-12	1.594E-04	7.92
13	1.152	6.526E-11	1.478E-04	3.60
14	1.211	2.026E-13	1.856E-04	7.35
15	1.271	7.469E-19	1.328E-04	3.76
16	1.330	7.145E-11	1.280E-04	5.90
17	1.400	2.842E-13	9.592E-05	3.81
18	1.457	1.105E-10	8.907E-05	5.46
20	1.535	2.173E-07	7.118E-05	4.77
21	1.602	7.661E-07	5.842E-05	6.04
22	1.667	1.618E-12	5.347E-05	11.73
23	1.667	5.548E-11	4.356E-05	5.59
24	1.742	4.580E-07	3.043E-05	10.35
25	1.814	1.501E-07	2.606E-05	6.97
26	1.884	3.741E-07	1.718E-05	18.06
27	1.973	3.474E-12	1.266E-05	16.07
28	2.049	3.033E-07	8.247E-06	36.36
29	2.084	6.892E-07	6.878E-06	36.84
30	2.123	6.180E-07	5.583E-06	22.32
31	2.192	1.610E-08	4.192E-06	72.29
32	2.252	2.043E-07	3.361E-06	31.25
33	2.379	9.703E-09	2.838E-06	55.79
34	2.580	5.202E-08	1.658E-06	58.74
35	2.778	9.308E-07	6.324E-07	86.59
36	2.977	3.534E-07	9.173E-07	41.97
37	3.175	2.546E-07	5.481E-07	79.48

Table A-10: Form factors for $\frac{3}{2}^{+}_{4}$ (10.8 MeV)

Run No.	q_{eff} (fm^{-1})	σ (fm^2/st)	$\mid FF \mid^2$	Err (%)
3	0.505	1.145E-10	2.979E-05	28.87
5	0.666	5.589E-11	1.008E-04	10.02
6	0.678	1.544E-10	3.404E-06	218.54
7	0.774	6.577E-11	3.723E-09	300.00
8	0.871	8.916E-15	7.464E-07	300.00
9	0.906	7.172E-11	1.732E-05	209.83
10	0.967	1.135E-10	4.136E-18	300.00
11	1.014	3.468E-11	2.358E-05	22.95
12	1.089	4.231E-15	1.983E-05	36.32
13	1.151	7.236E-12	1.969E-05	10.75
14	1.209	6.526E-11	1.921E-05	38.51
15	1.270	2.026E-13	2.769E-05	8.78
16	1.328	7.469E-19	1.697E-05	31.28
17	1.398	7.145E-11	1.983E-05	9.52
18	1.455	2.842E-13	2.977E-05	13.01
20	1.533	2.743E-11	2.262E-05	11.63
21	1.600	6.740E-15	2.325E-05	13.29
22	1.665	8.643E-12	6.104E-06	85.30
23	1.665	6.405E-14	1.591E-05	14.40
24	1.740	1.053E-10	2.588E-05	14.86
25	1.812	8.454E-11	1.590E-05	12.86
26	1.882	6.906E-08	1.059E-05	39.23
27	1.970	3.741E-07	9.176E-06	30.44
28	2.047	3.474E-12	1.085E-05	45.98
29	2.082	3.033E-07	2.987E-09	300.00
30	2.120	6.892E-07	6.808E-06	28.33
31	2.190	6.180E-07	4.478E-06	123.37
32	2.249	1.610E-08	6.119E-06	29.36
33	2.377	2.043E-07	4.531E-06	55.01
34	2.578	9.703E-09	3.383E-06	45.33
35	2.776	5.202E-08	2.376E-06	44.10
36	2.974	9.308E-07	1.043E-07	300.00
37	3.173	3.534E-07	4.194E-07	151.01

Table A-11: Form factors for $\frac{3}{2}^+_5$ (11.78 MeV)

Run No.	q_{eff} (fm^{-1})	σ (fm^2/st)	$\mid FF \mid^2$	Err (%)
5	0.663	1.145E-10	7.113E-05	20.09
6	0.676	5.589E-11	1.219E-04	13.48
7	0.772	1.544E-10	1.341E-04	12.17
8	0.868	6.577E-11	1.080E-04	6.64
9	0.902	8.916E-15	1.257E-04	46.77
10	0.964	7.172E-11	1.222E-04	7.53
11	1.012	1.135E-10	1.112E-04	10.48
12	1.087	3.468E-11	1.509E-04	11.21
13	1.149	4.231E-15	1.254E-04	4.57
14	1.207	7.236E-12	1.233E-04	13.01
15	1.268	6.526E-11	1.015E-04	5.33
16	1.326	2.026E-13	1.087E-04	10.36
17	1.395	7.469E-19	7.833E-05	5.64
18	1.452	7.145E-11	9.819E-05	8.11
20	1.531	2.842E-13	8.864E-05	6.15
21	1.597	2.743E-11	5.793E-05	9.90
22	1.663	6.740E-15	5.220E-05	25.84
23	1.662	8.643E-12	4.887E-05	7.79
24	1.737	6.405E-14	4.961E-05	12.40
25	1.809	1.053E-10	3.996E-05	8.90
26	1.879	2.099E-11	1.894E-05	33.49
27	1.967	1.391E-14	2.499E-05	18.66
28	2.043	2.282E-13	2.819E-05	28.33
29	2.080	5.142E-11	1.452E-05	50.42
30	2.116	3.921E-13	2.046E-05	15.50
31	2.186	2.821E-10	3.300E-07	300.00
32	2.245	2.706E-07	2.252E-05	14.27
33	2.374	1.610E-08	1.269E-05	29.14
34	2.575	2.043E-07	3.282E-06	83.79
35	2.773	9.703E-09	5.310E-06	48.34
36	2.971	5.202E-08	3.332E-11	300.00
37	3.169	9.308E-07	1.399E-06	108.99

Table A-12: Form factors for $\frac{3}{2}^+_6$ (13.39 MeV)

Run No.	q_{eff} (fm^{-1})	σ (fm^2/st)	$\mid FF \mid^2$	Err (%)
5	0.659	1.145E-10	1.618E-04	9.41
6	0.673	5.589E-11	7.179E-05	19.64
7	0.768	1.544E-10	8.840E-05	21.01
8	0.864	6.577E-11	4.702E-05	12.50
10	0.959	8.916E-15	5.427E-05	13.42
11	1.010	7.172E-11	5.444E-05	15.68
12	1.084	1.135E-10	3.844E-05	29.94
13	1.145	3.468E-11	4.664E-05	6.96
14	1.204	4.231E-15	4.217E-05	26.97
15	1.264	7.236E-12	3.389E-05	9.42
16	1.322	6.526E-11	5.272E-05	18.32
17	1.391	2.026E-13	3.029E-05	10.89
18	1.448	7.469E-19	2.494E-05	23.72
21	1.593	7.145E-11	1.971E-05	23.78
23	1.657	2.842E-13	9.229E-06	34.47
24	1.732	2.743E-11	1.174E-05	300.00
25	1.804	6.740E-15	1.377E-05	21.54
26	1.874	8.643E-12	1.288E-05	85.82
27	1.962	6.405E-14	1.124E-05	28.72
28	2.037	1.053E-10	9.933E-08	300.00
29	2.076	2.099E-11	1.057E-05	74.92
30	2.110	1.391E-14	2.197E-06	139.46
31	2.180	2.282E-13	1.075E-05	83.18
32	2.239	5.142E-11	6.375E-06	45.64
34	2.570	3.921E-13	5.307E-11	300.00
35	2.767	7.003E-11	8.156E-07	298.66
36	2.965	4.704E-13	1.670E-08	300.00
37	3.163	1.961E-11	3.509E-09	300.00

Table A-13: Form factors for $\frac{5}{21}^+$ (5.27 MeV)

Run No.	q_{eff} (fm^{-1})	σ (fm^2/st)	$\mid FF \mid^2$ *Tot.*	Err (%)	$\mid FF \mid^2$ *Long.*	Err (%)
4	0.589	1.145E-10	1.845E-04	11.04	1.616E-04	19.67
5	0.684	2.251E-10	2.752E-04	11.26	2.523E-04	13.16
6	0.692	8.068E-06	3.072E-04	8.02	2.887E-04	9.08
7	0.790	4.333E-07	7.292E-04	5.35	7.035E-04	5.58
8	0.889	1.942E-06	7.588E-04	3.69	7.269E-04	3.86
9	0.930	6.921E-06	1.492E-03	5.37	1.435E-03	5.59
10	0.986	4.387E-07	1.056E-03	3.73	1.021E-03	3.87
11	1.025	1.018E-09	1.259E-03	4.39	1.236E-03	4.47
12	1.100	2.994E-07	1.568E-03	4.90	1.541E-03	4.99
13	1.163	1.018E-07	1.593E-03	3.26	1.562E-03	3.33
14	1.222	1.388E-06	1.388E-03	5.49	1.353E-03	5.63
15	1.283	8.562E-07	1.868E-03	3.25	1.826E-03	3.33
16	1.343	2.826E-07	1.106E-03	5.15	1.058E-03	5.39
17	1.413	3.186E-09	2.492E-03	3.13	2.441E-03	3.19
18	1.471	2.963E-07	1.344E-03	3.88	1.291E-03	4.04
20	1.550	4.138E-09	1.748E-03	3.44	1.689E-03	3.57
21	1.617	1.548E-07	1.415E-03	3.64	1.349E-03	3.83
22	1.676	7.661E-07	2.010E-03	8.65	1.957E-03	8.89
23	1.683	1.618E-12	5.045E-04	6.10	4.301E-04	7.21
24	1.759	5.548E-11	1.001E-03	5.04	9.213E-04	5.50
25	1.831	4.580E-07	8.269E-04	3.93	7.486E-04	4.39
26	1.903	1.501E-07	6.331E-04	33.82	5.563E-04	38.50
27	1.992	3.741E-07	5.424E-04	7.40	4.670E-04	8.66
28	2.069	3.474E-12	3.608E-04	11.65	2.869E-04	14.72
29	2.095	3.033E-07	1.046E-04	54.88	6.355E-05	90.40
30	2.143	6.892E-07	3.087E-04	6.29	2.376E-04	8.35
31	2.213	6.180E-07	1.210E-04	33.11	5.514E-05	73.34
32	2.273	1.610E-08	1.617E-04	8.82	1.003E-04	15.65
33	2.393	2.043E-07	1.508E-04	8.86	1.230E-04	10.97
34	2.594	9.703E-09	1.597E-05	71.58	1.000E-10	300.00
35	2.793	5.202E-08	1.948E-11	300.00	1.000E-10	300.00

Table A-14: Form factors for $\frac{5^+}{2_2}$ (7.15 MeV)

Run No.	q_{eff} (fm^{-1})	σ (fm^2/st)	$\mid FF \mid^2$ *Tot.*	Err (%)	$\mid FF \mid^2$ *Long.*	Err (%)
5	0.679	1.145E-10	3.791E-05	42.16	3.771E-05	42.39
6	0.688	5.589E-11	1.645E-05	54.61	1.602E-05	56.12
7	0.785	1.544E-10	2.764E-05	35.83	2.405E-05	41.33
8	0.884	6.577E-11	5.260E-05	8.04	4.489E-05	9.97
9	0.923	3.591E-14	1.687E-08	300.00	1.000E-10	300.00
10	0.980	6.921E-06	6.970E-05	7.83	6.001E-05	9.37
11	1.022	4.387E-07	7.993E-05	8.96	7.519E-05	9.65
12	1.097	1.018E-09	9.259E-05	11.03	8.530E-05	12.04
13	1.159	2.994E-07	9.919E-05	3.98	9.094E-05	4.72
14	1.218	1.018E-07	1.328E-04	8.84	1.242E-04	9.70
15	1.279	1.388E-06	1.141E-04	3.93	1.022E-04	4.98
16	1.338	8.562E-07	1.317E-04	5.94	1.177E-04	6.93
17	1.408	2.826E-07	1.251E-04	3.65	1.110E-04	4.69
18	1.466	3.186E-09	1.241E-04	4.84	1.099E-04	5.99
20	1.545	2.963E-07	1.230E-04	4.03	1.090E-04	5.27
21	1.612	4.138E-09	1.164E-04	4.61	1.032E-04	5.97
22	1.672	1.548E-07	1.113E-04	9.95	1.024E-04	11.03
23	1.677	7.661E-07	1.037E-04	4.12	9.125E-05	5.81
24	1.753	1.618E-12	9.508E-05	5.77	8.360E-05	7.75
25	1.826	5.548E-11	8.563E-05	4.29	7.501E-05	7.15
26	1.896	4.580E-07	6.850E-05	7.83	5.887E-05	11.81
27	1.985	1.501E-07	6.174E-05	6.77	5.230E-05	11.97
28	2.062	3.741E-07	4.797E-05	11.11	3.852E-05	18.65
29	2.090	3.474E-12	3.301E-05	14.00	2.773E-05	19.34
30	2.136	3.033E-07	3.110E-05	7.38	2.222E-05	24.49
31	2.206	6.892E-07	1.955E-05	21.82	1.211E-05	54.09
32	2.266	6.180E-07	1.720E-05	10.31	1.093E-05	48.53
33	2.388	1.610E-08	9.277E-06	21.10	6.321E-06	46.88
34	2.588	2.043E-07	2.299E-06	31.09	1.221E-07	300.00
35	2.787	9.703E-09	4.945E-07	79.32	1.000E-10	300.00
36	2.986	5.202E-08	2.201E-07	105.50	7.843E-08	300.00
37	3.185	9.308E-07	1.782E-10	300.00	1.000E-10	300.00

Table A-15: Form factors for $\frac{5}{2}^+_3$ (9.15 MeV)

Run No.	q_{eff} (fm^{-1})	σ (fm^2/st)	$\mid FF \mid^2$ *Tot.*	Err (%)	$\mid FF \mid^2$ *Long.*	Err (%)
3	0.513	1.145E-10	3.313E-06	257.38	1.000E-10	300.00
4	0.576	5.589E-11	5.363E-05	20.79	3.172E-05	35.31
5	0.673	1.544E-10	8.628E-05	19.18	7.164E-05	23.15
6	0.684	6.577E-11	1.129E-04	9.48	1.015E-04	10.58
7	0.781	8.916E-15	1.509E-04	8.26	1.397E-04	8.97
8	0.878	7.172E-11	1.532E-04	4.43	1.401E-04	5.02
9	0.915	1.135E-10	1.705E-04	28.65	1.467E-04	33.37
10	0.974	3.468E-11	2.011E-04	4.52	1.856E-04	4.98
11	1.018	4.231E-15	2.412E-04	5.18	2.285E-04	5.51
12	1.093	7.236E-12	3.070E-04	5.99	2.884E-04	6.45
13	1.155	2.628E-10	2.978E-04	3.37	2.781E-04	3.76
14	1.214	1.028E-06	3.256E-04	6.16	3.058E-04	6.63
15	1.275	2.826E-07	3.198E-04	3.37	2.999E-04	3.73
16	1.334	3.186E-09	3.563E-04	4.61	3.351E-04	4.98
17	1.404	2.963E-07	3.439E-04	3.34	3.194E-04	3.69
18	1.461	4.138E-09	3.117E-04	4.03	2.841E-04	4.51
20	1.540	1.548E-07	3.365E-04	3.47	3.045E-04	3.92
21	1.606	7.661E-07	2.766E-04	3.93	2.408E-04	4.65
22	1.668	1.618E-12	2.823E-04	9.52	2.541E-04	10.61
23	1.671	5.548E-11	2.643E-04	3.65	2.244E-04	4.48
24	1.747	4.580E-07	2.242E-04	4.70	1.811E-04	6.08
25	1.819	1.501E-07	2.012E-04	3.80	1.564E-04	5.42
26	1.890	3.741E-07	1.562E-04	6.42	1.094E-04	9.93
27	1.979	3.474E-12	1.363E-04	6.00	8.972E-05	10.17
28	2.055	3.033E-07	1.059E-04	9.25	5.992E-05	17.52
29	2.085	6.892E-07	7.542E-05	12.40	4.998E-05	19.16
30	2.129	6.180E-07	8.337E-05	5.72	4.029E-05	15.50
31	2.199	1.610E-08	6.595E-05	14.75	2.877E-05	37.84
32	2.258	2.043E-07	4.574E-05	7.89	1.238E-05	52.16
33	2.382	9.703E-09	2.840E-05	15.41	9.877E-06	46.54
34	2.582	5.202E-08	7.271E-06	37.57	1.000E-10	300.00
35	2.780	9.308E-07	5.184E-06	34.23	1.000E-10	300.00
36	2.979	3.534E-07	7.311E-07	94.12	3.061E-07	264.21
37	3.178	2.546E-07	1.304E-06	62.16	7.926E-07	120.93

Table A-16: Form factors for $\frac{5}{2}^+_4$ (10.53 MeV)

Run No.	q_{eff} (fm^{-1})	σ (fm^2/st)	$\mid FF \mid^2$	Err (%)
3	0.508	1.145E-10	4.140E-05	21.68
5	0.669	5.589E-11	9.689E-05	9.91
6	0.681	1.544E-10	1.930E-05	41.53
7	0.777	6.577E-11	1.860E-05	45.93
8	0.875	8.916E-15	1.473E-20	0.00
9	0.910	7.172E-11	3.779E-05	97.62
11	1.016	3.468E-11	2.315E-05	22.27
12	1.090	4.231E-15	3.013E-05	23.91
13	1.153	7.236E-12	2.531E-05	7.75
14	1.211	6.526E-11	2.613E-05	26.03
15	1.272	2.026E-13	3.720E-05	6.27
16	1.331	7.469E-19	4.228E-05	11.51
17	1.400	7.145E-11	2.788E-05	6.38
18	1.457	2.842E-13	3.621E-05	9.00
20	1.536	2.743E-11	4.104E-05	6.23
21	1.603	6.740E-15	3.787E-05	7.44
22	1.665	8.643E-12	2.652E-05	16.39
23	1.667	2.580E-13	3.621E-05	6.18
24	1.743	1.253E-07	3.699E-05	9.11
25	1.815	4.580E-07	3.220E-05	6.30
26	1.885	1.501E-07	2.670E-05	13.27
27	1.974	3.741E-07	2.235E-05	11.03
28	2.050	3.474E-12	2.133E-05	18.16
29	2.082	3.033E-07	1.612E-05	19.80
30	2.124	6.892E-07	1.774E-05	10.12
31	2.194	6.180E-07	1.045E-09	300.00
32	2.253	1.610E-08	1.270E-05	12.46
33	2.378	2.043E-07	4.703E-06	40.26
34	2.577	9.703E-09	9.081E-07	125.71
35	2.776	5.202E-08	8.735E-13	300.00
36	2.974	9.308E-07	8.514E-08	300.00
37	3.172	3.534E-07	1.280E-09	300.00

Table A-17: Form factors for the 12.52-MeV level

Run No.	q_{eff} (fm^{-1})	σ (fm^2/st)	$\mid FF \mid^2$ *Tot.*	Err (%)	$\mid FF \mid^2$ *Long.*	Err (%)
5	0.663	1.145E-10	2.438E-04	7.25	1.980E-04	4.90
6	0.677	5.589E-11	1.516E-04	141.45	1.137E-04	7.10
7	0.773	1.544E-10	1.921E-04	12.00	1.358E-04	6.90
8	0.869	6.577E-11	1.579E-04	8.16	8.115E-05	7.91
9	0.902	8.916E-15	3.026E-04	18.94	1.588E-04	9.77
10	0.964	7.172E-11	2.323E-04	6.56	1.265E-04	7.23
11	1.012	1.135E-10	2.449E-04	8.27	1.631E-04	6.32
12	1.087	3.468E-11	2.920E-04	15.71	1.830E-04	8.47
13	1.148	4.231E-15	2.978E-04	4.09	1.764E-04	5.54
14	1.207	7.236E-12	3.461E-04	10.60	2.124E-04	8.38
15	1.267	6.526E-11	3.539E-04	3.87	2.064E-04	5.43
16	1.326	2.026E-13	3.595E-04	5.35	2.005E-04	6.81
17	1.395	7.469E-19	3.742E-04	3.44	2.024E-04	5.67
18	1.452	7.145E-11	3.915E-04	4.68	2.082E-04	6.65
20	1.531	2.842E-13	3.916E-04	3.57	1.930E-04	6.51
21	1.597	2.743E-11	3.914E-04	4.09	1.805E-04	7.62
22	1.661	6.740E-15	2.923E-04	9.39	1.328E-04	15.30
23	1.662	8.643E-12	3.853E-04	3.54	1.608E-04	8.18
24	1.737	6.405E-14	3.843E-04	4.20	1.511E-04	10.03
25	1.809	1.053E-10	3.710E-04	3.74	1.326E-04	11.03
26	1.879	2.099E-11	3.391E-04	5.08	9.475E-05	18.16
27	1.967	1.391E-14	2.969E-04	4.80	5.357E-05	28.40
28	2.043	2.282E-13	2.724E-04	6.03	3.059E-05	53.26
29	2.077	5.142E-11	1.822E-04	9.33	4.877E-05	28.09
30	2.116	3.921E-13	2.659E-04	4.28	3.127E-05	41.92
31	2.186	7.003E-11	2.329E-04	8.09	1.119E-05	152.55
32	2.245	4.704E-13	1.941E-04	5.26	1.000E-10	300.00
33	2.371	1.961E-11	1.046E-04	9.92	2.466E-05	32.20
34	2.571	6.346E-11	3.100E-05	11.08	1.000E-10	300.00
35	2.769	4.109E-11	1.126E-05	11.17	1.000E-10	300.00
36	2.967	2.565E-15	1.099E-05	300.00	9.145E-06	25.32
37	3.165	2.985E-13	7.729E-06	16.29	5.513E-06	46.23

Table A-18: Form factors for $\frac{5}{2}^+$ (13.61 MeV)

Run No.	q_{eff} (fm^{-1})	σ (fm^2/st)	$\mid FF \mid^2$	Err (%)
5	0.660	1.145E-10	6.174E-05	20.17
6	0.675	5.589E-11	2.808E-05	63.07
7	0.770	1.544E-10	4.654E-05	29.79
8	0.866	6.577E-11	2.406E-05	21.89
10	0.961	8.916E-15	1.597E-05	39.48
11	1.010	7.172E-11	3.313E-05	34.55
12	1.085	1.135E-10	2.146E-05	51.50
13	1.146	3.468E-11	1.946E-05	16.81
14	1.205	4.231E-15	2.338E-05	52.03
15	1.265	7.236E-12	1.502E-05	21.97
16	1.324	6.526E-11	2.189E-05	35.57
17	1.393	2.026E-13	1.215E-05	72.43
18	1.450	7.469E-19	1.281E-05	37.66
21	1.594	7.145E-11	1.113E-05	37.64
23	1.659	2.842E-13	1.096E-05	77.29
24	1.733	2.743E-11	6.187E-06	200.82
25	1.805	6.740E-15	3.531E-06	300.00
26	1.875	8.643E-12	1.003E-03	247.41
27	1.963	6.405E-14	5.405E-06	88.87
28	2.039	1.053E-10	1.602E-06	300.00
29	2.074	2.099E-11	1.473E-08	300.00
30	2.112	1.391E-14	3.515E-06	300.00
31	2.182	2.282E-13	3.810E-06	266.70
32	2.241	5.142E-11	5.937E-07	300.00
34	2.568	3.921E-13	6.087E-07	300.00
35	2.766	7.003E-11	2.341E-09	300.00
36	2.963	4.704E-13	4.786E-11	300.00
37	3.161	1.961E-11	3.509E-07	300.00

Table A-19: Form factors for $\frac{7^+}{2_1}$ (7.57 MeV)

Run No.	q_{eff} (fm^{-1})	σ (fm^2/st)	$\mid FF \mid^2$ *Tot.*	Err (%)	$\mid FF \mid^2$ *Long.*	Err (%)
5	0.677	1.145E-10	2.822E-04	7.85	2.758E-04	8.04
6	0.687	5.589E-11	2.638E-04	5.61	2.586E-04	5.73
7	0.784	1.544E-10	5.726E-04	4.18	5.630E-04	4.25
8	0.882	6.577E-11	6.223E-04	3.30	6.008E-04	3.43
9	0.921	8.916E-15	7.651E-04	7.94	7.184E-04	8.48
10	0.979	7.172E-11	8.964E-04	3.25	8.657E-04	3.38
11	1.021	4.571E-10	1.075E-03	3.38	1.052E-03	3.46
12	1.096	1.018E-09	1.357E-03	3.66	1.322E-03	3.76
13	1.158	2.994E-07	1.409E-03	3.09	1.369E-03	3.18
14	1.218	1.018E-07	1.727E-03	3.68	1.683E-03	3.78
15	1.278	1.388E-06	1.672E-03	3.03	1.620E-03	3.13
16	1.337	8.562E-07	1.681E-03	3.29	1.622E-03	3.41
17	1.407	2.826E-07	1.784E-03	3.13	1.723E-03	3.24
18	1.465	3.186E-09	1.693E-03	3.19	1.630E-03	3.32
20	1.544	2.963E-07	1.754E-03	3.05	1.687E-03	3.18
21	1.611	4.138E-09	1.545E-03	3.20	1.473E-03	3.37
22	1.671	1.548E-07	1.416E-03	8.69	1.361E-03	9.04
23	1.676	7.661E-07	1.448E-03	3.16	1.370E-03	3.35
24	1.752	1.618E-12	1.255E-03	3.27	1.177E-03	3.51
25	1.824	5.548E-11	1.057E-03	3.20	9.865E-04	3.46
26	1.895	4.580E-07	8.299E-04	3.72	7.664E-04	4.09
27	1.984	1.501E-07	6.726E-04	3.77	6.088E-04	4.27
28	2.061	3.741E-07	5.055E-04	4.62	4.395E-04	5.49
29	2.089	3.474E-12	4.447E-04	8.88	4.073E-04	9.72
30	2.134	3.033E-07	3.840E-04	3.87	3.200E-04	4.99
31	2.205	6.892E-07	2.704E-04	6.51	2.146E-04	8.57
32	2.264	6.180E-07	1.908E-04	4.81	1.418E-04	7.30
33	2.386	1.610E-08	1.282E-04	9.02	1.064E-04	10.94
34	2.587	2.043E-07	3.199E-05	11.00	1.775E-05	20.53
35	2.785	9.703E-09	8.850E-06	14.36	6.645E-07	218.86
36	2.984	5.202E-08	3.121E-06	21.55	1.704E-06	92.03
37	3.183	9.308E-07	2.268E-06	26.53	5.631E-07	300.00

Table A-20: Form factors for $\frac{9}{2}^+_1$ (10.69 MeV)

Run No.	q_{eff} (fm^{-1})	σ (fm^2/st)	$\mid FF \mid^2$ *Tot.*	Err (%)	$\mid FF \mid^2$ *Long.*	Err (%)
3	0.508	1.145E-10	6.322E-05	15.04	6.745E-05	20.98
5	0.669	5.589E-11	1.412E-04	7.41	1.311E-04	8.01
6	0.681	1.544E-10	7.298E-05	12.45	6.416E-05	14.17
7	0.777	6.577E-11	9.085E-05	11.13	7.386E-05	14.86
8	0.874	8.916E-15	6.217E-05	6.62	3.778E-05	15.29
9	0.909	7.172E-11	1.352E-04	27.22	8.927E-05	41.64
10	0.970	1.135E-10	8.761E-05	6.46	4.819E-05	14.64
11	1.016	3.468E-11	1.337E-04	6.28	9.908E-05	9.58
12	1.090	4.231E-15	1.673E-04	7.52	1.258E-04	10.16
13	1.152	7.236E-12	1.635E-04	3.55	1.179E-04	5.54
14	1.211	6.526E-11	2.202E-04	6.78	1.705E-04	9.07
15	1.272	2.026E-13	1.902E-04	3.52	1.361E-04	6.18
16	1.330	7.469E-19	1.883E-04	5.26	1.287E-04	8.71
17	1.400	7.145E-11	1.975E-04	3.43	1.302E-04	6.23
18	1.457	2.842E-13	1.851E-04	4.33	1.107E-04	7.99
20	1.536	2.743E-11	1.983E-04	3.65	1.169E-04	6.84
21	1.602	6.740E-15	1.791E-04	4.17	9.481E-05	8.84
22	1.665	8.643E-12	1.590E-04	9.65	9.678E-05	16.16
23	1.667	6.405E-14	1.779E-04	3.74	9.033E-05	8.73
24	1.742	4.241E-10	1.594E-04	4.85	7.030E-05	13.71
25	1.814	6.053E-07	1.484E-04	3.87	5.931E-05	16.56
26	1.885	1.501E-07	1.454E-04	5.93	5.629E-05	24.07
27	1.973	3.741E-07	1.146E-04	5.70	1.932E-05	56.25
28	2.050	3.474E-12	1.097E-04	8.06	7.774E-06	140.94
29	2.081	3.033E-07	8.006E-05	10.94	2.168E-05	42.72
30	2.123	6.892E-07	9.059E-05	5.20	1.000E-10	300.00
31	2.193	6.180E-07	8.894E-05	10.81	1.000E-10	300.00
32	2.252	1.610E-08	6.782E-05	6.33	1.000E-10	300.00
33	2.377	2.043E-07	3.250E-05	12.38	1.232E-06	300.00
35	2.775	5.202E-08	7.078E-06	20.59	1.000E-10	300.00
36	2.973	9.308E-07	2.962E-06	26.26	1.000E-10	300.00
37	3.172	3.534E-07	2.104E-06	54.74	1.000E-10	300.00

Table A-21: Transverse form factors for $\frac{5}{21}^+ + \frac{1}{21}^+$ (5.30 MeV)

Run. No.	q_{eff} (fm^{-1})	$\mid FF \mid^2$ Trans.	Err. (%)
38	0.510	1.484E-05	175.20
40	0.824	3.730E-05	6.00
41	0.919	3.800E-05	5.00
42	0.971	3.570E-05	9.00
43	1.015	3.680E-05	6.00
44	1.117	4.390E-05	6.00
45	1.216	5.060E-05	7.00
46	1.317	6.440E-05	6.00
47	1.516	6.670E-05	6.00
48	1.713	8.180E-05	5.00
49	1.908	6.500E-05	7.00
50	2.104	4.980E-05	5.00
51	2.254	3.410E-05	11.00
52	2.401	2.660E-05	6.00
53	2.737	8.840E-06	6.00
54	2.974	3.680E-06	9.00
55	3.262	1.100E-06	20.00

Table A-22: Transverse form factors for $\frac{1}{24}^+$ (11.44 MeV)

Run. No.	q_{eff} (fm^{-1})	$\mid FF \mid^2$ Trans.	Err. (%)
39	0.693	7.760E-06	15.00
42	0.939	9.690E-06	25.01
43	0.983	1.660E-05	18.00
44	1.086	1.460E-05	23.00
46	1.286	1.800E-05	27.00
47	1.485	2.460E-05	10.00
48	1.684	2.000E-05	30.00
49	1.877	2.310E-05	32.00
50	2.073	2.680E-05	18.00
51	2.224	1.840E-05	21.00
52	2.370	7.000E-06	66.00
53	2.706	4.510E-06	35.01
54	2.944	1.020E-06	38.00

Table A-23: Transverse form factors for $\frac{3}{2}^+_1$ (7.30 MeV)

Run. No.	q_{eff} (fm^{-1})	$\mid FF \mid^2$ Trans.	Err. (%)
38	0.494	1.739E-06	109.26
39	0.715	2.040E-06	33.00
40	0.814	3.160E-06	50.00
41	0.908	1.160E-06	100.00
42	0.962	1.950E-06	62.00
43	1.005	2.320E-06	68.02
44	1.107	9.960E-06	16.00
45	1.206	6.860E-06	58.99
46	1.307	1.220E-05	25.00
47	1.506	2.600E-05	15.00
48	1.703	2.930E-05	13.00
49	1.898	3.350E-05	14.00
50	2.094	2.180E-05	19.00
51	2.244	1.670E-05	17.00
52	2.391	1.000E-05	11.00
53	2.728	1.760E-06	41.00
54	2.964	5.600E-07	83.00
55	3.250	6.000E-08	100.00

Table A-24: Transverse form factors for $\frac{3}{2}^+_2$ (8.57 MeV)

Run. No.	q_{eff} (fm^{-1})	$\mid FF \mid^2$ Trans.	Err. (%)
39	0.708	2.400E-05	5.00
40	0.807	1.730E-05	14.00
41	0.902	2.110E-05	12.00
42	0.954	2.000E-05	7.00
43	0.998	2.200E-05	10.00
44	1.100	2.440E-05	6.00
45	1.199	2.150E-05	9.00
46	1.301	1.650E-05	10.00
47	1.499	1.070E-05	25.00
48	1.696	9.400E-06	27.00
49	1.892	5.370E-06	48.99
53	2.721	2.110E-07	24.00
55	3.250	7.000E-10	10.00

Table A-25: Transverse form factors for $\frac{3}{2}^+_3$ (10.07 MeV).

Run. No.	q_{eff} (fm^{-1})	$\mid FF \mid^2$ Trans.	Err. (%)
39	0.700	1.933E-05	7.00
40	0.798	2.889E-05	13.00
42	0.946	1.974E-05	8.00
43	0.990	1.082E-05	35.00
44	1.090	1.730E-05	17.00
46	1.293	7.440E-06	70.00
47	1.492	9.110E-06	24.00

Table A-26: Transverse form factors for $\frac{5}{2}^+_2$ (7.15 MeV)

Run. No.	q_{eff} (fm^{-1})	$\mid FF \mid^2$ Trans.	Err. (%)
39	0.716	2.220E-06	31.00
40	0.814	6.400E-06	22.00
41	0.909	1.070E-05	18.00
42	0.962	1.070E-05	12.00
43	1.005	7.250E-06	26.00
44	1.107	1.220E-05	13.00
45	1.206	1.240E-05	31.00
46	1.308	1.910E-05	16.00
47	1.507	1.710E-05	20.00
48	1.704	1.220E-05	27.00
49	1.899	8.050E-06	48.00
50	2.094	6.480E-06	52.01
51	2.245	3.490E-06	80.00
53	2.728	1.430E-06	45.00
54	2.965	3.700E-07	100.00
55	3.250	1.000E-07	100.00

Table A-27: Transverse form factors for the 9.15-MeV level

Run. No.	q_{eff} (fm^{-1})	$\mid FF \mid^2$ Trans.	Err. (%)
39	0.706	1.606E-05	9.00
40	0.804	1.412E-05	13.00
41	0.898	1.600E-05	15.00
42	0.951	1.498E-05	9.00
43	0.995	1.860E-05	13.00
44	1.097	3.000E-05	15.00
46	1.298	2.720E-05	15.00
47	1.496	3.640E-05	8.00
48	1.693	4.326E-05	7.00
49	1.889	4.037E-05	9.00
50	2.085	3.140E-05	8.00
51	2.235	1.830E-05	17.00
52	2.381	1.830E-05	7.00
53	2.717	6.880E-06	9.00
54	2.955	1.900E-06	23.00
55	3.250	3.000E-07	100.00

Table A-28: Transverse form factors for the 12.52-MeV level

Run. No.	q_{eff} (fm^{-1})	$\mid FF \mid^2$ Trans.	Err. (%)
39	0.687	5.890E-05	4.00
40	0.786	7.880E-05	4.00
42	0.934	1.020E-04	4.00
43	0.977	1.170E-04	4.00
44	1.079	1.680E-04	4.00
46	1.280	2.100E-04	4.00
47	1.479	2.310E-04	4.00
48	1.676	2.380E-04	4.00
49	1.872	2.110E-04	5.00
50	2.063	1.670E-04	4.00
51	2.218	1.200E-04	5.00
52	2.364	7.860E-05	4.00
53	2.701	2.520E-05	8.00
54	2.938	8.490E-06	7.00
55	3.250	1.300E-06	100.00

Table A-29: Transverse form factors for $\frac{7}{2}^+_1$ (7.57 MeV)

Run. No.	q_{eff} (fm^{-1})	$\mid FF \mid^2$ Trans.	Err. (%)
38	0.494	2.070E-06	96.62
39	0.713	8.700E-06	9.00
40	0.812	1.500E-05	12.00
41	0.907	3.120E-05	10.00
42	0.960	3.080E-05	6.00
43	1.003	3.550E-05	7.00
44	1.105	5.790E-05	5.00
45	1.204	6.210E-05	6.00
46	1.306	7.940E-05	4.00
47	1.505	7.750E-05	6.00
48	1.702	8.290E-05	5.00
49	1.897	5.300E-05	9.00
50	2.093	4.620E-05	9.00
51	2.243	2.740E-05	10.00
52	2.389	2.090E-05	6.00
53	2.725	7.700E-06	8.00
54	2.963	3.380E-06	14.00
55	3.250	1.000E-06	100.00

Table A-30: Transverse form factors for $\frac{9}{2}^+_1$ (10.69 MeV)

Run. No.	q_{eff} (fm^{-1})	$\mid FF \mid^2$ Trans.	Err. (%)
39	0.697	1.530E-05	8.00
40	0.796	2.520E-05	29.00
42	0.943	3.280E-05	6.00
43	0.987	5.290E-05	15.00
44	1.089	6.460E-05	5.00
46	1.290	7.710E-05	10.00
47	1.489	9.600E-05	4.00
48	1.686	9.190E-05	5.00
49	1.881	7.660E-05	12.00
50	2.077	7.288E-05	5.00
51	2.228	4.920E-05	9.00
52	2.374	3.020E-05	6.00
53	2.710	9.360E-06	17.00
54	2.947	2.750E-06	16.00

Appendix B

Fitting Function

The resolution function used in the lineshape analysis can be described as an asymmetric hypergausian function with tails. This is given in formula B.1 and illustrated in figure B.1. The subscripts r and l on the parameters, assume that the data is ploted such that the kinematic variable x(excitation energy) increases to the right.

$$\begin{aligned} F_j(x) = &\ h \times exp\{- \mid (x-p)/(k \times w_l) \mid^{\gamma}\} \quad p - m_l \leq x \leq p \\ = &\ h \times exp\{- \mid (x-p)/(k \times w_r) \mid^{\gamma}\} \quad p \leq x \leq p + m_r \qquad (B.1) \\ = &\ h \times w\{t_1/(x-p-m_r-s)\} \qquad x \geq p + m_R \end{aligned}$$

where ,

$w_l = w(1-a)$

$w_r = w(1+a)$

$k = 0.25(ln2)^{-l/\gamma}$

$m_{r,l} = k \times w_{r,l} \ [\ -ln(f_{r,l})\ ]^{l/\gamma}$

$s = -t_1 \times w/f_r$;

The free parameters, some of which are illustrated in figure B.1, are given below:

h = peak height(counts/(MeV $\times$ μ C))

p = peak position (-MeV)

w = $0.5(w_r + w_l)$ = width(FWHM) (MeV)

a = $(w_r - w_l)/(w_r + w_l)$ = asymmetry

γ = exponent(determines the flatness of the top)

f_r = relative match amplitude to hyperbolic part

t_1 = fall-off of hyperbolic part.

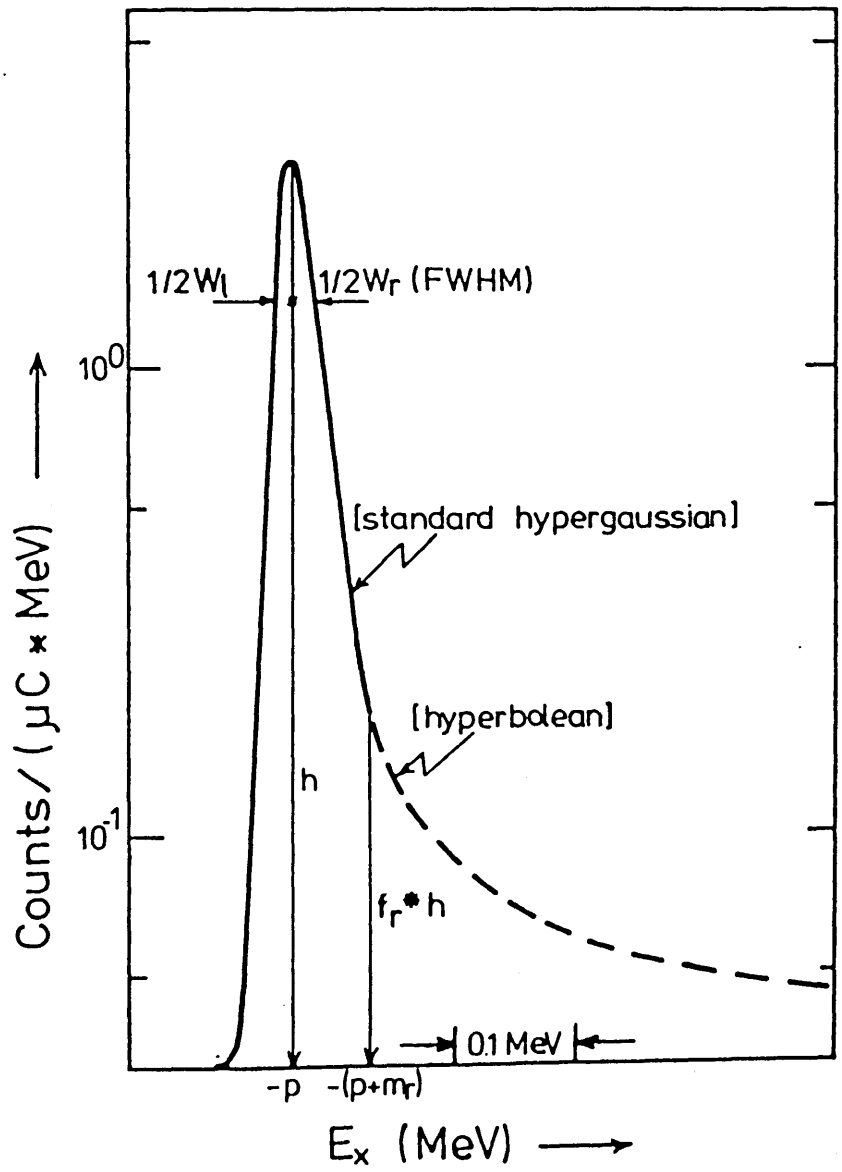

Figure B.1: *The fit function and its parameters used in the fitting procedure[67].*

Bibliography

[1] J.M.Cavedon, B.Frois, D.Goutte, M.Huet, P.Leconte, C.N.Papanicolas, X.H.Phan, S.K.Platchkov, S.E.Williamson, W.Boeglin, and I.Sick, Phys. Rev. Lett. **49** (1982) 978 ;
B.Frois et al., Nucl. Phys. **A396** (1983) 409.

[2] J.W.deVries Ph.D Thesis, University of Utrecht, The Netherland, 1987.

[3] R.Moreh, W.C.Sellyey, and R.Vodhanel, Phys. Rev. **C23** (1981) 988

[4] G.W.Phillips and W.W.Jacobs, Phys. Rev. **184** (1969) 1052

[5] A.Amokrane, M.Allab, H.Beaumevieille, B.Faid, O.Bersillon, B.Chambon, D.Drain and J.L.Vidal, Phys. Rev. **C6** (1972) 1934

[6] W.Kretschmer, G.Probstle and W.Stach, Nucl. Phys. **A333** (1980) 13

[7] J.Bommer, M.Ekpo, H.Fuchs, K.Grabisch and H.Kluge, Nucl. Phys. **A252** (1975) 246 ; Nucl. Phys. **A251** (1975) 257

[8] S.Lie, T.Engeland, and G.Dahll, Nucl. Phys. **A156** (1970) 449; S.Lie, T.Engeland, *ibid.* **A169** (1971) 617; **A267** (1976) 123

[9] V.Bechtold, J.Friedrich, P.Doll, K.T.Knopfle, G.Mairle and G.J.Wagner, Phys. Lett. **72B** (1977) 169

[10] G.Mairle and G.J.Wagner, Z. Physik **258** (1973) 321

[11] M.Yasue, J.J.Hamill, H.C.Bhang, M.A.Rumore and R.J.Peterson, Phys. Rev. **C30** (1984) 770

[12] D.J.Millener and D.Kurath, Nucl. Phys. **A255** (1975) 315

[13] M.H.Harakeh, P.Paul, H.M.Kuan and E.K.Warburton, Phys. Rev. **C12** (1975) 1410

[14] H.R.Weller, R.A.Blue, N.R.Roberson,D.G.Rickel, S.Maripuu, C.P.Cameron, R.D.Ledford, and D.R.Tilley, Phys. Rev. **C13** (1976) 922

[15] E.J.Ansaldo, J.C.Bergstrom and R.Yen, Phys. Rev. **C18** (1978) 587

[16] F.Ajzenberg-Selove, Nucl. Phys. **A449** (1986) 113

[17] A.P.Shukla and G.E.Brown, Nucl. Phys. **A112** (1968) 296

[18] D.J.Millener, private communication.

[19] D.E.Alburger and D.J.Millener, Phys. Rev. **C20** (1979) 1891

[20] E.B.Dally, M.G.Croissiaux and B.Schweitz, Phys Rev. **C2** (1970) 2057

[21] J.C.Kim, H.S.Caplan and I.P.Auer, Phys Lett. **56B** (1975) 442; J.C.Kim, H.S.Caplan and J.C.Bergstrom, Nucl. Phys. **A246** (1975) 282

[22] M.W.S.Macauley, R.P.Singhal, R.G.Arthur, S.W.Brain, W.A.Gillespie, A.Johnston, E.W.Lees and A.G.Slight, J. Phys **G2** (1976) 751

[23] K.Van Der Borg, R.J.DE Meijer, A.Van Der Woude and H.T.Fortune Phys Lett. **34B** (1979) 51

[24] W.R.Falk, A.Djaloeis and D.Ingham, Nucl. Phys. **A252** (1975) 452

[25] A.F.Zeller, K.W.Kemper, T.R.Ophel and A.Johnston, Nucl. Phys. **A344** (1980) 307

[26] I.Tserruya, B.Rosner and K.Bethge, Nucl. Phys. **A213** (1973) 22

[27] T.deForest and J.D.Walecka, Advances in Physics **15**, (1966) 1

[28] H.Uberall, **Electron Scattering from Complex Nuclei**, Academic Press, New York (1971).

[29] L.C.Maximon, Rev. Mod. Phys. **41** (1969) 193

[30] L.Landau, Jour. of Phys. **8** (1944) 201

[31] J.Heisenberg, in **Advances in Nuclear Physics Vol. 12**, (1981).

[32] A.R.Edmonds, **Angular Momentum in Quantum Mechanics.**, (1960).

[33] R.S.Willey, Nucl. Phys. **40** (1963) 529

[34] R.Simon, Ph.D. dissertation, University of Mainz, 1978 (unpublished).

[35] R.S.Willey, Nucl. Phys. **40** (1963) 529 Tables **23** (1979) 103

[36] B.Frois, S.Turck-Chieze, J.B.Bellicard, M.Huet, P.Lecont et al., Phys. Lett. **122B** (1983) 347

[37] D.Goutte, J.B.Bellicard, J.M.Cavedon, B.Frois, M.Huet, et al., Phys. Rev. Lett. **45** (1980) 1618

[38] C.N.Papanicolas, J.Heisenberg, J.Lichtenstadt, J.S.McCarthy, D.Goutte, et al., Phys. Lett. **108B** (1982) 279

[39] H.G.Andresen, The International Conference on Nuclear Structure Studies Using Electron Scattering and Photoreaction, Sendai, 1972 D.Goutte, et al., Phys. Lett. **108B** (1982) 279

[40] C.deVries, C.W.deJager, L.Lapikas, G.Luijckx, R.Maas, H.deVries and P.K.A.deWitt Huberts, Nucl. Instr. & Meth. **223** (1984) 1

[41] H.Blok, Ph.D. Thesis, Vrije Universiteit Amsterdam, 1986

[42] T.N.Buti, Ph.D. Thesis, Massachusetts Institute of Technology, 1984

[43] L.Lapikas, NIKHEF-K Internal Reports on energy calibration, 1982-1983

[44] C.E.Hyde-Wright, Ph.D. Thesis, Massachusetts Institute of Technology, 1984

[45] E.A.J.M.Offerman, private communication.

[46] R.P.Singhal, private communication.

[47] J.C.Bergstrom, M.I.T, Ph.D. Thesis, 1970

[48] C.Creswell, L.N.S.-M.I.T Internal Report, **761** (1976)

[49] C.R.Ottermann, G.Kobschall, K.Maurer, K.Rohrich, Ch.Schmitt and V.H.Walther Nucl. Phys. **A436** (1985) 688

[50] F.Borkpwski et al., Nucl. Phys. **B93** (1975) 461

[51] W.Schutz, Z.Physik **A273** (1975) 69

[52] P.R.Bevington, Data Reduction and Error Analysis for the Physical Sciences, McGraw Hill (1969)

[53] S.Gamba, G.Ricco and G. Rottigni, Nucl. Phys. **A213** (1973) 383

[54] G.E.Brown and A.M.Green, Nucl. Phys. **75** (1966) 401

[55] B.A.Brown, A.Arima, J.B.McGrory, Nucl. Phys. **A277** (1977) 77

[56] R.H.Bassel, B.A.Brown, R.Lindsay, N.Rowley, J. Phys. **G8** (1982) 1215

[57] Bohr and Mottelson, 1975 **Nuclear structure**, Vol.2 (New York: Benjamin).

[58] T.Suzuki, Phys. Rev. **C8** (1973) 2111

[59] T.Carey et al, Phys. Lett. **45** (1980) 239

[60] R.P.Singhal et al, Phys. Rev. **C28** (1983) 513

[61] S.J.Seestrom-Morris, D.Dehnhard, C.L.Morris, D.J.Millener, D.P.Saunders, P.A.Seidl, Rex R.Kiziah and C.Fred Moore, Phys. Rev. **C31** (1985) 923

[62] T.S.H. Lee and D. Kurath, Phys. Rev. **C21** (1980) 293; **C22** (1980) 1670

[63] C.L.Blilie, D.Dehnhard, M.A.Franey, D.H.Gay, D.B.Holtkamp, S.J.Seestrom-Morris, P.J.Ellis, C.L.Morris, D.J.Millener, Phys. Rev. **C30** (1984) 1989

[64] S.Chakravarti, D.Dehnhard, M.A.Franey, S.J.Seestrom-Morris, D.B.Holtkamp, C.L.Blilie, A.C.Hayes, C.L.Morris, D.J.Millener, Phys. Rev. **C35** (1987) 2197

[65] R.H.Helm, Phys. Rev. **104** (1956) 1466

[66] L.J.Tassie, Aust. J. Phys. **9** (1956) 407

[67] A.M.Selig, Ph.D. Thesis, University of Amsterdam, 1985

[68] S.Cohen and D.Kurath, Nucl. Phys. **73** (1965) 1

[69] T.T.S.Kuo and G.E.Brown, Nucl. Phys. **85** (1966) 40

[70] D.J.Millener and Kurath, Nucl. Phys. **A255** (1975) 315

[71] P.W.M. Glaudemans, Miniconference **Nuclear Structure in 1p shell** Amsterdam (1985) 1, and private communication.

[72] R.S.Hicks, R.A.Lindgren, M.A.Plum, G.A.Peterson, H.Crannell, D.I.Sober, H.A.Thiessen, D.J.Millener, Phys. Rev. **C34** (1986) 1161

[73] T.W.Donnelly and W.C.Haxton, At Data Nucl. Data Tables **23** (1979) 103

[74] T.W.Donnelly, A.S.Raskin and J.Dubach, To be published (1988)